Development and understanding of III-N layers for the improvement of high power transistors

Romain Bouveyron

UNIVERSITÉ DE GRENOBLE

THÈSE

Pour obtenir le grade de

DOCTEUR DE L'UNIVERSITÉ DE GRENOBLE

Spécialité : **Matériaux, Mécanique, Génie Civil, Electrochimie**

Arrêté ministérial : 7 août 2006

Présentée par

Romain Bouveyron

Thèse dirigée par **Jean-Michel Hartmann**
et codirigée par **Matthew Charles**

préparée au sein du **CEA-LETI - Laboratoire des surfaces et interfaces**
et de **l'école doctorale Ingénierie des Matériaux, Mécanique, Energétique, Environnement, Procédés et Production (I-MEP2)**

Development and understanding of III-N layers for the improvement of high power transistors

Thèse soutenue publiquement le **31 octobre 2017**,
devant le jury composé de :

Dr. Yvon Cordier
Directeur de recherche au CRHEA-CNRS, Rapporteur
Prof. Georges Brémond
Professeur à l'INSA de Lyon, Rapporteur
Prof. Nicolas Grandjean
Professeur à l'EPFL, Examinateur
Prof. Daniel Bellet
Professeur à Grenoble INP, Examinateur
Dr. Rose-Marie Sauvage
Responsable scientifique à la DGA, Examinateur
Prof. Jean-Michel Hartmann
Directeur de recherche au CEA-LETI, Directeur de thèse
Dr. Matthew Charles
Ingénieur de recherche au CEA-LETI, Co-Encadrant de thèse

Expliquer toute la nature est une tâche trop ardue pour un seul homme ou une seule époque. Il est plus sage de faire peu en étant sûr de soi et laisser le reste à ceux qui viendront après, que présumer de tout sans être sûr de rien.
Isaac Newton

Remerciements

A lot of people contributed to the success of this thesis and I would like to thank all of them.

My first thanks are addressed to Chrystel Deguet and Véronique Carron, successively at the head of the surfaces and interfaces processes service (SSURF) within CEA LETI, for welcoming me to their service between 2013 and 2016. They were able to put, at my disposal, all the means necessary so that the technical work is facilitated.

I was really happy and full of enthusiasm by the quality and the fame of my thesis jury. Thus, I extend sincere thanks to all members of my thesis jury, that is to say reporters Yvon Cordier and Georges Brémond, examiners Nicolas Grandjean and Rose-Marie Sauvage, and to finish the president of the jury Daniel Bellet. I thank them for taking the time to read in detail my thesis manuscript, to have made a detailed report for the reporters, and to have been able to create, thanks to their questions, an extremely interesting discussion the day of my thesis defense. The analysis you have done of my work, and the criticisms made, have helped to give it even more sense and value.

Then I would like to thank my thesis supervisor, Jean-Michel Hartmann, for his involvement and his advices distilled throughout my thesis. His great experience in research and especially epitaxy proved to be an important support in order to make my work and results more coherent, and my communication more accurate for conferences and all of oral presentations I did, including my thesis defense. I thank him for his sympathy and his warm welcome each time I needed his help.

A special and huge thank goes to my technical supervisor, Matthew Charles. It had the privilege to do a thesis with him. His long-standing expertise in the epitaxy world of III-Ns, his sharpness of spirit, his daily involvement in my work and his great sympathy have succeeded in making my research work to excellent results, writing a quality manuscript and finally realizing a very good thesis defense.

A good thesis implies a good supervision. But there are a lot of people who provided technical expertise in physical and chemical characterizations without whom the production of measurements and experimental results would not have been possible. I have to thank Denis Mariolle (AFM), Olivier Renault (XPS), Eugénie Martinez (XPS and AES), Névine Rochat (cathodoluminescence), François Pierre (RBS), Anass Benayad (XPS), Anne-Marie Papon (TEM), and Emmanuel Nolot (XRR, WDXRF).

I also thank my colleague in the SSURF service for their support occasionally and their sympathy, and my thesis fellows for the atmosphere of joy that reigned in the service : Paul, Jérôme, Joris, Mickaël,

Aurélien, Marwan, Victor, Pierre-Edouard, Gaëtan, Sylvain Vial, Raphael, Rafael, Xavier, Louis, Toshi and probably some others who will recognize themselves.

Finally I sincerely thank the members of my close family for their support during my thesis, starting with my girlfriend, Anne-Lise thanks to whom any difficulty is no longer one and which offers me emotional support and an incomparable love, my parents, Sylvie and Gérard for their unconditional love and generosity, my brother Anthony with whom I always had a great complicity, my grandparents Lucienne, Claudius, Sylvana and Jean who inspired me the values of work, love and respect, so important to me.

Table des matières

1 Framework and requirements of the thesis **3**

1.1 III-Nitrides historical . . . 4

1.2 General properties of III-Nitrides . . . 5

1.2.1 Large band gap materials . . . 5

1.2.2 III-N crystal and wurtzite structure . . . 6

1.2.3 Ternary and quaternary alloys . . . 10

1.3 Crystal defects and dislocations . . . 13

1.3.1 Point defects in crystals : vacancies and impurities . . . 13

1.3.2 Stacking faults . . . 14

1.3.3 Dislocation . . . 15

1.4 III-Nitrides polarization . . . 19

1.4.1 Spontaneous polarization . . . 19

1.4.2 Piezoelectric polarization . . . 20

1.4.3 Two-dimensional electron gas generation in III-nitrides . . . 21

1.5 III-N materials based applications and devices . . . 22

1.5.1 High electron mobility transistors . . . 22

1.5.2 LEDs and LDs . . . 23

Bibliographie . . . 25

2 Growth by MOCVD and samples characterization methods **29**

2.1 MOCVD process of III-N alloys . . . 30

2.1.1 MOCVD introduction . . . 30

2.1.2 Theory of MOCVD and physical processes description . . . 31

2.1.3 MOCVD tool : AIXTRON CRIUS . . . 37

2.1.4 Overall setup . . . 37

2.1.5 Bubbler operation and precurors choice . . . 40

2.1.6 Buffer layers and standard structures . . . 50

2.1.7 Growth of indium containing III-N alloys and phase separation . . . 51

2.2 Characterization techniques . . . 52

2.2.1 Atomic Force Microscopy : AFM . . . 53

2.2.2 X-ray Reflectometry : XRR . . . 59

2.2.3 Photoluminescence : PL . . . 62

2.2.4 X-Ray Diffraction : XRD . . . 64

2.2.5 X-ray Photoelectron Spectrometry : XPS . . . 69

2.2.6 Auger Electron Spectroscopy : AES . . . 73
2.2.7 Wavelength Dispersive X-ray Fluorescence : WDXRF . . . 78
2.2.8 Sheet resistance measurement . . . 79
Bibliographie . . . 83

3 Gallium nitride growth at low temperature 85
3.1 Context of low temperature gallium nitride growth . . . 86
3.2 GaN layers under different growth conditions . . . 87
3.2.1 Influence of growth temperature and thickness on V-defect size . . . 87
3.2.2 Influence of growth rate on V-defect size . . . 91
3.2.3 Influence of MO precursors and carrier gas on V-defect size . . . 91
3.3 V-defects : a model of formation and evolution . . . 93
Bibliographie . . . 99

4 InAlN and InGaAlN : a study of indium incorporation and gallium contamination. 101
4.1 Indium content determination : issues of XPS, WDXRF, and XRD . . . 102
4.2 InGaAlN growth by MOCVD : process conditions, characterizations, and indium incorporation . . . 104
4.2.1 InGaAlN growth under nitrogen carrier gas . . . 105
4.2.2 InGaAlN growth under hydrogen carrier gas . . . 121
4.3 Growth of InAlN layers without gallium pollution . . . 124
Bibliographie . . . 129

5 InGaAlN alloys : phase separation, gallium pollution of MOCVD reactors, and electrical properties. 131
5.1 A study of phase separation in InGaAlN alloys . . . 132
5.1.1 Correlation between band gap energy and lattice parameter . . . 132
5.1.2 PL non emission by InGaAlN samples . . . 133
5.1.3 Quantification of indium segregation using AES measurements . . . 136
5.2 Gallium pollution in MOCVD reactors growing Ga containing alloys . . . 141
5.2.1 Calculation of a virtual TMGa flow from pollution sources in the reactor . . . 142
5.2.2 Cleaning test with Cl_2 : growth of pure InAlN . . . 143
5.3 Surface diagram of InGaAlN layers . . . 144
5.4 Electrical characterization : Rsheet measurements . . . 148
Bibliographie . . . 153

6 InGaAlN capping by SiN and GaN 155
6.1 SiN capping of InGaAlN layers . . . 156
6.1.1 SiN deposition under nitrogen . . . 156
6.1.2 SiN deposition under hydrogen . . . 161
6.2 GaN capping of InGaAlN and InAlN layers . . . 164
6.2.1 Thickness GaN cap optimization . . . 166
6.2.2 Cap temperature variations . . . 167
6.2.3 GaN cap on InAlN barrier layer . . . 169

Bibliographie 175

Appendix : Composition and strain calculation in InGaAlN and InAlN layers using RSM and WDXRF measurements **181**

Communications and publications **183**

Table des figures

1.1 Band gap energy versus a lattice parameter of different semiconductors. Note that the current band gap of InN is 0.65eV. Picture by Nicolas Grandjean. 6
1.2 III-N binary compounds : gap energy versus temperature.[23] 7
1.3 Atoms arrangement in wurtzite and zinc-blende structures. 7
1.4 III-N material layers polarity in wurtzite and zinc blende structure. 8
1.5 Definition of the four parameters of the III-Ns mosaic structure. 9
1.6 Evolution of the band gap depending on the composition and thus the lattice parameter. [30] 12
1.7 (a) Theoretical illustration InGaAlN quaternary band gap. In green color, uniform material. In black color, material with indium-rich areas. (b) Band gap versus indium ratio for an InGaAlN matched on GaN.[29] 13
1.8 V for vacancy, S for atom in substitution and I for interstitial atom. Cubic structure. . 14
1.9 (a) Intrinsic stacking fault, (b) extrinsic stacking fault in ABC sequence of face centered cubic structure. Planes normally arranged compared to each other are symbolized by a triangle pointing upwards, and planes undergoing a stacking fault error are symbolized by triangle pointing downwards. 14
1.10 Stacking faults in III-N materials with hexagonal ABAB sequence along the [0001] direction : a) type I, b) type II, c) type III, and d) extrinsic. The stacking faults are indicated by black arrows and the black and white circles denote cations and anions respectively.[33] 15
1.11 a) Normal cubic structure with black balls as atoms and springs as bonds, b) Positive DC edge dislocation (half plane inserted above DC), c) left-hand DC screw dislocation by relative displacement of crystal faces each side of ABCD, d) right-hand DC screw dislocation.[31] 16
1.12 Burger circuit of cubic crystal with positive edge dislocation, and b) normal cubic crystal. Burger vector represented on b) with a black arrow.[31] 17
1.13 Burger circuit of cubic crystal with positive edge dislocation, and b) normal cubic crystal. Burger vector represented on b) with a black arrow.[31] 17
1.14 a) Simple representation of a mixed dislocation and effect on crystal, and b) Burgers vector **b** of dislocation XY is resolved into a pure edge component **b1** and a pure screw component **b2**.[31] 18
1.15 Model of surface depression connected to a dislocation line.[34] 18
1.16 1x1μm^2 AFM picture of GaN surface grown at 930°C. 19
1.17 Dipolar moment and spontaneous polarization of III-N materials. 20

1.18 Total polarization orientation in AlGaN/GaN heterostructure. 21
1.19 Valence and conduction band versus the depth of the material. Highlighting of the potential well.[37] 22
1.20 III-N HEMT heterostructure 22
1.21 Example of an LED heterostructure 23

2.1 Geometric representation of epitaxy. 31
2.2 MOVPE chemical processes in parallel with physical processes 32
2.3 Growth efficiency (growth rate / TMGa molar flow) as a function of the inverse of the temperature.[1] 33
2.4 Mass transport regime : illustration of physical processes. 34
2.5 Representation of the boundary layer close the growing surface. 35
2.6 Illustration of parasitic reactions. 37
2.7 a) Photo of the AIXTRON CRIUS MOCVD tool, and b) a view of the SiC coated graphite susceptor. 38
2.8 Gas lines in AIXTRON Crius. 39
2.9 growth chamber of AIXTRON CRIUS. 39
2.10 Bubbler schematic. 40
2.11 a) A simple dilution bubbler, and b) a double dilution bubbler for lower MO flow. . . 42
2.12 Three dimension representation of a) the trimethyl structure, b) the NH_3 molecule, c) the methyl radical, and d) the ethyl radical 43
2.13 Influence of temperature gradient, lattice mismatch, and CTE difference on wafer bowing. The CTE case is illustrated for the effect of increasing the temperature of a wafer . . 45
2.14 Detection of wafer bowing using two beam reflected at the surface and detected by 2D CCD camera. Interpretation of laser spot spacing. 46
2.15 Configuration of geometrical parameters defining the bow. 46
2.16 Schematic of the optical configuration of an incident beam refracted and reflected from a surface and an interface between two materials. In reality, the beams are normal to the growth surface. 47
2.17 Three cases of Fabry-Pérot oscillations depending on materials properties : ideally transparent and without roughness, absorbent, and roughening. 48
2.18 Planck's law. 49
2.19 Example of curvature measurement of the buffer structure from the silicon substrate to the thick GaN layer. 50
2.20 Example of reflectance measurement of the buffer structure from the silicon substrate to the thick GaN layer. 51
2.21 a) Phase diagram of InGaN ternary by Stringfellow [6], b) phase diagram of InGaN ternary by Burton [7], c) phase diagram of InAlN ternary by Burton [7]. 52
2.22 Surface tip interaction curve. 54
2.23 Shift of the resonant frequency with the distance tip-surface. 55
2.24 Peak force mode layout 55
2.25 Four parts photodiode and laser reflection. Value of parallel and perpendicular displacement. 56
2.26 Interaction laser-tip-photodiode. 57

2.27 General layout of AFM electronic control. 57
2.28 Bruker Fastscan A Tip zoom and specifications. [9] 58
2.29 1x1 μm AFM picture in tapping mode on 12nm thick InGaAlN layer 58
2.30 XRR layout, mechanism and intensity angle relation. 59
2.31 Incident and reflected X-ray beams at surface sample. [10] 60
2.32 XRR layout, mechanism and intensity angle relation. 61
2.33 XRR measurement on a 12nm thick InAlN layer on 2μm GaN layer. Interpretation of the critical angle, of the inter-fringe spacing, and the slope of the signal. 62
2.34 Luminescence mechanism from a direct band gap semiconductor after laser excitation. 63
2.35 Photoluminescence emission from an InN segregated InGaAlN material. 2D (parallel to surface) point of view. 64
2.36 Photoluminescence measurement : mapping and corresponding spectrum at one pixel. 65
2.37 Bragg's law definition. 65
2.38 X-ray emissions from copper. 66
2.39 General layout of a high resolution double axis XRD. 67
2.40 General layout of a high resolution triple axis XRD. 67
2.41 Superposition of three XRD profiles corresponding to three 200nm thick InGaAlN layers with different In/In+Al solid ratios. The ratios are given in the insert for each sample whose peak InGaAlN peak position is indicated by a line in dotted line. 68
2.42 Photoelectron emission mechanism. 71
2.43 X-ray generation and collimation for XPS analysis. 72
2.44 Hemispherical sector analyzer (photoelectron analyzer). [16] 73
2.45 a) In3d2 and 5d2, b) Ga2p3, c) Al2p, and d) Al2p rays detected by XPS. 74
2.46 Relative composition of the different elements of an InGaAlN layer by XPS measurement. We added the presence of oxygen. 74
2.47 X-ray and Auger electron emission mechanism. 75
2.48 HUV electron gun for AES. [16] 76
2.49 Auger spectra for a) derivative indium signal with the raw signal in the insert, b) and c) the derivative of the gallium and aluminum signals respectively. d) The SEM image that shows the morphology we used to accurately place two measurement areas. 77
2.50 Rsheet measurement setup. 80

3.1 a) TEM cross section image of V-defects in InGaN-GaN multi-quantum wells grown at LETI, b) V-defects seen from the c direction of the crystal. The dislocation line is clearly seen as the source of the pits. Measurements by Nicolas Mante. 86
3.2 V-defect size measurement using Gwyddion software on 120nm thick GaN sample grown at 740°C. Bottom left of figure, the 1x1 μm^2 AFM image with the cut line in black. At the top, the V-defect profile with red points for diameter measurement and blue ones for depth measurement. 88
3.3 V-defect size measurement using Gwyddion software on 120nm thick GaN sample grown at 940°C. Bottom left of figure, the 1x1 μm^2 AFM image with the cut line in black. At the top, the V-defect profile with red points for diameter measurement and blue ones for depth measurement. 89

3.4 1x1 μm^2 AFM images of low temperature GaN grown at three temperatures for two different thicknesses, using N_2 as carrier gas and TMGa as gallium precursor. Vg=540nm/h. 90
3.5 The figure shows the evolution of V-defect diameter versus growth temperature. Growth rates are fixed at 540 nm/h and 180 nm/h with TMGa precursor and N_2 carrier gas. . 91
3.6 1x1 μm^2 AFM images of low temperature GaN grown at three temperatures, using N_2 as carrier gas and TMGa as gallium precursor. Vg=180nm/h for a thickness of 40nm. 91
3.7 Graph showing the average diameter (left), and depth of V-defects (right) in GaN versus the temperature, for two growth rates and a thickness of 40 nm. TMGa and N_2 carrier gas were used. 92
3.8 Average diameter of V-defects in GaN plotted against growth temperature for two MO precursors and two carrier gas. The GaN layers are 40 nm thick with a growth rate of 540 nm/h. 93
3.9 1x1 μm^2 AFM images of GaN grown at various temperatures, using H_2 and N_2 as carrier gas and TMGa and TEGa as gallium precursors. 94
3.10 V-defect model by Franck [12]. 94
3.11 Left, the V-defect profile obtained by AFM measurements on a low temperature GaN layer. The blue line corresponds to the measured height, and the red and green lines are the expected angles of crystallographic planes. Right, a 1x1 μm^2 AFM image showing V-defects from which the profile on the left was extracted (red line). 95
3.12 Schematic of the different growth scenarios, with a "floating" V-defect on the left. . . . 96
3.13 Epitaxial lateral overgrowth (ELOG) [5] and favored planes versus growth temperature 96

4.1 $In/(In + Al)$ ratio measured by WDXRF versus XPS for thirteen InGaAlN samples. . 103
4.2 XRD measurement on 3 different InGaAlN samples 200nm thick. InGaAlN peak positions are given by dotted lines, with indium composition in insert estimated from Bragg's law assuming relaxed layers with no gallium pollution. 104
4.3 Structure of the studied stack of layers : orientation and thickness 105
4.4 Effect of thickness on topology on 1x1μm^2 AFM pictures, and alloy composition by XPS. T=730°C, Vg=3nm/min, TMIn/(TMIn + TMAl) : 41% in the gas phase, carrier gas : N_2. 106
4.5 PL measurements on 15nm, 30nm, 100nm, and 200nm thick InGaAlN samples grown under N_2 and with the same conditions. The dashed lines show the maximum intensity and thus the luminescence wavelength of each sample. 107
4.6 RSM measurements of 30nm and 200nm thick InGaAlN barrier layers. 108
4.7 Luminescence wavelength and band gap energy versus layer thickness of InGaAlN layers grown under same conditions. 109
4.8 Effect of TMIn flow at fixed TMAl flow : on topology on 1x1μm^2 AFM pictures, and gas-alloy composition by XPS. Thickness=200nm, T=730°C, Vg=3nm/min, carrier gas : N_2. 110
4.9 PL spectra of three 200nm thick samples having a In/(In+Al) ratio of 14.5%, 19.2%, and 23.4%. 110
4.10 Spectra of sample 1 : comparison of PL and CL. 3x3μm^2 pictures showing with luminescence at different energy. TMIn flow study 111

4.11 Spectra of sample 2 : comparison of PL and CL. 3x3μm^2 pictures showing luminescence at different energy. TMIn flow study. 112
4.12 RSM measurements on InGaAlN barrier layers with increasing indium content from top to bottom. 113
4.13 Effect of growth temperature : 1x1μm^2 AFM images, and alloy composition by XPS. Thickness=30nm, gas mixture : 41% of indium precursors in the gas phase, Vg=3nm/min, carrier gas : N_2. 115
4.14 PL spectra of three 30nm thick samples having a, In/(In+Al) ratio of 6%, 12%, and 15%.115
4.15 Effect of growth temperature : 1x1μm^2 AFM images, and alloy composition by XPS. Thickness=12nm, gas mixture : 41% of indium precursors in the gas phase, Vg=3nm/min, carrier gas : N_2. 116
4.16 Cross-sectionnal view from 1x1μm^2 AFM images on a) 12nm, and b) 200nm thick InGaAlN sample showing the grain structure at the surface. 117
4.17 Spectra of sample 3 : comparison of PL and CL. 3x3μm^2 pictures showing luminescence at different energy. Temperature study. 117
4.18 Effect of growth rate : 1x1μm^2 AFM images, and alloy composition by XPS. Thickness=30nm, gas mixture : 41% of indium precursors in the gas phase, T=730°C, carrier gas : N_2. 118
4.19 PL spectra of three 30nm thick samples having a growth rate of 3nm/min, 4.5nm/min, and 6nm/min. 119
4.20 Effect of ammonia flow : 1x1μm^2 AFM images, and alloy composition by XPS. Thickness=30nm, gas mixture : 41% of indium precursors in the gas phase, T=730°C, Vg=3nm/min, carrier gas : N_2. 120
4.21 Spectra of sample 1 : comparison of PL and CL. 3x3μm^2 pictures showing luminescence at different energy. 120
4.22 Spectra of sample 2 : comparison of PL and CL. 3x3μm^2 pictures showing luminescence at different energy. 121
4.23 Effect of TMIn and TMAl flow : 1x1μm^2 AFM images. Gas phase composition specified below AFM pictures. Thickness=13nm, gas mixture : 41% of indium precursors in the gas phase, T=750°C, carrier gas : H_2. 122
4.24 Effect of TMIn and TMAl flow : 1x1μm^2 AFM images. Gas phase composition specified below AFM pictures. Thickness=30nm, T=750°C, Vg=3nm/min , carrier gas : H_2. . . 123
4.25 Effect of T and Vg : 1x1μm^2 AFM pictures. Gas phase composition specified below AFM images. Thickness=13nm, gas mixture : 41% of indium precursors in the gas phase, carrier gas : H_2. 124
4.26 Effect of growth temperature : on topology on 1x1μm^2 AFM pictures, and alloy composition by XPS. Thickness=30nm, gas mixture : 41% of indium precursors in the gas phase, Vg=3nm/min, carrier gas : N_2. 125
4.27 Effect of thickness : on topology on 1x1μm^2 AFM pictures, and alloy composition by XPS. T=730°C, Vg=3nm/min, gas mixture : 41% of indium precursors in the gas phase, carrier gas : N_2. 126
4.28 TEM cross section of 100nm thick InAlN with EDX analysis on oxygen. 126

5.1 Band gap energy measured by PL versus lattice parameter extracted using XPS measurements. . . . 133
5.2 Correlation between PL peaks and theoretical band gap energy using XPS measurements. Samples without PL emission are plotted on the x-axis. . . . 135
5.3 Band gap energy measured by PL versus lattice parameter extracted using XPS measurements. Points with theoretical PL peak for barrier layer have been added. . . . 135
5.4 SEM picture (zone1) of 100nm thick InAlN surface (sample 1) and two points of measurements for indium segregation study. . . . 137
5.5 Second SEM picture (zone2) of 100nm thick InAlN surface (sample1) and two points of measurements for indium segregation study. . . . 137
5.6 1x1μm^2 AFM picture showing the surface morphology of a 100nm thick InAlN sample (sample1). Below, a section showing the profile of the topology. . . . 138
5.7 SEM picture of 200nm thick InGaAlN surface (sample 3) and two points of measurements for indium segregation study. Sample 2 is similar. . . . 139
5.8 Different cases of indium variation detection by AES as a function of spot size, indium-rich phases size and spot position. The red squares represent the measurement spot, and the light and dark blue areas represent low and high indium content areas respectively 140
5.9 Theoretical influence of indium segregation rate on a lattice parameter. Correlation with PL peak position. . . . 141
5.10 EDX analysis of TEM pictures of InAlN/GaN (sample 1) . . . 142
5.11 Effective TMGa flow coming from the pollution versus real TMIn flow. Except for two points indicated by arrows, all the other samples were grown at 100mbar. . . . 143
5.12 Cleaning process between GaN and InAlN layers. . . . 144
5.13 Comparison between topologies (1x1μm^2 AFM pictures) and compositions (XPS), of InGaAlN samples with and without Cl_2 cleaning after the GaN buffer layers. . . . 145
5.14 Surface diagram of InGaAlN samples using 1x1μm^2 AFM pictures. Correlation of morphology, indium content and temperature. . . . 146
5.15 Surface diagram of InGaAlN samples using 1x1μm^2 AFM pictures. Correlation of morphology, indium content and temperature, with samples showing differences in growth rates superposed at 730°C. . . . 147
5.16 Surface diagram of InGaAlN samples using 1x1μm^2 AFM pictures. Correlation of morphology, indium content and thickness at 730°C. . . . 148
5.17 Rsheet values of InGaAlN and InAlN samples with or without AlN spacer, versus total polarization of the barrier layer. Measurements at the centre of the wafer. . . . 150
5.18 Rsheet values of InGaAlN and InAlN samples with or without AlN spacer, versustotal polarization of the barrier layer. Measurements at the edge of the wafer. . . . 150
5.19 Comparison of 1x1μm^2 AFM pictures of two 12nm thick InGaAlN samples grown under N_2 with and without an AlN spacer . . . 151

6.1 1x1μm AFM pictures of 25nm thick $Al_{0.25}Ga_{0.75}N$ layers having different SiN cap thicknesses. . . . 157
6.2 Comparison of noise in Rsheet measurements on AlGaN barrier layers different thicknesses of SiN cap. . . . 157

6.3 Natural logarithm of SiN deposition rate versus inverse of deposition temperature. The linear behavior indicates that the growth rate follows the Arrhenius law in kinetic regime. 159
6.4 1x1μm^2 AFM images of 12nm thick InGaAlN layers having different SiN deposition time grown under nitrogen at 725°C. 159
6.5 1x1μm^2 AFM pictures of 12nm thick $In_{0.08}Ga_{0.21}Al_{0.71}N$ layers having SiN caps grown at different temperatures under nitrogen at 725°C. 160
6.6 Comparison between Rsheet measurements on AlGaN barrier layers with and without an SiN cap, and on an InGaAlN barrier with a SiN cap grown at 830°C during 320s. . 160
6.7 In, Ga, Al and O concentration profiles by XPS measurement along a SiN cap and InGaAlN barrier layer, both grown under nitrogen. 161
6.8 1x1μm^2 AFM pictures of 12nm thick $In_{0.10}Ga_{0.19}Al_{0.71}N$ layers having different SiN cap SiN growth temperature grown under hydrogen. 162
6.9 In, Ga, Al and O concentration profiles by XPS measurement along a supposed SiN cap and an InGaAlN barrier layers, under different cap process conditions. Si element shown only in the first second samples but present in each one. 162
6.10 Rsheet measurements on InGaAlN barrier layers under nitrogen carrier gas with different growth conditions of an SiN cap under hydrogen carrier gas (left). The standard deviation of Rsheet measurements on the same three same samples.(right) 163
6.11 1x1μm^2 AFM picture, and concentration profile by XPS along an SiN cap and an InGaAlN barrier layer, both under hydrogen carrier gas at 750°C during 320s. 165
6.12 Rsheet measurements of InGaAlN barrier layers covered or not by an SiN cap versus the barrier band gap energy. 165
6.13 1x1μm^2 AFM pictures of three different thicknesses of GaN caps on12nm thick InGaAlN barrier layer. T_{cap}=730°C. 166
6.14 Cross sections from 1x1μm^2 AFM pictures of three different thicknesses of GaN caps on 12nm thick InGaAlN barrier layer. T_{cap}=730°C. In red ovals, non covered InGaAlN areas. 167
6.15 Rsheet versus GaN cap thickness : 2nm, 4nm, 8nm. No AlN spacer between GaN pseudosubstrate and InGaAlN barrier layer. 168
6.16 1x1μm^2 AFM pictures of GaN cap 4nm thick grown on 12nm thick InGaAlN layer at 660°C, 730°C. Carrier gas for barrier and cap : N_2. InGaAlN composition shown below each picture. 169
6.17 1x1μm^2 AFM pictures of a 12nm thick $In_{0.27}Al_{0.73}N$ barrier layer, and of a 5nm thick GaN cap grown on 12nm thick $In_{0.27}Al_{0.73}N$ layer. 170
6.18 Two TEM pictures placed side by side of GaN pseudo-substrate, AlN spacer and InAlN layer. Left picture : 7-8nm thick InAlN layer. Right picture 3-4nm thick GaN cap on 10-11nm thick InAlN. 170
6.19 Comparison of AFM tip size versus InAlN layer roughness on TEM picture. Red curve : roughness profile from an AFM picture on the same sample. 171
6.20 XRR profiles of 8nm thick InAlN barrier layer and an 11nm thick InAlN barrier layer with a 4nm thick GaN cap. 172

Liste des tableaux

1.1 Bowing parameters in electron volt for the ternary alloys, and their values for x=0.5. [29] 11

2.1 Chemical properties of MO precursors. 41
2.2 Relationship between quantum numbers, spectroscopists' notation and X-ray notation. 70

4.1 Summary of XPS compositions, barrier layer PL peak positions and theoretical linear band gaps and wavelenghts of four samples having different thicknesses : 15nm, 30nm, 100nm, and 200nm. 107
4.2 Summary of experiments showing the comparison between different barrier layers peak positions in photo and catodoluminescence spectra. TMIn flow study 111
4.3 Summary of a and c lattice parameters calculated using RSM measurements, the strain associated with the in-plane lattice parameter a, and the composition calculated from the equation described in the text. 114
4.4 Summary of experiments showing the comparison between different barrier layers peak positions in photo and catodoluminescence spectra.Temperature study. 114
4.5 Summary of experiments showing the comparison between different barrier layers peak positions in photo and cathodoluminescence spectra. Ammonia flow study. 119

5.1 Summary of samples used for In segregation study by Auger electron spectroscopy. . . 138

6.1 Summary of SiN cap experiments performed on InGaAlN barriers grown under nitrogen and hydrogen. Theoretical deposition rate and thus thicknesses of SiN are calculated using the Arrhenius law that we can be drawn in kinetic regime (cf. figure 6.3) using experimental data of SiN cap on AlGaN layers deposited under hydrogen. Therefore values for SiN cap under nitrogen are not exactly the real theoretical ones but nevertheless close to reality. 158
6.2 Summary of Rsheet values depending on the heterostructure in the GaN cap study. . . 168

Résumé

Dans le tout premier chapitre de ce manuscrit de thèse, après un bref rappel historique sur la croissance des matériaux III-N au cours du XXème siècle, et ce depuis les années 1930, nous avons commencé par définir ce qui les caractérise et détailler leurs propriétés. Leur famille comprend trois semi-conducteurs binaires à gap direct, InN, GaN et AlN, dont l'association en alliages ternaires ou quaternaires permet d'obtenir des semi-conducteurs dont la valeur de bande interdite varie sur une large plage de 0.78 eV à 6.2 eV. Cela correspond typiquement à un balayage spectral du proche infrarouge à l'UV lointain, ce qui en fait de bon candidats pour les applications optiques mais pas uniquement. Pour les ternaires, une composition chimique donnée implique un ensemble de paramètres de maille a et c et une énergie particulière de bande interdite. D'un autre côté, l'un des grands avantages des alliages quaternaires est de maintenir, par exemple, les paramètres de maille du cristal, mais de changer l'énergie de la bande interdite en modifiant la composition puisque le troisième binaire de l'alliage offre un degré de liberté supplémentaire. En outre, alors que leur paramètre de maille suit la loi linéaire de Vegard, l'évaluation théorique de l'énergie de bande interdite nécessite le calcul ou au moins la détermination expérimentale de paramètres de courbures dont l'intérêt est de reproduire l'écart de la variation de l'énergie de bande interdite par rapport à une loi linéaire.

La structure cristalline stable des matériaux III-N est de type hexagonal et est plus précisément nommée wurtzite. Elle est en fait une interpénétration de deux mailles hexagonales translatées de 5/8 du paramètre c selon l'axe [0001]. Afin de lui correspondre pour entamer une croissance, des substrats de natures différentes ont été essayés et aujourd'hui, les plus communs sont le carbure de silicium SiC, le saphir Al_2O_3 pour les petits diamètres et, dans notre cas, le silicium cubique orienté (111) avec cette fois ci un diamètre de 200mm et un faible prix comparé aux deux précédents substrats.

Ensuite, nous avons énuméré les défauts cristallins que l'on retrouve usuellement dans les matériaux semi-conducteurs épitaxiés. On retrouve à ce titre des lacunes, des impuretés (interstitielles et en substitution), des fautes d'empilement et enfin des dislocations. Le rôle néfaste des dislocations reste aujourd'hui assez ambigu dans la littérature bien qu'elles soient souvent citées comme étant des centres de recombinaison d'excitons (non radiatives), des pièges de charge, et surtout des initiatrices de la formation d'un défaut de surface nommé V-defect, tel que prédit par Frank dans les années 1950.

Toujours dans le chapitre 1, nous avons également expliqué que l'interface entre deux matériaux III-N différents, est une zone où un gaz d'électrons à deux dimensions (2DEG) est formé par une discontinuité de polarisation entre les deux couches en contact. La polarisation de ces couches provient des dipôles formés à l'échelle de la maille cristalline par les liaisons entre les atomes d'azote et les

atomes métalliques. Elle est divisée en polarisation spontanée (sans contrainte) et en polarisation piézoélectrique induite par une contrainte élastique supplémentaire sur le matériau par le substrat ou la couche d'en dessous dans l'hétérostructure.

Enfin nous avons clôturé ce premier chapitre en décrivant les deux principales applications des nitrures d'éléments III, qui sont les transistors à haute mobilité électronique (HEMT) fonctionnant sur le principe du mouvement d'électrons au sein d'un gaz bidimensionnel d'électrons (2DEG), et la LED qui fonctionne grâce à la structure de type multipuits quantiques inséré entre des couches de GaN dopé n et p.

Cette thèse a été effectuée dans un contexte industriel au CEA LETI de Grenoble avec l'idée de produire, en fin de compte, des wafers de matériaux III-N de haute qualité, avec un rythme soutenu de production. Dès l'entame du chapitre 2 nous avons donc décrit l'équipement de production d'échantillons utilisé qui un réacteur MOCVD entièrement automatisé de la société AIXTRON. Il contient un système nommé close coupled showerhead et qui constitue un système d'injection des gaz réactifs dans la chambre de croissance grâce à une sorte de pommeau de douche pour assurer la croissance de couches homogènes. Un système de chargement et déchargement automatique d'échantillons optimise quant à lui le rythme de production.

Le processus de nettoyage de la chambre de croissance ne nécessite pas son ouverture comme la plupart des réacteurs mais est effectué de manière intrinsèque par du chlore gazeux. Ce réacteur nous permet par ailleurs de développer des matériaux III-N sur des substrats de silicium larges de 200 mm sous azote et hydrogène en tant que gaz porteur et ce en prenant comme précurseurs organométalliques le TMIn, TMGa, TMAl et TEGa et bien sûr de l'ammoniac comme précurseur pour l'azote.

Le système présente un moniteur de croissance avec des capteurs de courbure de wafer et de température in situ, ainsi qu'une réflectométrie pour les étalonnages des vitesses de croissance. A l'intérieur de l'équipement, il est important de contrôler le fonctionnement du bulleur et donc le stockage des organométalliques. Un contrôle très précis de ses paramètres physiques (température et pression), permet d'envoyer vers le réacteur la bonne quantité de mélange de précurseurs organométalliques qui régira la vitesse de croissance et la composition des alliages dans le régime de croissance limité par le transport de masse. La croissance de nos échantillons se fait toujours dans ce régime puisque la vitesse de croissance est indépendante de la température et ne requiert que l'ajustement du flux d'organométallique pour le moduler et modifier la qualité et les propriétés du cristal fabriqué.

De manière théorique, nous avons pu détailler les processus physiques et chimiques qui régissent la croissance par MOCVD et traiter du problème de la séparation de phases dans la croissance des matériaux III-N contenant l'indium, un élément chimique qui a tendance à ségréger et promouvoir la formation des phases riches en indium et d'autres beaucoup plus pauvres en ce dernier. C'est très préjudiciable puisque cela génère des inhomogénéités de composition dans les matériaux qui peuvent influencer plusieurs propriétés physiques : la luminescence, la rugosité, la résistance locale parmi d'autres.

Dans la deuxième partie du chapitre 2, nous avons décrit toutes les caractérisations que nous avons employées durant cette thèse afin d'étudier notre matériau. Tout d'abord, pour mesurer la rugosité

des surfaces, nous avons évoqué le microscope à force atomique (AFM) et notamment les modes tapping et peak force que nous avons sélectionné. Pour les caractérisations par rayons X, nous avons utilisé la réflectométrie des rayons X (XRR) pour les mesures d'épaisseur de couche, la diffraction des rayons X (XRD) pour l'étude de la structure cristalline et, habituellement, l'analyse de la composition chimique des alliages, la spectrométrie photoélectrique des rayons X (XPS) et la fluorescence des rayons X (WDXRF) pour la composition d'alliages à différentes échelles. L'utilisation de la spectrométrie d'électrons Auger (AES) a donné des informations supplémentaires sur la composition des alliages à l'échelle nanométrique. Elle a notamment permis d'avoir les premiers indices mettant en évidence le phénomène de séparation de phase dans les alliages III-N à base d'indium. Enfin, nous avons utilisé la photoluminescence pour mesurer l'énergie de bande interdite de notre matériau et la technique de mesure quatre points pour évaluer la résistivité du gaz d'électrons à deux dimensions (2DEG).

Dans le troisième chapitre nous avons mis en évidence les défis de la croissance des nitrures d'éléments III à basse température (entre 740 ˚C et 940 ˚C), en particulier pour les alliages contenant de l'indium, et en particulier sur le problème de la présence de défauts en V à la surface de ces alliages. Ainsi, nous avons essayé différents paramètres de croissance pour la production de couches de GaN en dessous de la température de croissance habituelle de 1050 ˚C avec pour gaz porteur l'azote et en utilisant le précurseur TMGa qui est notre norme pour la croissance des alliages contenant de l'indium. La variation de la température de croissance entre 740 ˚C et 940 ˚C influence notamment la taille des défauts en V qui diminue au-dessus d'une certaine température critique. Augmenter également l'épaisseur augmente la taille des défauts en V, mais pas à la température la plus élevée, c'est-à-dire 940 ˚C. Parallèlement, nous avons vu que la vitesse de croissance n'a pas influencé la taille des défauts en V ou même la morphologie de surface. Arbitrairement nous avons retenu une vitesse de 540 nm/h dans notre étude.

Par la suite, nous avons utilisé l'hydrogène comme gaz porteur et la température critique pour la réduction de la taille des défauts en V a été réduite d'environ 100 ˚C. En effet, sous hydrogène, la taille des défauts en V est similaire à celle observée sous azote mais 100 ˚C plus chaud. Le changement des précurseurs organométalliques de TMGa à TEGa semblait augmenter le diamètre des défauts en V d'une douzaine de nanomètres à 750 ℃ et 840 ˚C. Nous attribuons cette augmentation de taille de défauts en V à des vitesses de croissance réelles légèrement différentes de celles calculées de manière théorique et dont nous nous servons pour ajuster les flux de précurseurs pendant les expérimentations. Cela résulte finalement d'un léger manque de calibration entre l'utilisation du TMGa et du TEGa.

Ensuite, nous avons développé un modèle basé sur celui de Frank dans les années 1950, et nous avons examiné le rôle joué par l'énergie de surface des plans inclinés dans les défauts en V. Nous suggérons qu'ils équilibrent la force résultant du champ de contrainte élastique autour de la ligne de dislocation ouverte par le défaut en V. Selon la température et l'atmosphère pendant la croissance, l'énergie de surface des plans inclinés peut changer, ce qui entraîne deux cas. Un cas A où le défaut atteind sa taille d'équilibre et "flotte" à la surface, et le cas B où le défaut continue de croître indéfiniment. Ce modèle correspond parfaitement à nos résultats expérimentaux et implique que le gaz porteur hydrogène stabilise le plan (0002), réduisant la température critique à partir laquelle le défaut ne s'accroît plus avec l'épaisseur. Ainsi, nous montrons l'impact positif de l'utilisation de l'hydrogène en tant que gaz porteur pour la croissance des couches de GaN à basse température.

Le chapitre 4 relate notre aventure dans l'étude matériaux des alliages InGaAlN et InAlN. Avant toute discussion concernant la composition d'alliage, nous avons élaboré un protocole de caractérisation afin d'obtenir la stœchiométrie de notre matériau le plus simplement et le plus précisément possible. Il est vrai que l'XRD est généralement utilisé pour la détermination des compositions chimiques d'alliages épitaxiés. Cependant les quelques essais effectués ont souffert de notre structure complexe comprenant plusieurs couches tampons dans le buffer, et nous avons légitimement décidé d'utiliser systématiquement des mesures XPS dont l'incertitude sans échantillons de calibration est de 5 %. Pour un groupe d'échantillons choisis, la technique de mesure de composition chimique par fluorescence X, qui n'est pas destructive, et qui permet plusieurs points de mesure sur le wafer, s'est avérée beaucoup plus rapide (quelques minutes contre plusieurs heures en XPS selon la résolution en profondeur). La corrélation entre les deux techniques a d'ailleurs montré une relation linéaire et a pu justifier une utilisation ultérieure intéressante de la WDXRF.

Dès lors, nous avons étudié intensivement les alliages d'InGaAlN qui ont subi une croissance en présence de deux gaz porteurs, l'azote et l'hydrogène. Sous azote, qui on le sait stabilise bien mieux l'indium dans les couches de matériaux III-N, nous avons analysé les effets du temps de croissance (donc de l'épaisseur des couches), de la température, du ratio TMIn/TMAl, de la vitesse de croissance et enfin du flux d'ammoniac sur : la morphologie de surface, la composition des alliages, les propriétés de luminescence et les performances électriques. L'étude du temps de croissance, et donc de l'épaisseur des couches, nous a apporté des informations intéressantes sur la rugosité de ces dernières et a pu mettre en évidence un phénomène de séparation de phases (riches et faibles en indium dans les alliages InGaAlN) grâce à des mesures de photoluminescence. Au même titre, une augmentation de la vitesse de croissance a montré un déplacement des pics de photoluminescence, malgré une composition constante des alliages d'InGaAlN. En parallèle, pour augmenter l'incorporation d'indium, nous avons procédé à la diminution de la température de croissance jusqu'à 670 °C (température à partir de laquelle elle s'est stabilisée) et à l'augmentation du ratio TMIn/TMAl.

Dans le cas de l'hydrogène en tant que gaz porteur, l'intégration d'indium dans les mêmes fenêtres procédé que sous azote est impossible même si nous augmentons fortement le flux de TMIn et/ou réduisons celui de TMAl. La clé de cette problématique réside plutôt dans la diminution de la température entre 611 °C et 674 °C pour commencer l'incorporation d'indium dans les couches d'InGaAlN. Là, le taux de croissance apporte une vraie influence et, tout en étant doublé, augmente de manière significative la teneur en indium dans la couche.

Enfin, alors que toutes les couches d'InGaAlN présentaient une pollution au gallium provenant du réacteur, les premiers échantillons étaient de purs alliages ternaire d'InAlN. Ainsi, certaines tendances des couches, en particulier l'évolution de la rugosité et de la teneur en indium, ont été tirées de quelques séries d'expérimentations dans lesquelles nous avons fait varier la température de croissance et l'épaisseur des couches d'InAlN.

Un résultat notable est que nous avons réussi à produire des couches avec des valeurs de bande interdite supérieures à 4 eV, ce qui n'est pas facile en raison de la séparation de phase dans ces types de couches

quaternaires.

Le chapitre 5 est un chapitre de synthèse et d'analyse de résultats. Nous avons établi la corrélation entre l'énergie bande interdite et le paramètre de maille du réseau cristallin de nombreux échantillons d'InGaAlN. Les valeurs des énergies citées dans le chapitre sont potentiellement décalées par rapport à la réalité car les échantillons sont soumis à un phénomène de séparation de phase tel qu'évoqué dans les paragraphes précédents. Par conséquent cela induit une recombinaison des paires électron-trou formées lors d'une quelconque excitation, préférentiellement dans les zones riches en indium puisque l'énergie de bande interdite y est plus faible à ces endroits par rapport au reste de la couche. Lorsque nous avons représenté la valeur de bande interdite en fonction du paramètre de maille de nos couche d'InGaAlN nous avons constaté que beaucoup de nos points expérimentaux étaient proches des limites formées par les lignes courbées qui rejoignent les binaires GaN et AlN, et ce malgré la proportion relativement élevée d'indium mesurée par XPS dans ces mêmes couches.

Partant de ce phénomène de séparation de phase nous avons essayé de le quantifier en employant la technique de caractérisation chimique par spectroscopie Auger, avec un succès notable uniquement sur un échantillon. Ce cas a montré des fluctuations de composition de l'indium à la surface, mais nous avons à terme besoin de plus de mesures pour vraiment commencer à comprendre et à quantifier le phénomène de séparation de phases riches et pauvres en indium dans les couches d'InGaAlN. En outre, la spectroscopie Auger est une caractérisation de surface ayant une excellente résolution (nanométrique) latérale. Cependant la séparation de phase du matériau se produit également à l'intérieur du matériau et sur des échelles pour l'instant inconnues. La tomographie par sonde atomique serait une technique intéressante pour faire progresser cette étude et lui donner encore plus de poids, même s'il est vrai que la préparation d'échantillons de type InGaAlN peut s'avérer difficile.

En troisième grand point du chapitre 5 nous avons examiné et essayé de comprendre le problème de la pollution au gallium dans notre réacteur de MOCVD. Nous avons finalement trouvé un modèle empirique qui prédit l'incorporation du gallium dans les échantillons en simulant l'existence d'un flux de gallium virtuel effectif généré par les sources de pollution présentes dans le réacteur, le tout en fonction du flux de TMIn. Les deux sont fortement corrélés, ce qui peut rendre l'incorporation de l'indium complexe surtout sous hydrogène. Parallèlement, nous avons développé un processus pour éviter cette pollution en effectuant un nettoyage du réacteur entre le moment où le substrat de GaN est fabriqué et le moment où la couche d'In(Ga)AlN est épitaxié. L'élément gallium entre parenthèse traduit cet acte non volontaire de l'intégrer dans les couches qui sont théoriquement d'InAlN.

De manière indépendante nous avons également pu résumé les morphologies de surface mesurées par AFM en fonction des différentes conditions de croissance des alliages et nous avons construit ce que nous pourrions nommer des diagrammes de phase de surface. Des points dans le procédé de croissance sont clairement mis en lumière afin de prédire la fabrication d'un matériau plus ou moins rugueux, avec une structure de grain en surface, ou plutôt de marches atomiques, présentant des fissures, etc. Cela nous a permis de voir une corrélation claire entre l'effet d'une augmentation de la température et d'une diminution de la vitesse de croissance, ce qui implique que la morphologie de la surface est en grande partie régie par la mobilité des atomes adsorbés à la surface lors de la croissance de la couche d'InGaAlN.

La clôture de ce chapitre très riche en résultats est attribuée à une corrélation effectuée entre les valeurs de résistivité du 2DEG mesurées et la polarisation totale du matériau. Dans le cas d'une couche d'InGaAlN sur un substrat GaN sans spacer AlN, l'augmentation de la polarisation totale ou de l'épaisseur de la couche barrière diminue la résistivité du 2DEG. D'autre part, si on place une fine couche d'AlN (nommé spacer), connue pour mieux confiner le 2DEG dans le substrat de GaN, sous l'interface avec la couche barrière, la résistivité du 2DEG ne change pas de manière significative avec la polarisation et il est difficile d'en tirer une tendance.

Le dernier chapitre de ce manuscrit est une étude dont le but a été l'encapsulation (capping) de notre couche barrière par deux types de matériaux : le SiN et le GaN. Les expériences d'encapsulation avec du SiN déposé in-situ, ont débuté avec l'utilisation de gaz porteur azote pour ne pas désorber l'indium de la surface. Une morphologie de surface similaire entre les échantillons avec ou sans ouche d'encapsulation théorique nous a fait penser que le SiN n'avait pas été déposé ou alors en couche très ou trop mince. Même une augmentation de la température de 730 ˚C à 830 ˚C pour favoriser la cinétique du dépôt de SiN n'a pas eu d'effet notable. En parallèle, les mesures de résistivité du 2DEG montrent une valeur de Rsheet bruitée par rapport au temps, qui n'est pas corrélée avec la réponse habituelle des couches d'encapsulation de SiN sur les couches barrière de type AlGaN habituellement fabriquées. Des mesures XPS nous ont permis d'identifier clairement la présence de silicium dans (dopage) ou sur (cap SiN) la couche d'InGaAlN.

Dès lors nous avons décidé d'opter pour le gaz porteur hydrogène, dans le but d'examiner son influence sur le dépôt de SiN par rapport à celui sous azote. Les résultats étaient identiques à l'exception d'un échantillon ayant subi un long temps de dépôt de 960 s à 850 ˚C, ce qui devrait correspondre à un cap de SiN de 9,7 nm. Dès lors, la surface de l'échantillon présentait des fissures qui pouvaient être attribuées soit à la désorption d'indium très superficielle, soit à l'effet du silane sur les défauts de surface. Ce long temps de dépôt de SiN donne également un échantillon ayant un bruit de mesure de résistivité du 2DEG inférieur à celui des deux autres dont les couches d'encapsulation étaientt déposé à 750 ˚C et 850 ˚C mais pendant 320 s. Dans ce cas, la réduction du bruit de mesure peut être dû à des couches de SiN très fines. D'autre part, sous azote ou hydrogène, les mesures des valeurs moyennes de résistivité du 2DEG ont montré des valeurs proches des échantillons d'InGaAlN sans encapsulation ayant un spacer AlN, ces derniers n'ayant pas été insérés dans l'étude avec encapsulation à base de SiN. Cet argument pourrait suggérer un dopage au silicium, mais en toute objectivité, il est difficile d'en être sûr.

Finalement, nous avons recouvert nos échantillons d'InGaAlN avec une couche d'encapsulation à base de GaN épitaxié. Trois épaisseurs de 2 nm, 4 nm et 8 nm ont d'abord été testés, et on a pu observer que des zones en surface laissaient encore apercevoir l'InGaAlN sous-jacent jusqu'à 4 nm d'épaisseur de GaN. En outre, au-dessus de cette épaisseur, nous avons montré que la résistivité du 2DEG était augmentée. Le changement de la température de croissance, pour la couche barrière ainsi que pour la couche d'encapsulation de GaN de 4 nm d'épaisseur, démontre que la structure de grain en surface de l'échantillon d'InGaAlN sans encapsulation à basse température n'est pas nivelée par la couche d'encapsulation de type GaN. Enfin, nous avons encaspulé avec succès une couche

d'InAlN avec du GaN de 5 nm d'épaisseur, et nous avons alors clairement vu ses avantages sur la rugosité grâce à des mesures TEM, même si la résistivité du 2DEG augmentait de 230 Ohm/sq à 409 Ohm/sq.

List of abbreviation

III-N, III-nitride – *Nitride of group III elements*

HVPE – *Hydride Vapour Phase Epitaxy*

MOCVD – *Metalorganic Chemical Vapor Deposition*

MOVPE – *Metalorganic Vapour Phase Epitaxy*

MBE – *Molecular Beam Epitaxy*

LED – *Light Emitting Diode*

LD – *Laser Diode*

HEMT – *High Electron Mobility Transistor*

UV – *Ultraviolet*

Eg – *Band gap energy*

2H – *Wurtzite structure*

3C – *Zinc-blende structure*

CTE – *Coefficient of Thermal Expansion*

GaN – *Gallium Nitride*

AlN – *Aluminum Nitride*

InN – *Indium Nitride*

InAlN – *Indium Aluminum Nitride*

AlGaN – *Aluminum Gallium Nitride*

InGaN – *Indium Gallium Nitride*

InGaAlN – *Indium Gallium Aluminum Nitride*

$A_xB_{1-x}N$ – *Nitride ternary alloy with two A and B elements as cations with respective x and 1-x compositions*

$A_xB_yC_{1-x-y}N$ – *Nitride quaternary alloy with three A, B and C elements as cations with respective x, y and 1-x-y compositions*

a_{AN} – *"a" lattice parameter of AN type binary*

c_{AN} – *"c" lattice parameter of AN type binary*

ϵ_x – *in-plane biaxial strain*

ϵ_z – *out-plane biaxial strain*

$b_{A_xB_{1-x}N}$ – *Bowing parameter of ABN type ternary alloy*

P_{SP} – *Spontaneous polarization*

P_{PE} – *Piezoelectric polarization*

Ns – *Charge carrier density*

C_{13} – *Elastic constant from deformaiton tensor*

C_{33} – *Elastic constant from elastic tensor*

Vg – *Growth rate*

Rsheet – *Sheet resistance*

V-defect – *Surface defect on III-N materials with an inverse pyramid shape*

ELOG – *Epitaxial Lateral OverGrowth*

MQW – *Multiple Quantum Well*

MO – *Metalorganics*

TMGa – *Trimethylgallium*

TMAl – *Trimethylaluminum*

TMIn – *Trimethylindium*

TEGa – *Triethylgallium*

N_2 – *Nitrogen*

H_2 – *Hydrogen*

AFM – *Atomic Force Microscopy*

XRR – *X-Ray Reflectivity*

PL – *Photoluminescence*

XRD – *X-Ray Diffraction*

XPS – *X-ray Photoelectron Spectrometry*

AES – *Auger Electron Spectroscopy : AES*

WDXRF – *Wavelength Dispersive X-ray Fluorescence*

4PP – *Sheet resistance measurement*

TEM/HRTEM – *Transmission Electron Microscopy / High Resolution Transmission Electron Microscopy*

SEM – *Secondary Electron Microscopy*

RBS – *Rutherford Backscattering Spectrometry*

General introduction

The work of this thesis is part of the development of high electron mobility transistors (HEMTs), on 200mm diameter (111) silicon substrates. Currently, CEA LETI is using an AlGaN on GaN heterostructure for the fabrication of devices. As InAlN and InGaAlN alloys grown on GaN already demonstrated the possibility to surpass the AlGaN on GaN performance from an electrical point of view, we have the objective to overcome the inherent difficulties to produce good crystal and surface quality layer in order to replace these AlGaN alloys with InAlN or InGaAlN. Such alloys being also used in optoelectronical devices, the prospects for multiquantum-well and then LEDs, Bragg reflectors and other optical applications are also interesting. Around this central part of the study we progressively directed our work toward peripheral developments as growth of GaN at low temperature and the capping of our InGaAlN and InAlN layers.

In the first chapter, after a history of the III-Ns developments, we will detail the general properties of III-nitrides. We will deal with the different substrates that allow a crystalline growth and detail the different kinds of alloys that can be grown and the advantages for each of them. Then we will describe the different crystal defects in monocrystalline semiconductors and give some examples of the effects of dislocation on the III-N materials. As a final point, we will explain the formation of a two-dimensional electron gas in a heterostructure made of two III-N layers, and how this is used in HEMTs.

Chapter 2 combines experimental and theoretical details. In a first part we will detail the MOCVD tool we used during the thesis and the different precursors we used. We will also explain thermodynamic and kinetic concepts currently used to understand the growth by MOCVD. We will also explain the physical reason that make it hard to incorporate indium in III-N layers, which is one of our main issues. After that we will deal with each characterization we performed : atomic force microscopy (AFM) for topology analysis, X-ray diffraction (XRD) for crystal structure and usually composition analysis, X-ray reflectometry (XRR) for layer thickness measurements, X-ray photoelectron spectrometry (XPS) and X-ray fluorescence (WDXRF) for alloys composition at different scales, Auger electron spectrometry (AES) for alloys composition and especially indium segregation study, photoluminescence to measure the band gap energy and Rsheet measurements by four probe points to evaluate the sheet resistivity of the two dimensional electron gas.

In chapter 3 we will determine the growth parameters that change the V-defect size at the surface of GaN layers grown at low temperature which means below 1050°C. We will see that the change of carrier gas between nitrogen and hydrogen is particularly interesting. Then we will develop our own model of V-defects size evolution from the model of Franck in the 1950s, to explain two different modes

of growth which lead to large V-defects, or a limitation of their size.

Chapter 4 is dedicated to the InGaAlN and InAlN alloys, and we will first explain the difficulties we had to correctly measure the alloy composition. From that point, we changed several growth parameters such as temperature, growth time, TMIn/TMAl flow ratio, growth rate and finally ammonia flow to see the effects on surface morphology, alloy composition, luminescence and electrical performances. The use of different carrier gases which are nitrogen and hydrogen showed different behavior of indium incoporation in the layers, and we succeeded in incorporating indium even under hydrogen. The chapter is ending by pure InAlN which were obtained at the beginning of thesis. We will discover that InGaAlN layers which were supposed to be InAlN contained gallium due to contamination from the growth chamber.

The characterization results of chapter 4 gives us a lot of data that can be explored by looking at specific characterisations across many samples : this is the purpose of chapter 5. We will deal with the phenomenon of separation between indium rich and poor phases examined at different point in chapter 4. We will explain why we are suffering from gallium pollution in our reactor and how growth parameters affect it, also showing a new process to avoid this phenomenon. Then we will build a surface phase diagram to see the evolution of the morphology of our InGaAlN surface depending of growth parameters. And finally, we will report on the electrical results to position our material on the scale of current developments.

This work is ended by a sixth chapter dedicated to the capping of InGaAlN and InAlN layers by SiN and GaN. We will see that our difficulties to produce high quality SiN layers on that kind of alloys were restrained by technological aspects related to our silane flow. Thus, GaN caps will offer us the possibility to correctly protect our alloys while keeping excellent sheet resistivity values.

In addition, the four experimental chapters must also answer at least three points which will constitute our specifications and our guideline in this work. First of all, InGaAlN and InAlN alloys must have an In/(In+Al) ratio as close as possible to 18% to be lattice matched on GaN thick GaN pseudosubstrate and have a strong spontaneous polarization in the same time. Secondly, we will try to produce low temperature GaN layers with the least amount of surface defects to ensure a high-quality capping of InGaAlN and InAlN barrier layers. And finally, we will try to build a complete HEMT heterostructure with the GaN substrate, the InGaAlN or InAlN barrier layer, and the GaN cap, whose sheet resistivity will have to be below 300 Ohm.cm, which means below the sheet resistivities of more standard AlGaN/GaN heterostructures.

1 | Framework and requirements of the thesis

Sommaire

1.1 III-Nitrides historical 4
1.2 General properties of III-Nitrides 5
1.2.1 Large band gap materials 5
1.2.2 III-N crystal and wurtzite structure 6
1.2.3 Ternary and quaternary alloys 10
1.3 Crystal defects and dislocations 13
1.3.1 Point defects in crystals : vacancies and impurities 13
1.3.2 Stacking faults 14
1.3.3 Dislocation 15
1.4 III-Nitrides polarization 19
1.4.1 Spontaneous polarization 19
1.4.2 Piezoelectric polarization 20
1.4.3 Two-dimensional electron gas generation in III-nitrides 21
1.5 III-N materials based applications and devices 22
1.5.1 High electron mobility transistors 22
1.5.2 LEDs and LDs 23
Bibliographie 25

Being based on the study of the III-N materials we will first start by giving a little historical of their discovery and their development mainly until the beginning of the 21st century. We will continue by addressing the different physical and chemical properties of these materials. From these properties we will turn our attention to the polarization effect present in III-nitrides and its implication in the generation of a two dimensional electron gas at an interface between two different materials. To finish the chapter 1 we will give an overview of the main applications arising from the use of the III-N materials in micro and optoelectronics.

1.1 | III-Nitrides historical

In the study of III-nitrides materials, gallium nitride (GaN) has been the most investigated in terms of growth, and analyzed for its physical, chemical, and optical properties. Everything starts in the beginning of the 20th century with the synthesis of polycristalline aluminum nitride (AlN) by Fichter et al. [1]. We had to wait 1932 for the first synthesis of GaN with the works of Johnson et al. [2]. New studies from Juza et al. [3] appear in 1938 with the synthesis of GaN and the investigation of its crystal structure.

For more than twenty years there were no significant innovations until the 1960's where the use of Hydride Vapor Phase Epitaxy (HVPE) allowed the growth of monocrystalline GaN. Finally in 1969 there is the first reference to GaN growth on sapphire substrates by Metal-Organic Chemical Vapor Deposition (MOCVD) [4], a common industrial process on which we will focus in this thesis and which was under development in the 1970s. Maruska et al. also measured for the first time the band gap of GaN at 3.39eV at room temperature.

In the 1970s, growth by MOCVD was still under development for the GaN [5] and Molecular Beam Epitaxy under ultra high vacuum began to appear with the studies of Yoshida et al. [6]. In 1971 Pankove brought to the III-N community an interesting device - a blue diode based on a metal/insulator/semiconductor heterostructure [7] which was a direct observation of the optical properties of GaN.

After these developments, the research community focused on different problems related to growth of III-N materials, that is to say : the difficulty of getting p-doped material since the nitrides are naturally n-doped because of their big number of N-vacancies in the crystal lattice, and the poor surface and crystal quality. Indeed, the lack of convenient substrate for the heteroepitaxy of III-N materials implies a lot of internal defects like dislocations, bulk stacking faults, inversion domain boundaries, and of course surface cracks after relaxation for instance.

It was only in the 1980s that the idea of a two step process appeared, first by MBE in 1983 [8] with a first layer of low temperature AlN under GaN, and then by MOCVD between 1986 and 1989 [9][10][11]. Moreover, in 1991 Nakamura showed the same benefits on the quality of the GaN layer using a low temperature GaN below [12]. The second difficulty in GaN growth which was the impossibility to get a p-type layer was solved in 1989 by Amano and Akasaki [9][13] .

In the last decade of the 20th century there has been an acceleration in III-N materials research essentially since Nakamura developed his first blue light emitting diodes (LEDs) made of GaN and InGaN combined in a multi-quantum-well structure. This is worth emphasizing that from 1993, the company he worked for, Nichia, began mass production of LEDs and laser diodes (LDs) from 1996. A new optimization of the layers quality and the p dopage [14][15] allowed the development of high intensity InGaN based LEDs again by Nakamura in 1994 [16].

For a lot of the III-nitride history, the majority of the investigations concerned optical applications. However, in the early 1990s the polarization of III-N materials was highlighted and opened new perspectives in the field of high power and high frequency electronics with the production of high electron mobility transistors (HEMTs) [17][18]. These field effect transistors with a high density of charge carriers having a high mobility already existed using traditional cubic III-V materials and alloys but needed doping in the barrier layer (the last in the heterostructure). We can also ad that there is a particular case with III-Sb that does not require doping also. In the case of III-Ns the benefits of the polarization replace the dopage process and allow much higher sheet carrier densities. Since these first developments, the most common stack to make a HEMT is an AlGaN layer above a GaN layer. In 2001 Kuzmik proposed the use of InAlN instead of AlGaN to decrease the strain in the material and increase electrical performance [19][20].

Today InAlN still presents difficulties in its growth (morphology and In/Al ratio control) since it implies the growth of a ternary alloy for which the two binary alloys, AlN and InN have growth temperatures are far away from each other (1400°C and 550°C respectively). However good materials quality has been achieved, principally on small diameter substrates like sapphire and silicon carbide which are expensive compared to silicon. The study of InAlN/GaN/Si 200mm is the least represented and requires first of all a specific heterostructure to produce the GaN pseudosubstrate, and then adapted chemical and physical characterizations.

1.2 | General properties of III-Nitrides

In this section, we will describe successively the different properties of III-nitride materials which make them a good candidate for high power and high frequency applications, and also for optoelectronic systems.

1.2.1 | Large band gap materials

III-N materials can be differentiated from other semiconductors since they are large direct band gap materials (cf. figure 1.1. Indeed while III-Vs like GaAs have a gap energy of 1.4eV (direct gap) and silicon a gap energy of 1.1eV (indirect gap), III-Ns have a gap energy ranging from 0.65eV for InN to 6.2eV for AlN through the value of GaN to 3.4eV. Thus there is at first sight a big interest in the use of these binary compound and their different combinations in alloys. In theory, these energies allow us to produce optical devices emitting from near infrared to deep UV and so also in the visible spectrum.

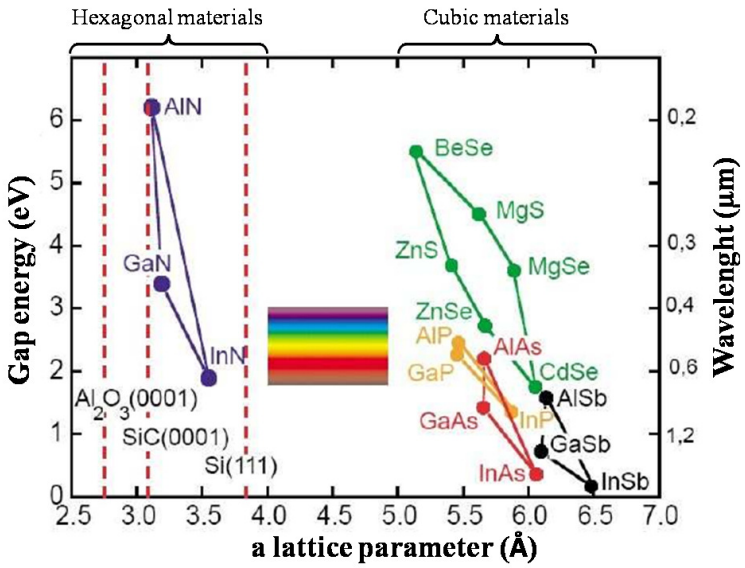

Fig. 1.1 – Band gap energy versus a lattice parameter of different semiconductors. Note that the current band gap of InN is 0.65eV. Picture by Nicolas Grandjean.

In all semiconductor the change of the band gap energy depends on the crystal lattice deformation (strain) induced by stress. It directly changes the distance between the atoms in the real and so the reciprocal space from which we define the first Brillouin zone and then the energy position of the different bands in the material. Also the temperature has an impact because it implies first lattice vibrations (phonons) appear, which again move the atoms relative to each other, and secondly a thermal dilatation of the material which increases the interatomic distances. [21][22] We can express the band gap value versus the temperature with the Varshni model :

$$E_g(T) = E_g(0) - \frac{\alpha \cdot T^2}{T + \beta} \tag{1.1}$$

$E_g(0)$ is the band gap energy at T=0 K, α (meV/K) is the gap linear regression coefficient at high temperature while β (K) is the temperature from which the slope is changing. This kind of model is useful for instance to estimate the band gap energy of our material during devices operation at different temperatures.

A large band gap like in III-Ns is interesting for power applications since it implies large breakdown voltage. Moreover these materials have stronger bonds in their structure compared to silicon or III-V materials. That makes them very tolerant in aggressive environments : at high temperature, in corrosive solutions or even in space exposed to ionizing radiations. There is a detrimental counterpart : it is very tough to etch them by chemical attack, and often difficult to dope them effectively.

1.2.2 | III-N crystal and wurtzite structure

1.2.2.1 Wurtzite and zinc blende structure

III-N materials and their different alloys can crystallize in two different allotrope forms. One belongs to the hexagonal system and is the wurtzite structure (2H) and is the most stable. It corresponds to an interpenetration of two hexagonal lattices translated of a 5/8 ratio along the c-axis of the elementary

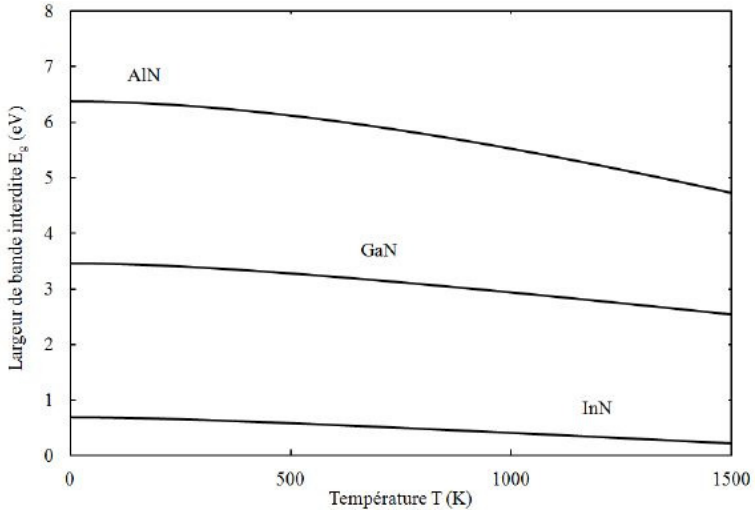

Fig. 1.2 – III-N binary compounds : gap energy versus temperature.[23]

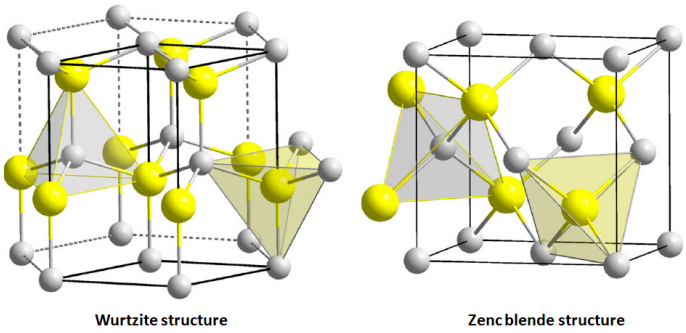

Fig. 1.3 – Atoms arrangement in wurtzite and zinc-blende structures.

cell. Thus one of this lattice is made of metal atoms (Ga, In and Al) and the other contains the nitrogen atom (N).

The second possible structure is metastable for the III-nitrides and is called the zinc-blend structure (3C). It consists in an interpenetration of two cubic lattices translated of a 1/4 ratio along a, b, and c axis of the elementary cell (1/4 of the main diagonal). Both crystal lattices are shown in figure 1.3.

If we have a look at the chemical bonds between each atom inside the elementary cell we can imagine tetrahedrons composed of one central atom (metal or nitrogen) and four surrounding atoms (nitrogen or metal respectively) connected to the central one by an ionic bond. The difference between the wurtzite and the zinc blende structure comes from the position of the third nearest neighbor of each atom. Typically in the zinc-blend structure compared to the wurtzite one, tetrahedrons whose central atom is a metal (or nitrogen) are rotated compared to the tetrahedrons of the other type through an angle of 60°.

1.2.2.2 Layers polarity

The wurtzite structure doesn't present any symmetry relative to the (0001) basal plan (parallel to the surface). Thus [0001] and [000-1] directions are not equivalent. We define the direction from the

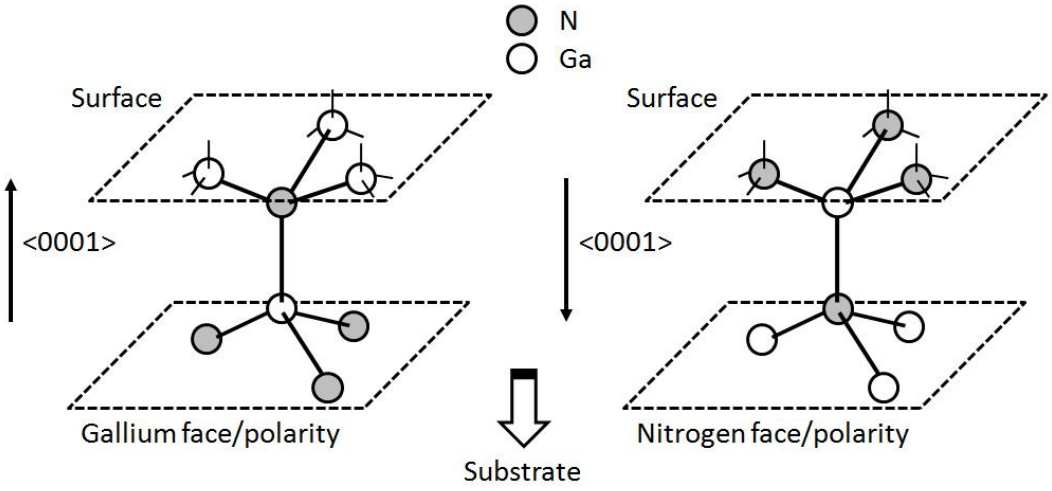

Fig. 1.4 – III-N material layers polarity in wurtzite and zinc blende structure.

metal atom to the nitrogen atom as the [0001] direction. When it is in the same direction as the axis of growth, we speak of metal polarity or metal face. However, this does not mean that the atoms present on the surface are the metal ones and those connected to the substrate nitrogen ones. This refers only to the orientation of the crystalline structure. When we are in N-polarity or nitrogen face, the direction of the metal-nitrogen bond is in the opposite direction. Cf. figure 1.4 for illustration of polarity in III-N crystal.

At first glance, this distinction may seem to be a convention. However, the particular chemical, morphological, electrical properties of the surface of III-nitrides and the 2DEG location differ, depending on whether the crystal is in metal or nitrogen face. For the remainder of our report, and especially when we will discuss the phenomena of spontaneous and piezoelectric polarizations, we always will consider that we are in metal face. For growth of a III-N material by MOCVD on silicon, we are still facing metal, unless we bring a special treatment to the substrate (nitridation) and/or changes of the buffer layers properties. [24][25]

1.2.2.3 The mosaic model

Even if we are growing III-N single crystal layers on oriented substrates, we may not have a perfect layer following exactly the orientation of the substrate. Locally it is true, but at larger scale (for instance a few micrometers) this is false. The growth starts with an AlN nucleation layer, and the AlN buffer undergoes high stress due to a lattice mismatch with the silicon. This leads to columnar grains slightly misoriented relative to each other (cf. figure 1.5), with tilt and twist. This occurs through dislocation formations, a plastic strain relaxation of the material.

The misorientation or the grains is characterized by two angles called tilt and twist. The twist α_{twist} is an in-plane rotation and the tilt α_{tilt} an out-of-plane one. X-ray diffraction is a good means to evaluate the amount of tilt and twist in the layers, and therefore to estimate dislocation density.[26] The boundary between grains is necessarily a dislocation rich zone since we have a contact with two single crystals with a different orientation.

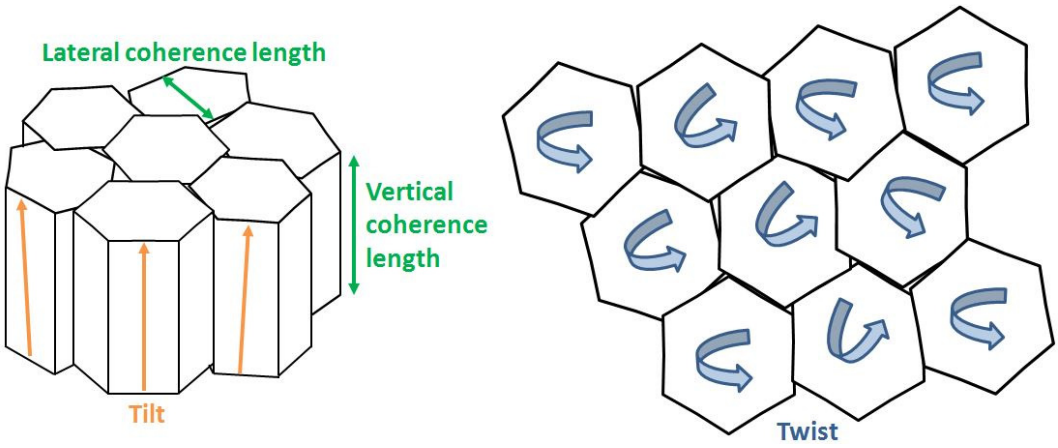

Fig. 1.5 – Definition of the four parameters of the III-Ns mosaic structure.

In this mosaic model we can also add two parameters that describe the columnar grains : the lateral and vertical lengths. The first one is simply related to the mean diameter of grains and the second corresponds to the thickness of the epilayer in the case of thin films.

1.2.2.4 Substrates for the growth of III-Ns

As well as for their binary counterparts GaN, AlN and InN, ternary and quaternary alloys combining these three compounds suffer from lack of bulk substrates. Therefore, it is very expensive and restrictive (substrate size) to perform a homo-epitaxial growth in order to have a very low concentration of dislocations and other structural defects in the layers. So the research community has spent a lot of time to find good alternatives as substrates.

A good substrate for an hetero-epitaxy is not only a material with the lattice parameter as close as possible. We also have to take into account the coefficient of thermal expansion (CTE) which could imply the emergence of cracks and/or wafer bowing in the layer during the cooling or warming phases in the growth process. If the epilayer has a CTE lower than the substrate one, it becomes in compression as the wafer cools down from high temperature and the wafer becomes convex. On the contrary, if its CTE is higher than the substrate one, it becomes in tension and the wafer becomes concave. Moreover we are stacking several layers from the substrate to the active layer (InAlN of InGaAlN) since we are adjusting the lattice parameters between them using buffer layers. So the wafer is sometimes concave, sometimes convex. It is important to control the stress in the wafer changing the composition of epilayers to avoid it breaking in the MOCVD reactor because of too much mechanical stress at certain temperatures.

In addition to the above constraints, the substrate has to be very stable at the high temperatures required for the growth of III-Ns and show a high thermal dissipation to avoid the self-heating of power devices. So the most common substrates currently used are silicon carbide (SiC), sapphire (Al_2O_3) and silicon with respectively a difference in lattice parameter of 3,5%, 14%, and 17%. Hexagonal silicon carbide is currently very expensive even if it has a CTE close to GaN and an excellent conductivity (4.9 W.cm-1.K-1), but is essential for RF power switching. Sapphire is preferred for growth on small diameters (2, 4, 6 inches) except for power devices, as its lower thermal conductivity (0.5 W.cm-1.K-1) means there is a lot of self-heating. Cubic silicon with the [111] orientation is an interesting candidate

for large wafer production (200mm) even if the lattice and CTE mismatch are high with GaN compared to sapphire and SiC. Moreover its thermal conductivity is three time better than for sapphire (1.5 W.cm-1.K-1). Also from the technological point of view, the knowledge of the silicon treatments in devices processes is an advantage and the actual performance of III-Ns based HEMTs especially on silicon is already very good.

In materials such as GaN on hetero substrates, we find a dislocation density of around 10^8-10^{10} cm^{-2}, whereas in today mature techniques such as silicon and GaAs respectively one is 10^1 cm^{-2} and 10^5 cm^{-2}. The direct consequences of a large amount of crystal defects are reduced performance of light emitting devices, as well as a premature aging of devices with high current density such as lasers.

There was no development related to substrates during this thesis since the buffer of GaN on silicon had been previously developed at CEA LETI, and this structure was sufficient for the work on InGaAlN alloys.

1.2.3 | Ternary and quaternary alloys

1.2.3.1 Three ternaries, one quaternary

As mentioned above there are three main binary elements in the field of the III-N materials. They are indium nitride, gallium nitride and aluminum nitride. These three binary systems can be combined into one ternary or even quaternary alloys. For instance the three ternary alloys studied currently are AlGaN, InGaN, and InAlN. As for the quaternary alloy it is InGaAlN. Thus while growing all of these alloys we will change the ratio between Al and Ga, In and Ga, In and Al and finally In, Ga and Al in order to modify the a (a=b in wurtzite structure) and c lattice parameters and the band gap energy. We know from the literature the lattice parameter value for each binary. From those values and according to the ratios between each one we can calculate the lattice parameters for the ternary and quaternary alloy with Vegard's law. It describes a linear evolution of the lattice parameter (a or c) versus the alloy composition. This law is not perfect but gives an excellent approximation of the lattice parameters.

Consider a ternary alloy $A_xB_{1-x}N$ and a quaternary $A_xB_yC_{1-x-y}N$. From Vegard's law : [27]

$$a_{A_xB_{1-x}N} = x.a_{AN} + (1-x).a_{BN} \tag{1.2}$$

$$a_{A_xB_yC_{1-x-y}N} = x.a_{AN} + y.a_{BN} + (1-x-y)a_{CN} \tag{1.3}$$

Vegard's law is linear, but it does not apply to the theoretical evaluation of a gap. We must add one or even several quadratic terms. So for a ternary alloy, an approximation of the experimental band gap E_g is given by the relation : [28]

$$E_{g,A_xB_{1-x}N} = x.E_{g,AN} + (1-x).E_{g,BN} - b_{A_xB_{1-x}N}.x.(1-x) \tag{1.4}$$

For a quaternary alloy $A_xB_yC_{1-x-y=z}N$: [29]

Alloy	α	β	γ	**b(x=0.5)**
$In_xAl_{1-x}N$	6.9	-8	3	3.7
$In_xGa_{1-x}N$	1.74	-0.68	0	1.4
$Ga_xAl_{1-x}N$	0.75	-0.07	0	0.71

Tab. 1.1 – Bowing parameters in electron volt for the ternary alloys, and their values for x=0.5. [29]

$$E_{g,A_xB_yC_zN} = x.E_{g,AN} + y.E_{g,BN} + z.E_{g,CN} - (1-z).x.y.b_{ABN} - (1-y).x.z.b_{ACN} - (1-x).y.z.b_{BCN} \quad (1.5)$$

The parameters b are the parameters of the "bowing". Their value depends on the composition of the ternary in the case of assessment of a gap for a ternary alloy : [29]

$$b(x) = \alpha + \beta.x + \gamma.x^2 \quad (1.6)$$

The values α, β, and γ are referenced in table 1.1 for each III -N ternary.

In the case of a quaternary alloy, we cannot use the direct concentration of this or that element of the quaternary in the formula of the parameter b, knowing that it is normally calculated for a ternary. Therefore, in the formula of b, we must replace x by x/(x + z), x/(x + y), and y/(y + z) respectively for InAlN alloys, InGaN and AlGaN entering in the quaternary alloy.[29]

It should be also noted that the value of the bowing parameter, and therefore the gap value depends on the fluctuations in concentration of the elements constituting the alloy studied. These fluctuations are particularly strong in the III-N alloys containing indium. Typically these fluctuations result in a decline in the gap value.[29]

In quaternaries, the non-homogeneity of the indium distribution in the crystalline network remains true, just as the effects mentioned above. It also adds to a significant thermodynamic instability when indium and aluminum are in a high proportion. In this case, there are regions in the material within which there is a phase separation and the appearance of the InGaN ternary or more often indium-rich quaternary phases.[29]

1.2.3.2 Use of InAlN compared to AlGaN and flexibility of III-N quaternary

In the embodiment of III-N alloys based heterojunctions for HEMTs production, AlGaN alloys as a barrier layer have been widely studied and it has proven its effectiveness. One challenge is to associate indium and aluminum in the InAlN ternary alloy.

The challenge of growing InAlN comes mainly from the fact that that InN is deposited at around

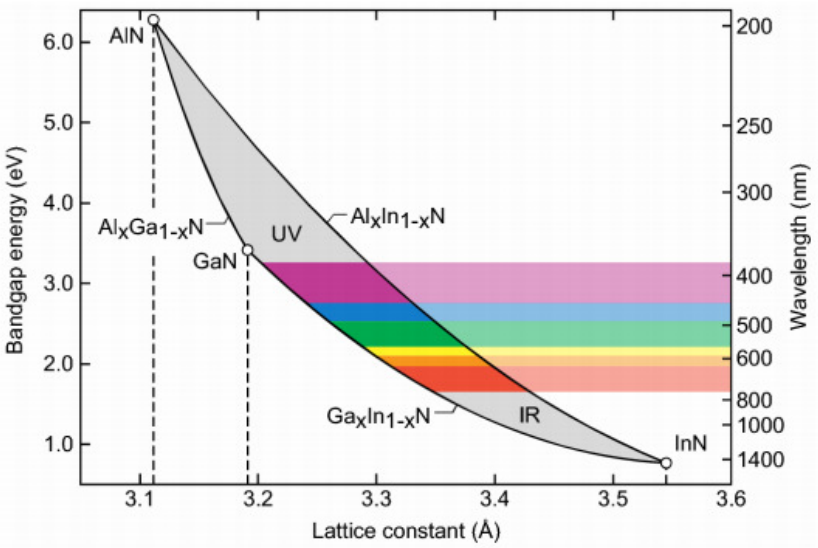

Fig. 1.6 – Evolution of the band gap depending on the composition and thus the lattice parameter. [30]

550°C, and AlN around 1300°C in MOCVD. We must find a compromise on the temperature to be adopted during growth, and adjust the other growth parameters to optimize the integration of indium up to 18%, which would give lattice matched material. At the same time, we ensure a good crystal structure, no increase of dislocations, and a sufficiently low surface roughness.

Overcoming these challenges is not important for the use of InAlN. This material has on the ability to have the same a lattice parameter than that of GaN if indium is present at 18%. This allows us to provide a growth of InAlN layer without the generation of mechanical stress and cracks. Moreover InAlN has a stronger spontaneous polarization than that of the other two ternary III-N since it combines the two binaries InN and AlN having the highest spontaneous polarizations. This would therefore contribute to a significant increase in the charge carrier density in the two-dimensional electron gas at the InAlN/GaN interface. cf section 1.4 for more information.

With III-N ternaries, if we make a choice of composition to have a specific lattice parameter, the band gap energy has a definite value that cannot change. Equally if you decide to set the value of the gap changing the composition, it imposes a lattice parameter. The interest of quaternary InGaAlN is to possibly modulate, in a certain range of values, the band gap when we fixed the lattice parameter or vice versa.

In the 3D graph (a) of figure 1.7, we can see the comparison between the theoretical calculation of the gap of the quaternary alloy in case the Al and In atoms are perfectly distributed on the lattice, and in the case where indium-rich areas are present. What interests us in this figure is the blue and red lines that actually correspond to the evolution of the gap versus the concentration of indium and aluminum when the quaternary alloy has the same lattice parameter than GaN. These two curves are plotted in Figure (b) depending on the indium composition. Thus we can see the band gap value range that we get for a III-N quaternary when it is grown on relaxed GaN layers. Note that the amplitude of the bottom curve (inhomogeneous material) is lower as well as all values that constitute it, compared to

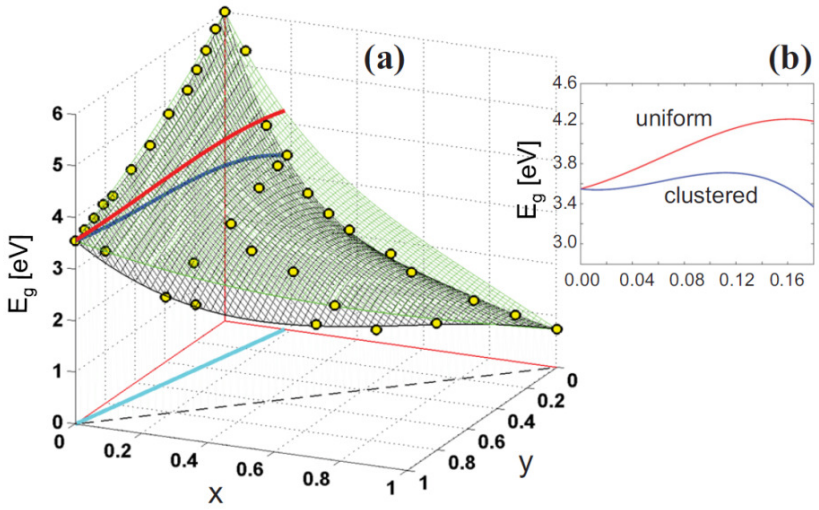

Fig. 1.7 – (a) Theoretical illustration InGaAlN quaternary band gap. In green color, uniform material. In black color, material with indium-rich areas. (b) Band gap versus indium ratio for an InGaAlN matched on GaN.[29]

the top curve (homogeneous materials). The experimental band gap that could be measured should be between these two curves since our epitaxial material is not supposed to be perfect, nor is it likely to be entirely clustered, where there is a real phase segregation between aluminum and indium in the alloy.

1.3 | Crystal defects and dislocations

We will now describe the different crystal defects in semi-conductors. When we try to formulate theoretical physical models to describe crystal properties, we are more or less close to the reality and this can be due to crystal defects and especially dislocations. Therefore they deserve special attention to understand them and what their effects on crystal lattice are. Dislocations are particularly interesting for us since they have a very high density in III-N material, mainly due to a lack of suitable substrates for the growth of III-nitrides.

1.3.1 | Point defects in crystals : vacancies and impurities

The two first defects we discuss are vacancies and impurities. A vacancy is simply a lack of one atom at a certain point in the crystal lattice. It can diffuse within the material, and typically their displacement rate increases exponentially with the temperature. For impurities, there are two possibilities when there is the incorporation of an impurity atom in the crystal. First it may take the place of another atom in a specific crystal site in the lattice, which we refer to as substitution. Secondly, it may be inserted between the atoms of the lattice and we refer to these as interstitial impurities. The ability of certain atom to be incorporated in the crystal depends mainly on its size and its steric hindrance compared to the space between atoms of the lattice.[31]

Typically in the context of III-nitrides growth by MOCVD, vacancies are important on the atomic site of nitrogen due to the low decomposition rate of ammonia except at high partial pressure as explained

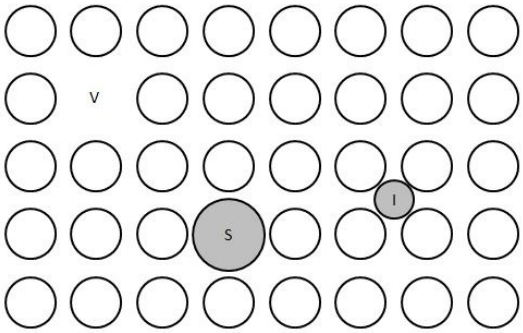

Fig. 1.8 – V for vacancy, S for atom in substitution and I for interstitial atom. Cubic structure.

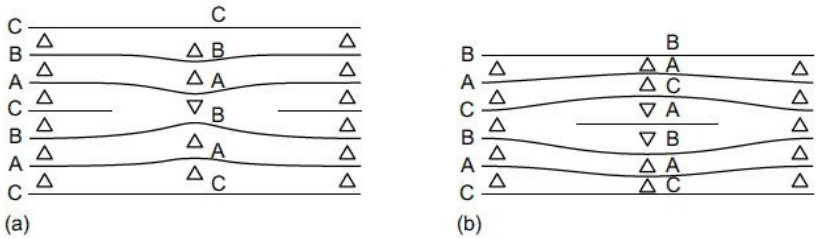

Fig. 1.9 – (a) Intrinsic stacking fault, (b) extrinsic stacking fault in ABC sequence of face centered cubic structure. Planes normally arranged compared to each other are symbolized by a triangle pointing upwards, and planes undergoing a stacking fault error are symbolized by triangle pointing downwards.

in chapter 2. The first effect we can notice in that case is the natural n-type doping of the material. Interstitial and substitution impurities may be incorporated by in-situ doping to change the resistivity by doping the material p (magnesium) or n (silicon). In other semiconductors or monocrystalline materials, punctual crystalline defects generation can be favored by plastic deformation, implantation, quenching, etc.[31]

1.3.2 | Stacking faults

Stacking faults are 2D crystal defects in semiconductors. The first is the stacking fault, a defects which can occur in close packed planes of ABCABC types : for example face centered cubic structure and (111) planes. It occurs also in III-N materials in the ABAB sequence of wurtzite structure along the c-direction [32][31]. This defect can be seen as part of an atomic plane which is inserted (extrinsic stacking fault) or removed (intrinsic stacking fault) in the usual sequence of atomic planes in the material. The figure 1.9 illustrates the two types of stacking faults. Note that the energy required to produce one stacking fault is higher in the case of extrinsic one.[31]

The main effect of such a defect is an extra peak in the luminescence spectrum. Indeed the variation of the ABAB sequence with the introduction of a C layer induces the formation of a zinc-blende area in the material with a band gap energy lower than that of wurtzite structure. Therefore the zinc-blende area may allow the exciton to be localized in this zone before recombination[33][32].

We illustrate the stacking faults of four types in figure 1.10 from an article of C. Stampfl and Chris G. Van de Walle. The formation energy of each one is classified from the lowest to the higher respectively

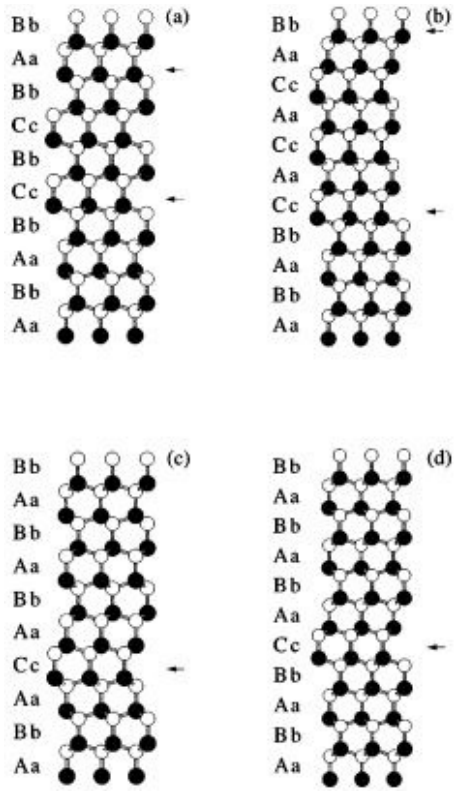

Fig. 1.10 – Stacking faults in III-N materials with hexagonal ABAB sequence along the [0001] direction : a) type I, b) type II, c) type III, and d) extrinsic. The stacking faults are indicated by black arrows and the black and white circles denote cations and anions respectively.[33]

from type a) to d).[33]

1.3.3 | Dislocation

1.3.3.1 Definition and schematic

The most important defects in crystals and especially in III-V and III-N material, according to their detrimental effects on luminescence, electronic, mechanical, structural (surface and bulk) properties, and so on are dislocations. They consist of broken atomic bonds on a half plane in a crystal. There are two types of dislocations : edge and screw dislocations. The best way to understand what happens in the crystal in both cases is to look at the structure before and after the appearance of the dislocation. For that we will use a simple lattice which is the cubic structure as shown in figure 1.11.

In the case of an edge dislocation, a half atomic planes is inserted where the bonds perpendicular to the ABCD rectangle have broken. The crystal movement induced by the dislocation is in the sense of the arrows on schematic. We define the dislocation line along the [DC] segment. Sometimes we make the distinction between positive (extra half plane inserted above DC line or removed below DC) and negative (extra half plane inserted below DC or removed above DC) edge dislocations. It is a convention for mechanical and energy calculations.[31]

The movement is different in the screw dislocation case. Indeed the same bonds are broken than for edge dislocations (perpendicular to ABCD rectangle) but the top of the crystal undergoes a movement

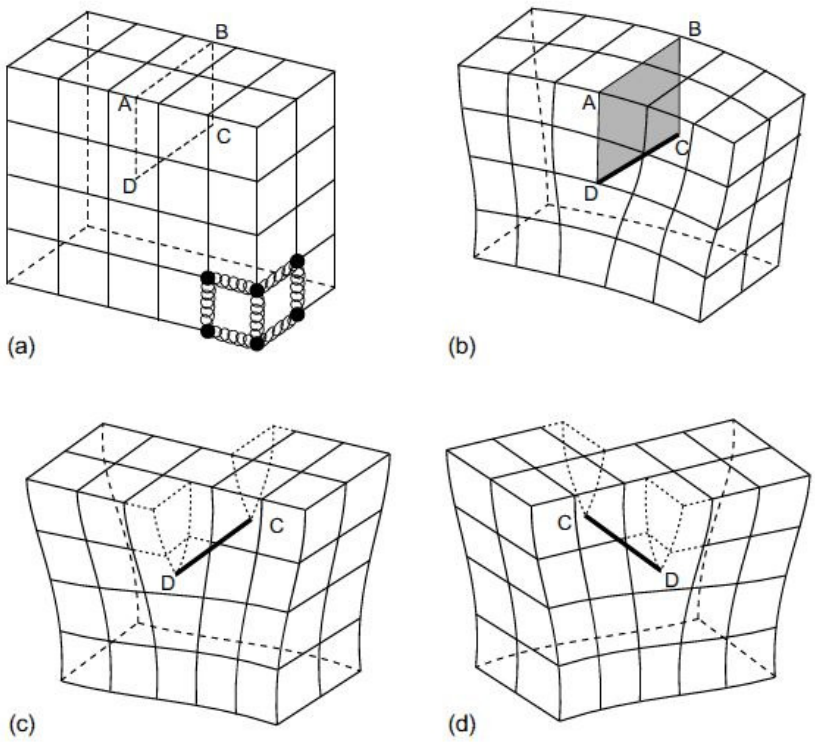

Fig. 1.11 – a) Normal cubic structure with black balls as atoms and springs as bonds, b) Positive DC edge dislocation (half plane inserted above DC), c) left-hand DC screw dislocation by relative displacement of crystal faces each side of ABCD, d) right-hand DC screw dislocation.[31]

parallel to the rectangle, symbolized by arrows. As for edge dislocations there is a specific convention depending on the sense of displacement. As we can see a screw dislocation generates a helical surface around the dislocation line. Therefore, while turning in the clockwise direction around the dislocation line, if we move from an atomic plane the dislocation is called right-hand screw, and in the opposite direction it is called left-hand screw.[31]

Dislocations always end at the surface or at grain edges when present in the material. Dislocation lines can stay straight, be curved under mechanical stress, form loops and branching or gathering. At the opposite of a branching node, if we take all the Burger circuits in the clockwise direction, the sum of all Burger vectors (cf. section 1.3.3.2 for definition) gives **0**.[31]

Dislocation lines are not immobile in a crystal and are subjected to external stress. They can be bent ; they can move and also slip on another plane. Typically in the case of edge dislocations, the movement of the dislocation line is in the slip plane is defined by the dislocation line and the Burger vector defined in section 1.3.3.2. In the case of screw dislocations, the movement is in any plane.[31]

1.3.3.2 Burger vectors and elastic energy

One parameter allows us to estimate the amplitude of a dislocation : the Burger vectors. It is defined as follow. Starting from the perfect crystal (still cubic structure in our example), we can draw a close circuit in a plane perpendicular to the dislocation line. The Burger vector **b** is the vector which allows us to switch from the drawn circuit with the dislocation to the one without dislocation.

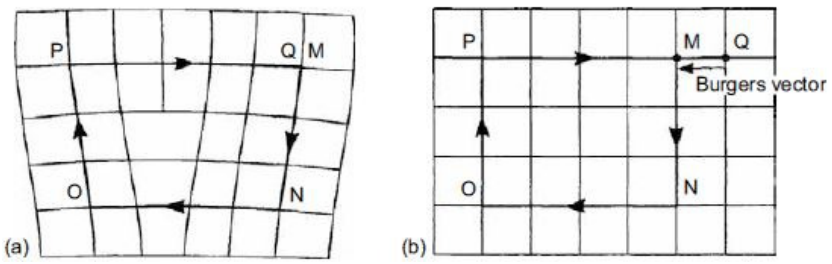

Fig. 1.12 – Burger circuit of cubic crystal with positive edge dislocation, and b) normal cubic crystal. Burger vector represented on b) with a black arrow.[31]

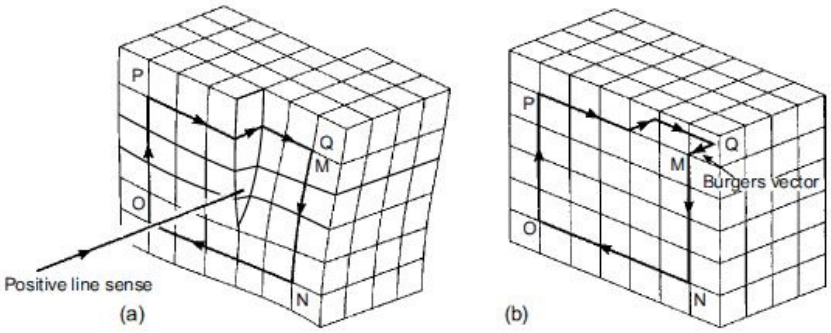

Fig. 1.13 – Burger circuit of cubic crystal with positive edge dislocation, and b) normal cubic crystal. Burger vector represented on b) with a black arrow.[31]

Schematics of the circuit and Burger vectors for both edge and screw dislocation are represented in figures 1.12 and 1.13. We recognize edge dislocations when the Burger vector is perpendicular to the dislocation line and screw dislocations when it is parallel. We can note that its norm is the value of the lattice parameter along the same direction. This value is important since it permits us to calculate the elastic strain and so elastic energy induced by the dislocation formation (locally) using the shear modulus and the Poisson ratio. We do not show the different calculations since they was not used quantitatively in this thesis. We will just notice that the dislocation energy (formation energy of the dislocation) is a sum of a dislocation core energy at the dislocation line (not easy to estimate and corresponding to a small part of the sum) and a dislocation elastic energy (based on the model of an empty cylinder around the dislocation line undergoing plane slips perpendicularly and in parallel to the its axes respectively for edge and screw types) whose value depends on dislocation type. In any case the elastic energy is proportional to Gb^2, with G the shear modulus and b the Burger vector norm . Please refer to reference for calculation details.[31]

Often dislocations are a combination of edge and screw type and are defined as mixed. An illustration of a mixed dislocation is shown in figure 1.14. At point S, **b** is parallel to the dislocation line, so at this point it is a pure screw component. At E, **b** is perpendicular to the dislocation line and we have the pure edge component. So here the total Burger vector is the sum of all components. [31]

1.3.3.3 Dislocation influence on GaN surface

The definitions given in the previous section are more than enough to represent what a dislocation is and to present their effects on the surface of III-N materials. One very common effect is the surface

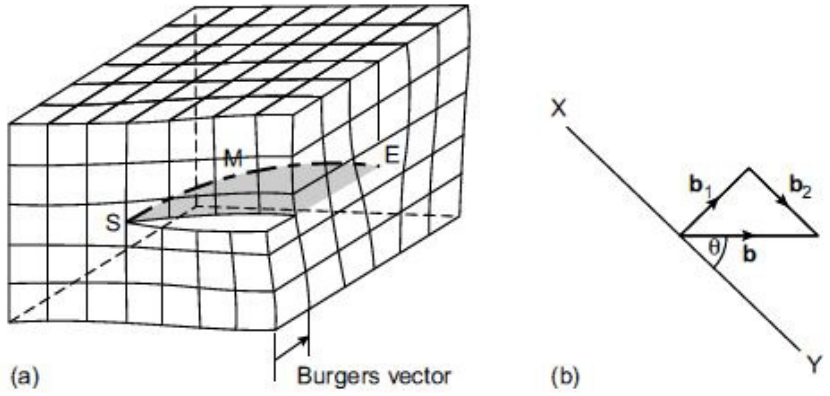

Fig. 1.14 – a) Simple representation of a mixed dislocation and effect on crystal, and b) Burgers vector **b** of dislocation XY is resolved into a pure edge component **b1** and a pure screw component **b2**.[31]

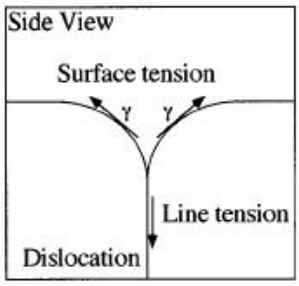

Fig. 1.15 – Model of surface depression connected to a dislocation line.[34]

depression usually called V-pits or V-defects of few nanometers to several dozen of nanometers diameter depending on the layer growth condition. According to F.C. Frank in early 1950's [34], surface depressions are connected to dislocations leading to the surface. Indeed the elastic strain field formed along the dislocation line generates a force inward toward the material which has to be balanced by a change of surface energy to stay at equilibrium. Figure 1.15 offers us a schematic of this simple model. We used this idea to develop our own model which anticipates the V-defect size according to the growth conditions in chapter 3.

For the moment we will illustrate these surface depressions with an AFM picture of a GaN surface grown at 930°C in figure 1.16. Here we can see two depression sizes. The smallest ones are due to pure edge dislocations and the largest ones to mixed or screw type dislocations [34]. Two mixed dislocation, thus containing a screw component are connected to one surface atomic step and form what we call a pinned step structure. The more the growth conditions are close to the thermodynamic (low driving force of the growth, cf. chapter 2 for more details) equilibrium during the growth, the more the step line is straight.[34] On the contrary, when the equilibrium is balancing from one side to another (driving force positive or negative respectively), the step is either curved. The curvature radius of steps is inversely proportional to the driving force value.[34] Mixed dislocation always form an impediment to the advance of an atomic step during growth.[34] As there is a helical surface at the material surface in case of a screw type dislocation, the step growth mode is automatically affected by this type of dislocation. On the contrary pure edge dislocations do not affect the atomic steps at the surface. If an edge dislocation line is ending at the surface, this surface remains flat and is not affected except

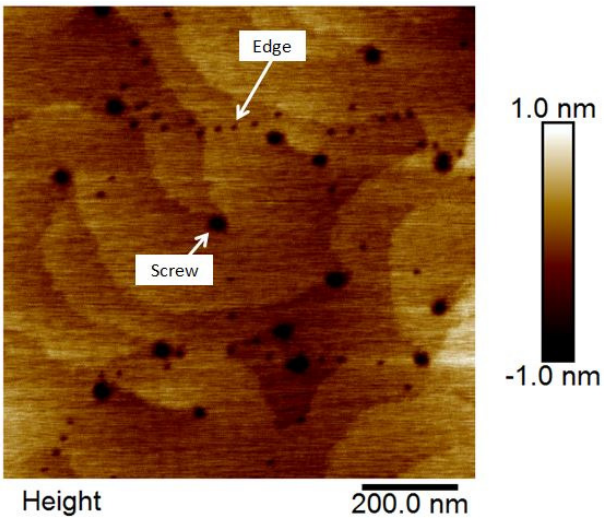

Fig. 1.16 – 1x1μm^2 AFM picture of GaN surface grown at 930°C.

at the dislocation core where an atom at the surface is missing. We see easily in the AFM picture in figure 1.16 that lines of several surface depressions at the surface can be formed on some steps without affecting their form.

1.4 | III-Nitrides polarization

This section will be dedicated to an important phenomenon which is the polarization in III-N materials. It is actually a combination of two components : the spontaneous polarization and the piezoelectric one. The polarization in III-N materials is a lot stronger than in other semiconductors, and this opened the power and high frequency field for devices application. This polarisation directly allows us to make high electron mobility transistors without any doping in contrast to most of III-V materials.

1.4.1 | Spontaneous polarization

The bonds between metal and nitrogen atoms are covalent and partially ionic. Indeed nitrogen atoms are more electronegative than that of gallium, aluminum or indium. Thus a dipole moment is created, directed towards the metal atom along the bond. In a perfect tetrahedron, the four dipole moments present on the four bonds framing each atom would be nullified. However, the hexagonal crystal structure induces a deformation of the tetrahedron. This simply involves the fact that the barycentre of positive charge does not coincide with that of negative charges. This therefore results in a so-called spontaneous polarization P_{SP} independent of the stress state of the material. Bonds and global polarization of III-N materials are shown in figure 1.17.

Values are subject to debate, but it is nevertheless accepted that for GaN, AlN and InN binary, spontaneous polarizations have respective values : -0.034 C/m^2, -0.090 C/m^2 and -0.042 C/m^2.[35]

Direction of polarization is defined from N to Ga (charge - to charge +). Thus, when we are in gallium face we can easily see that the spontaneous polarization is negative because at the opposite direction

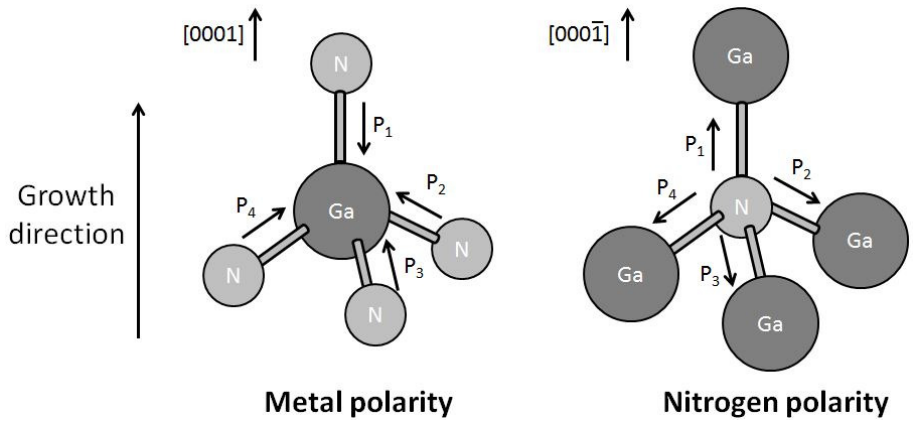

Fig. 1.17 – Dipolar moment and spontaneous polarization of III-N materials.

of growth direction. On the other hand the polarization is positive in nitrogen face.

1.4.2 | Piezoelectric polarization

There is another component to the total polarization of III-N materials, which is the piezoelectric polarization P_{PE}. It starts when the layer deposited on the substrate is strained, that is to say in tension or compression. If the layer is under tension (case of an AlGaN on thick relaxed GaN, for instance), then the piezoelectric polarization has the same sign as the spontaneous polarization when growing in the c-direction with gallium face. The two polarization components are added together. By contrast, they have opposite signs if it is in the case of a compression layer on GaN, and of course one subtracts from the other. So we define in both cases the total polarization $P_{TOT} = P_{SP} + P_{PE}$ which is the algebraic sum of the spontaneous and the piezoelectric polarization. Along the z axis (parallel and oriented in the same direction as the growth) and considering that the III-N layer is subjected to an isotropic biaxial stress in the plane (0001), the expression of the piezoelectric polarization is as following.[36]

$$P_{PE} = e_{33}.\epsilon_z + e_{31} \cdot (\epsilon_x + \epsilon_y) \tag{1.7}$$

$\epsilon_x = \epsilon_y = \frac{a-a_0}{a_0}$ corresponds to deformations in the plane. e_{ij} are elements of the piezoelectric tensor in C/m^2 unity. a, c are the two lattice parameters of the materials epitaxied and a_0 and c_0 are the lattice parameter of the same material when it is relaxed.

In the case where the stresses are isotropic in the planes of the epitaxial layers, we can connect the deformation in z with the x and y ones.[36]

$$\epsilon_z = -2\frac{C_{13}}{C_{33}} \cdot \epsilon_x \tag{1.8}$$

C_{13} and C_{33} are the elastic constants of the material for which we are studying the deformation. From (1.7) and (1.8) we can deduce : [36]

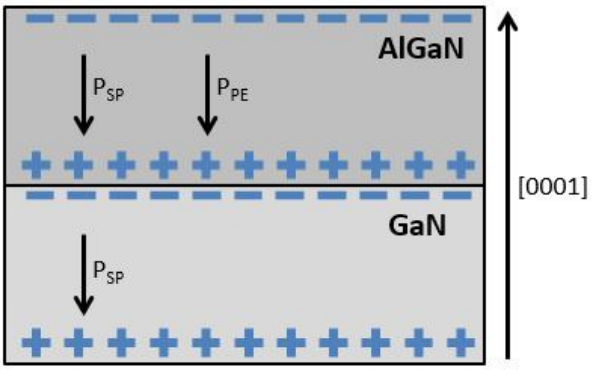

Fig. 1.18 – Total polarization orientation in AlGaN/GaN heterostructure.

$$P_{PE} = 2\frac{a - a_0}{a_0} \cdot \left(e_{31} - e_{33} \cdot \frac{C_{13}}{C_{33}} \right) \tag{1.9}$$

1.4.3 | Two-dimensional electron gas generation in III-nitrides

The principle of operation of an HEMT is based on the presence of a 2D electron gas in the GaN confined at the interface between a GaN pseudosubstrate for example and the barrier layer made of a ternary alloy which is typically AlGaN or InAlN (cf. figure 1.18. This gas is characterized by a high electron density of about 10^{13} cm^{-2} for an AlGaN/GaN structure, which is two to five times higher compared to a material such as GaAs. The electron mobilities are at 300K around 2000 cm^2/V.s for AlGaN/GaN.

The electron mobility of the bulk GaN is about 900 cm^2/V.s. If it increases at the interface with the barrier layer, this is because there are fewer interactions of the electrons with the crystal network thanks to the confinement of the latter within the 2D gas.

The two-dimensional electron gas is formed in the following manner. For example the polarization is determined at the interface of AlGaN/GaN stack by the following equation : [36]

$$\Delta P = P_{int} = P_{SP,AlGaN} + P_{PE,AlGaN} - P_{SP,GaN} - P_{PE,GaN} \tag{1.10}$$

This resultant polarization is nothing other than a virtual surface charge density fixed at the interface of the stack. Note that if this is the the case of a relaxed thick GaN pseudosubstrate : $P_{PE,GaN} = 0$. These positive fixed charges in the case of an AlGaN / GaN heterostructure, will then attract electrons from GaN bulk and surface. We can calculate the concentration with the following equation : [36]

$$N_s = \frac{-\Delta P}{e} \tag{1.11}$$

e is the charge of an electron (1,602.10^{19}C). These electrons are mainly derived from the material surface states.

On the other hand the contacting of the two semiconductors causes a discontinuity in their valence and conduction bands. Furthermore, the fact that an electric field is resulting from the polarization of the

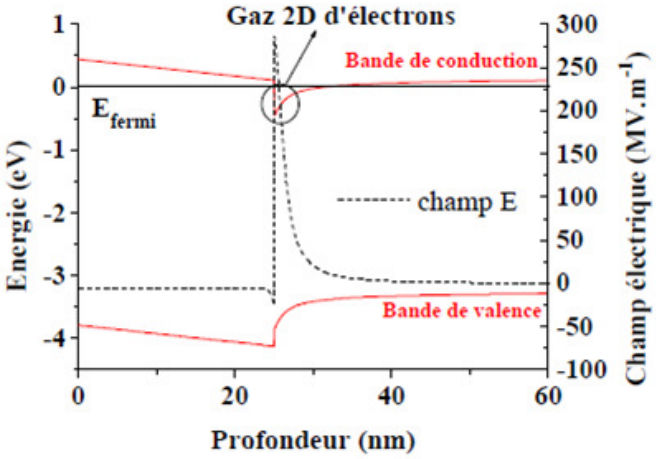

Fig. 1.19 – Valence and conduction band versus the depth of the material. Highlighting of the potential well.[37]

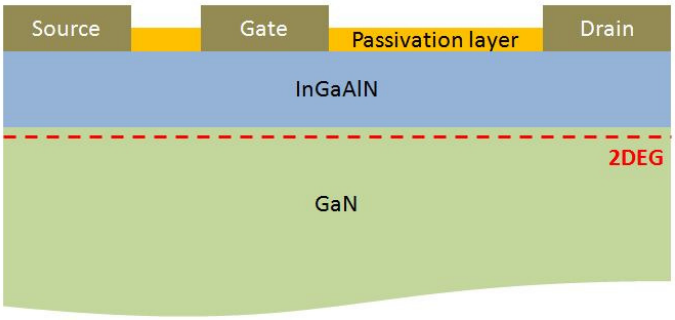

Fig. 1.20 – III-N HEMT heterostructure

layers, the potential well formed by the contact between the AlGaN and GaN tends to have a triangular shape in which the quantized energy levels take different values from that a classical potential well having a rectangular shape. The electrons attracted to the interface are thus trapped and confined in the potential well, thus the GaN layer. The quantum well formed at the interface is illustrated in figure 1.19.

1.5 | III-N materials based applications and devices

We finish this first chapter by describing the two main applications of III-N materials and their alloys. The first one is the high electron mobility transistor and the seconds the LED.

1.5.1 | High electron mobility transistors

In the structures that we use in this thesis, we have a buffer layer on silicon followed by nearly two micrometers GaN on which we will grow a barrier layer. This is the ternary (or quaternary) alloy with a specific composition and thus a specific polarization, which will imply specific electrical properties (carrier density and mobility) and take an important part in the HEMTs performances. As mentioned before the standard way consist to use AlGaN barrier layer but in this thesis we develop the interest of InAlN and InGaAlN.

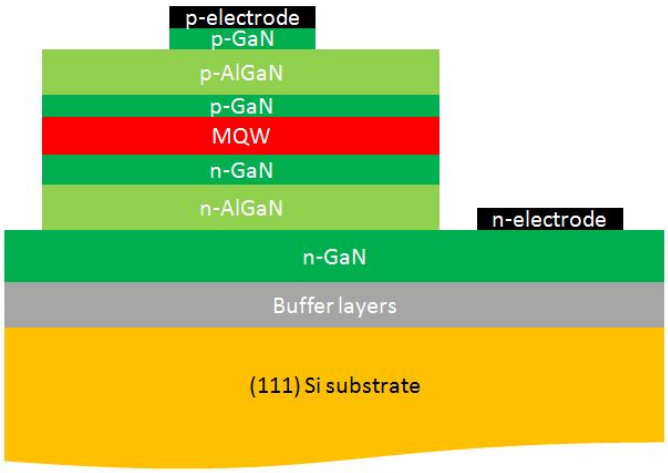

Fig. 1.21 – Example of an LED heterostructure

The buffer layer is made of different III-N alloys allowing a tuning of the GaN lattice parameter with the substrate.

The HEMT operation is globally the same as a field effect transistor. We apply a potential difference between the source and the drain, and then we control the current with the voltage applied at the gate.

Today HEMT use is used for high frequency or high power switching applications. In the first field of application we will find the different RF systems and for instance electronic devices in radar and communications. In the second field of application we have mainly the DC/DC and AC/DC converters. Electric cars are specifically interesting here since we need devices able to support high current densities between the electricity storage module (battery) and the motor which requires this energy.

1.5.2 | LEDs and LDs

Before the resolution of the difficulty of p-doping the GaN material, LEDs heterojunctions were made using III-V materials. Knowing their band gap we can only consider an application for infrared emissions and from red to green in the visible spectrum. The benefit of III-N materials is that we can use them to cover the entire visible spectrum and even from near infrared to deep UV. That is the reason why there was a strong development of the III-N LEDs devices by Nichia from the beginning 1990s just after the problem of the p-type doping was solved.

An LED heterojunction is made of several layers from the thick GaN pseudosubstrate. We start by an n-type GaN layer and finish by a p-type GaN layer. This is the basic p/n diode structure from which we get charges injection in the LED's heart : one quantum well of a multi-quantum-well heterostructure. This is the emitting part of the LED. It corresponds to a repeated structure of two different layers having two different band gap values. The lowest is for the well : electrons and holes are confined inside. The layers with higher gap allow the confinement in the well. When we inject the charges they are all in the conduction and valence band of the successive wells and recombined with holes of the valence band emitting at the wavelength corresponding to their energy in the well.

Summary of chapter 1

After a brief historical reminder of III-N materials growth in the 20^{th} century since 1930's, we detailed their properties. They allow the production of alloys whose direct band gap varies across a huge window from 0.78eV to 6.2eV ; that is to say from the near infrared to deep UV making it a good candidate for optical applications. III-Ns are grown in the wurtzite stable form which is typically an interpenetration of two hexagonal close packed structure. Different substrates were tried and today the most common are SiC, Al_2O_3 for small diameters and as in our case silicon in bigger size thanks to its low price. Three binaries alloys make up the family of nitrides which are InN, GaN, and AlN. These can be combined by two or even three to form ternary and quaternary alloys. For ternaries, one chemical composition implies one set of a and c lattice parameters for a particular band gap energy. On the other hand, one of the big advantages of quaternary alloys is to keep for example the lattice parameters constant but change the band gap energy by changing the composition since the third binary in the alloy offers an additional degree of freedom. Also, while their lattice parameter follow the linear Vegard's law, their theoretical band gap evaluation requires the calculation or at least experimental bowing parameters which cause deviations from the linear law.

Next, we explained that crystal defects are numerous in grown crystal material. There are often vacancies, impurities (interstitial and in substitution), bulk stacking faults and dislocations. Dislocations are particularly detrimental since they are recombination centres of excitons, charge traps and form one common default at material surface called V-defect, as predicted by Frank in the 1950's. We also showed that interface between two different III-nitrides is the zone where a two dimension electron gas can be formed by a discontinuity of polarizations between the two layers in contact. Polarization comes from the dipoles formed by bonds in the tetrahedral structure of III-Ns. It is divided in spontaneous polarization (without strain) and piezoelectric polarization induced by an additional stress to the material by the substrate or the layer below.

Finally, we give the two main applications of nitrides which are high electron mobility transistors (HEMTs) working on the principle of 2DEG movement, and the LED working on the principle of the multi-quantum well structure embedded in n-GaN/p-GaN stack.

Bibliographie

[1] F. Fichter, « Über aluminiumnitrid », *Zeitschrift für anorganische Chemie*, vol. 54, no. 1, p. 322–327, 1907. 4

[2] W. C. Johnson, J. B. Parson et M. C. Crew, « Nitrogen compounds of gallium iii », *J. Phys. Chem.*, vol. 36 (10), p. 2651–2654, 1932. 4

[3] R. Juza et H. Hahn, « Über die kristallstrukturen von cu3, gan und inn metallamide und metallnitride », *Z. Anorg. Allgem. Chem.*, p. 234–282, 1938. 4

[4] H. P. Maruska et J. J. Tietjen, « The preparation and properties of vapor deposited single crystalline gan », *Applied Physics Letters*, vol. 15, no. 10, p. 327–329, 1969. 4

[5] H. M. Manasevit, F. M. Erdmann et W. I. Simpson, « The use of metalorganics in the preparation of semiconductor materials : Iv . the nitrides of aluminum and gallium », *Journal of The Electrochemical Society*, vol. 118, no. 11, p. 1864–1868, 1971. 4

[6] S. Yoshida, S. Misawa et A. Itoh, « Epitaxial growth of aluminum nitride films on sapphire by reactive evaporation », *Applied Physics Letters*, vol. 26, no. 8, p. 461–462, 1975. 4

[7] J. I. Pankove, E. A. Miller et J. E. Berkeyheiser, « Gan electroluminescent diodes », *in 1971 International Electron Devices Meeting*, vol. 17, p. 78–78, 1971. 4

[8] S. Yoshida, S. Misawa et S. Gonda, « Improvements on the electrical and luminescent properties of reactive molecular beam epitaxially grown gan films by using aln-coated sapphire substrates », *Applied Physics Letters*, vol. 42, no. 5, p. 427–429, 1983. 4

[9] H. Amano, M. Kito, K. Hiramatsu et I. Akasaki, « P-type conduction in mg-doped gan treated with low-energy electron beam irradiation (leebi) », *Japanese Journal of Applied Physics*, vol. 28, no. 12A, p. L2112, 1989. 4

[10] H. Amano, N. Sawaki, I. Akasaki et Y. Toyoda, « Metalorganic vapor phase epitaxial growth of a high quality gan film using an aln buffer layer », *Applied Physics Letters*, vol. 48, no. 5, p. 353–355, 1986. 4

[11] H. Amano, I. Akasaki, T. Kozawa, K. Hiramatsu, N. Sawaki, K. Ikeda et Y. Ishii, « Electron beam effects on blue luminescence of zinc-doped gan », *Journal of luminescence*, vol. 40, p. 121–122, fév. 1988. 4

[12] S. Nakamura, « In situ monitoring of gan growth using interference effects », *Japanese Journal of Applied Physics*, vol. 30, no. 8R, p. 1620, 1991. 4

[13] H. Amano, T. Tanaka, Y. Kunii, K. Kato, S. T. Kim et I. Akasaki *Appl. Phys. Lett.*, vol. 64, p. 1377, 1994. 4

[14] S. Nakamura, N. Iwasa, M. Senoh et T. Mukai, « Hole compensation mechanism of p-type gan films », *Japanese Journal of Applied Physics*, vol. 31, no. 5R, p. 1258, 1992. 5

[15] C. WANG et R. F. DAVIS, « Deposition of highly resistive, undoped, and p-type, magnesium-doped gallium nitride films by modified gas source molecular beam epitaxy », *Applied Physics Letters*, vol. 63, no. 7, p. 990–992, 1993. 5

[16] S. NAKAMURA, T. MUKAI et M. SENOH, « High brightness ingan/algan double heterostructure blue green light emitting diodes », *Journal of Applied Physics*, vol. 76, no. 12, p. 8189–8191, 1994. 5

[17] M. A. KHAN, J. M. V. HOVE, J. N. KUZNIA et D. T. OLSON, « High electron mobility gan/alxga1-xn heterostructures grown by low-pressure metalorganic chemical vapor deposition », *Applied Physics Letters*, vol. 58, no. 21, p. 2408–2410, 1991. 5

[18] M. A. KHAN, A. BHATTARAI, J. N. KUZNIA et D. T. OLSON, « High electron mobility transistor based on a gan/alxga1-xn heterojunction », *Applied Physics Letters*, vol. 63, no. 9, p. 1214–1215, 1993. 5

[19] J. KUZMIK, « Power electronics on inaln/(in)gan : Prospect for a record performance », *IEEE Electron Device Letters*, vol. 22, p. 510–512, Nov 2001. 5

[20] S. C. JAIN, M. WILLANDER, J. NARAYAN et R. V. OVERSTRAETEN, « Iii-nitrides : Growth, characterization, and properties », *Journal of Applied Physics*, vol. 87, no. 3, p. 965–1006, 2000. 5

[21] H. Y. FAN, « Temperature dependence of the energy gap in semiconductors », *Phys. Rev.*, vol. 82, p. 900–905, Jun 1951. 6

[22] Y. VARSHNI, « Temperature dependence of the energy gap in semiconductors », *Physica*, vol. 34, no. 1, p. 149 – 154, 1967. 6

[23] F. LECOURT, *Hétérostructures AlGaN/GaN et InAlN/GaN pour la réalisation de HEMTs de puissance hyperfréquence en band Ka.* Thèse doctorat, Université des sciences et technologies de Lille, 2012. xi, 7

[24] R. COLLAZO, S. MITA, A. ALEKSOV, R. SCHLESSER et Z. SITAR, « Growth of ga- and n- polar gallium nitride layers by metalorganic vapor phase epitaxy on sapphire wafers », *Journal of Crystal Growth*, vol. 287, no. 2, p. 586 – 590, 2006. The 16th American Conference on Crystal Growth and Epitaxy The 12th Biennial Workshop on OMVPE. 8

[25] M. SUMIYA et S. FUKE, « Review of polarity determination and control of gan », *MRS Internet Journal of Nitride Semiconductor Research*, vol. 9, 2004. 8

[26] R. CHIERCHIA, T. BÖTTCHER, H. HEINKE, S. EINFELDT, S. FIGGE et D. HOMMEL, « Microstructure of heteroepitaxial gan revealed by x-ray diffraction », *Journal of Applied Physics*, vol. 93, no. 11, p. 8918–8925, 2003. 8

[27] L. VEGARD, « Die konstitution der mischkristalle und die raumfüllung der atome », *Zeitschrift für Physik*, vol. 5, no. 1, p. 17–26, 1921. 10

[28] I. VURGAFTMAN et J. R. MEYER, « Band parameters for nitrogen-containing semiconductors », *Journal of Applied Physics*, vol. 94, no. 6, p. 3675–3696, 2003. 10

[29] I. Gorczyca, T. Suski, N. E. Christensen et A. Svane, « Band gap bowing in quaternary nitride semiconducting alloys », *Applied Physics Letters*, vol. 98, no. 24, p. 241905, 2011. xi, xix, 10, 11, 13

[30] A. Vilalta-Clemente, *Structure des couches d'InN et d'alliages (In,Al)N.* Thèse doctorat, Université de Caen, 2013. xi, 12

[31] D. Hull et D. Bacon, *Introduction to dislocation (Fifth edition).* 2011. xi, 13, 14, 15, 16, 17, 18

[32] J. Lähnemann, U. Jahn, O. Brandt, T. Flissikowski, P. Dogan et H. T. Grahn, « Luminescence associated with stacking faults in gan », *Journal of Physics D : Applied Physics*, vol. 47, no. 42, p. 423001, 2014. 14

[33] C. Stampfl et C. G. V. de Walle, « Energetics and electronic structure of stacking faults in aln, gan, and inn », 1998. xi, 14, 15

[34] B. Heying, E. J. Tarsa, C. R. Elsass, P. Fini, S. P. DenBaars et J. S. Speck, « Dislocation mediated surface morphology of gan », *Journal of Applied Physics*, vol. 85, no. 9, p. 6470–6476, 1999. xi, 18

[35] H. Morkoç, *Handbook of Nitride Semiconductors and Devices : Materials Properties, Physics and Growth, Volume 1.* Wiley, 2009. 19

[36] O. Ambacher, J. Smart, J. R. Shealy, N. G. Weimann, K. Chu, M. Murphy, W. J. Schaff, L. F. Eastman, R. Dimitrov, L. Wittmer, M. Stutzmann, W. Rieger et J. Hilsenbeck, « Two-dimensional electron gases induced by spontaneous and piezoelectric polarization charges in n- and ga-face algan/gan heterostructures », *Journal of Applied Physics*, vol. 85, no. 6, p. 3222–3233, 1999. 20, 21

[37] N. Sarazin, *HEMTs à base de nitrure de gallium : Evolution vers un nouveau système de matériaux, une nouvelle génération de composants.* Thèse doctorat, Université des sciences et technologies de Lille, 2007. xii, 22

2 | Growth by MOCVD and samples characterization methods

Sommaire

2.1 MOCVD process of III-N alloys 30
2.1.1 MOCVD introduction 30
2.1.2 Theory of MOCVD and physical processes description 31
2.1.3 MOCVD tool : AIXTRON CRIUS 37
2.1.4 Overall setup 37
2.1.5 Bubbler operation and precurors choice 40
2.1.6 Buffer layers and standard structures 50
2.1.7 Growth of indium containing III-N alloys and phase separation 51
2.2 Characterization techniques 52
2.2.1 Atomic Force Microscopy : AFM 53
2.2.2 X-ray Reflectometry : XRR 59
2.2.3 Photoluminescence : PL 62
2.2.4 X-Ray Diffraction : XRD 64
2.2.5 X-ray Photoelectron Spectrometry : XPS 69
2.2.6 Auger Electron Spectroscopy : AES 73
2.2.7 Wavelength Dispersive X-ray Fluorescence : WDXRF 78
2.2.8 Sheet resistance measurement 79
Bibliographie 83

In the first part of this second chapter we will examine the different aspects of MOCVD growth, looking at the specific tool we are using, the kind of precursors we employed and its properties, the in-situ characterizations we have, and finally some theoretical elements on MOCVD growth. Then in a second section we will detail the different physical and chemical characterizations we performed on our samples. We will see that some of them are not conventionally used in single crystal layer studies but were very useful for us. Some of them were continually used and others at specific times depending of the expected needs.

2.1 | MOCVD process of III-N alloys

2.1.1 | MOCVD introduction

Microelectronics is a very important part of world trade. In this context over the last forty years, new materials, components, manufacturing processes, and new physical concepts have been developed that meet the growing needs from manufacturers. The variety of semiconductors available for these applications has expanded, and the methods by which it used to build them have been highly diversified. Thus the appearance of structures such as superlattices, multiple quantum wells, the stacks for the production of complex components such as transistors, LEDs or laser diodes LDs have prompted the areas of research and development to focus their efforts in the development of epitaxy growth techniques.

The general specifications that led to these research orientations have been the need to obtain thinner monocrystalline layers of semiconductor (sometimes as little as several angstroms) with excellent interfaces, a perfect control of the composition of the layers or elements doping, and of course the ability to incorporate more elements in alloys formed (four or more).

Several techniques have been developed and two remain commonly used for III-V, III-N, IV-IV and II-VI alloys. These are MOCVD (MetalOrganic Chemical Vapor Deposition) and MBE (Molecular Beam Epitaxy). The first was developed with industrial perspectives such as high growth rates, good quality of the grown layers (surface density of defects, dislocations, etc.), and large grown areas. The second is more common in academic laboratories (lower growth rates, difficulty to automate the loading of substrates, more regular change of sources, etc, difficulties of maintaining ultra-high vacuum conditions). Nevertheless both have their advantages and drawbacks, and both have been used for production of III-V materials.

MOCVD was started in the late 1960s and enjoyed a growing success during the years 1980-1990. With this technique, the growth occurs using gas delivery of elements on a substrate. One of the specificities is that the precursors used combine an organic compound (C-H) and a metal : for example Tri-Methyl Gallium (TMGa). MOCVD is able to provide atomically sharp interfaces between several layers of high purity. The main difficulty which has remained associated with this technique relates to the large number of parameters that can be controlled during the growth of layers, namely : the reactor temperature, pressure, the flow of injected gas, the pressure and temperature bubblers, etc. These parameters influence the layer growth rate, their crystalline quality and surface, the rate of

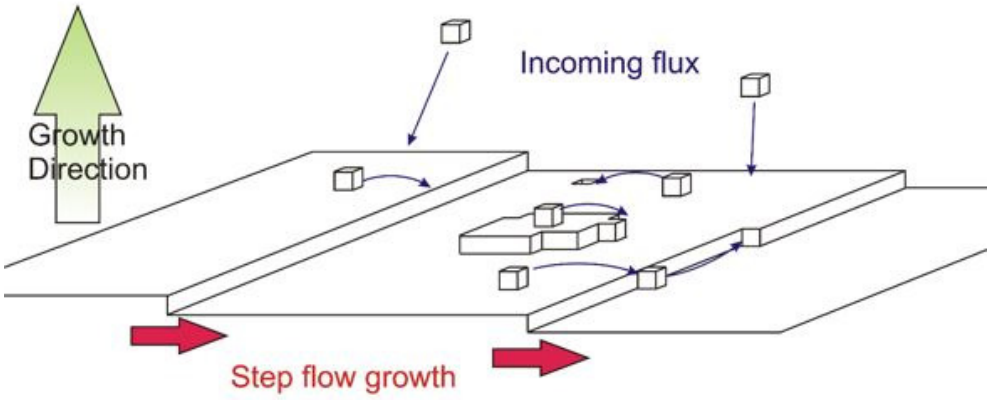

Fig. 2.1 – Geometric representation of epitaxy.

incorporation of certain component elements, the generation of parasitic reactions in the growth chamber, the homogeneity of the layers, and reproducibility.

2.1.2 | Theory of MOCVD and physical processes description

2.1.2.1 MOCVD : a technique for epitaxy

Before speaking about MOCVD and its particularities, we examine first what epitaxy is. All chemical elements, once solidified, crystallize under different structure. Some of them take the form of naturally single crystalline materials like minerals even if several twins can be nested. There, all the atoms of the material follow an ordered structure with a geometric pattern repeated in the three directions of space. And others, like metals for instance, have polycrystalline structures with lots of single crystal phases having the same structure but misoriented from each other. The principle of epitaxy is to grow a single crystal of one specific material combining one or several elements, using as starting points for the manufacture of crystal, a monocrystalline mechanical support called a substrate. Therefore, atoms of the material we want to grow will be able to rely on this structure perfectly oriented in order to form a material with the same geometry. When the process of epitaxy takes place on a substrate of the same nature as the grown material we speak about homoepitaxy. On the contrary when the substrate nature is different from the growing material, we speak about heteroepitaxy.

We can examine an illustration in figure 2.1 of epitaxy made of a surface made of chemical elements represented as small cubes which interlock with each other. In this ideal model, we consider epitaxy as the growth of a film atom by atom, and for single material systems, this often takes the form of 2-dimensional step flow growth. The growth can be catalyzed on the surface, or at step edges, with atoms being incorporated at steps for 2D growth, or on terraces to form islands, according to the growth conditions. We can imagine chemical bonds on the six faces of the cubes. In that case it is always easier to incorporate a cube at an angle where at least three other chemical bond are available than on the surface where the cube is attached by only one chemical bond. A cube at the surface is more easily desorbed than one integrated into it.

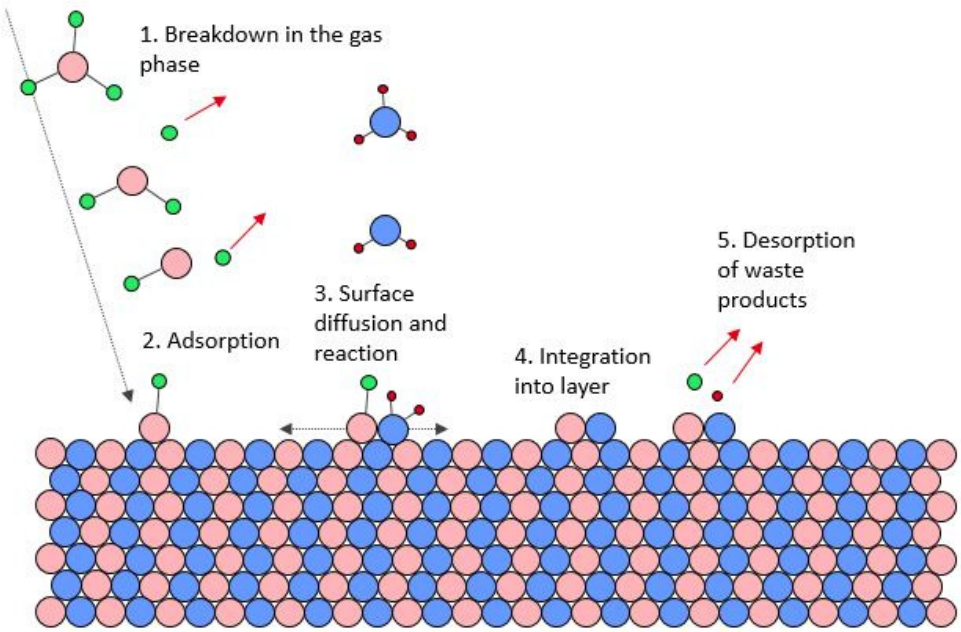

Fig. 2.2 – MOVPE chemical processes in parallel with physical processes

MOCVD is an epitaxy technique where the growth of a single crystal takes place at an interface between a gas phase where we find the reactants and a substrate. Gases must be introduced into the chamber in a controlled manner. Then the molecules have to breakdown by pyrolysis close to the substrate, and diffuse to its surface. The physical and chemical processes are shown in figure 2.2. This is simplified and does not take into account complex reactions in the gas phase and at the surface, and also the integration of wasted products which could generate a doping effect as previously discussed.

2.1.2.2 Overview of the MOCVD process : physical and chemical approach

The study of MOCVD is a highly complex set of different physical and chemical fields, whose goal is to explain the phenomena occurring during the crystal growth. The overall crystal growth process can be divided into distinct components. The thermodynamics of the growth brings together the elements needed to estimate the overall driving force of the epitaxy process. It therefore takes into account the possible maximum growth rate, the stoichiometry and the degree of incorporation of dopants, the composition of solid alloys formed, or surface reconstructions. [1]

The kinetic component brings into play the speeds at which different steps take place. This can be at the surface physical processes (reconstructions, anomalies formations, diffusion, and bitri/-dimensional nucleation). This can also be in homogeneous chemical reactions in the gas phase (adduct formation, pyrolysis of precursors and adducts reactions of complexassions) or heterogeneous reactions with the substrate surface (surface reconstructions, dislocations density, precursors adsorption / desorption and other intermediaries, desorption of the products). [1]

In addition to the thermodynamic and kinetic components, we have the influence of mass transport and heat. This involves hydrodynamics (boundary layer flow circulation, ”dead” zones), the temperature profiles in the substrate, the phenomena of diffusion and convection, and the effects of walls. [1]

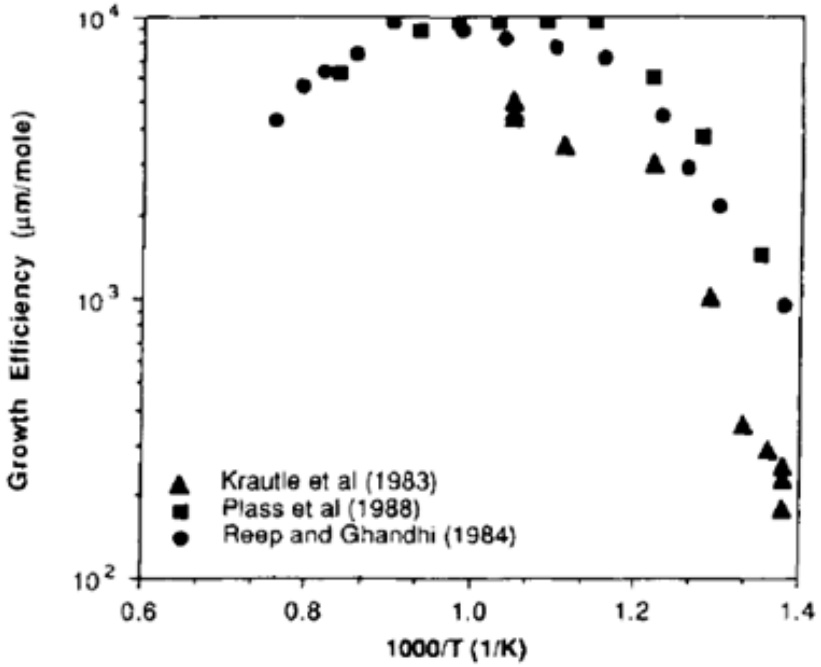

Fig. 2.3 – Growth efficiency (growth rate / TMGa molar flow) as a function of the inverse of the temperature.[1]

We can consider a very well-known example : the growth of GaAs. In figure 2.3 experimental points are shown that represent the growth efficiency depending on the temperature. One can discern the different regimes that constitute it.

Between 550°C and 750°C, the growth rate is constant, it is therefore considered that one is dependent on mass transport only (cf. figure 2.4). The molecules breakdown very quickly on the surface, so the growth rate becomes limited by the delivery of molecules to the epitaxy surface, therefore the growth rate barely changes with temperature. It was also shown that in this growth pattern, the orientation of the substrate has no influence on the growth rate. This is typically the preferred regime for growth, because the alloys and doping are linked to the gas input, rather than the temperature, and so easier to control and predict. This is the regime which is modelled by the boundary layer approximation. Cf. section 2.1.2.3. [1]

Now, if the temperature is lowered, the growth rate decreases, passing into kinetic regime. At these temperatures, certain reactions limit the growth, especially the rate at which the MO molecules break down on the material surface. This gives the growth rate a strong dependence on the temperature, and also on the orientation of the wafers, as reactions at different rates according to the surface they are on. [1]

Finally, above 750°C, processes such as desorption of certain species, or thermodynamics such as the evaporation of some elements (Group III for example), limit the growth rate. During this thesis we typically grew our III-N samples in the mass transport regime. This has two advantages – firstly, the growth rate is linearly dependant on the metalorganic flow and secondly, and the composition is easier to control. [1]

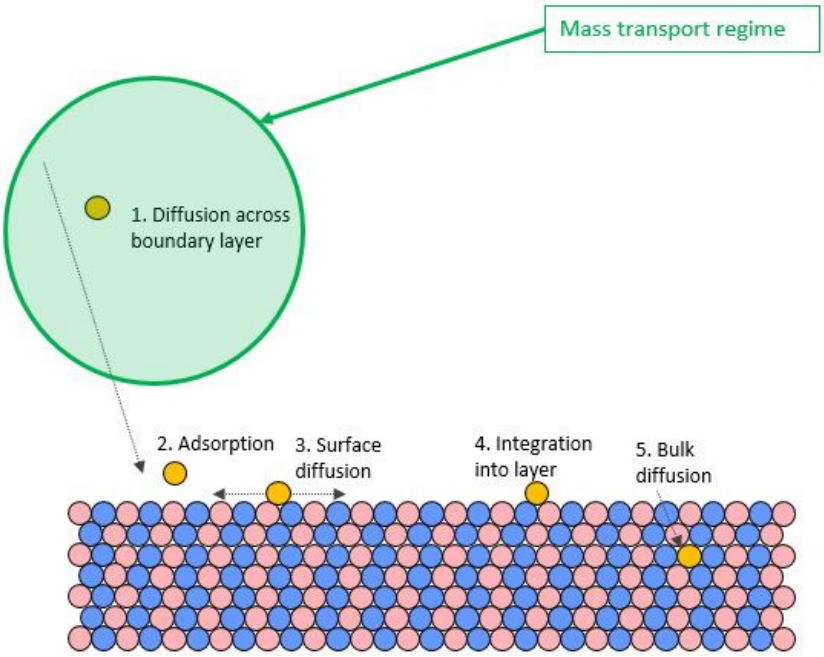

Fig. 2.4 – Mass transport regime : illustration of physical processes.

2.1.2.3 Important quantities and concepts of MOCVD

Diffusion across boundary layer and maximum growth rate

The thermodynamic study of the MOCVD process allows, among other, to calculate the maximum of growth rate. The growth rate is proportional to the flux J of group III elements which are arriving at the interface of growth. This is the main limitation in the mass transport regime.

$$J = \frac{D(p^* - p^i)}{RT\delta_0}) \tag{2.1}$$

where D is the diffusion coefficient of a group III element and δ_0 is the thickness of a laminar-flow boundary layer through which species are diffusing from the gas phase to the interface. Cf. figure 2.5. p^* and p^i are respectively the partial pressures of group III elements in the gas phase and at the growth interface. $R = 8,314 J.mol^{-1}.K-1$ is the ideal gas constant.[1]

From formula 2.1, we can draw four conclusions. First the growth rate should be proportional to group III flux if there are no kinetic barriers. Second, it should then be proportional to p* if the material is consumed rapidly at the interface. Third there is still a slight dependence on temperature, although this also affects the diffusion coefficient. And finally the boundary layer thickness is important for controlling growth rates.

Note that the boundary layer is a thickness above the growing surface where gases velocity is reduced. It is important that the gas flow is laminar and not turbulent, otherwise there is no boundary layer. This should be achieved through good reactor design and it is important to avoid thermal buoyancy effects, very high gas velocity or jetting of gas.

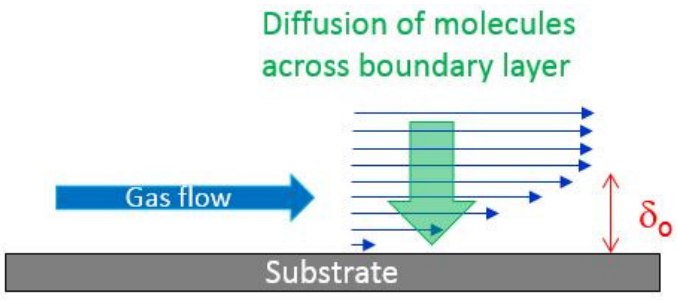

Fig. 2.5 – Representation of the boundary layer close the growing surface.

The boundary layer thickness can be changed by multiple factors such as an higher gas flow velocity to reduce it, changes in carrier gas composition, a change in reactor pressure (but can also change the diffusion coefficient, so no net effect in showerhead systems), and finally an higher rotation speed which can reduce it.

Detailed hydrodynamic studies and simulations have been undertaken which show that this idea of a stationary boundary layer is not a true description of the behaviour of gases in an MOCVD system. However, as a first approximation, this is an good way to approach simple growth calculations.

The last points leads us to examine ways of changing the boundary layer thickness. It can be changed by multiple factors like higher gas flow velocity which reduces the boundary layer, changes in carrier gas composition, a change in pressure, and higher rotation speed which can reduce the boundary layer, due to the turbo pumping effect.

The III/V ratio

We will now look at the V/III gas ratio. The partial pressure of the different group V and group III elements at the growth interface controls the some elements of the growth, although the stoichiometry is not strongly affected due to the strongly covalent bonds. For III-N growth by MOCVD, the V/III ratio is much higher than 1. This means that Ga is nearly depleted (equation 2.2) at the interface and NH_3 partial pressure is hardly diminished (equation 2.3). This means we have the following relationships : [1]

$$p^i_{Ga} \ll p^*_{Ga} \tag{2.2}$$

$$p^i_N \approx p^*_N \tag{2.3}$$

where $p^i_G a$ and p^i_N are the partial pressures of Ga and N at growth interface respectively, and $p^*_G a$ and p^*_N are the partial pressure of Ga and N in the gas phase (input).

So according to the previous discussion, what interests us is the V/III ratio at the interface, i.e. p^i_V/p^i_{III}. We can also express the equilibrium constant $K_{III/V}$ of the chemical reaction forming our III/V material from the gas phase : [1]

$$K_{III/V} = \frac{a_{III/V}}{p^i_{III} p^i_V} = \frac{a_{III/V}}{p^i_{III} p^*_V} \tag{2.4}$$

We can finally calculate the real V/III ratio : [1]

$$\frac{p^i_V}{p^i_{III}} = \frac{K_{III/V}}{a_{III/V}} p^{*2}_V \tag{2.5}$$

Which shows that in fact the V/III ratio at the growth surface is proportional to the square of the partial pressure of the group V element, and not related to the group III partial pressure, which only controls the growth rate.

Precursor pyrolysis

As explained previously, in the kinetic regimes where the growth rate depends on the temperature, one of the reactions that can limit the overall growth rate is the pyrolysis of MO precursors and ammonia. For TMGa, TMIn and TMAl the three main successive steps of homogeneous reaction that allow the metal release are described as follow : [1]

$$\mathrm{Ga(CH_3)_3} \longrightarrow \mathrm{Ga(CH_3)_2} + \mathrm{CH_3}$$

$$\mathrm{Ga(CH_3)_2} \longrightarrow \mathrm{Ga(CH_3)} + \mathrm{CH_3}$$

$$\mathrm{n - Ga(CH_3)_2} \longrightarrow \mathrm{[Ga(CH_3)]_n(s)}$$

$$\mathrm{Ga(CH_3)} \longrightarrow \mathrm{Ga} + \mathrm{CH_3}$$

Each step has its own rate and temperature at which it happens. Typically for TMIn pyrolysis, the three bonds break above 480°C with second break having a much higher rate than the first one so that the two first steps occur nearly simultaneously. The third bond is then lost at the growth surface. The pyrolysis of TMGa is similar to that of TMIn with bonds broken above 550°C. [1]

For our last MO precursor, TEGa, the pyrolysis steps are as follows : [1]

$$\mathrm{Ga(C_2H_5)_3} \longrightarrow \mathrm{Ga(C_2H_5)_2} + \mathrm{C_2H_5}$$

$$\mathrm{Ga(C_2H_5)_2} \longrightarrow \mathrm{Ga(C_2H_5)} + \mathrm{C_2H_5}$$

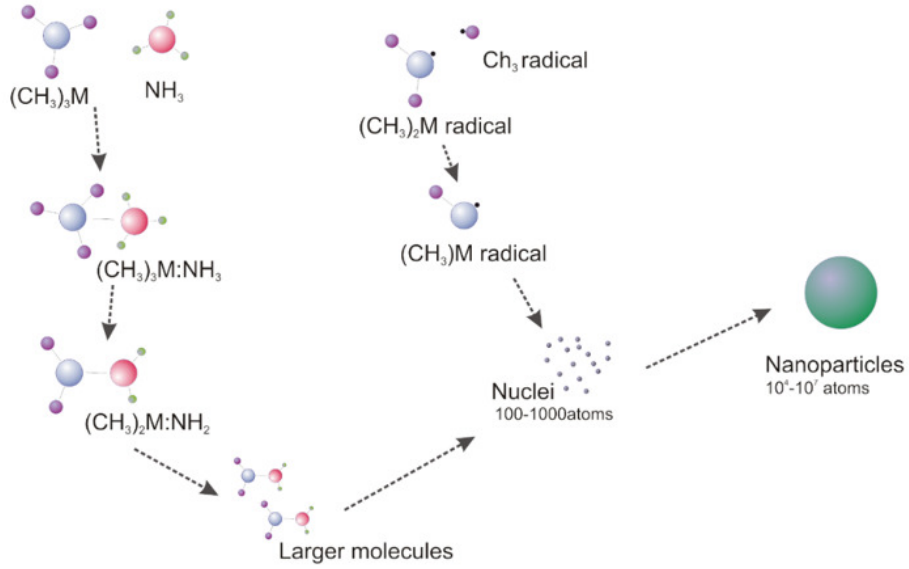

Fig. 2.6 – Illustration of parasitic reactions.

$$Ga(C_2H_5) \longrightarrow Ga + C_2H_5$$

As described later in this chapter, the ethyl bond breaks more easily than the methyl bond, and through a process called "beta elimination", the gallium can lose all of its organic groups before arriving at the growth surface. Thus it typically has a much lower carbon incorporation into layers than TMGa.

Parasitic gas phase reactions

Before pyrolysis, some MO precursors are likely to react with each other which can lead to a decrease of the growth rate, changes in solid stoichiometry or even a non-growth. These parasitic reactions are encouraged by very reactive precursors such as TEAl, high reactor pressures, high growth temperatures or a poor separation of gases in the reactor.

The typical example is TMAl with NH3. Indeed the growth of usual Al containing alloys like AlN and AlGaN requires high temperatures. But TMAl and NH3 have strong reactions. So the growth of AlN orAlGaN must be performed at low pressure

2.1.3 | MOCVD tool : AIXTRON CRIUS

2.1.4 | Overall setup

We grew all of our samples using a fully automated AIXTRON with a close coupled showerhead system. The reactor accommodates one 200mm silicon wafer at a time. The showerhead architecture is interesting since it distributes the gas homogeneously across the substrate ensuring good growth homogeneity.

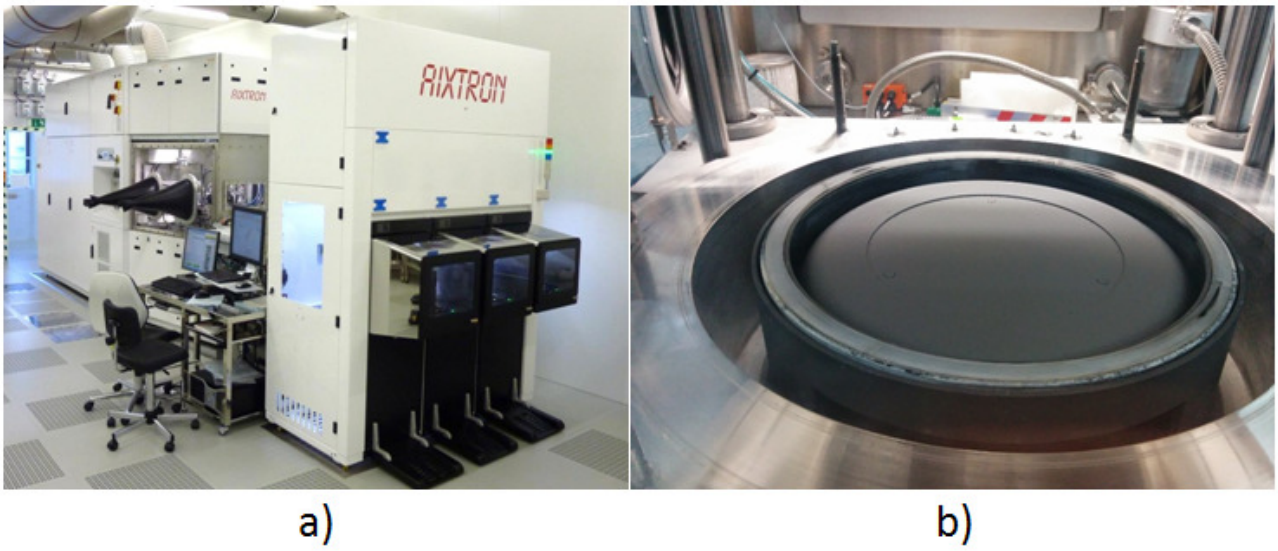

Fig. 2.7 – a) Photo of the AIXTRON CRIUS MOCVD tool, and b) a view of the SiC coated graphite susceptor.

In the layout of our tool we have gas lines bringing the different reactants using carrier gas into a growth chamber also referred to as a reactor. Downstream, waste gases are sent to a scrubber by a pump where they are treated. There is a filter which protect the pump from particles or condensation. The scrubber treats the polluting gases coming out of the system. There hydrogen is burned for safety reasons, and hydrides are caught in cartridges or burned like ammonia. MOs are trapped too for large machines due to increasingly stringent environmental rules.

On the gas lines side, we have two sources of carrier gas : nitrogen and hydrogen. The ammonia source and the different metalorganic bubblers are connected independently to one or another the carrier gas and a mix of them is also possible. First, carrier gases are there to push the reactants to the reactor with a controlled flow and thus a constant gas velocity which simplify growth calculations. Then, they are carrying active gases rapidly to the reactor and then purging the waste. In addition, they avoid gas phase prereactions between the reactants by diluting them. Finally, they may have different thermal and also chemical effects, and depending on the grown materials, we will prefer one or the other carrier gas to influence material properties (cf. chapter 3, 4, 5, and 6).

We can refer to figure 2.8 for a better overall view. First note that MO and hydride (ammonia) sources are separated for an accurate control of the gas mixing in the growth chamber, and to avoid prereactions. Each of them can be sent on two different lines : vent and run. The run line is sent to the reactor and the vent bypasses the reactor and goes directly to the scrubber. Each reactant source can be switched to run or vent line during the growth. The role of vent and run lines is important. Using differential pressure sensors between them we keep both lines at the same pressure. So when a source is switched from the vent to the run, there are no gases pulsing effects which could influence the quality of interfaces between two materials in an heterostructure.

Inside the reactor is an SiC coated graphite susceptor on which the substrate is placed by the transfer robot. Below the susceptor is the heater, composed of a planar coil divided into three parts separately

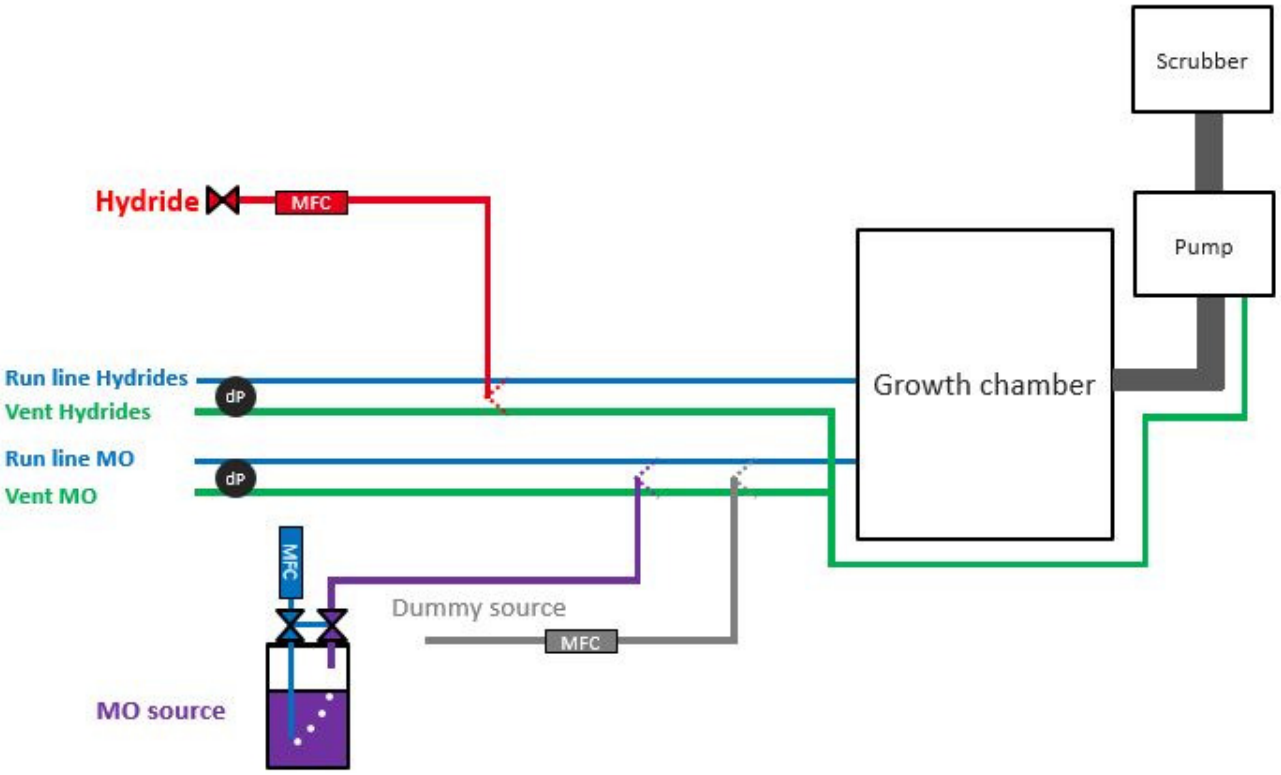

Fig. 2.8 – Gas lines in AIXTRON Crius.

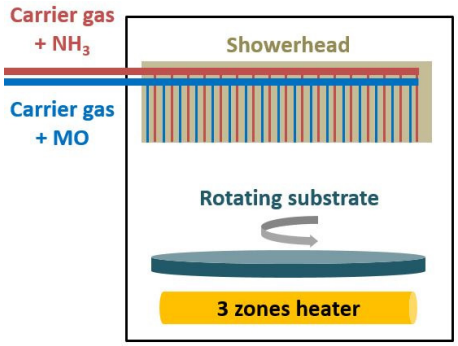

Fig. 2.9 – growth chamber of AIXTRON CRIUS.

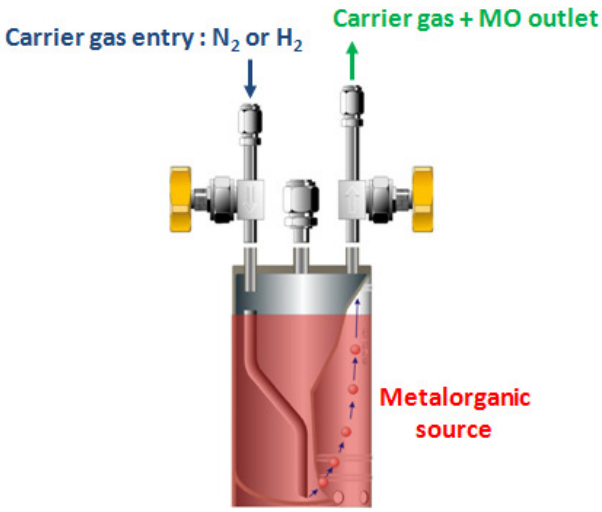

Fig. 2.10 – Bubbler schematic.

controlled and heated. This allows us to have a uniform temperature on the substrate. Indeed, depending on the coefficient of thermal expansion difference between all the layer of the stacks made, a bow can appear on the wafer. If the wafer became convex we have to apply a higher power the central zone and if it became concave we have to apply a higher power the edge zone in order to keep the temperature uniform on the wafer surface.

The showerhead is 11 mm above the susceptor The showerhead is aptly named and allows a homogeneous gas distribution on the substrate which is in rotation by the way. It is made of more than thousands of holes, through which alternately MO + carriers gas mixture and ammonia + carrier gas mixture are injected (cf. figure 2.9). Thus, all the gases are well mixed when they arrive at the substrate. The low distance between the substrate and the shower head prevents us from having the gas mix too far away from the substrate and thus avoids too many parasitic chemical reactions before deposition at the surface.

2.1.5 | Bubbler operation and precurors choice

2.1.5.1 Bubbler operation

In the general MOCVD layout, the bubbler is the part dedicated to the storage and the diffusion of MO precursors through the different gas lines toward the reaction chamber. Inside, the source materials can be either in the solid state like a powder for example or in the liquid state depending of on the temperature of the bubbler and source material.

In a bubbler in MOCVD, the carrier gas (H_2 or N_2) is entering directly into the MO precursor. The carrier gas bubbles through the liquid or the powder, and becomes saturate in MO molecules and it leaves the bubbler by an exit connected with the reactor by run-vent valves, as described above.

It is important to describe the bubbler operation precisely since its good control is necessary to know exactly what is the amount of source molecules sent to the growth reactor. This relative amount of

Chemical Name	Formula	Melting Point (°C)	A	B
Trimethylgallium	$(CH_3)_3Ga$	-15.8	1703	8.07
Triethylgallium	$(C_2H_5)_3Ga$	-82.3	2162	8.083
Trimethylindium	$(CH_3)_3In$	88	3014	10.52
Trimethylaluminum	$(CH_3)_3Al$	15.4	2135	8.224

Tab. 2.1 – Chemical properties of MO precursors.

MO reactants will drive the stoichiometry of grown alloys. It depends on the flow of carrier gas passing through the bubbler, the temperature of it and the pressure inside.

$$\frac{F_{MO}}{F_{H_2}} = \frac{P_{MO}}{P_{H_2}} = \frac{P_{MO}}{P_{Bubbler} - P_{MO}} \tag{2.6}$$

Thus :

$$F_{MO} = F_{H_2} \cdot \frac{P_{MO}}{P_{Bubbler} - P_{MO}} \tag{2.7}$$

where F_{MO} is the flow of metalorganic molecules leaving the bubbler, F_{H_2} is the flow of hydrogen carrier gas entering the bubbler, P_{MO} is the vapor pressure of the MO source, and finally $P_{Bubbler}$ is the pressure of the bubbler.

The vapour pressure is calculated using an empirical law :

$$P_{MO} = 10^{B - \frac{A}{T}} \tag{2.8}$$

where P_{MO} is the vapour pressure of the MO in mmHg, T is the temperature in °C, and A and B are experimental parameters explicited in table 2.1.

Depending on the MO flow quantity we want to send to the growth chamber we can use two types of bubbler with different dilution system : the simple dilution and double dilution ones represented in figure 2.11. In the diagram, mass flow controllers and pressure controllers are represented by rectangles, with the value indicated being those of carrier gas. The molar flow of metalorganic source has to be calculated using formula 2.6, 2.7 and 2.8.

2.1.5.2 Metalorganic precursors and other sources in MOCVD process of III-Ns

The molecule providing the metal atom for the growth of a material by MOCVD is a metalorganic precursor in which the metal atom is surrounded by one or more alkyl radicals. Usually these precursors are very hazardous and toxic materials. All of them are pyrophoric in III-N growth which means that they combust spontaneously in air. Suppliers have to take extreme precautions while synthesizing them and as MOCVD process users we have to be careful with their storage and handling. As the bub-

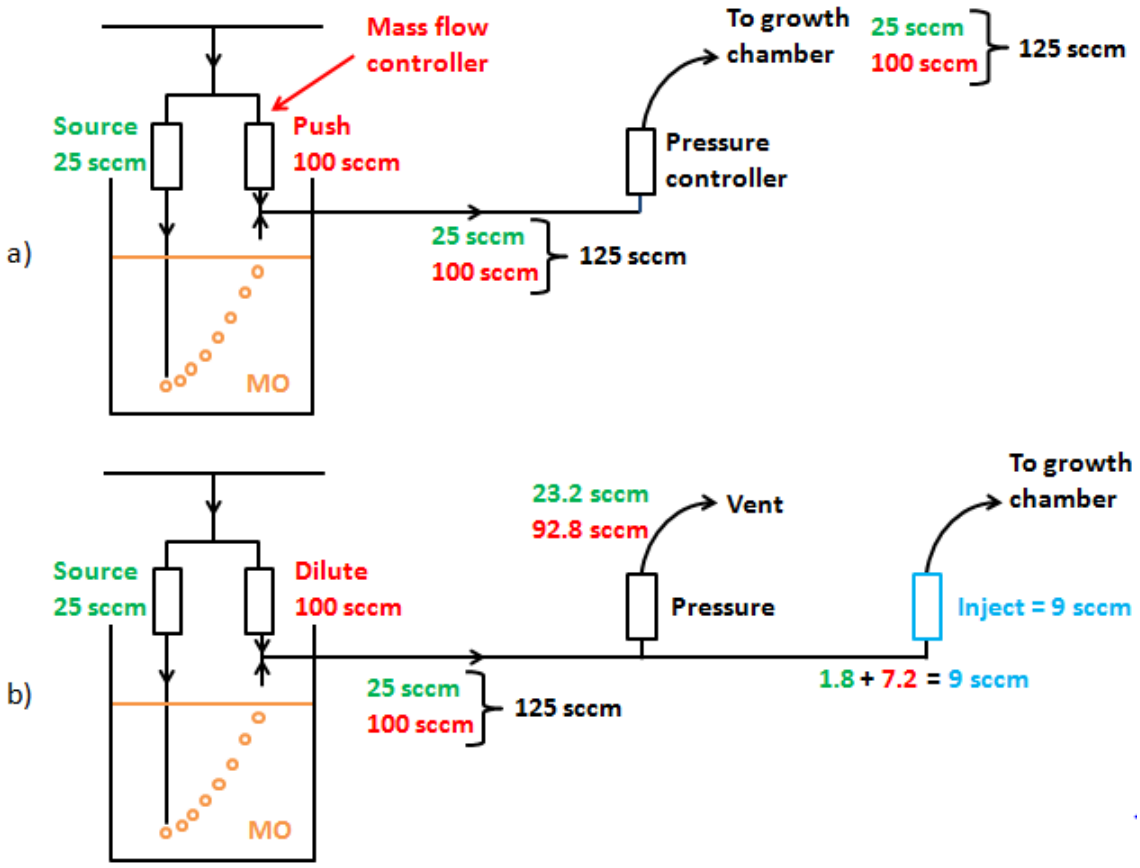

Fig. 2.11 – a) A simple dilution bubbler, and b) a double dilution bubbler for lower MO flow.

bler is closed there is no apparent risk. The most delicate step is the bubbler exchange when one is empty.

There are today several precursors for each atom which have to be incorporated in the grown layers. They were developed according to the needs to have materials with different properties implying the efficiency of pyrolysis of the MO precursor at a specific temperature, the quantity of carbon and oxygen it incorporates in the layer, etc. The kinetic of pyrolysis is one of the most important step of MOCVD process since it directly defines the way that metal atom can be made available for an integration into the layer.

We used four MO sources in our experiments : trimethylgallium (TMGa), triethylgallium (TEGa), trimethylaluminum (TMAl) and trimethylindium (TMIn). Group III molecules with three ligands are all planar with three covalent bonds separated by an angle of 120°. Moreover the electronic configuration of these molecules makes the group III alkyls electron acceptors also known as Lewis acids. For the group V element, the nitrogen atom is supplied by ammonia NH_3. The molecule looks like a stool with three feet. The angle between each bond is 109.5°.

The ease with which the source molecule pyrolizes is defined by the metal-carbon bond strength. This is the bond which must be broken to allow the metal atom to be free and thus integrated into the layer. The bond strength depends both on the nature of the metal atom and therefore its electro negativity, and also the type, size and configuration of the alkyl radical. Generally as a first order

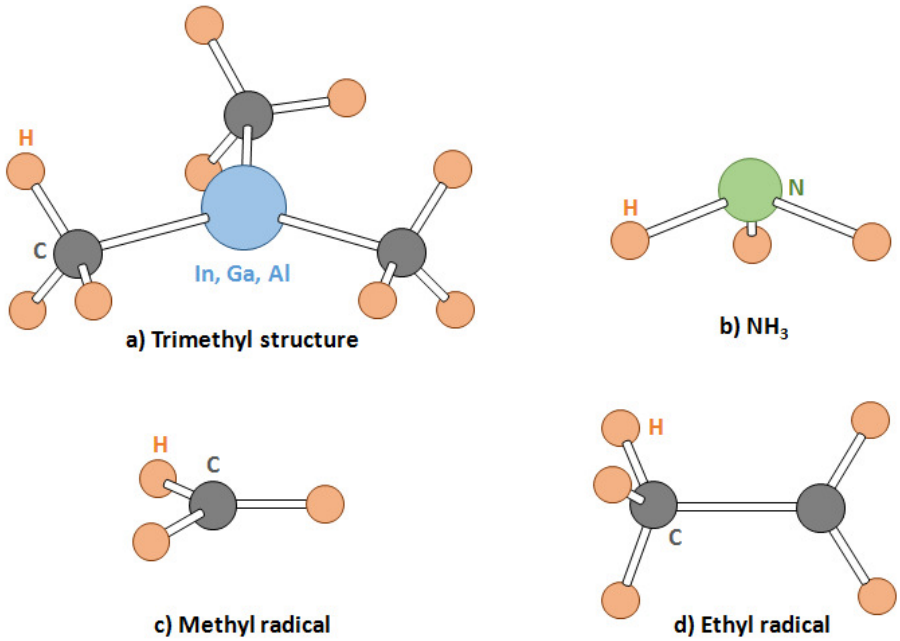

Fig. 2.12 – Three dimension representation of a) the trimethyl structure, b) the NH_3 molecule, c) the methyl radical, and d) the ethyl radical

approximation, the metal-carbon strength decreases with the increase of the number of carbon atoms attached to the metal one. Secondly as the size of the radical increases at a fixed value of carbon atoms attached to the metal atom, the bond strength decreases. The results of this metal-carbon bond strength are reflected in the pyrolysis temperature and thus the growth temperature. Depending on the constraints of epitaxy by material we have to choose the most appropriate source molecule. [1]

It is worth noticing that the last important parameter related to the source molecules and especially the MO ones stored in bubblers is the vapor pressure. Previously we gave an empirical formula that makes the link between temperature and vapor pressure for one precursor. The higher this vapor pressure is, the easier it will be to extract the MO molecules from the bubbler. As a general rule, molecules with ethyl groups have a lower vapour pressure, than those with methyl groups. [1]

Knowing the two last point we can understand why tri-methyl sources are frequently used in MOVPE : They have a higher vapor pressure and have a greater stability. However, as we will discuss below, there can also be good reasons to choose tri-ethyl sources.

Ammonia is a highly stable molecule which requires high temperature to be decomposed. That is one of the reasons why growth temperatures above 1000°C are used for the growth of the majority of III-nitrides which do not contain indium, indium nitride being volatile. Typically ammonia decomposes only 15% at 950°C, even catalyzed by GaN. However, nitrogen atoms are volatile and suffer from desorption at these high temperature. This explains the fact that III-N materials contain lots of nitrogen vacancies, making it n type. The N vacancies problem can be partly solved using either lower growth temperature or a higher ammonia concentration and thus higher nitrogen concentration in the nutrient gas phase. There are other nitrogen precursor like hydrazine N_2H_4 which pyrolyzed well below 1000°C but these are even more toxic than MO sources and explosive, and so are not installed on our tool. [1]

The use of MO precursors implies carbon chains from which carbon atoms can be incorporated in the growing layer during the pyrolyzis. The carbon incorporation can change the intrinsic resistivity of our material in two different ways. It can act as a trap, and so reduce the mobility in 2DEG structures, or increase the resistance of doped layers. However, it can also have positive effects on the breakdown voltage of our structures, so it is important to master this doping. The alkyl group the more likely to cause incorporation of carbon atoms is the methyl one : CH_3. Actually methyl radical can lose one hydrogen atom while on the surface. The thus formed CH_2 element is highly reactive and decomposes to produce one carbon atom in the layer. Kinetically the desorption of CH_3 from the surface is a slow reaction compare to its hydrogen loss. It is enhanced when aluminum atom are at the surface. One element can eventually accelerate its desorption : hydrogen coming from NH_3 pyrolysis which reacts with CH_3. In our case we have two Ga precursors : TMGa and TEGa. The ethyl groups break off from the gallium atoms before they arrive on the surface, reducing carbon incorporation. Also ethyl groups and other bigger than methyl ones can be more easily desorbed from the surface in case of previous adsorption. Thus although above we said that methyl groups are preferred in order to have more stable molecules and higher vapour pressures, ethyl groups are an interesting option for reducing carbon doping. [1]

2.1.5.3 In-situ characterizations

The growth of multiple samples in an automated tool requires a precise monitoring of several physical parameters during the growth. Installed above the reactor and communicating inside with optical fibers, we have the EpicurveTT module from Laytec which combines a curvature sensor, a two wavelength reflectometer and a pyrometer. They are allowing respectively the wafer curvature with a double parallel laser beam, a two wavelength reflectance of the sample, and the measurement of the emissivity corrected pyrometry at 950nm.

Curvature sensor

The bow of wafers needs to be controlled to avoid too much mechanical stress stored in the sample, which could induce damages in it or even its break in the reactor during the growth or temperature ramps, or in other processes applied to the sample. Moreover we are growing layers containing indium which is very sensitive to temperature changes. A bow would induce composition inhomogeneities in the wafer along the diameter. If the wafer is convex, edges are hotter, and if the wafer is concave, edges cooler. There are several causes of a bow appearing in the wafer, for example due to the growth of a material on a substrate with a different lattice parameter. If the top material has a higher in plane lattice parameter than the bottom one the wafer becomes convex.

Bow can also be attributed to different coefficients of thermal expansion between the two materials in contact even if they have the same lattice parameters. If the CTE of the top material is higher than the bottom one, the wafer becomes concave as the temperature is reduced. Finally for one material only, a temperature gradient between the top and the bottom face of the substrate can induce a bowing. If the temperature at the top is lower than at the bottom the wafer become concave. The real case is a

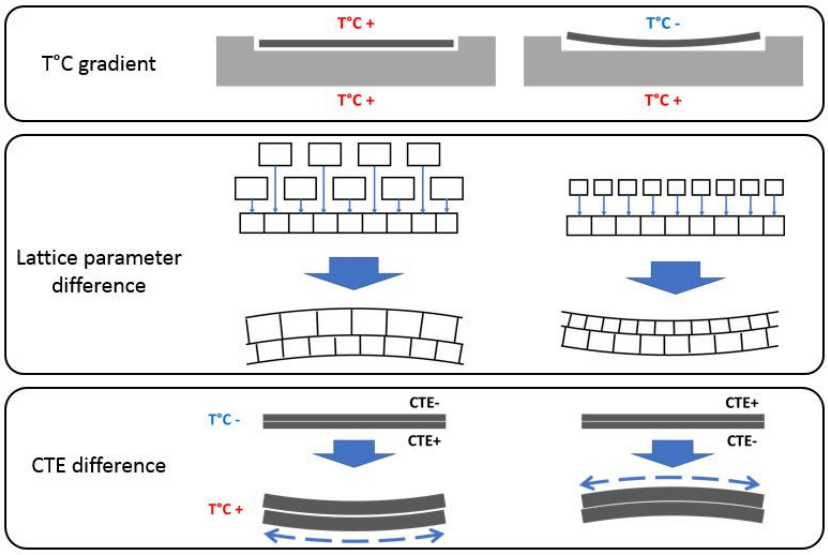

Fig. 2.13 – Influence of temperature gradient, lattice mismatch, and CTE difference on wafer bowing. The CTE case is illustrated for the effect of increasing the temperature of a wafer

combination of each of these causes since we are doing heteroepitaxy of different materials and there is a temperature gradient along the wafer thickness since the substrate is placed on the heated susceptor and there is a steep thermal gradient to the showerhead cooled at 50°C. The three causes of bowing are shown in figure 2.13.

The measurement principle of our EpiCurve system is simple. By one hole called a view-port in the showerhead, a parallel laser double beam is sent to the sample surface and reflected, then caught on a 2D CCD camera. If the wafer is flat, which means no bow, the two reflected beams are parallel and they form two points on the CCD screen the same distance apart as they started. If the wafer is convex, the reflected beams are not parallel anymore and the points on the CCD are more distant. For concave wafers, the points would become closer together. Cf. figure 2.14 for illustration. Then by a geometric calculations it is easy to find the curvature which is the inverse of the curvature radius as defined in figure 2.15. [2]

We can calculate the bow b using the next formula : [2]

$$b = R.\left(1 - cos\left(\frac{r}{R}\right)\right) \tag{2.9}$$

where b, R, and r are defined in figure 2.15.

Two wavelength reflectance

In order to follow the growth of crystalline layer during the MOCVD process, we use their reflectance. Typically the EpiTT module has two LEDs, one at 405nm and 950nm, which are selected depending on their absorbance in the growing material. Using a different aperture in the showerhead than for the curvature control, LED light beams are sent to the wafer surface with a normal incidence and a detector receives the reflected signal. We call reflectance the ratio between the reflected signal intensity

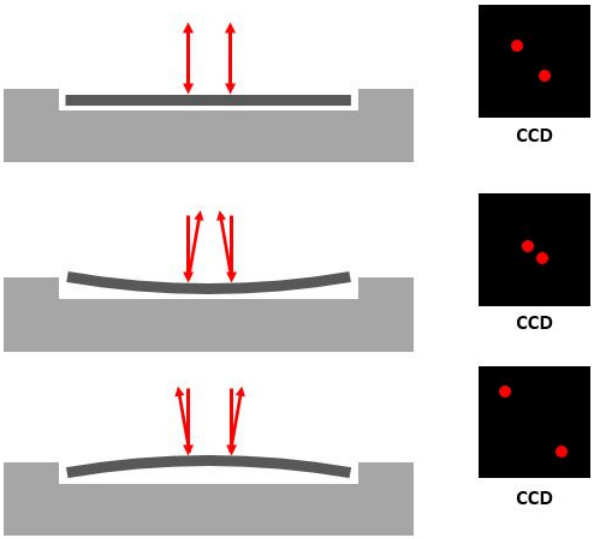

Fig. 2.14 – Detection of wafer bowing using two beam reflected at the surface and detected by 2D CCD camera. Interpretation of laser spot spacing.

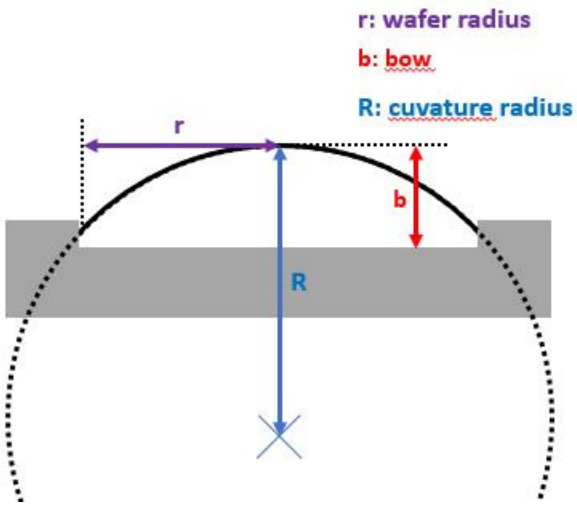

Fig. 2.15 – Configuration of geometrical parameters defining the bow.

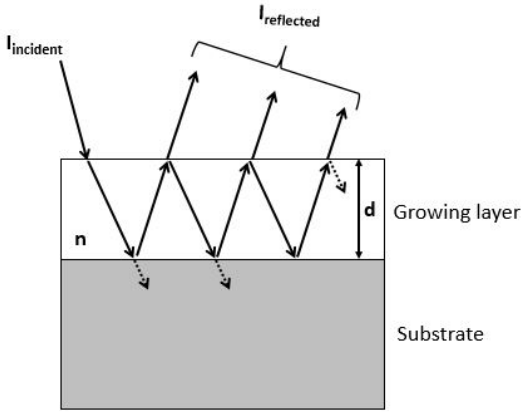

Fig. 2.16 – Schematic of the optical configuration of an incident beam refracted and reflected from a surface and an interface between two materials. In reality, the beams are normal to the growth surface.

and the incident signal intensity.

Analysis of the growing material is simpler if the layer is fully transparent, but in reality there is always absorption of the incident intensity. From a physical point of view (cf. figure 2.16) when the incident beam reaches the layer surface, a part of the beam is directly reflected. The other part is refracted in the material and reaches the interface below, deep inside the layer. At this interface, the same process occurs and one fraction of the intensity is reflected and the other refracted. The total reflected intensity at the substrate-thin film interface and at the surface form interferences having an oscillation form versus the time (and thus the thickness) which are successive constructive and destructive fringes called Fabry-Pérot oscillations.

Physically, between two maxima (or minima) on the oscillations figure recorded during the growth, the layer has been increased of a thickness d which depends of the wavelength : [2]

$$d = \frac{\lambda}{2n} \tag{2.10}$$

where n is the refractive index of the growing layer. Therefore it is easy to calibrate the growth rate in a specific set of growth parameters (MO precursor, MO flow, temperature in kinetic regime) by dividing the thickness grown during a certain time by this time. Therefore, with the 405nm and 950nm wavelengths, the distance between two maxima (or minima) corresponds respectively to GaN thicknesses equal to 86nm and 202nm. We remind that the refractive indexes of GaN and AlN are respectively 2.35 and 2.15.

The oscillation intensity depends on different physical parameters and it can allow certain interpretations as shown in figure 2.17. If the growing layer is transparent to the LED beam, and flat, the amplitude of oscillation stays constant. If the layer presents a certain absorbance at the wavelength of the incident beam, the amplitude is decreasing while the layer growth in thickness. This case can also been attributed to composition fluctuations and thus refractive index changes during the growth. And finally an average value of the intensity of oscillations which is decreasing indicates a surface which is

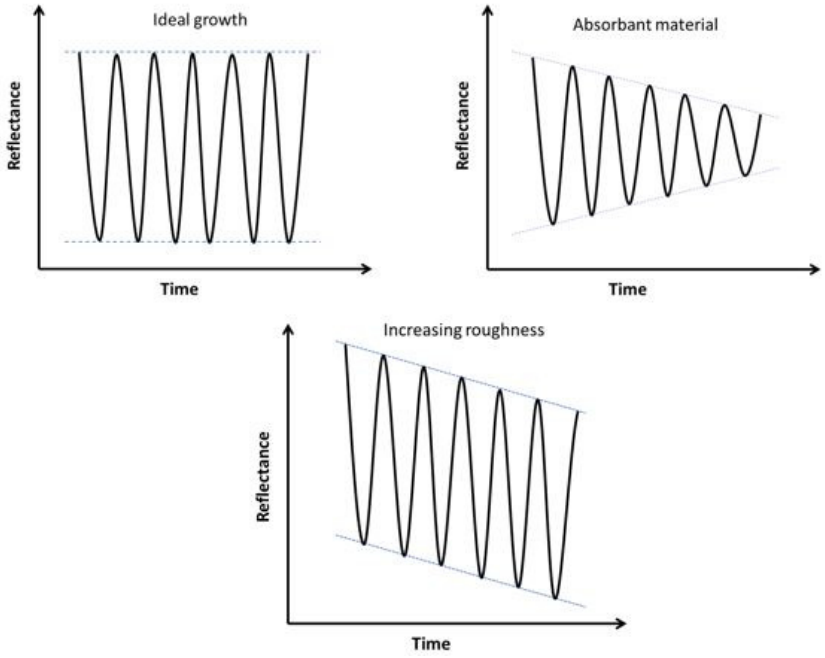

Fig. 2.17 – Three cases of Fabry-Pérot oscillations depending on materials properties : ideally transparent and without roughness, absorbent, and roughening.

roughening. Of course real cases are often a combination of two or the three cases. [2]

Temperature sensor

Temperature of wafers is of course one of the most important parameter to check during the growth as it is likely to have a strong effect on indium containing alloys composition, roughness, and so on. In our tool, there is a thermocouple, on the backside of the sample holder. But the susceptor is subject to temperature gradients which depend on the gas conductivity in the chamber, and the deposition on the cooled showerhead for example. Moreover the wafer is not directly resting on the susceptor, but by little tips called lift pins, to avoid a direct contact and ensure a better temperature homogeneity in case of bowing effect. Thus the temperature of samples during the growth is measured using the EpiTT module from Laytec. It combines a pyrometer and a reflectance measurement giving us an emissivity corrected temperature in six points at half radius of each wafer. We used the mean of these six values for each sample.

The measurement is based on the theory of the black body which specifies that a heated material, whose absorption is 100% at any wavelength, emits an electromagnetic radiation called thermal radiation or incandescent intensity. At a fixed temperature, the incandescent intensity is a function of the wavelength and its temperature dependence follow the Planck's law. At any wavelength, increaing the temperature leads to an increase in the incandescent intensity (cf. figure 2.18). So if we know the incandescent intensity and the wavelength of emission we can calculate the temperature from Planck's law, but for a black body. Our material does not have an absorption of 100% and does not emit a radiation fully corresponding to its temperature. So the Planck's law must be corrected with the emissivity of the material $\epsilon(\lambda, T) = \frac{P}{P_s}$, P and P_s being the respective emission of a real material and a black body. It

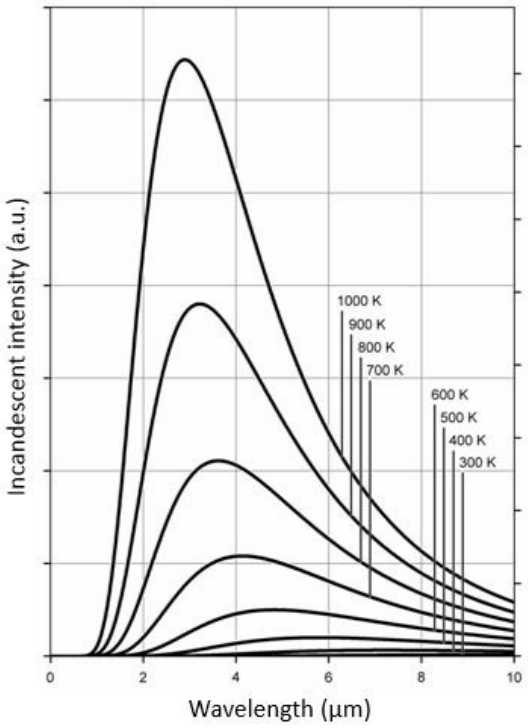

Fig. 2.18 – Planck's law.

represents the fraction of the emitted radiation with respect to that of a black body. Therefore the Planck's law giving us the theoretical incandescent intensity is : [2]

$$dP = \epsilon.dP_s = \epsilon.\frac{2}{h^4c^3}.\frac{(\hbar\omega)^5}{e^{\frac{\hbar\omega}{k_BT-1}}}.d\lambda \tag{2.11}$$

where h is the Planck's constant, c the speed of light in vacuum, $\hbar = \frac{h}{2\pi}$, λ is the wavelength of emission, $\omega = \frac{2\pi c}{\lambda}$, T is the temperature of the material emitting, and k_B is the Boltzmann's constant.

Typically the optical properties such as the refractive index of the growing material (substrate and layers), its surface roughness and its band gap, which changes with the temperature, modify its emissivity. Moreover thermal radiation also undergoes refractions and reflections at surfaces and interfaces which generate interferences whose fringes spacing in depending on the thickness. Thus this can be analyzed by reflectometry at the same wavelength as that of the pyrometry (950nm). The technique works well with opaque substrate such as our silicon, even with growing layers which are transparent. We know that for any material exposed to an electromagnetic radiation, the transmission part T, the reflection one R (measured by reflectometry) and its absorption coefficient α form a sum equal to unity. If the material is opaque, $T = 0$ and then $\alpha = 1 - R$. Finally the Kirchoff's law informs us that the absorption equal the emissivity : $\alpha(\lambda, T) = \epsilon(\lambda, T)$. We finally have all the experimental parameters that allow us a good estimation of the temperature. [2]

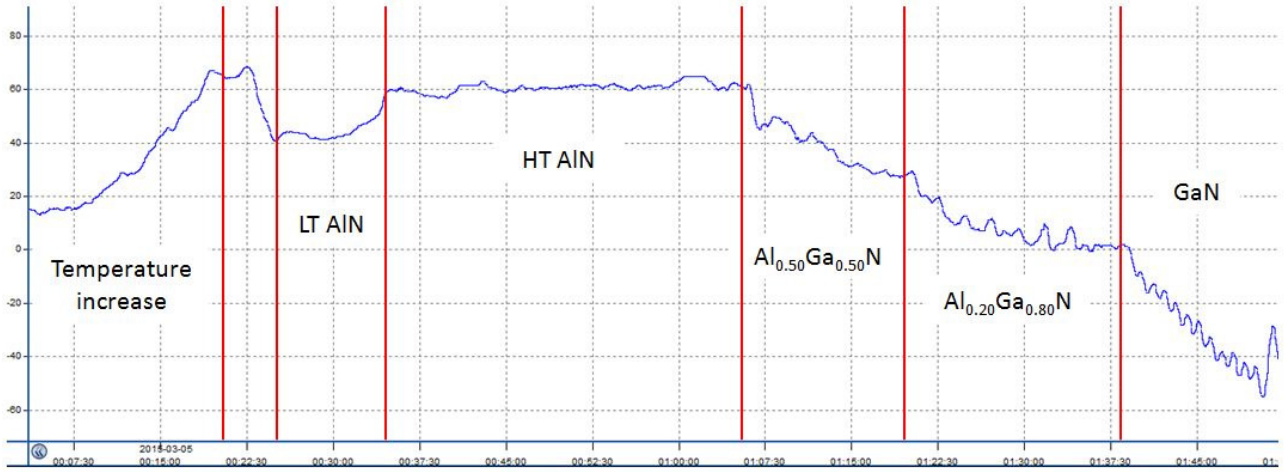

Fig. 2.19 – Example of curvature measurement of the buffer structure from the silicon substrate to the thick GaN layer.

2.1.6 | Buffer layers and standard structures

The use of silicon as a substrate for our samples requires the epitaxy of several buffer layers in order to reach the lattice parameter of GaN and then the one of InAlN or InGaAlN barrier layers or multi-quantum wells. We also need these layers to compensate for the difference in thermal expansion coefficients between III-Nitrides and silicon. After the substrate is heated under hydrogen to desorb all the oxide, and rearrange the surface atoms, we start the buffer layer deposition with a 30nm thick AlN layer grown at 1000°C to favor the adsorption of aluminum species. At this step, many dislocations are formed in the basal plane (misfit dislocations) and thus normal to the surface (threading dislocations) to release the layer stress induced by the substrate "a" lattice mismatch. The mosaic structure described in chapter 1 section 1.2.2.3 is appearing due mainly to these dislocations and other crystal defects. [3][4][5]

This is followed by the growth of a 210nm thick AlN layer at 1100°C to improve the crystal quality. After that, two AlGaN layers, with first a composition of $Al_{50}Ga_{50}N$ (500nm) and then $Al_{20}Ga_{80}N$ (800nm), are successively grown at 1080°C to approach the GaN a lattice parameter. And so we can start the growth of a 2μm thick GaN pseudosubstrate at 1050°C that we need before growing barrier layers, multi-quantum wells or other epilayers.

We will illustrate this growth with two in situ characterizations - the curvature sensor (cf. figure 2.19) and the reflectance (cf.figure 2.20).

The curvature measurement shows us that during the temperature increase before any growth, the substrate become concave because of the temperature gradient along its thickness and it is colder at its surface. Then, during the growth of the two AlN layers, the curvature is not changing except during the temperature decrease before the low temperature AlN growth and increase before the high temperature growth. Next, during the growth of AlGaN layers and GaN the layers are under compression due to its lattice mismatch compared to AlN. Therefore the wafer becomes progressively convex. Moreover we regularly observe bursts in the concavity direction (to the top) during the growth of AlGaN layers and more accurately the GaN layer. They correspond to artefacts in

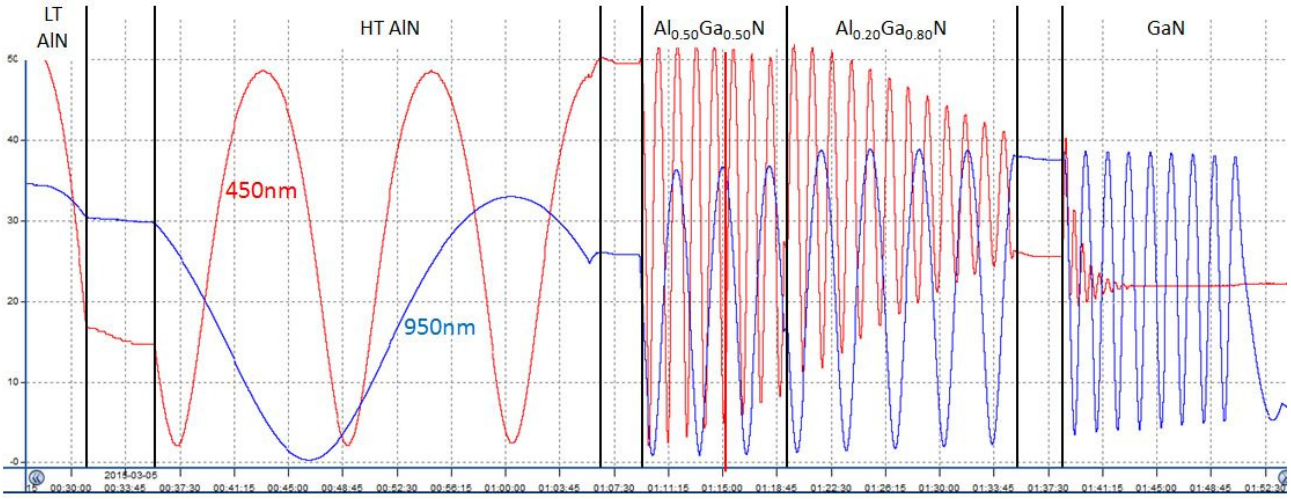

Fig. 2.20 – Example of reflectance measurement of the buffer structure from the silicon substrate to the thick GaN layer.

the measurement when the laser has destructive interference between the substrate and the layer surface.

The reflectance measurements shows the use of the two wavelengths : 405nm and 950nm. We can see that the information derived from the two measurements is complementary. The 405nm signal is absorbed by the GaN material (and AlGaN one) and does not show the entire growth of it. With the 950nm signal we can follow all the GaN growth and estimate the thickness. However arches are closer in the case of the 405nm signal and thus thinner layers could be measured.

2.1.7 | Growth of indium containing III-N alloys and phase separation

We have detailed the MOCVD process in a previous section and we would like to give a description of a thermodynamic effect which concern III-N materials containing indium in their lattice. They are all, at different scales, confronted with indium segregation and phase separation.

In the range of growth temperatures usually used in MOCVD process for III-N alloys, namely ranging roughly from 600°C to 1100°C, few of them is stable but is at best metastable. Stringfellow showed [6] that such alloys would be stable and so alloy composing binaries miscible across all compositions, at a minimum of 1473°C. This is much too high for real growth, especially for indium containing alloys undergoing indium desorption due to the high vapor pressure of InN compared to that of GaN and AlN. [6]

The driving force of such phase separations in wurtzite is the internal strain at the crystal lattice scale. There is a big difference between the lattice parameter of InN and that of GaN and AlN due to the very different tetrahedral radii. To relax the strain, Stringfellow first showed by a thermodynamics approach that it was possible to estimate the maximum of indium solubility in a wurtzite InGaN layer, and consequently drew a theoretical phase diagram of InGaN ternary (cf. figure 2.21). The bell shape of solidus line suggest that the more we decrease the growth temperature, the lower the indium content we can incorporate without segregation at equilibrium. This has been observed for instance by MBE by D. Doppalapudi and S. N. Basu. [6] The result is exactly the same in InAlN [7] ternary since the lattice mismatch is higher than in InGaN crystals, and of course by deduction in InGaAlN quaternary

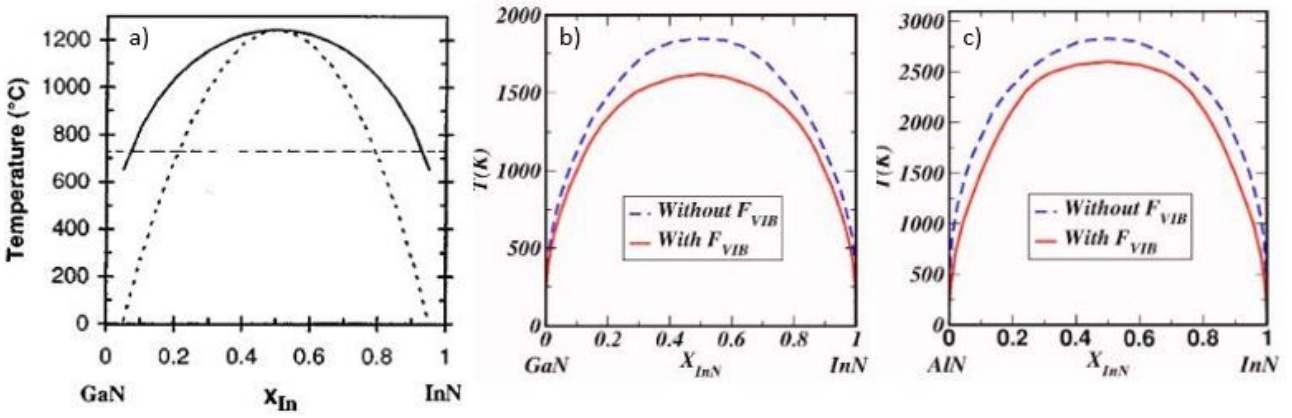

Fig. 2.21 – a) Phase diagram of InGaN ternary by Stringfellow [6], b) phase diagram of InGaN ternary by Burton [7], c) phase diagram of InAlN ternary by Burton [7].

since it is a combination of two other mismatches.

This phenomenon starts the main problem of In containing nitrides growth. We want to reduce the temperature to avoid indium desorption and surface roughening, but if we decrease the temperature too much, we make the indium form droplets which play the role of sink for InN formation or at least indium-rich phases in InGaN, InAlN or InGaAlN bulk material. Moreover, there are different scenari that could occur to form these indium-rich areas. It depends on the temperature and so the mobility either of adatoms or atoms directly embedded in the material. First, at the highest temperatures, where phase separation occurs (depending on material and growth techniques), it is supposed that InN phases could be formed by coalescence of In droplets on the surface during the growth. Second, a direct precipitation of InN from the ternary or quaternary bulk lattice by nucleation followed by a crystal growth mechanism could occur. This requires long distance diffusion and thus an enough high temperature and growth time. Third, a mechanism called spinodal decomposition can be highlighted. Here, the diffusion of atoms is possible on long and shorter range and thus working at lower temperatures. This last mechanism does not require a nucleation to form precipitates, and this typically works when the indium content is high enough to initiate the condensation of an unstable alloy. [6]

2.2 | Characterization techniques

In this second part of Chapter 2, we will focus on the different characterization methods we used on our samples to highlight their surface properties (Atomic Force Microscopy - AFM), their thickness (X-Ray Reflectometry - XRR), their luminescence properties (PhotoLuminescence - PL), their composition (Wavelength Dispersive X-ray Fluorescence - WDXRF, X-ray Photoelectron Spectrometry - XPS, Auger Electron spectroscopy - AES, Plasma profiling time of flight mass spectroscopy - PP-TOFMS), and their sheet resistivity (Four Points Probe - 4PP). Some of them such as AFM, XRR, XPS and 4PP were systematically performed for each sample, while others were used less frequently, depending on the needs.

2.2.1 | Atomic Force Microscopy : AFM

2.2.1.1 Generalities and physical mechanisms

Scanning probe microscopy is a technique which allows lots of surface characterization including topology, chemistry, electrical and mechanical properties among others and this at scales going from 30x30μm^2 to nearly 500x500nm^2. For instance, in our case we did all of our measurements in a window of 1x1μm^2, and we used atomic force microscopy to examine the surface morphology only. The scanning area of 1x1μm^2 allows us to get appropriate data considering the surface structure of our materials which are mainly GaN and InGaAlN. Note that all the explanations about this characterization technique as a theoretical or technical point of view are taken from the internal documentation on AFM characterization available in the CEA-LETI and developed by Denis Mariolle and François Bertin. [8]

AFM tools have a tip made of silicon which will perform the surface analysis by moving up and down revealing the surface structure. The tip is moved wih=th piezoelectrics which control the displacement parallel (X and Y axis) and perpendicular to the surface (Z axis). We can use different measurement techniques and we actually chose the tapping and peak force modes according to our needs. On the tip a laser is reflected at the surface and its reflected intensity is projected on a photodiode in 4 quarters which converts the light into an electrical signal. Depending on the mode adopted it is differently treated by a control loop. The different parts of the tool will be described in next sections.

Interaction between a tip and a surface sample

Before developing the principles of tapping and peak forces modes used in AFM measurements, it is important to understand the different interaction regimes that the tip is undergoing when it is gets close to the surface of a material. If we were drawing the cantilever (tip flexible support) deflection versus the distance from the tip to the surface we get a graph shown in figure 2.22. Following the cycle from point A to point D, we have different interaction forces. From A to B the tip is far enough away from the sample to avoid sample interaction. As a consequence the cantilever is not deflected. While the tip is between B and B‘ we are entering into the attractive forces field (van der Waals (vdW) interactions, electrostatic forces and chemical forces) and the tip accelerates during its sample approach. We call this phase the jump contact or pull-on. Then we are in the repulsive forces field and we linearly increase the cantilever deflection while we are approaching again the surface from B‘ to C‘. The color of the path is related to the direction of the cycle : the approach is in blue/green and the return in red. In contact mode, we keep the cantilever deflection positive and constant during the sample scan and so with the position of the tip between C and C‘. For the reverse path of the tip, removing the tip from the sample from C‘ to D we can see that the tip is released from repulsive forces (hard sphere repulsions, Pauli-exclusion interactions, and electron–electron Coulomb interactions) at a different point compared to the approach path. This creates a hysteresis loop and is attributed to the presence a thin water layer at the surface in the shape of a meniscus, causing attractive forces (capillary forces) between the tip and the surface of the sample. The point at which the tip finally leaves the sample (D) is called the pull-off one. [8]

Tapping mode

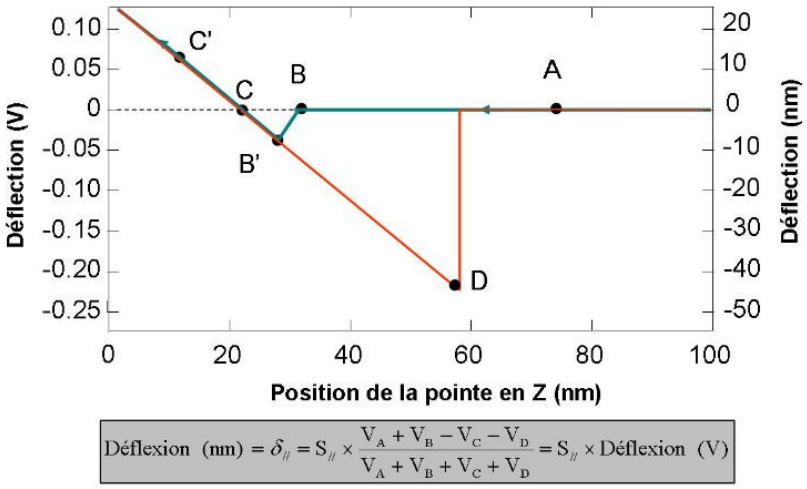

Fig. 2.22 – Surface tip interaction curve.

AFM in tapping mode is also called amplitude modulation AFM (AM-AFM). In this measurement mode the tip oscillates using a piezoelectric element at a frequency close to its resonant frequency. To find this frequency specific to each tip, we oscillate the tip on a large frequencies range and we choose the one for which the amplitude of vibration is the highest. [8]

when we are scanning our surface we keep the oscillation amplitude constant and slightly smaller than the resonance one. This is our set point. When the sample is close to the surface, the resonant frequency is smaller than away from the surface. That is why we choose a frequency of vibration a little bit less than the one at a long distance. When the tip is approaching the surface, the shift of resonant frequency is accompanied by an increase in amplitude oscillation (cf. figure 2.23). We call this repulsive tapping. In that case the tip is touching the surface at each vibration.[8]

As the surface topology changes, the amplitude vibration changes since it changes the distance between the tip and the surface and therefore the interaction force. Then the servo system, previously described, changes the tip height to have again the optimal oscillation amplitude. A cartography of the height changes allow us to have the topology information we need to characterize our surface. [8]

Peak force mode

The principle of the peak force mode is close to that for tapping mode. The set point is not an oscillation amplitude but a certain force intensity which has to be constant during the measurement. In parallel there is a modulation of the tip movement along the Z axis with a sinusoidal signal. The frequency used is in the peak force mode far away from the one of the tapping mode. [8]

2.2.1.2 Tool and technical layout

We used the Bruker Dimension Fastscan during this thesis. It allows us faster AFM scans compared to the Icon system more adapted to larger scans until $30\mu m^2$.

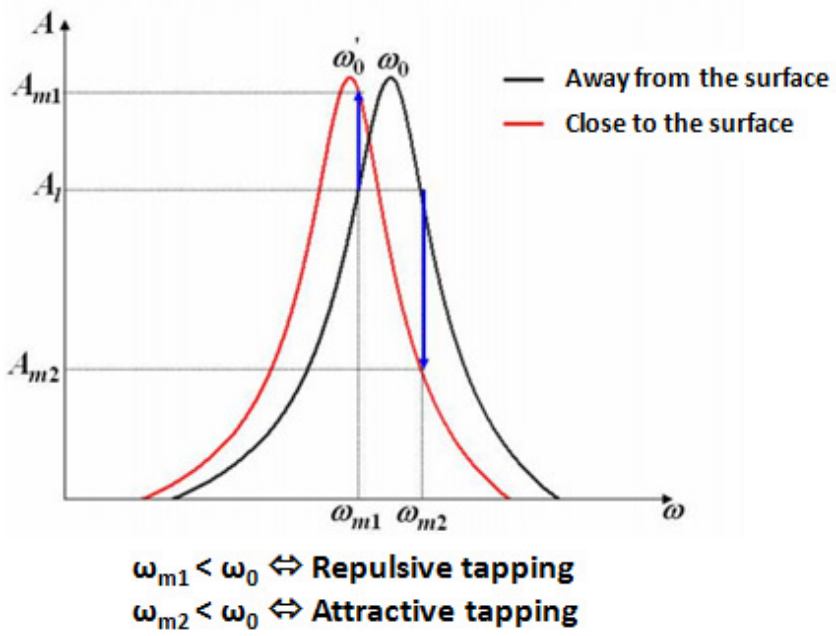

Fig. 2.23 – Shift of the resonant frequency with the distance tip-surface.

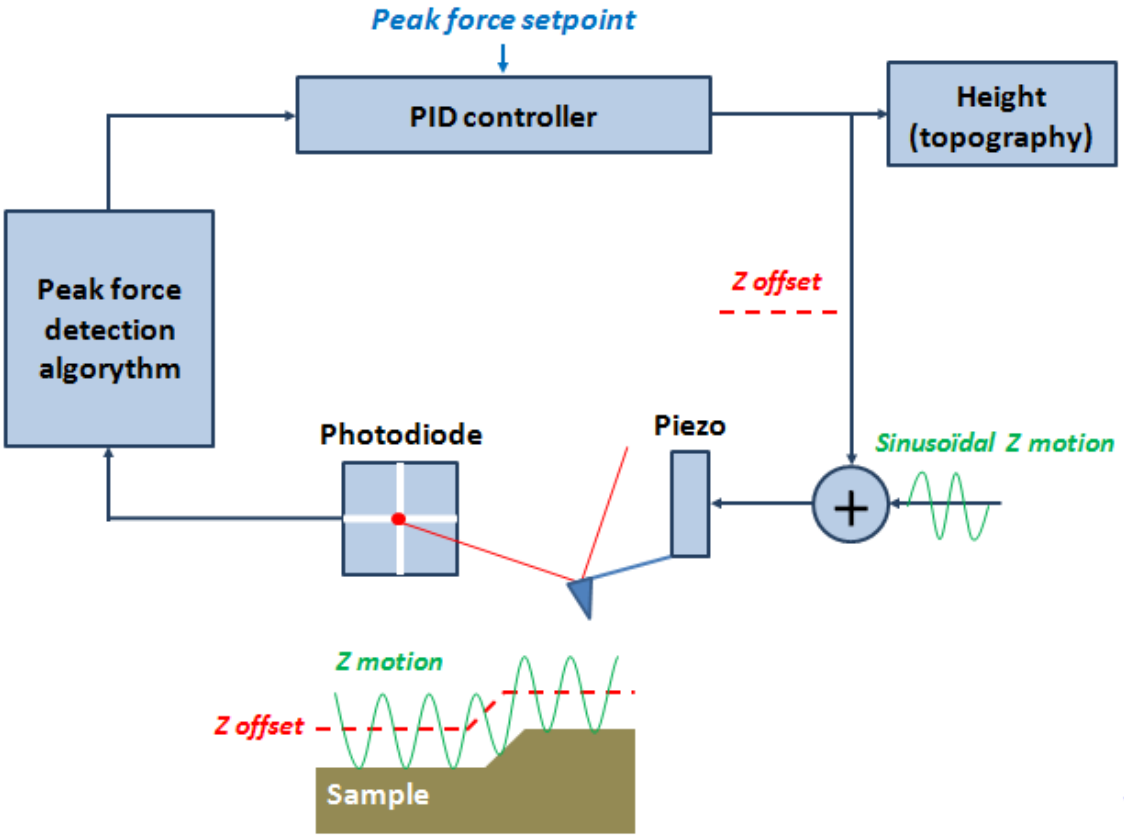

Fig. 2.24 – Peak force mode layout

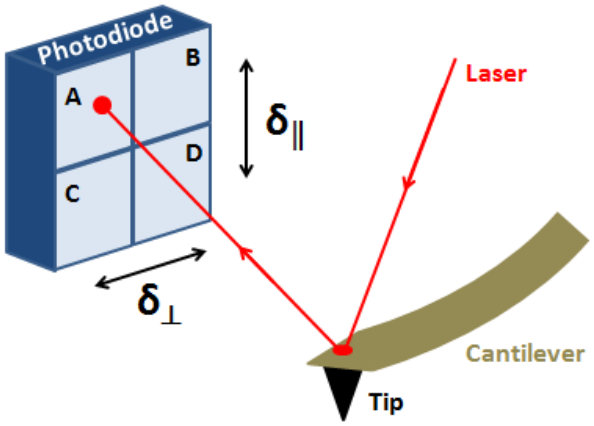

$$\delta_{\parallel} = S_{\parallel} \cdot \frac{V_A + V_B - V_C - V_D}{V_A + V_B + V_C + V_D}$$

$$\delta_{\perp} = S_{\perp} \cdot \frac{V_A + V_C - V_B - V_D}{V_A + V_B + V_C + V_D}$$

Fig. 2.25 – Four parts photodiode and laser reflection. Value of parallel and perpendicular displacement.

Movement detection by optical analysis

The detection of tip movements on the surface during the scanning time is based on a reflection of a red laser on the top of the tip. Close to the tip, the photodiode allow the reception of the reflected laser signal and its movement analysis is correlated to the tip displacement. The long distance between the tip and the detector (a few centimetres) compared to the cantilever size (100μ long) ensure a great sensitivity in movement detection. Typically we can detect a variation of surface height of 1Å. [8]

The photodiode is divided into four parts to detect longitudinal and transversal movements of cantilever end. The photodiode usually has a sensitivity of a few tens of nanometers per volt (output voltage of the photodiode). [8]

Servo system and steering of the tip position

Choice of the tip

The tip used during an AFM scan is different depending on the measurement mode we choose. For the tapping mode we used the Bruker FASTCAN A tip and for the peak force mode we use the Bruker FASTSCAN C tip. Both are made from silicon and present the same size and morphology but the FASTSCAN C presents a cantilever stiffness less important.

Both FASTSCAN A and C have a tetrahedron shape with the same sized and properties as shown in

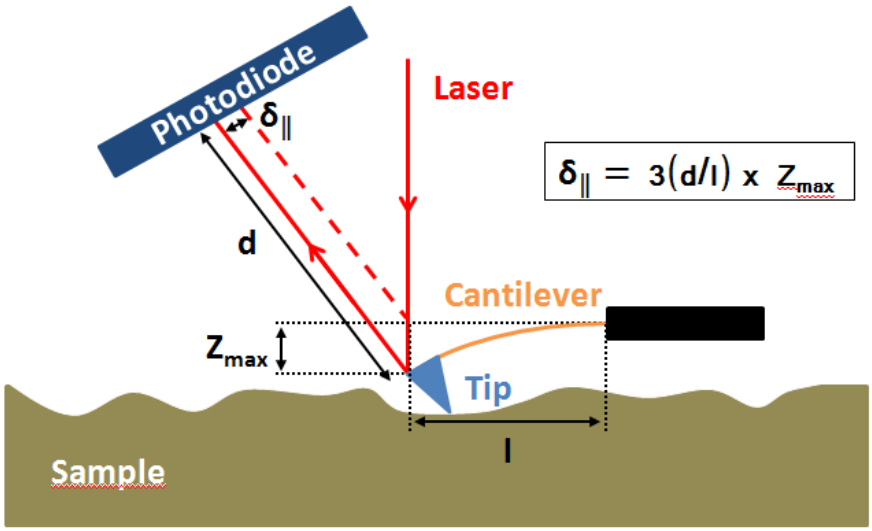

Fig. 2.26 – Interaction laser-tip-photodiode.

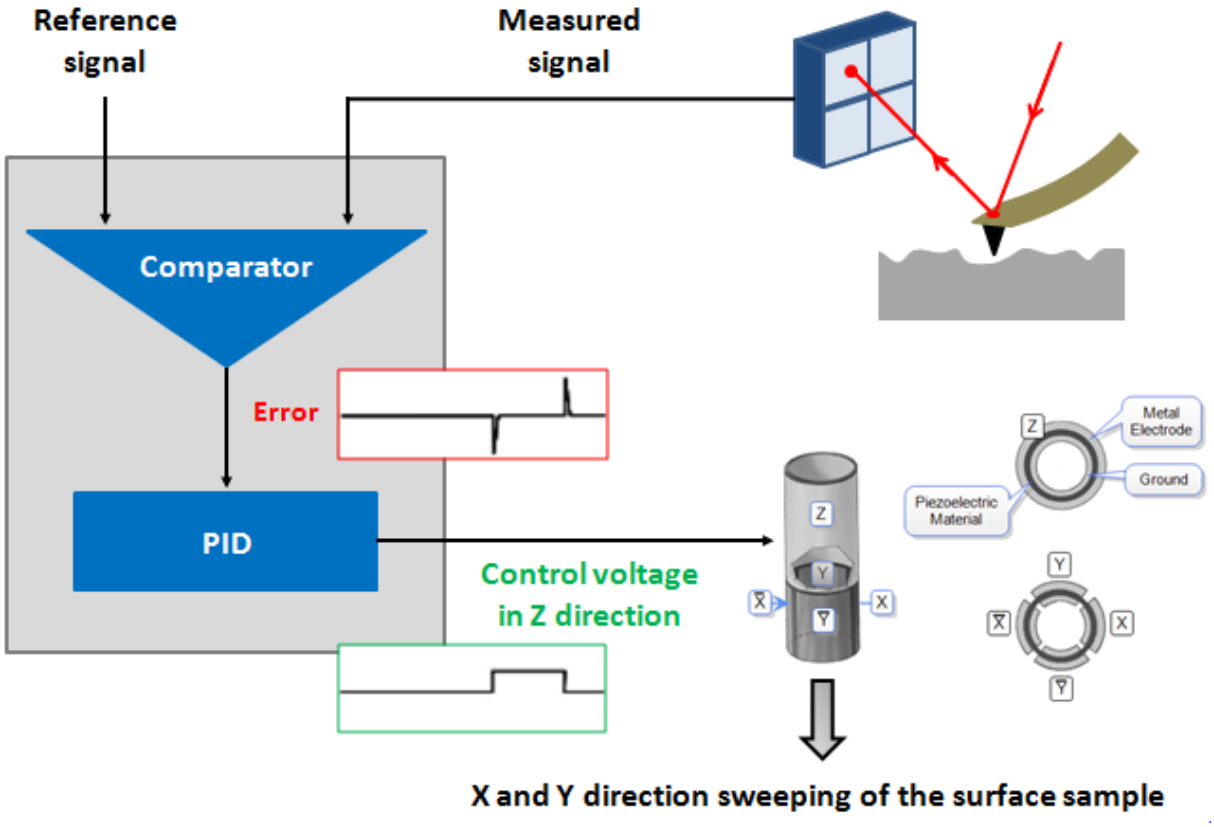

Fig. 2.27 – General layout of AFM electronic control.

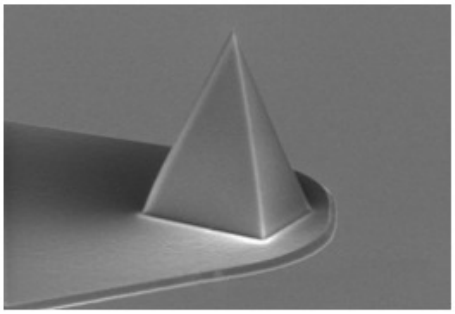

Geometry:	Rotated (Symmetric)
Tip Height (h):	2.5 - 8µm
Front Angle (FA):	15 ± 2.5°
Back Angle (BA):	25 ± 2.5 °
Side Angle (SA):	17.5 ± 2.5 °
Tip Radius (Nom):	5 nm
Tip Radius (Max):	12 nm
Tip SetBack (TSB)(Nom):	5 µm
Tip Set Back (TSB)(RNG):	0 - 7 µm

Fig. 2.28 – Bruker Fastscan A Tip zoom and specifications. [9]

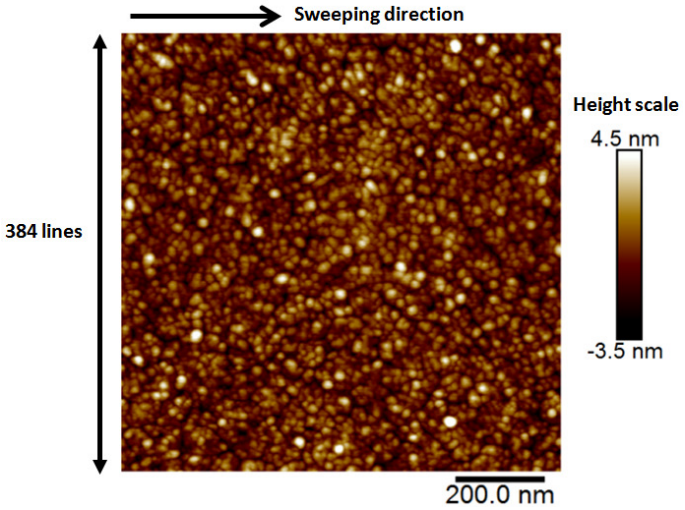

Fig. 2.29 – 1x1 μm AFM picture in tapping mode on 12nm thick InGaAlN layer

figure 2.28. The difference is related to the cantilever size and thickness and thus its spring constant and nominal resonant frequency. The nominal tip radius defines the in-plane resolution of AFM pictures as our image is a convolution of our tip and the sample surface. If we define the number of sweep lines for each AFM picture, the size of the picture divided by the number of lines should be roughly equal to the tip radius to optimise the resolution.

2.2.1.3 Example of AFM measurement

Here we present one example of a measurement done on an InGaAlN layer grown under H_2 carrier gas. While doing the scan, the tip is sweeping across the sample from one side to the other in the same direction for each next line. So we build the picture starting from the first line at the top of the picture toward the final line at the bottom. The scale on the right allows us to have the value of the height at each point of the AFM picture. The statistical analysis of all the images presented in this thesis have been done with Nanoscope Analysis or Gwyddion softwares.

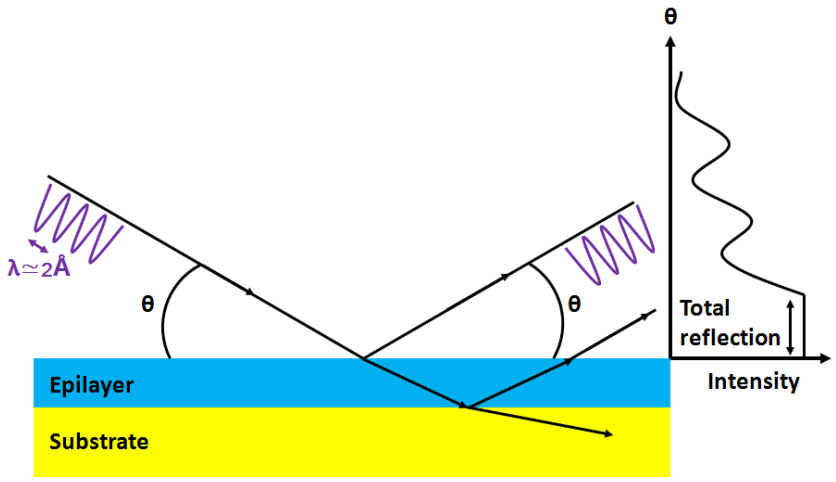

Fig. 2.30 – XRR layout, mechanism and intensity angle relation.

2.2.2 | X-ray Reflectometry : XRR

2.2.2.1 Generalities and physical mechanisms

The XRR characterization is useful to estimate the thickness of an heterostructure made of thin polycrystalline, crystalline or amorphous layers whose thicknesses range from 0.1nm to 1000nm. [10] We are in the right range for this method since we are studying layers ranging from nearly 7nm to 200nm of InGaAlN on thick GaN layers ($2\mu m$). In theory XRR also allows us to get the density of our surface material and an idea of the roughness at the interface between GaN and InGaAlN, plus the roughness at surface. We also used the method to study some multi-quantum-wells samples with lots of thin GaN and InGaAlN layers grown on the thick GaN pseudo substrate.

In XRR, the surface of the material is illuminated by a highly collimated X-ray beam (λ=1.54Å, $Cu - K_\alpha$) with a few degrees angle incidence. All materials have a refraction index less than 1 in the wavelength range corresponding to the X-ray used. So we have an angle range of beam incidence from 0°to a critical value for which the reflection is total. In that case the penetration depth is only of 30Å. From this critical angle if we increase slowly the beam incidence angle we start to penetrate the material across a surface of several hundred microns. At each interface between the different materials of the stack, the refraction index is changing. This index change implies a reflection of the incident X-ray beam at each interface and interference is generated by the entire reflected beam giving us the characteristic scan as shown in figure 2.33. It shows us the logarithm of reflected beam (interference figure) versus the incidence beam angle.

Analyzing an XRR profile can be performed using a fourier transform to analyse the thickness of different layers. However, we can get more information by using software which builds a model which fit the experimental data. From this simulation we can estimate the density of the materials in the stack, the thickness of each layer and the roughness at each interface. To understand how is done the analysis we will focus on a simple example : one layer on a thick substrate as in figure 2.30. [11]

First of all, as we can see on the experimental profile the intensity of the reflected signal suddenly

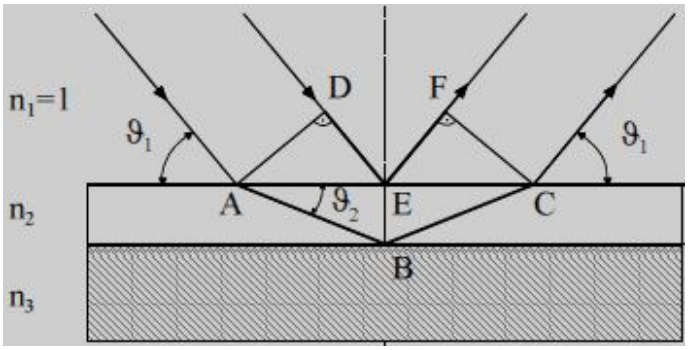

Fig. 2.31 – Incident and reflected X-ray beams at surface sample. [10]

drops down after a plateau. This drop point corresponds to the critical angle which is needed to find the density of the material at the surface. If we call θ_c the critical angle, under which the beam is totally reflected, λ the wavelength of the X-ray beam (1.54Åfor Cu) and ρ the surface layer density in g/cm^3 : [11]

$$\theta_c = k\lambda\sqrt{\rho} \tag{2.12}$$

where k is a constant of proportionality having the value 1.6×10^{-4}. Note that in the case of X-rays, the critical angle is always small (a few tenths of degrees), and we are in the case of grazing incidence. When the critical angle is reached, the refracted beam is parallel to the surface and nearly all the energy is reflected.

We used the Leptos software developed by Bruker to analyse our experimental data. This models the interfaces and the layers to calculate the theoretical curve which is compared to the experimental one. Simulations are then performed, with interations to best match the experimental data. If we want to do a basic analysis of the films by hand, we can calculate the thickness of the layer from the spacing between Kiessig fringes which for one film on a thick substrate is [10]

$$d = \frac{\lambda}{2\Delta\Theta} \tag{2.13}$$

where d is the thin film thickness, Δ the optical path difference shown in figure 2.31 showing the X-ray beam configuration at the sample surface, and Θ the angular distance of two successive maxima in the scan.

Physically Kiessig fringes are the result of interferences between two waves : the one reflected by the air-thin film interface and the one reflected by the thin film-substrate interface. The amplitude of the fringes depends on the relative intensity of the two waves which means the respective index of both materials (substrate and thin film) and so their relative absorption. [12]

Finally it is possible to use the technique in order to get an idea of the roughness of the interfaces. Usually roughness must not exceed 5nm at the surface. Roughness, which means at a micrometric scale (typically measurement by AFM) tends to diffuse reflection of the incident beam. This is reflected on the scan by the intensity of the secular reflected beam which decreases faster as the roughness increases.

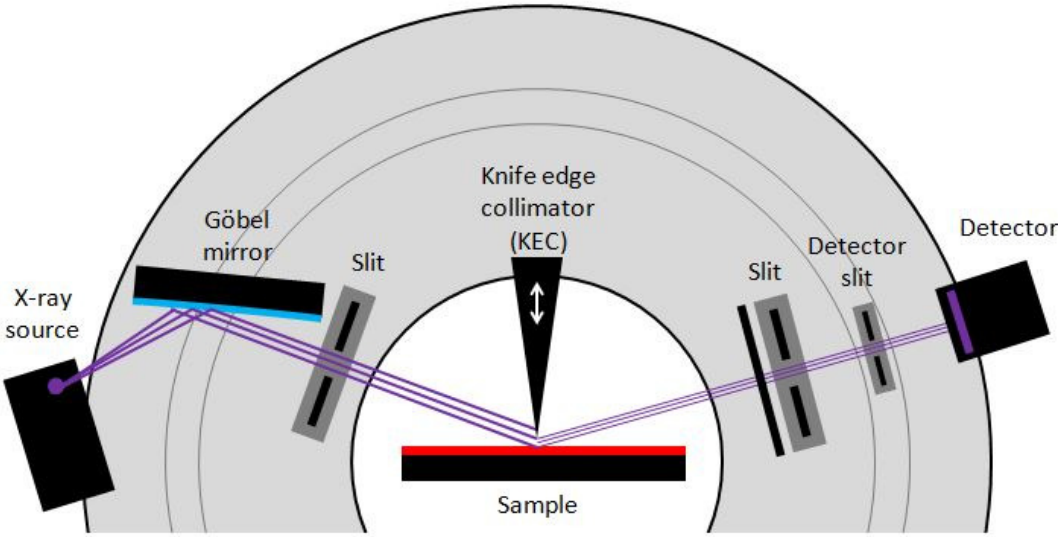

Fig. 2.32 – XRR layout, mechanism and intensity angle relation.

[12][10]

2.2.2.2 Tool and technical layout

We used the Bruker D8 FABLINE which permits a full sheet analysis and thus a measurement in different point (5cm diameter spot size) of the grown wafer. This is particularly interesting when we wanted to ensure a good growth process homogeneity. Typically we chose to make three measurements points : one at the centre, one at 45mm radius and one at 80mm, i.e. 20mm from the edge of the wafer. We can see the general experimental setup of an XRR tool in figure 2.32. It is composed of an X-ray source emitting at a specific wavelength : typically 1.54Å. Then a Göbel mirror forms an intense parallel and monochromatic beam with very low divergence from the angular beam emerging from X-ray source. Above the sample we find a knife edge collimator that can be mounted or lowered to adjust the spot size and make it at least smaller than the sample. Then the sample receives and reflects the beam which is sent to the detector.

2.2.2.3 Example of XRR measurement

In the case of the study of InGaAlN, it is hard to measure a clean signal for theoretical thickness above 100nm since it implies an important surface roughness after the growth and thus a reflected signal which quickly drop to the zero intensity. Fortunately, the majority of our samples have a thickness either close to 12nm or 30nm. As soon as we got some interesting results we studied the InGaAlN material for thicknesses close to 12nm, as this is roughly the thickness of an HEMT barrier layer which is intended as one of our final applications. On the contrary we can imagine that 30nm thick layer would be appropriate to study the total thickness of InGaAlN layers added in an InGaAlN/InGaAlN multi-quantum-well heterostructure.

Figure 2.33 shows an example of one of our measurements on an InAlN layer 12nm thick.

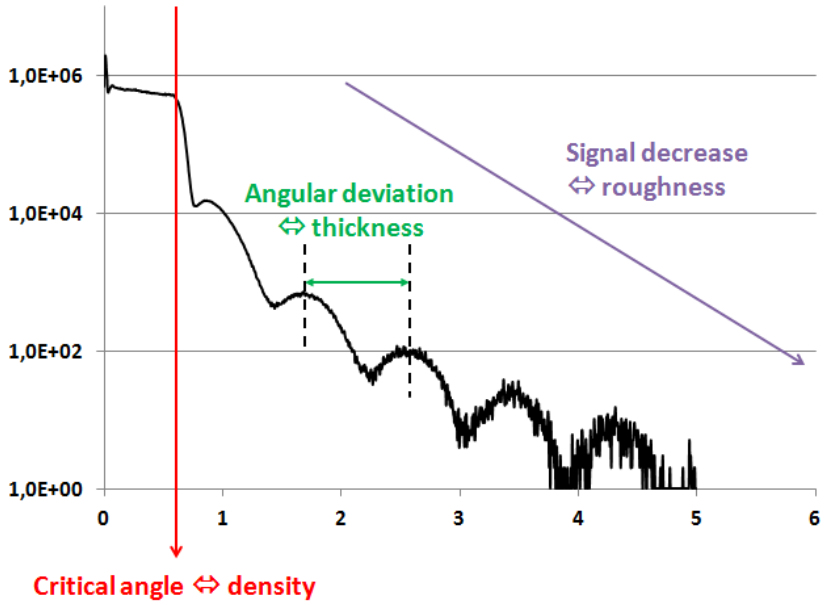

Fig. 2.33 – XRR measurement on a 12nm thick InAlN layer on 2μm GaN layer. Interpretation of the critical angle, of the inter-fringe spacing, and the slope of the signal.

2.2.3 | Photoluminescence : PL

2.2.3.1 Generalities and physical mechanisms

Photoluminescence is an optical characterization which allows us to find the band gap energy of a material. A laser with a specific energy, larger than the band gap energy of the studied material, is used to excite the material. Valence band electrons get an increase in their energy and are then located in the conduction band, creating a hole at the valence band. After a certain relaxation time, we have a spontaneous emission during which the electrons recombine with holes and emit a photon. This photon as the energy of the band gap material. [13]

If crystal or chemical defects are present in the material, it is possible to have a recombination of electron-hole pairs inside the forbidden band. These defects induce energy levels inside the forbidden band and give birth to other peaks at higher wavelength during the PL measurement. Some of them can also be non-radiative defects and produce mainly phonon vibrations during their relaxation. In our studies we have focused on the band edge emission, to find the band gap of the material, and we have not looked in detail at the defect bands. [13]

If PL measurements appear very simple and efficient for direct band gap semiconductors as III-N materials, there are different things to take into account if we want to measure our InGaAlN band gap.

In an heterostructure the stacking order of the single crystalline layers has an impact. The incident UV laser beam penetrates the heterostructure from the surface and thus the final layers. If the final layer has a band gap smaller than of one or all of the layers below it will be difficult to excite these deep layers due to absorption at the surface, although this will depend on the thickness of the layer. It implies that to make a deep layer luminescence we require that the layers above have a larger band gap.

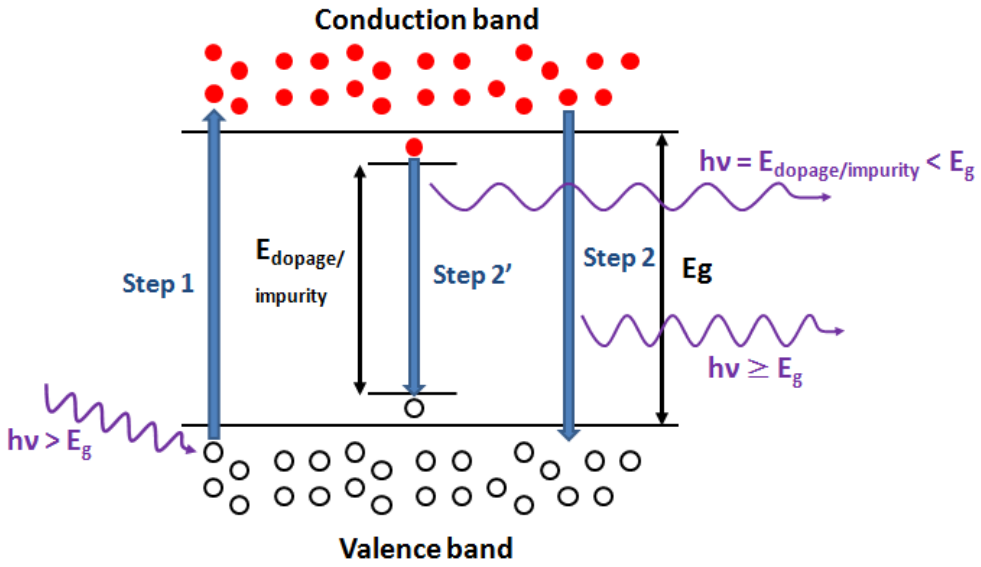

Fig. 2.34 – Luminescence mechanism from a direct band gap semiconductor after laser excitation.

Another constraint is that our InGaAlN layers are thin. When two semiconductors are in contact, the conduction band electrons belonging to the material which has the largest band gap change material have a tendency to move to the other semiconductor where the conduction band is lower in energy, and so it is more. So for our InGaAlN layers on GaN, it is possible that a part or all of excited electrons move down in the GaN layer below, depending on the InGaAlN layer thickness. Generally we place an AlN spacer of 1nm between the GaN and our alloy to avoid this phenomenon.

Finally as we will see in Chapter 4, InAlN and InGaAlN could be subjected to rich and poor indium phases separation. We can imagine that localized areas of indium-rich alloys areas uniformly distributed in the material could play the role of local quantum wells in which electron-hole pairs can preferentially recombine. We can imagine that depending on the phase size and composition, the behavior of it can be that of a quantum well or quantum dot.

2.2.3.2 Tool and technical layout

We used the Nanometrics RPM blue tool which allows us to measure the optical emission across the whole wafer at room temperature. The source of excitation is a UV laser whose wavelength is at 266nm, corresponding to a band gap of 4.7eV. Above this value, it would be impossible to excite the material and so impossible to get a luminescence from it.

2.2.3.3 Example of PL measurement

In figure 2.36 we give an example of our measurement on a 200nm InGaAlN layer. From one pixel of the mapping we can have access to the PL spectrum in which two peaks are identified in the detection window. On the right at 360nm, we have the luminescence peak corresponding to our gallium nitride

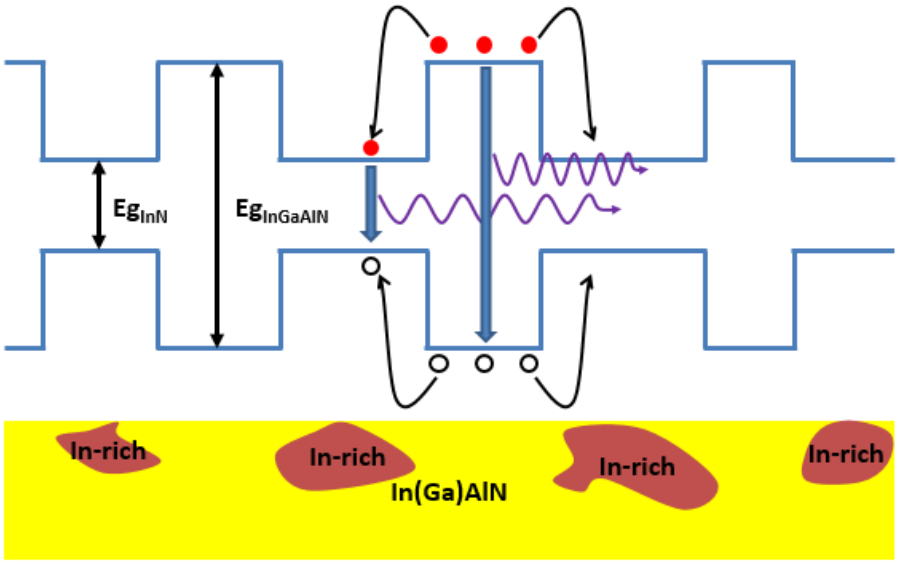

Fig. 2.35 – Photoluminescence emission from an InN segregated InGaAlN material. 2D (parallel to surface) point of view.

pseudo substrate. On the left is our InGaAlN peak at lower wavelength and thus higher band gap energy. When aluminum content is increased we expect the peak to move to the left, and when indium and/or gallium content is increased we would expect to move to the right. From this the peak position we can find the composition of a ternary alloy if we know the bowing factor (chapter 1). Also, given the fact that GaN peak is more intense than that of InGaAlN (mainly due to large thickness of GaN), we can lose the quaternary peak behind that of GaN for a certain composition range. We are studying layers with a maximum of 20% indium content which are expected to locate the peak to the left of the GaN peak.

2.2.4 | X-Ray Diffraction : XRD

2.2.4.1 Generalities and physical mechanisms

XRD characterization is a commonly used technique for poly- and single crystalline materials. It is particularly useful to study different crystal properties. For instance we can use it to search for the presence of specific crystal phases (cubic, hexagonal, etc.), specific crystalline planes, the stoichiometry of an alloy, the stress in epilayers, the lattice parameters, the qualitative crystal quality, and the thickness of thin layers in an heterostructure.

XRD is based on the diffraction of X-rays by specific crystal planes in the materials studied. When experimental conditions described below are satisfied we can detect, for specific incidence angles toward crystal planes and thus the material surface, a signal whose intensity depends on the crystal phase, the crystal plane and the chemical elements of the crystal.

The short wavelength of X-ray makes them sensitive to interatomic distance in a solid. So the X-ray beam coming from the tube is easily scattered by the different atoms of the material illuminated.

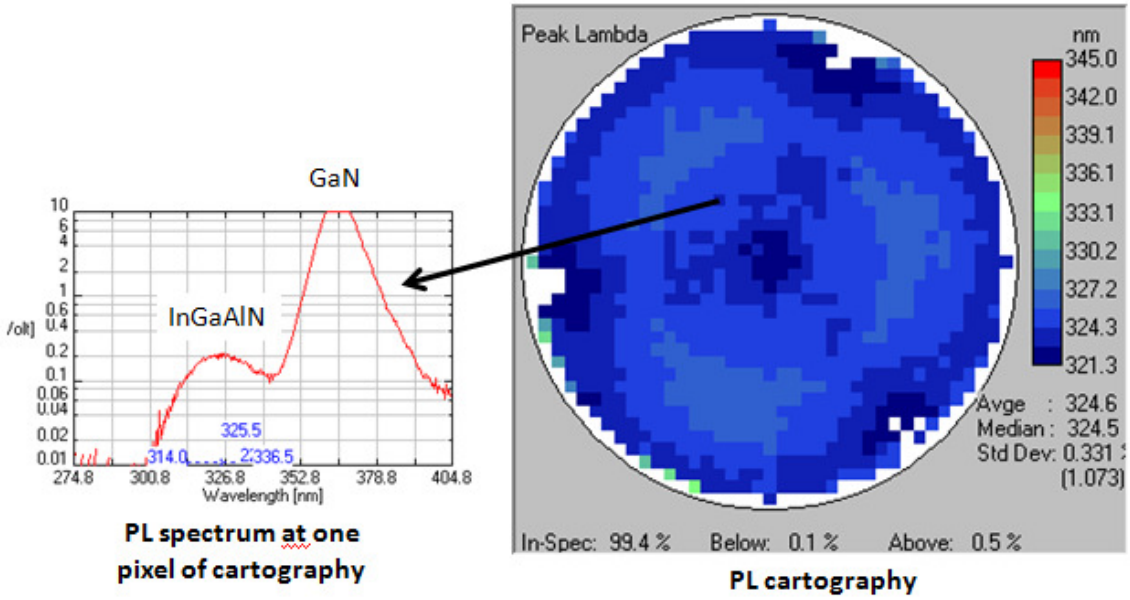

Fig. 2.36 – Photoluminescence measurement : mapping and corresponding spectrum at one pixel.

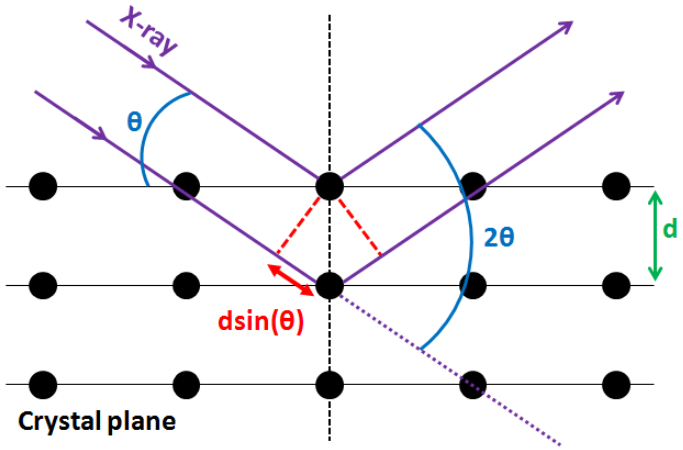

Fig. 2.37 – Bragg's law definition.

When the beam arrived at a given angle of a crystal plane, the different diffusion centers allow the construction of a diffraction figure on the side of the reflection area. In figure 2.14 the incidence beam causes each scattering center to re-emit a small portion of its intensity as a spherical wave. If these scattering centers are separated by the distance d, these spherical waves will add constructively only in directions where their optical path difference $2dsin(\theta)$ equals an integer multiple of the wavelength λ. This gives Bragg's law : [14]

$$2dsin(\theta) = n\lambda \tag{2.14}$$

To have the value of intensity I of a diffracted signal and know if one specific crystal plane can allows a diffraction in a calculated Bragg angle it is important to calculate the structure factor F_{hkl}. It is a parameter coupling the scattering strength of electrons, nucleus, atoms, unit cell and number of unit cells. The structure factor is expressed as follow : [14]

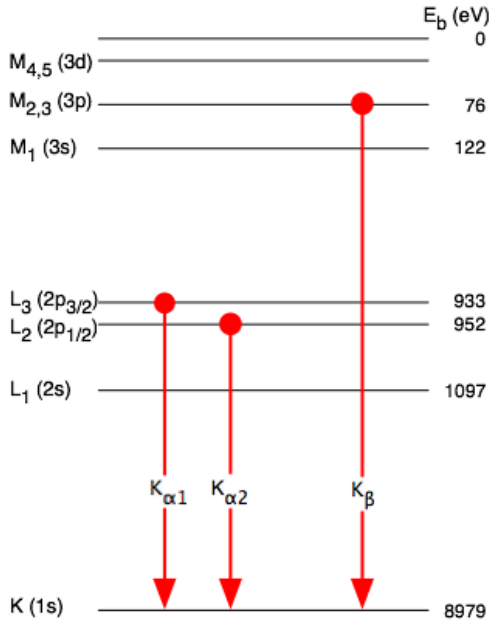

Fig. 2.38 – X-ray emissions from copper.

$$F_{hkl} = \sum_{i=1}^{n} f_i exp\{-2\pi i(hu + kv + lw)\} \tag{2.15}$$

where f_i is the atomic scattering factor of the atom of type i, h, k, and l are the miller indexes of the crystal plane, u, v, and w are the fractional coordinates of the vector linking to atoms of same type in the unit cell. The diffracted intensity is proportional to F_{hkl}^2.

2.2.4.2 Tool and technical layout

An X-ray tube illuminates the crystal we study and a detector gives us the intensity of X-rays in count/sec at a specific angle. An X-ray tube is simply a linear accelerator of electrons extracted from a heated tungsten filament and accelerated by an electrostatic field. At the end of the gun they hit a copper target, ejecting core electrons from the material. Electrons from an upper energy level will replace the ejected ones causing X-ray emission at specific wavelength depending on the gap between the two energy levels involved. There are several emissions extracted from the copper, and those which interest us our $K_{\alpha 1}$ and $K_{\alpha 2}$. They are detailed in figure 2.38.

We are using the XRD technique in high resolution (HRXRD) mode. This implies the use of monochromator at the output of X-ray tube. This is a crystal ((220) Ge) with four crystals which diffract the X-ray beam and ensure we keep only one wavelength among all those generated by the copper target in the X-ray tube. To complete the HR setup, we also employ an analyzer before the detector, forming a "triple axis" alignment. The analyser is a crystal which restricts the angular acceptance of the detector. It has the drawback of decreasing the signal intensity, but increases the angular resolution.

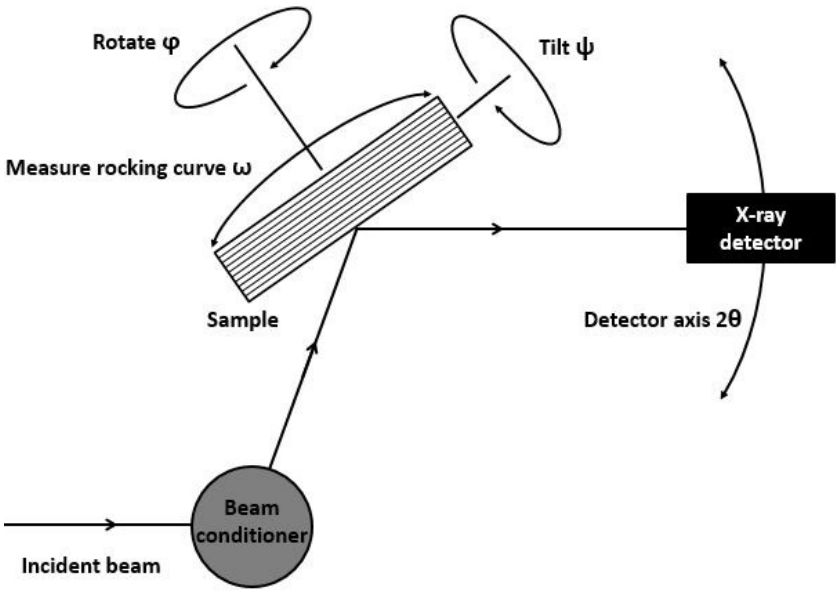

Fig. 2.39 – General layout of a high resolution double axis XRD.

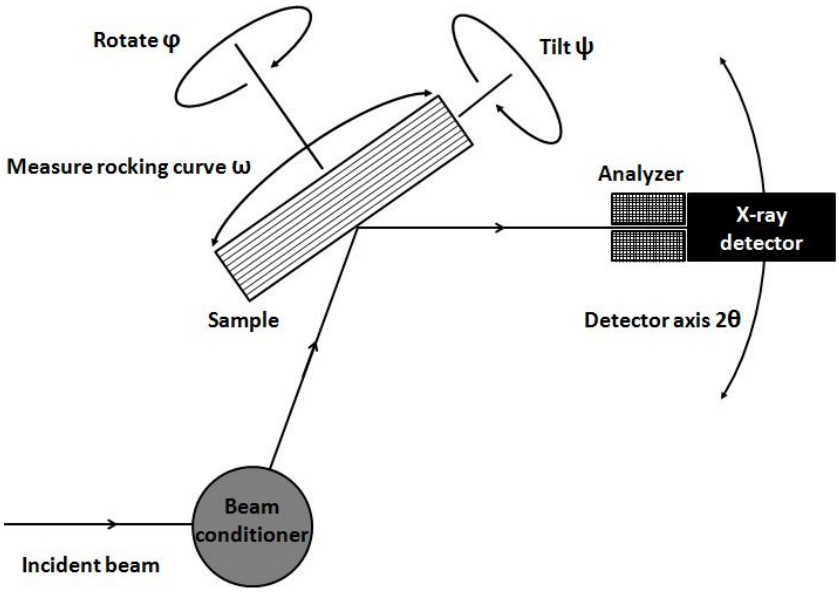

Fig. 2.40 – General layout of a high resolution triple axis XRD.

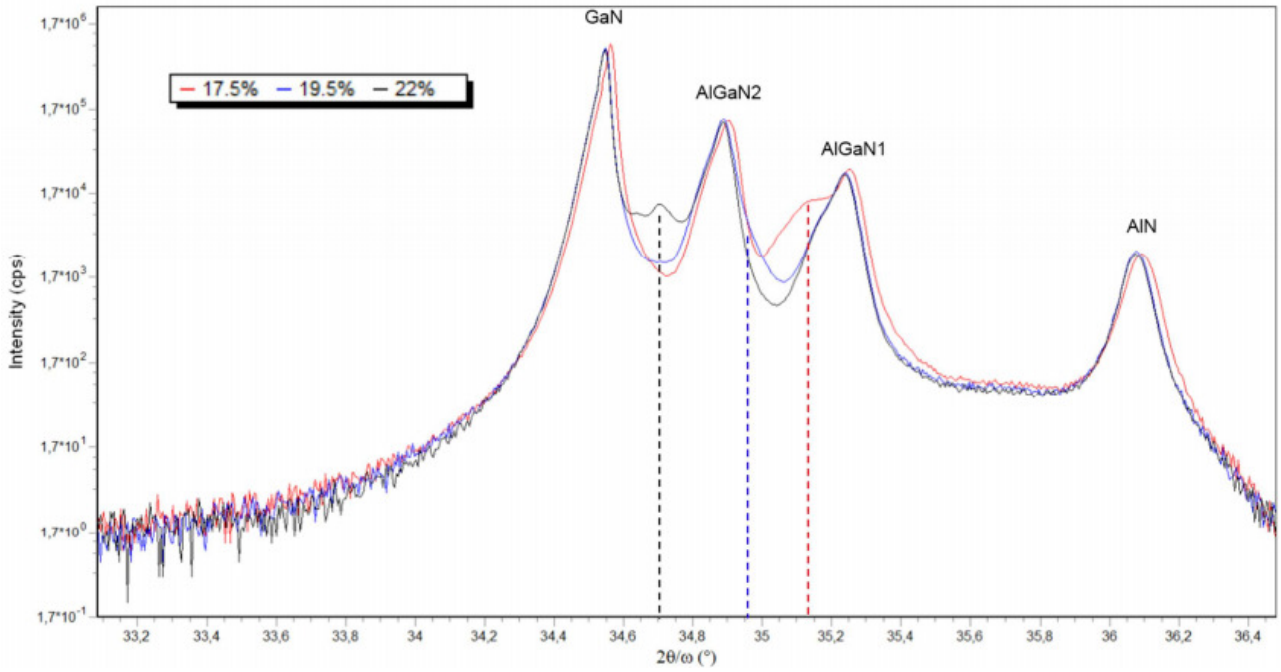

Fig. 2.41 – Superposition of three XRD profiles corresponding to three 200nm thick InGaAlN layers with different In/In+Al solid ratios. The ratios are given in the insert for each sample whose peak InGaAlN peak position is indicated by a line in dotted line.

2.2.4.3 Example of XRD measurement

As a tool we used the Panalytical XPER PRO in triple axis HR mode. We investigated our heterostructure made of several layers : a 1mm thick (111) silicon substrate, nucleation AlN layer of 240nm, a first $Al_{0.50}Ga_{0.50}N$ layer of 500nm, a second $Al_{0.20}Ga_{0.80}N$ of 800nm, a thick fully relaxed GaN layer of 2000nm and finally our InGaAlN alloy of 200nm in this example. In figure 2.41, we show the superposition of three profiles of $\omega - 2\theta$ measurements on (0002) atomic plane which is parallel to the surface. The three samples differ only by the composition of the InGaAlN layer. The gallium content is the same and we increased the indium percentage (and thus decreased the aluminum one) resulting in an InGaAlN peak shift to lower angles. If we increase the indium content, both the a and c lattice parameters are increased, and thus the Bragg angle is reduced according to Bragg's law (equation 2.14). We should note that an $\omega - 2\theta$ measurement on a specific plane consists of placing the sample so that the angle between the plane and the detector (2θ) is equal to the theoretical Bragg angle, itself equal to $\omega/2$ which is the angle between the plane and the X-ray emitter. While scanning ω (the sample position) is varying two times slower than 2θ (the detector) around this theoretical Bragg angle making the signal appear. This means that effectively we are changing the Bragg angle, but not the sample orientation, so that we measure the change in lattice spacing, but not the mosaicity of the sample. We can choose the angle step of scan, the range, and the time of exposure to X-ray at each step. The results are in figure 2.41.

On this example, the compositions given in the insert, and extracted from the system software, are wrong since we have a quaternary instead of a ternary alloy. In that case the In/(In+Al) ratio cannot be extracted using just Bragg's law on a $\omega - 2\theta$ scan on (0002) plans and we had to assume fixed gallium content and relaxed layers to extract these values.

2.2.4.4 Reciprocal space maps (RSMs)

A reciprocal space map (RSM) can also be performed on an XRD tool, in this case on our Bruker D8 Fabline tool. It consists of a series of 2θ scans at gradually changing *omega* values. The graphs showing 2θ versus *omega* are then mathematically transformed by our Leptos data treatment software from Bruker. These maps show the position of the peaks in reciprocal space as shown in figures 4.6 and 4.12 of chapter 4. This means that the a and c lattice parameters are an image of the q_x and q_z coordinates, with the a-parameter increasing from left to right, and the c-parameter increasing from top to bottom.

We do the RSM measurement on the asymmetric (20-24) planes. It is logical that if we want the values of lattice parameters of our material, we have to take an inclined plane compared to the surface. The definitions of q_x and q_z are as follows : [15]

$$\vec{q_z} = l.\vec{c^*} = 4.\vec{c^*} \tag{2.16}$$

$$\vec{q_x} = h.\vec{a^*} + k.\vec{a^*} = 2.\vec{a^*} \tag{2.17}$$

where h, k, l are the Miller index of the inclined plane ((20-24)), and a^*, c^* are the lattice parameters of the crystal in reciprocal space. Since $||\vec{c^*}|| = \frac{1}{c}$ and $||\vec{a^*}|| = \frac{2}{\sqrt{3}.a}$ in hexagonal lattice only, therefore, for (204) plane measured by RSM :

$$c = \frac{4}{q_z} \tag{2.18}$$

$$a = \frac{4}{\sqrt{3}.q_x} \tag{2.19}$$

These formula were used in chapter 4 section 4.2.1.2 to estimate the lattice parameters of four samples measured by RSM. In appendix of this thesis you will find a system of equations that allows the calculation of the composition and the strain in the barrier layer using the In/(In+Al) ratio extracted from WDXRF measurements. We will see in chapter 4 that this is not our standard process to calculate the composition but it could be an interesting alternative which deserves to be explained.

2.2.5 | X-ray Photoelectron Spectrometry : XPS

2.2.5.1 General aspect

XPS characterization allows the chemical characterization of layers and thus the determination of the composition of our InAlN or InGaAlN alloy. This is a surface characterization measurement which probes the material surface on a thickness close to 3nm. But we benefit of a coupled sputtering system using argon or argon clusters to sputter the material and get the alloy composition through the thickness of the layer(s).

The measurement is based on an X-ray photon beam directed toward the sample surface with a certain

Quantum numbers				Spectroscopists	X-ray notation
n	**l**	**s**	**j**		
1	0	+1/2, -1/2	1/2	$1s_{1/2}$	K
2	0	+1/2, -1/2	1/2	$2s_{1/2}$	L_1
2	1	+1/2	1/2	$2p_{1/2}$	L_2
2	1	-1/2, -1/2	3/2	$2p_{3/2}$	L_3
3	0	+1/2, -1/2	1/2	$3s_{1/2}$	M_1
3	1	+1/2	1/2	$3p_{1/2}$	M_2
3	1	-1/2	3/2	$3p_{3/2}$	M_3
3	2	+1/2	3/2	$3d_{3/2}$	M_4
3	2	-1/2	5/2	$3d_{5/2}$	M_5

Tab. 2.2 – Relationship between quantum numbers, spectroscopists' notation and X-ray notation.

angle, after which there is a generation of photoelectrons.

Reminder on quantum numbers and spectroscopy nomenclature

In the field of XPS we are dealing with specific nomenclature (cf.table 2.2). For one specific element, we have the principal quantum number n taking the integer value 0, 1, 2, 3, etc. This is corresponding to the main electronic layer around the atomic nucleus. Then we find the second number l which describes the orbital angular momentum of the electron. This is also taking the integer value 0, 1, 2, 3 etc. but we prefer using s, p, d, f etc. And finally we have the spin angular momentum s taking the value -1/2 or 1/2. So in theory we can describe each electron of one element with these values. But in practice the last two angular momentums l and s are coupled and correspond to another number : $j = |l + s|$. This implies a split of each peak of the spectrum into two peaks with different intensities depending on the electronic population of each configuration. This ratio is given by $(2j + 1)$. The spacing between the peaks of the doublets depends on the strength of the spin orbit coupling. If we fix both n and l, the separation increases with the atomic number of the atom. And for a specific element, it decreases both with increasing n and with increasing l. [16]

Photoelectron ejection mechanism

Depending on the X-ray energy $E_{X-ray} = h\nu$, different electrons from the deepest electronic layers are ejected from the material. Each of these electrons are received by a detector (electron spectrometer) which measures its kinetic energy. Finally the measurement results in a graph showing the intensity of each group of photoelectrons having the same energy (counts/s) versus this kinetic energy. If we want

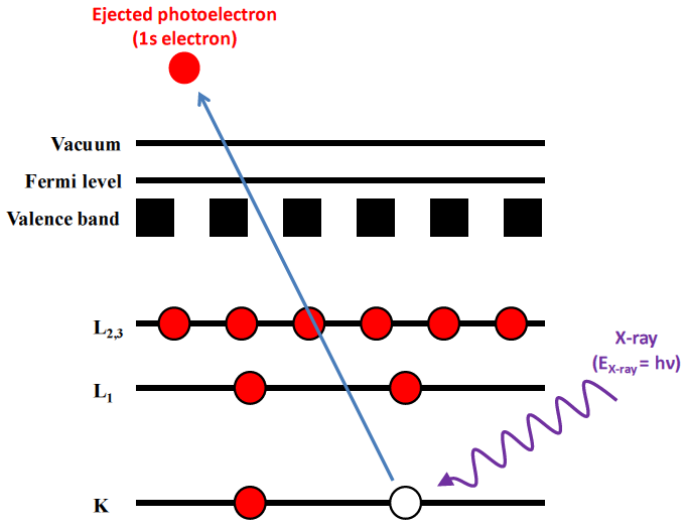

Fig. 2.42 – Photoelectron emission mechanism.

to be able to identify each peak (which is done by the analysis software) we have to find the binding energy E_B of each photoelectron expressed as follow : [16]

$$E_B = h\nu - E_k - W \tag{2.20}$$

where $h\nu$ is the photon energy, E_k is the kinetic energy of the electron, and W is the spectrometer work function.

It is worth noticing that each atom losing one electron is excited and relaxes either by emitting an X-ray photon (cf. figure 2.42), or by emitting an Auger electron (cf. figure 2.47). This last possibility generates some peaks at low energies compared to those corresponding to electrons kinetic energies. They also can be used as a chemical identification, as will be described below. [16]

2.2.5.2 Tool and technical layout

XPS tools require different parts in order to produce the measure. First, the sample is placed in a vacuum chamber whose pressure in between 10^{-8} and 10^{-10}mbar. If there are too many molecules in the chamber, low energy electrons are easily scattered, thus decreasing the final spectrum signal intensity. Also with a vacuum of only 10^{-6}mbar it takes 1s for molecules in the gas phase to be absorbed to form one monolayer at the material surface. This is shorter than the typical spectral acquisition time. [16]

Upstream from the sample, we find the X-ray source. High energy electrons coming from a heated filament of tungsten are accelerated under an electric field, induced by the high potential of an aluminum anode. The contact of the electron and the metal, and therefore the excitation of the metallic anode, allow the generation of X-ray photon at specific values depending on the electronic transition in the metal after the impact of the electrons. If we increase the density of electrons (the current) we increase the brightness (photon flux) of the X-ray beam and also the anode temperature. [16]

The X-ray beam is not directly sent toward the sample to generate the photoelectrons but passes

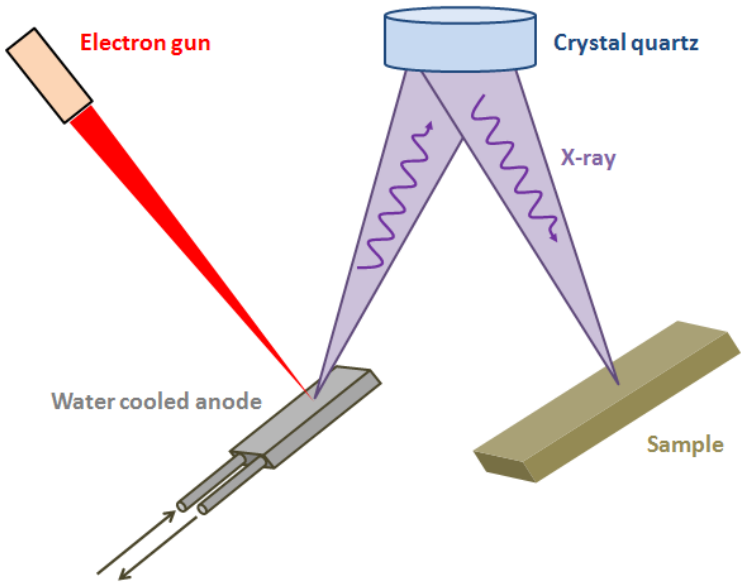

Fig. 2.43 – X-ray generation and collimation for XPS analysis.

through a monochromator. This is simply a crystal with a specific orientation that is used to diffract the incident beam and produce a narrow X-ray line. Also the satellite peaks and the Bremsstrahlung background are removed. Finally, when other samples are awaiting their measurement in the analysis chamber they are not damaged by the X-ray beam which is focus in a small point on one sample thanks to the collimator. Then photoelectrons are emitted by the material and analyzed by a hemispherical sector analyzer which will allow us to draw the intensity (proportional to the number of electrons) of signal at each energy window targeted. [16]

2.2.5.3 Example of XPS measurement

One of our measurements on InGaAlN is shown in figure 2.45 where we are getting some part of the total energy spectrum that the tool can analyze. We performed energy sweeps on specific energy lines corresponding to the elements we expect to have in the material. Also a first quick sweep across the entire energy range allows us to detect any unexpected elements. After this first survey we start the XPS measurement with high resolution on the previous described energy lines attributed to each element. Then the spectral analysis is done summing and normalizing the multiple sweeps that the spectrometer records around the different energy values. This sum allows a higher intensity relative to the background signal.

Once we have got all the peaks which interest us in the XPS spectrum, the data treatment software (Multipak) treats the data. It refers to a database of the various sensitivity factors attributed to each atomic orbital, to calculate the relative concentration of all the elements. It consists in doing the ratio between the different areas under the peaks that interest us multiplied by their sensitivity factors. Having such a concentration at different point along the layer, we can easily draw a chemical profile of our InAlN or InGaAlN layers. The uncertainty on the measurement we have done is roughly 5%. By looking at the different peak positions and their shift during the scattering it is also possible to

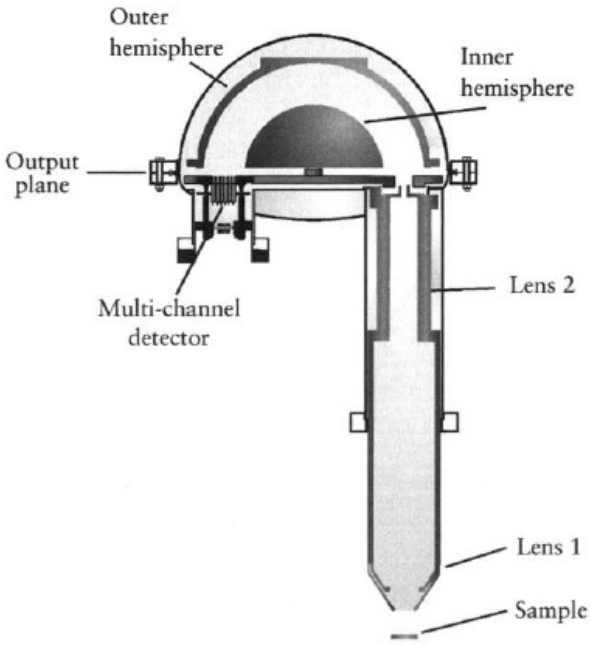

Fig. 2.44 – Hemispherical sector analyzer (photoelectron analyzer). [16]

study the oxide of our material since oxides are shifted toward lower kinetic energy compared to bulk material. However, we did not use XPS to evaluate the type of chemical bonds in our layers.

2.2.6 | Auger Electron Spectroscopy : AES

2.2.6.1 Generaities and physical mechanisms

AES characterization gives us nearly the same information as XPS. It is a surface characterization probing also the 3nm from the surface of the material. We still have a sputtering system to get the composition along the layer, but the real benefit of this technique compared to XPS its high lateral surface resolution due to the use of a focused electron beam (same resolution as a SEM). With the tool we used, we can make a measurement on an area no larger than 10x10nm^2. This is useful to investigate indium segregation at the surface of the samples.

Auger electron emission mechanism

When an incident electron comes into contact with a material, three mechanisms can occur. First of all, one of the electrons from deep energy levels can be ejected by the incident electron. This is quite similar than the photoemission in XPS. But in the case of AES we have no chemical information with these so-called secondary electrons. For the lowest energy it simply permits us to have good imaging as for a Scanning Electron Microscopy (SEM). This image is used so that we can look at the material surface and choose a specific measurement spot on the surface. When the atom is ionized it can go back to its ground state by emitting an X-ray, or if a hole is created on a deep electronic layer, an electron from a layer above can fill it. To respect the conservation energy law, the atom emits an electron from the highest electronic layers, known as an Auger electron. The naming of Auger electrons is as follows : If an electron is removed from the K layer, replaced by one of the L^1 and emitting a Auger from $L^{2,3}$,

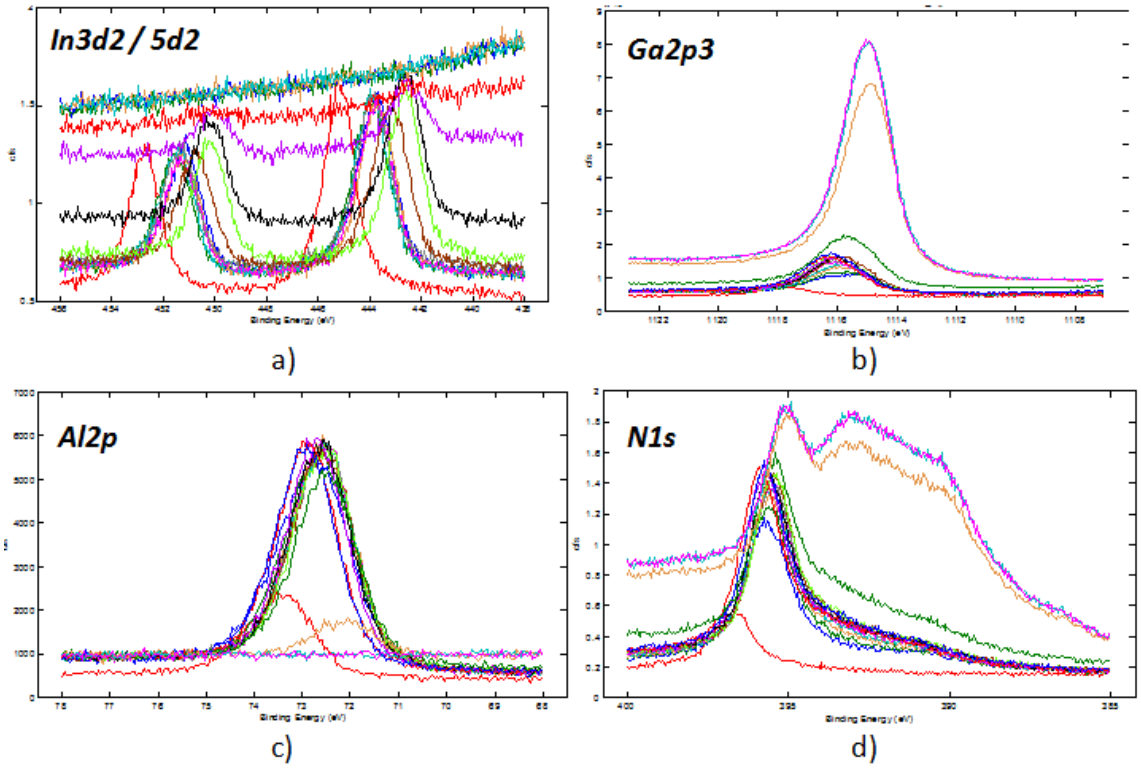

Fig. 2.45 – a) In3d2 and 5d2, b) Ga2p3, c) Al2p, and d) Al2p rays detected by XPS.

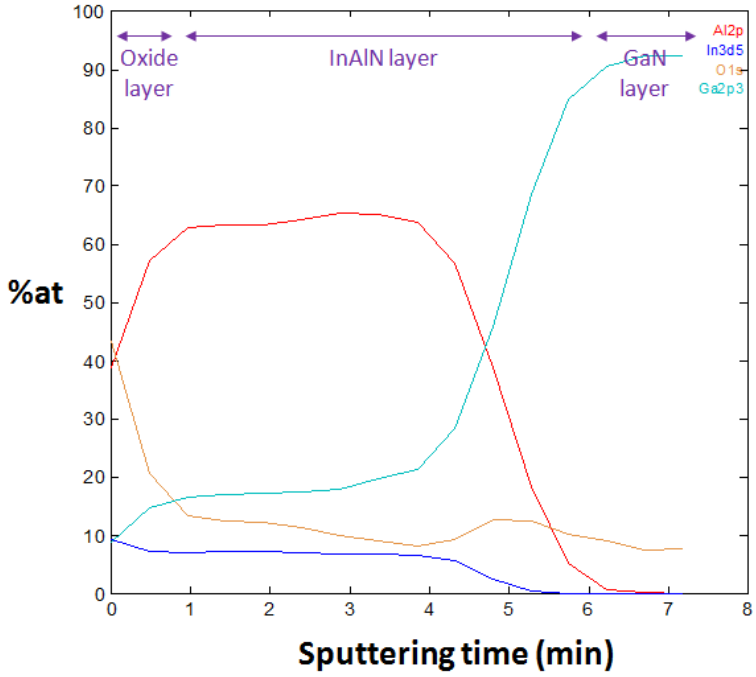

Fig. 2.46 – Relative composition of the different elements of an InGaAlN layer by XPS measurement. We added the presence of oxygen.

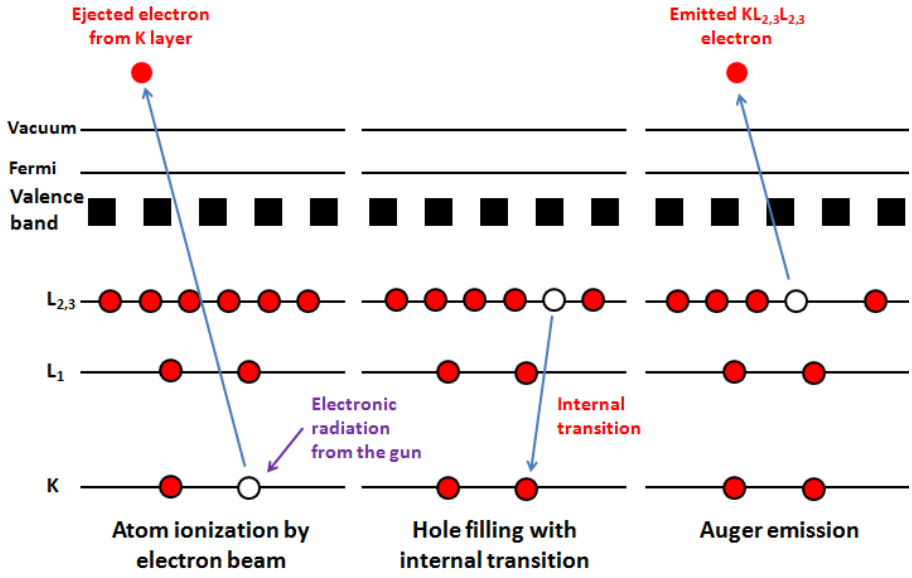

Fig. 2.47 – X-ray and Auger electron emission mechanism.

we call this Auger K L^1 $L^{2,3}$. [16]

We can calculate in a first approximation the kinetic energy $E_{KL_1L_{2,3}}$ of the Auger electron as follow : [16]

$$E_{KL_1L_{2,3}} = E_K - E_{L_1} - E_{L_{2,3}} \tag{2.21}$$

where E_K, E_{L_1}, and $E_{L_{2,3}}$ are respectively the energy levels of the three electronic sublayers K, L_1, $L_{2,3}$.

In this case, we assume that the interaction energies between the core holes (L_1 and $L_{2,3}$) in the final atomic state are negligible. We also don't take into account the inter- and extra-relaxation energies which come about as a result of the additional core screening needed. Thus we have an empirical model based on the energy calculation which couples the energy levels of one specific element with atomic number Z emitting the Auger electron and the next element in the periodic table. [16]

$$E_{KL_1L_{2,3}}(Z) = E_K(Z) - 1/2(E_{L_1}(Z) + E_{L_1}(Z+1)) - 1/2(E_{L_{2,3}}(Z) + E_{L_{2,3}}(Z+1)) \tag{2.22}$$

where $E_{KL_1L_{2,3}}(Z)$ is the kinetic energy of Auger electron emerging of the atom with atomic number Z, and $E_X(Z)$ and $E_X(Z+1)$) are respectively the energy of electronic level X (K, L, M, etc.) of chemical element with atomic number Z and Z+1.

2.2.6.2 Tool and technical layout

As for XPS and for the same reasons (cf 2.2.5.1), AES is always performed in a high vacuum chamber which means 10^{-8} to 10^{-10}mbar. We have an electron source coming either from thermionic emitter (tungsten filament heated), lanthanum hexaboride emitter or Schottky field emitter (tungsten

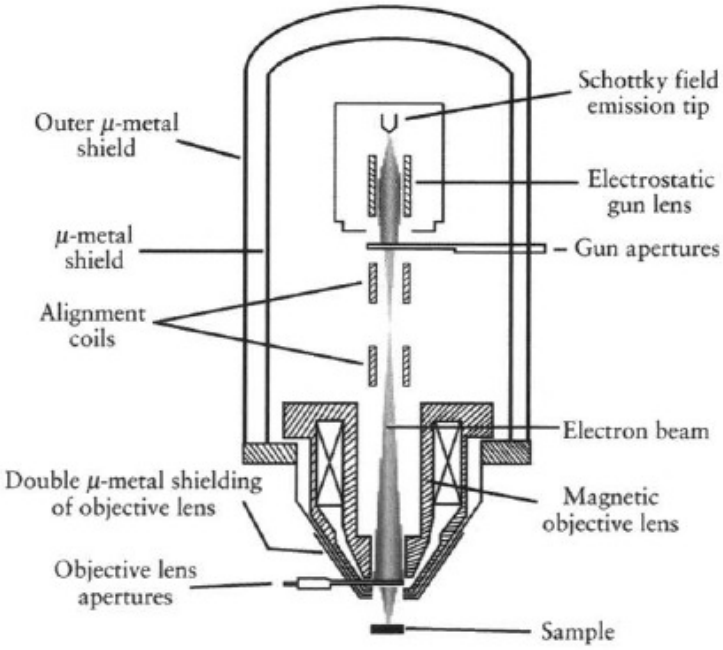

Fig. 2.48 – HUV electron gun for AES. [16]

crystal coated with zirconium oxide). Depending on applications and especially the spot area on the sample the electron beam coming from one of these specific sources is focused on the sample using an electromagnetic lens. These lenses are responsible for the scanning effect during the measurement by sweeping the sample on the specified spot area. [16]

The electrons coming from the gun with a certain energy (depending on the current and the voltage of the gun voltage) touch the material surface and generate an emission of different electrons as explained in 2.2.6.1. They are analyzed by a hemispherical sector analyzer as for XPS characterization. [16]

2.2.6.3 Example of AES measurement

At the end of an AES measurement, we get a spectrum where we can find the intensity corresponding to the number of Auger electron detected (in count/s) versus their kinetic energy. Also, the electron analyzer is sweeping the energy range on specific windows corresponding to the different elements under interest. A mathematical operation on the spectrum allows us to have the composition of our alloy as follows. The raw signal for each element is treated to give the first derivative. We then isolate the peak to valley absolute value of the derivative signals, which is proportional to the area of the initial signal. This is then divided by the sensitivity factor calculated using referenced elements. Then a ratio between the last numbers for each elements pair gives us the relative composition of them to each other.

Each peak of each window corresponds to the measurement at a certain thickness and the recombination of all the curves gives the relative composition along the layer.

In this example we performed two measurement points - one on the white part (the blue signal) of the SEM picture and the other on the black part (the red signal). We expected to have a real difference

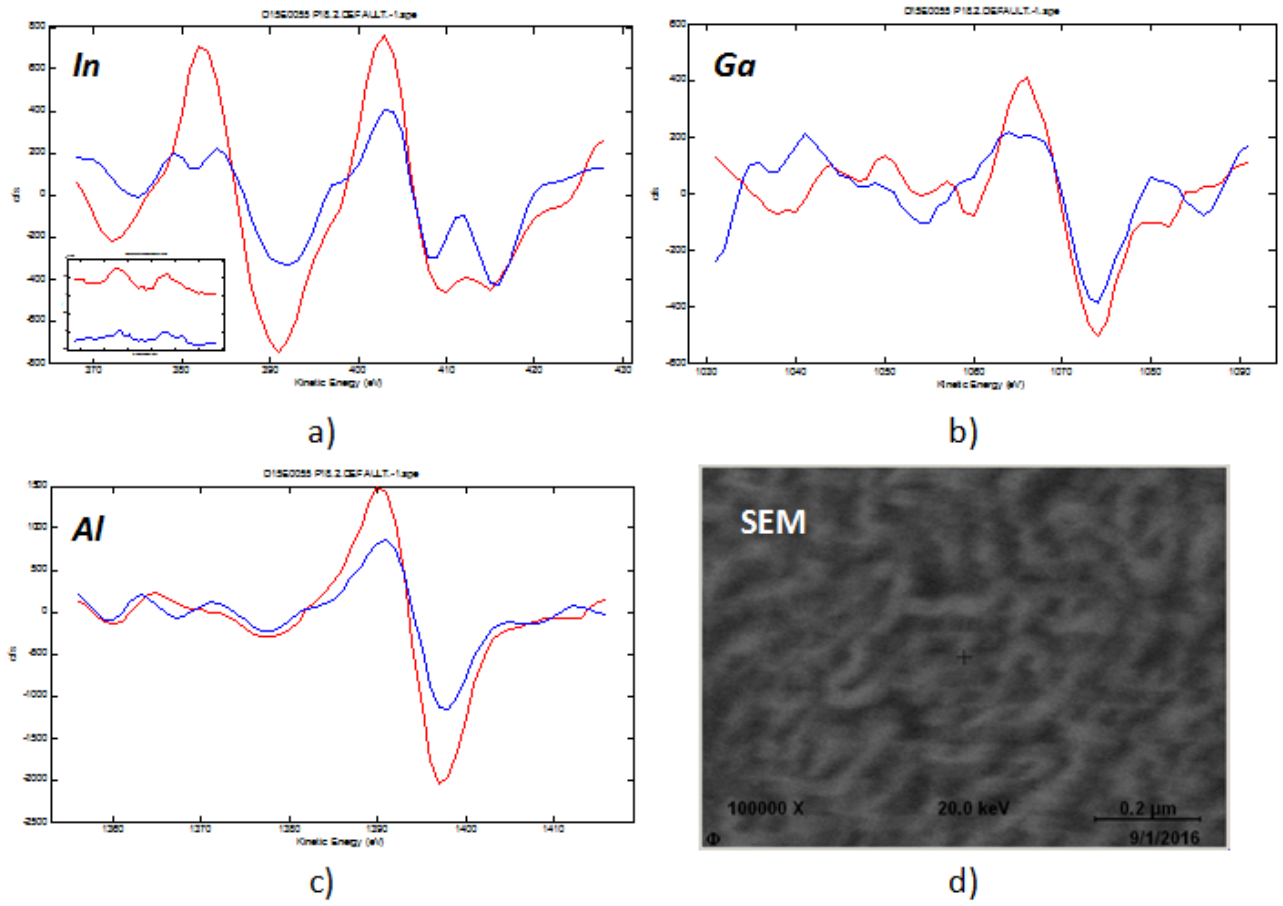

Fig. 2.49 – Auger spectra for a) derivative indium signal with the raw signal in the insert, b) and c) the derivative of the gallium and aluminum signals respectively. d) The SEM image that shows the morphology we used to accurately place two measurement areas.

in the indium content but that is actually not the case since both have nearly 8% of indium in the In/(In+Al) ratio. This will be discussed later in chapter 5.

2.2.7 | Wavelength Dispersive X-ray Fluorescence : WDXRF

WDXRF allows fast measurements on full wafers with different measurement points of few centimeters in diameter. An X-ray source produces a monochromatic parallel beam of X-ray photons with an energy sufficiently high to eject an electron of the K-shell generating a K_α radiation (cf. spectroscopist notation in table 2.2 and figure 2.38 for illustration) for the different chemical elements forming the sample. The intensity emitted by the fluorescence is then analyzed by a wavelength dispersive spectrometer that can separate the different lines of the re-emitted spectrum. [17]

While a fraction of the incident intensity I_0 is absorbed by the sample material, depending on the concentration C_i of the different chemical elements i, their respective mass absorption coefficient sμ_i and the material densities ρ, there are three scenarios that need to occur. Firstly, an electron of the K-shell, is ejected rather than from L-shell or M-shell. Secondly, it is a K_α line instead of the other K lines. And finally, after electron ejection, it is a K_α radiation that occurs instead of electron Auger emission (cf. section 2.2.6.1 for details). Each of these cases is symbolized by probabilities called respectively K-shell absorption jump ratio, transition probability, and fluorescence yield. And they must be multiplied together to form the excitation factor Q which needs to be calibrated for each element to be measured.

There is also a fraction of the fluorescent radiation emitted from element i which is re-absorbed by the material. Finally, we need to take into account the fraction of the whole fluorescent intensity, originally emitted in all directions, which is caught by the detector and its solid Ω angle formed by its geometry.

So at the end of the calculation of the fluorescence emerging from the sample for each chemical element, we have to deal with four components : the absorption of incident beam by element i, the factor of excitation, the absorption of intensity of i fluorescence by the material, and the geometry of detection. As we can see, the formal calculation is quite complex and detailed in ref [18]. However, in the case of thin films, the intensity of one radiation line in the detected spectrum is proportional to the concentration of element i associated with this line. The proportionality coefficient depends on I_0, μ_i, Q, Ω, ρ and the sample thickness h. [18] They are all experimental and referenced physical parameters which means that we can find the ratio between the intensities of chemical elements i in order to find their concentration in an alloy.

However, there may be other sources of error. Firstly, the X-ray beam can be slightly polychromatic depending on the source, the ideal being radioisotope emitting monochromatic γ-ray lines. Then the previous model in which we explain what physical quantity influence the chemical analysis of the material, concerns primary fluorescence. It consists in considering that each atom receives the incident X-ray beam and emits a fluorescence radiation according to certain probabilities. But a part of the primitive fluorescence can generate a secondary fluorescence and even a ternary one. This is the matrix effect and this can change the relative intensities of lines between the different chemical elements. A calibration with reference samples is effective since the calculation to take into account the matrix effect is more complex than for primary fluorescence. Moreover, while the ternary fluorescence reaches 2-3%

of the total fluorescence emission, secondary fluorescence can reach 50%. We were not able to optimize our calibration since we used a pure aluminum sample for aluminum and an InP sample for indium. We did calibrate the gallium since the measurements show a big part of the GaN pseudosubstrate with InGaAlN layer. So a gallium fluorescence signal from the top layer would be lost in a total signal from the 2μm GaN layer.

2.2.8 | Sheet resistance measurement

As explained in chapter 1, the heterostructure formed by two stacked III-N alloys can generate of a two dimensional electron gas at the interface. To measure its sheet resistance, we have used the four collinear probes method. It consists of placing four aligned evenly spaced points at the surface : two for a voltage measurement and two in order to apply a current.

This technique depends on an ohmic contact between the points and the sample, which is not the case typically for tungsten points on GaN. Thus we have developed a specific technique at LETI to allow us to make these measurements. The first step consists in reach the break down voltage of the barrier layer in order to measure directly the resistance of the 2DEG. We apply a high voltage between two points (1,2) and apply the voltage in one direction and then in the other. To ensure the breakdown under all the points, we repeat the process with the remaining pair, that is to say (3,4). We can also perform this breakdown by applying of voltage of 200V between the tips and the substrate, either all the points at the same time or point by point.

We assume that we have three conditions : four equally spaced collinear points, a conductor whose thickness is negligible compared with the spacing between points (conductive seen as purely 2D). The measurement setup where the current is applied between the external tips and the voltage read between the internal tips as shown in figure 2.50. Thus the calculation "applied current / measured voltage" gives a resistance that we multiply by $\frac{\pi}{ln(2)} \simeq 4.54$ (geometric factor) to get the sheet resistance, taking into account the three previous conditions. Also, the success of this measurement implies that we do not contact the substrate or that it is resistive compared to the substrate.

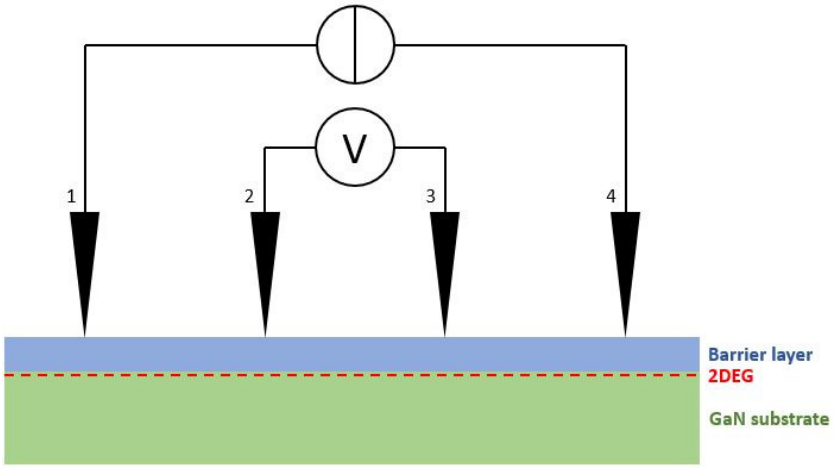

Fig. 2.50 – Rsheet measurement setup.

Summary of chapter 2

This thesis is in an industrial context with the idea of producing, ultimately, high quality wafers of III-N materials, with a sustained pace of production. So we used a fully automated MOCVD reactor from AIXTRON. It contains a close coupled showerhead system to ensure homogenous epilayers, and a sample automatic loading and unloading system which optimizes the production pace. The cleaning process of the growth chamber does not require its opening but is done by chlorine gas. The machine allows us growth of nitrides on 200mm (111) Si substrates under nitrogen and hydrogen carrier gas and taking as MO precursors TMIn, TMGa, TMAl and TEGa, and ammonia as nitrogen precursor. The system presents a growth monitor with in-situ curvature and temperature sensors, and with a reflectometry for growth rate calibrations. Inside the tool, the control of bubbler and thus MO storage and physical condition setting, is important to accurately send to the reactor the right amount of MO precursors mixture which will govern the alloy growth rate and composition in the mass flow transport regime. We are growing our samples in this regime since the growth rate is independent of temperature and require only the MO flow adjustment to modulate it and change the crystal quality and properties. While the MOCVD foundations were recalled from a thermodynamic and kinetic point of view, we dealt with the problem of rich and poor indium phases separation in indium containing III-N materials growth. It is detrimental since it generates composition inhomogeneities which can influence several physical properties : luminescence, roughness, local resistance, and so on.

We described all the characterizations we employed. First in order to measure the surface roughness we spoke about atomic force microscopy (AFM) and the tapping and peak force modes we chose. For X-ray based characterizations, we used : X-ray reflectometry (XRR) for layers thickness measurements, X-ray diffraction (XRD) for crystal structure and usually composition analysis, X-ray photoelectron spectrometry (XPS) and X-ray fluorescence (WDXRF) for alloys composition at different scales. The use of Auger electron spectrometry (AES) gave additional information for alloy composition and especially indium segregation estimation since the spot of measurement is around 10nm. Finally we have used photoluminescence to measure the band gap energy of our material and Rsheet measurements by four probe points to evaluate the sheet resistivity of the two dimensional electron gas (2DEG).

Bibliographie

[1] G. B. Stringfellow, *Organometallic Vapor-Phase Epitaxy, Second Edition : Theory and Practice 2nd Edition*. Elsevier, 1999. xii, 32, 33, 34, 35, 36, 43, 44

[2] LayTec, « Technical document on the use of the epicurvett module from laytec », rap. tech., LayTec. 45, 47, 48, 49

[3] T. A. Lafford, B. K. Tanner et P. J. Parbrook, « Direct measurement of twist mosaic in gan epitaxial films as a function of growth temperature », *Journal of Physics D : Applied Physics*, vol. 36, no. 10A, p. A245, 2003. 50

[4] E. Arslan, M. K. Öztürk, E. Tiras, T. Tiras, S. Özçelik et E. Özbay, « Buffer effects on the mosaic structure of the hr-gan grown on 6h-sic substrate by mocvd », *Journal of Materials Science : Materials in Electronics*, vol. 28, p. 3200–3209, 2017. 50

[5] P. Bhattacharya, R. Fornari et H. Kamimura, *Comprehensive Semiconductor Science and Technology*. Elsevier Science, 2011. 50

[6] D. Doppalapudi, S. N. Basu, K. F. L. Jr. et T. D. Moustakas, « Phase separation and ordering in ingan alloys grown by molecular beam epitaxy », *Journal of Applied Physics*, vol. 84, no. 3, p. 1389–1395, 1998. xii, 51, 52

[7] B. P. Burton, A. van de Walle et U. Kattner, « First principles phase diagram calculations for the wurtzite-structure systems aln-gan, gan-inn, and aln-inn », *Journal of Applied Physics*, vol. 100, no. 11, p. 113528, 2006. xii, 51, 52

[8] « Cea-leti, internal documentation on afm characterization ». . 53, 54, 56

[9] Bruker, « Technical documentation on bruker fastscan a type tip », rap. tech., Bruker. xiii, 58

[10] Bruker, « Technical document on xrr characterization », rap. tech., Bruker, 2010. xiii, 59, 60, 61

[11] Bruker, « D8 fabline instructions », rap. tech., Buker, 2012. 59, 60

[12] P. DHEZ, « Caractérisation des surfaces et des matériaux stratifiés par rayons x », *Techniques de l'ingénieur Études de structure et caractérisation*, vol. base documentaire : TIB386DUO., no. ref. article : p1085, 1996. fre. 60, 61

[13] I. Pelant et J. Valenta, *Luminescence Spectroscopy of Semiconductors*. Oxford, 2012. 62

[14] D. Bowen et B. K. Tanner, *High Resolution X-Ray Diffractometry And Topography*. 1998. 65

[15] INAC, « Internal documentation on xrd rsm measurements », rap. tech., INAC, CEA-LETI. 69

[16] J. F. Watts et J. Wolstenholme, *An Introduction to Surface Analysis by XPS and AES*. Wiley, 2005. xiii, 70, 71, 72, 73, 75, 76

[17] J. DESPUJOLS, « Spectrométrie d'émission des rayons x. fluorescence x », *Techniques de l'ingénieur Spectrométries*, vol. base documentaire : TIB390DUO., no. ref. article : p2695, 2000. fre. 78

[18] V. THOMSEN, « Basic fundamental parameters in x-ray fluorescence », *Spectroscopy*, vol. 22, no. 5, 2007. 78

3 | Gallium nitride growth at low temperature

Sommaire

3.1 Context of low temperature gallium nitride growth 86
3.2 GaN layers under different growth conditions 87
3.2.1 Influence of growth temperature and thickness on V-defect size 87
3.2.2 Influence of growth rate on V-defect size 91
3.2.3 Influence of MO precursors and carrier gas on V-defect size 91
3.3 V-defects : a model of formation and evolution 93
Bibliographie 99

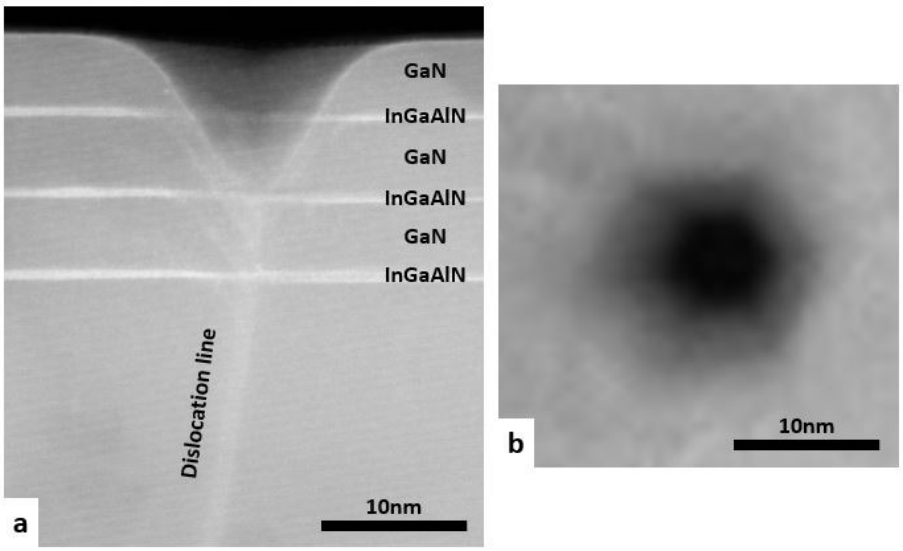

Fig. 3.1 – a) TEM cross section image of V-defects in InGaN-GaN multi-quantum wells grown at LETI, b) V-defects seen from the c direction of the crystal. The dislocation line is clearly seen as the source of the pits. Measurements by Nicolas Mante.

3.1 | Context of low temperature gallium nitride growth

GaN growth at low temperature is necessary for the development of III-N indium containing multi-quantum wells (MQWs) or simply GaN cap layers on indium containing barrier layers, as InN is volatile compared to GaN or AlN. Equally, these layers should not be heated too much after growth, to avoid indium segregation or phase separation [1]. In our standard conditions but with a temperature between 730°C and 940°C , the GaN growth morphology is altered by the formation of so-called V-defects [2][3][4][5][6][7] that we would like to avoid or reduce in size because of the drawbacks they can bring during device operation : recombination centers [4][8], carrier deep traps [5][9], low LED breakdown voltage, reverse current and electro-static discharge [7][10], thickness non-uniformity and surface roughness [6].

An example of the formation of V-defects in a multi-quantum well (MQW) is shown in the cross sectional TEM image in figure 3.1. These V-defects are surface depressions induced by the threading dislocations present in the previous layers. As explained in the model of B. Heying et al. [11][12], the dislocation line exerts a force which pulls on the surface layers at that point and causes the V-defect. Looking from a different perspective, a study based on the ELOG process showed the impact of the temperature on the favored GaN planes during the growth. In particular, they showed that inclined planes such as (11-22) are favored over the (0002) plane at low temperature implying that the surface energy of the different atomic planes plays a role in defining the morphology during growth [13][14]. Our study looks at the properties of the V-defects generated during low temperature GaN growth with a view to understanding and optimizing the growth of GaN layers for MQW barrier layers, and of course for capping applications in the field of HEMTs manufacture.

3.2 | GaN layers under different growth conditions

The first section of this chapter is dedicated to the study of the surface morphology of gallium nitride grown at low temperatures. Low temperatures imply here lower than the optimal one we usually use for GaN growth, which is typically performed around 1050°C. We will see how the V-defects evolve in size when we change the temperature, the growth rate, the film thickness, the metalorganic precursor, and the carrier gas.

The nitride structures used for this study have a simple buffer layer using an AlN nucleation layer on the silicon substrate, followed by AlGaN layers to control the strain in the GaN, and then a 2 μm thick bulk layer of GaN grown at a temperature of 1035°C. The low temperature GaN layer of several tens of nanometers is grown directly on top of this stack of layers in the same growth run. The growth rate of the layers was calculated from the 950nm reflectivity signal, while for thinner layers, thicknesses were calculated from calibration samples. All the AFM images were analyzed using Nanoscope analysis 1.5 for the imaging and Gwyddion software to measure the size of the surface depressions (V-defects).

For all of our samples, the V-defect density was found to be between $1.4 \times 10^9 cm^{-2}$ and $6.7 \times 10^9 cm^{-2}$ using AFM pictures. This is around the same value as the dislocation density of our thick 1050°C high temperature GaN layer which supports the theory that our V-defects are formed at dislocation lines [2][7] as shown in figure 3.1. Our analysis of defect size has been based principally on the comparisons of defect diameter, rather than depth, as the state of the AFM tip can impact the measured depth of the V-defects. V-defect diameters are calculated as a mean of the different V-defect diameters counted on each AFM picture. The uncertainty bars shown at each point of the graphs are simply the calculated standard deviation from all the V-defect sizes of each picture.

In figures 3.2 and 3.3 we show the interface of the Gwyddion software that we used to measure V-defects. It consists in making a cut along the V-defect diameter, before placing analysis points whose software gives us the vertical (Y axis) and horizontal (X axis) spacing points. Typically we placed these points on the edge of the hole formed on the cut to read the diameter. It is not easy because sometimes one or both edges can be more or less abrupt and we have to choose each time were we place the point on the slope of the edge. We defined the edge as the beginning of the slope from the flat surface. For the depth, we place one coordinate point at the level of the edges and one at the bottom of hole. If edges are not at the same Y coordinate we take the mean of both edges Y coordinates.

3.2.1 | Influence of growth temperature and thickness on V-defect size

We grew samples at 740°C, 840°C, and 940°C with the carrier gas switched to N_2 in the first instance. Regarding the potential application as a barrier layer, it allows us to not desorb too much indium during the first stages of growth if indium containing alloys are at the surface during the low temperature GaN growth. We fixed an ammonia flow of 10slm, with TMGa as the MO precursor, and a reactor pressure of 100mbar. The low temperature GaN growth was performed for two thicknesses, 40nm and 120nm at 540nm/min.

We show the AFM images in figure 3.4 where we can see that the diameter of V-defects around the

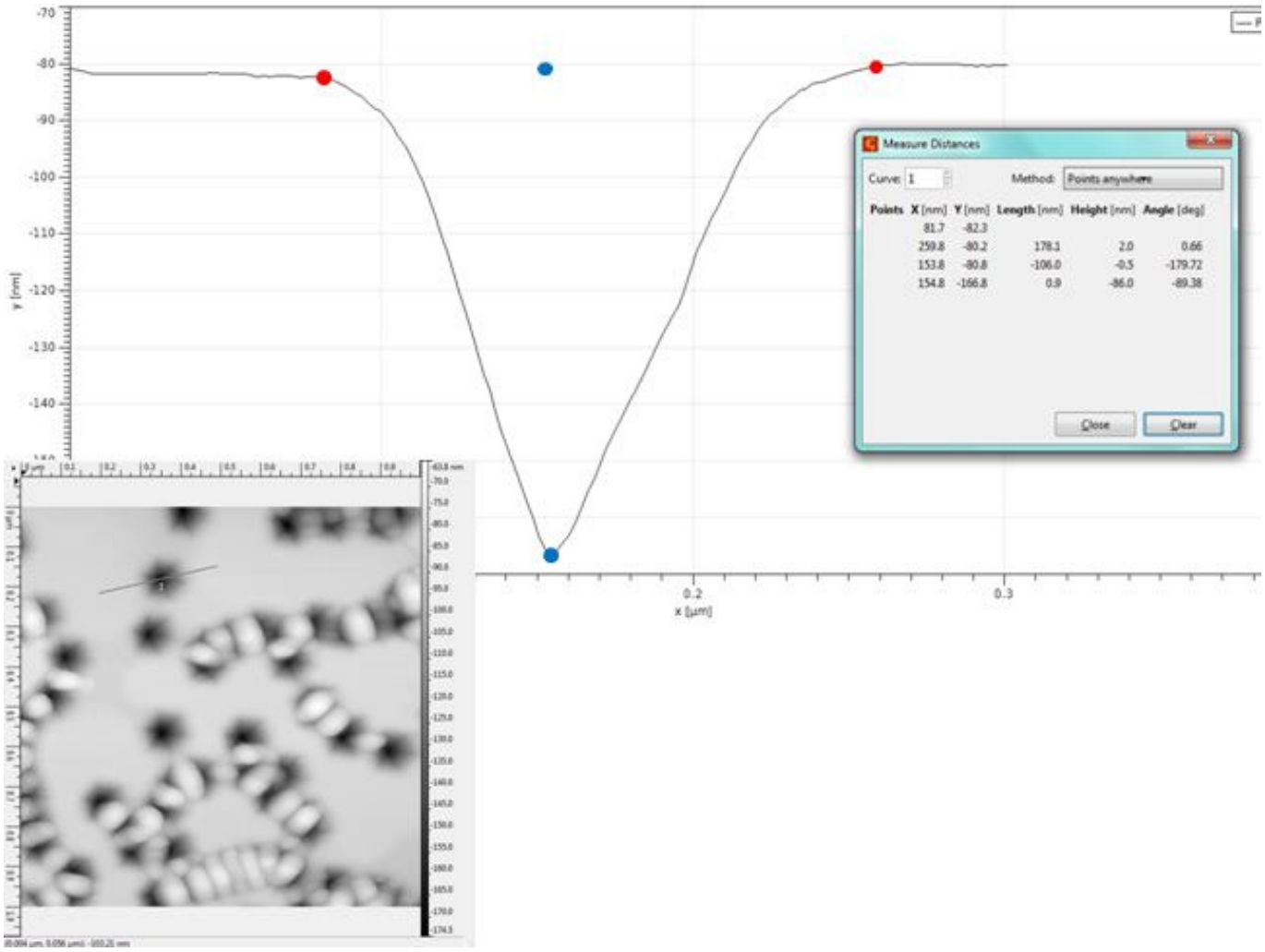

Fig. 3.2 – V-defect size measurement using Gwyddion software on 120nm thick GaN sample grown at 740°C. Bottom left of figure, the 1x1 μm^2 AFM image with the cut line in black. At the top, the V-defect profile with red points for diameter measurement and blue ones for depth measurement.

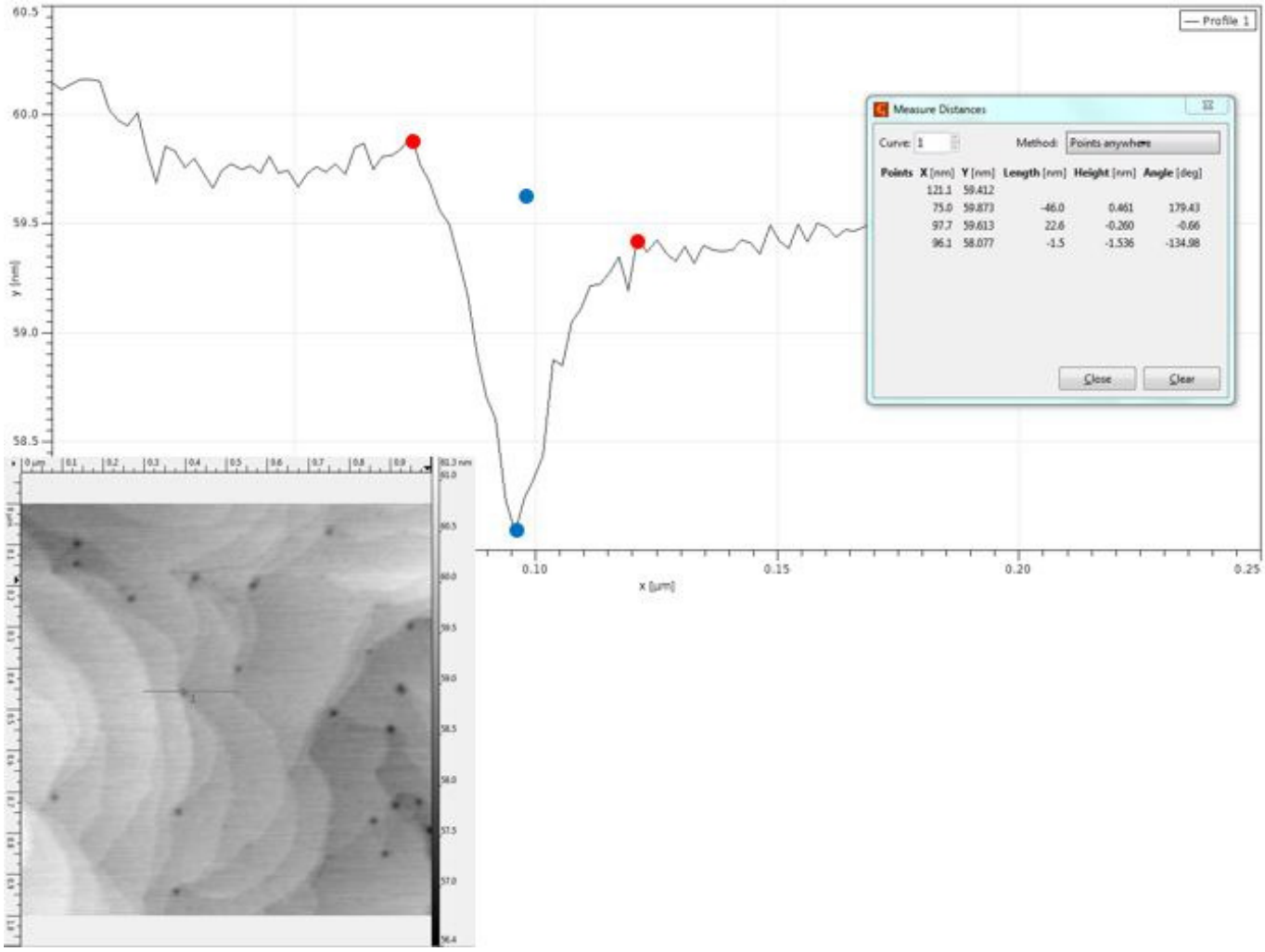

Fig. 3.3 – V-defect size measurement using Gwyddion software on 120nm thick GaN sample grown at 940°C. Bottom left of figure, the 1x1 μm^2 AFM image with the cut line in black. At the top, the V-defect profile with red points for diameter measurement and blue ones for depth measurement.

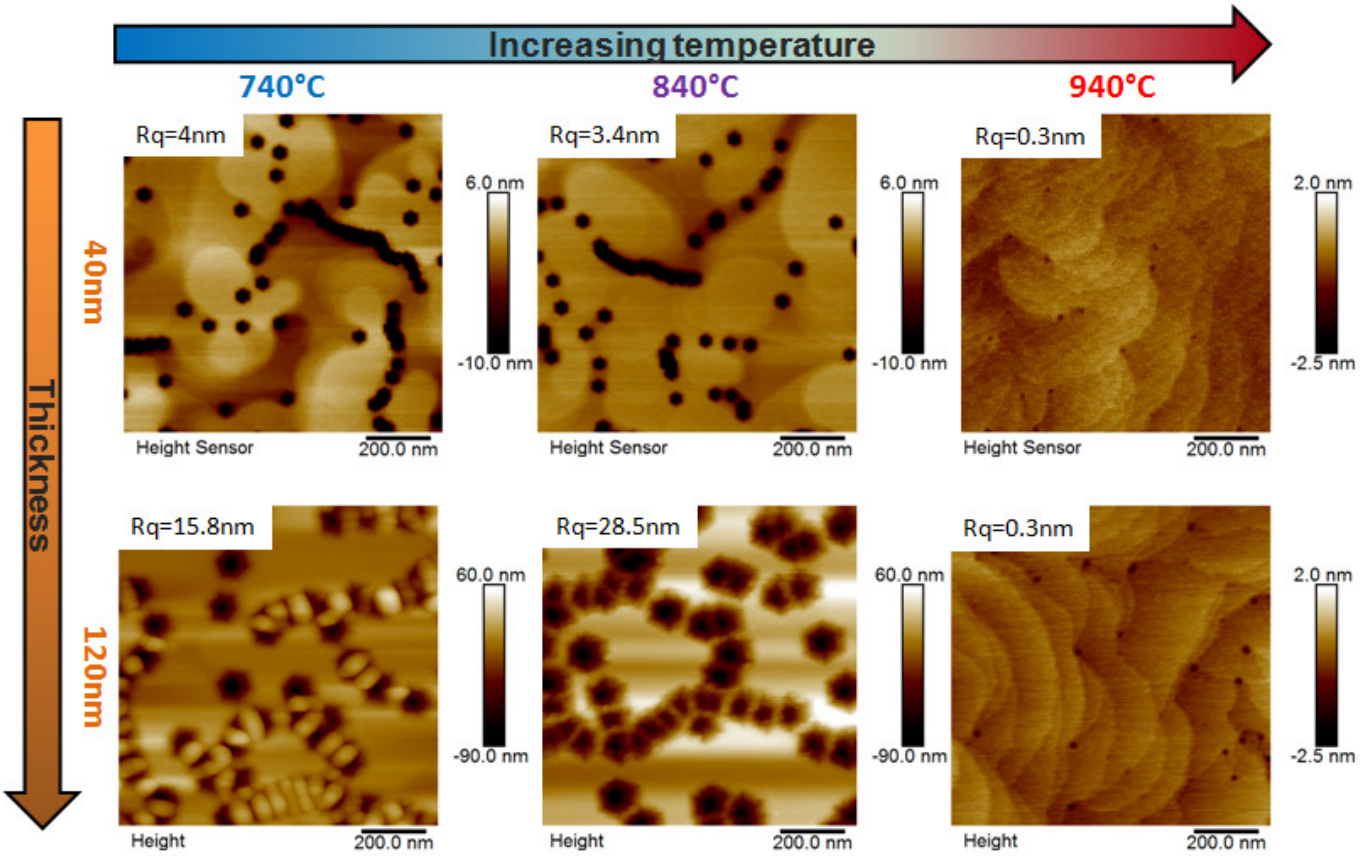

Fig. 3.4 – 1x1 μm^2 AFM images of low temperature GaN grown at three temperatures for two different thicknesses, using N_2 as carrier gas and TMGa as gallium precursor. Vg=540nm/h.

dislocations is larger for thicker films for the two lowest temperatures, although the size of these defects does not change between these two temperatures. However, at 940°C, the diameter of V-defects decreases for both thicknesses, and there is no longer an effect of thickness on their size. At low temperatures, all types of dislocations appear the same size, while at 940°C, mixed dislocations (the biggest V-defects seen on AFM measurements, which also pin step structures) and edge dislocations (the smallest V-defects also seen on AFM measurements) [12] have different sizes. These different sizes these have been averaged in the graph of figure 3.5. We can also note that, even if we have V-defects of different sizes up to several tens of nanometers, the material surface structure around it appears to be step structured as for that of a GaN layer grown under optimal conditions.

As part of the same series, the growth rate was changed from 540 nm/h to 180 nm/h and figures 3.6 and 3.7 show that the samples are similar in terms of V-defect diameter. At 730°C the average depth of V-defects seems to be lower at 540nm/h than at 180 nm/h in comparison with higher temperatures (840°C and 940°C). But the depth measurement is very sensitive to the AFM tip quality and radius as discusses above. This is why our real size estimation of V-defects is their diameter measurements. In the literature, Heying et al. have reported [12] that if they increase strongly the flow of TMGa they can fill up the V-defects, which might be expected from an kinetic point of view, but for our range of temperatures, using growth rates lower than those in the reference, we have not observed this effect.

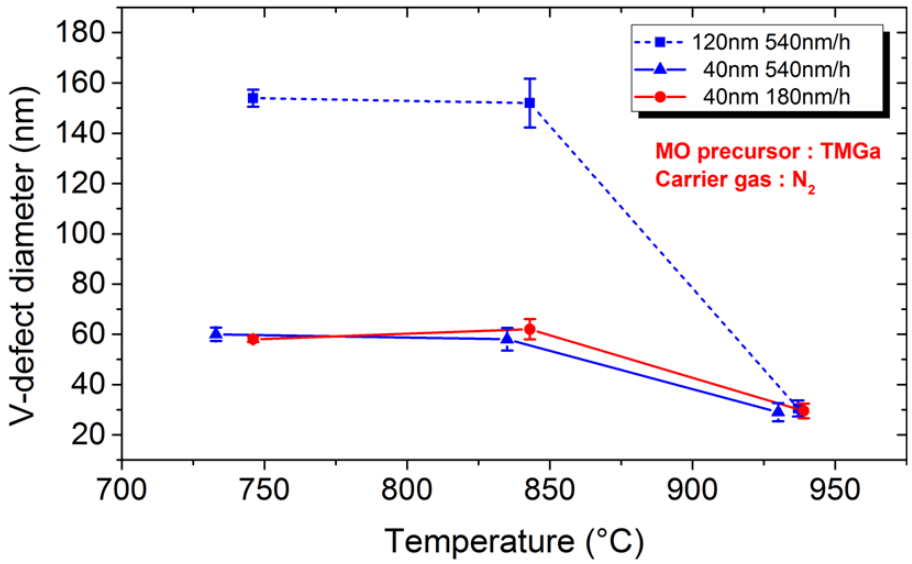

Fig. 3.5 – The figure shows the evolution of V-defect diameter versus growth temperature. Growth rates are fixed at 540 nm/h and 180 nm/h with TMGa precursor and N_2 carrier gas.

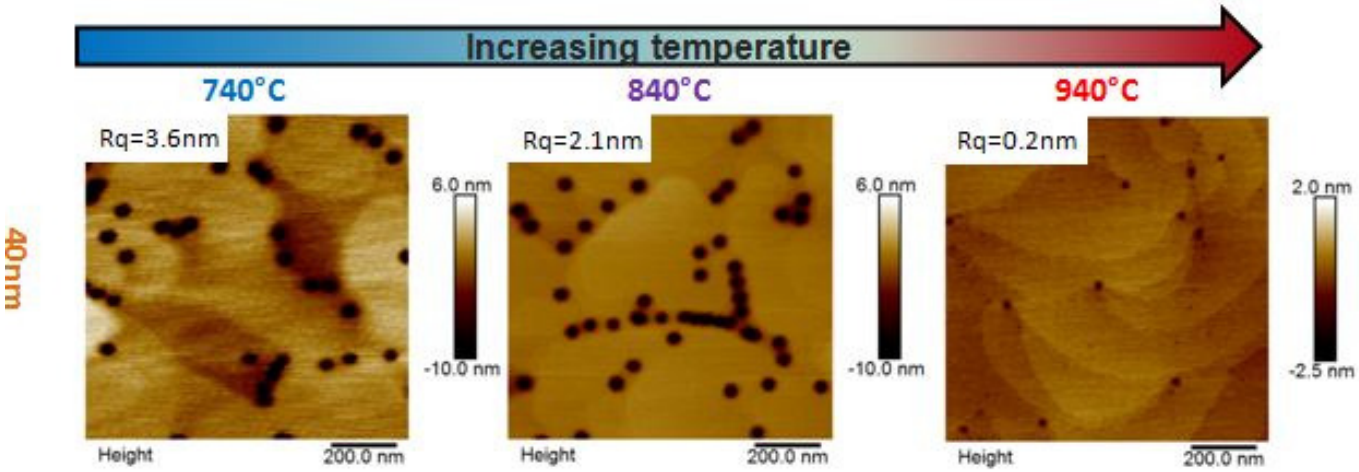

Fig. 3.6 – 1x1 μm^2 AFM images of low temperature GaN grown at three temperatures, using N_2 as carrier gas and TMGa as gallium precursor. Vg=180nm/h for a thickness of 40nm.

3.2.2 | Influence of growth rate on V-defect size

3.2.3 | Influence of MO precursors and carrier gas on V-defect size

To further understand the effect of different parameters on the size and shape of V-shaped defects, we looked at the effect of the MO precursor and the carrier gas, as shown in figure 3.8. Once again, the experiments were performed at 740°C, 840°C, and 940°C. The growth with TEGa produces slightly bigger V-defects than the TMGa, following the same trends for both N_2 and H_2 carrier gas. This cannot be due to an effect of different GaN surface energy using the two precursors since we isolated one specific inclined plane which is (11-22) as described below. This hole size difference may just be a problem of thickness calibration with the TEGa precursor, as we have seen in the previous section that thicker films have larger pits. This will be further analyzed below. It should be noted that the 40nm samples of figure 3.8 don't show the exact same V-defect diameters as those of figure 3.5 (TMGa+N_2).

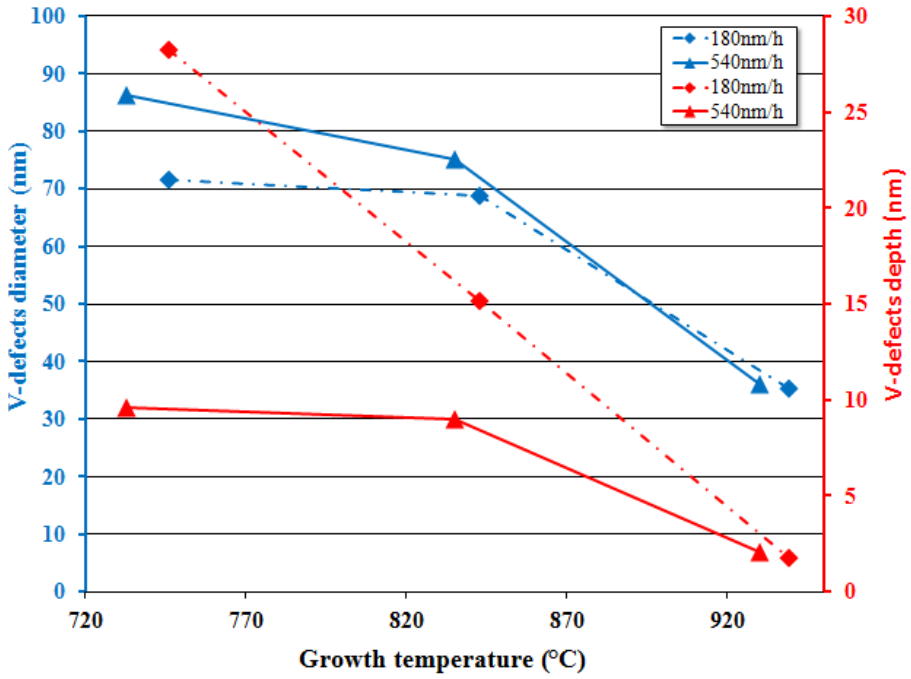

Fig. 3.7 – Graph showing the average diameter (left), and depth of V-defects (right) in GaN versus the temperature, for two growth rates and a thickness of 40 nm. TMGa and N_2 carrier gas were used.

These two sets of samples were grown with different NH_3 partial pressures, and so their thicknesses may also be slightly different. Moreover several months separate the two set of experiments. During this time the reactor underwent different hardware changes which could change a little the experimental growth rate while we kept the same recipe for the 40nm thick sample grown with TMGa under nitrogen at 540nm/min. This would explain the different pit sizes between these nominally identical samples.

In contrast to the effect of MO precursor, the change in carrier gas has a strong effect, for both types of precursor, as shown in figure 3.8. Under H_2 we can see that at around 800-850°C we have similar V-defects diameters as under N_2 at 900-950°C. This is a very significant difference that cannot be explained by differences in thicknesses of the layers. The change between the two carrier gases can be seen as a relative horizontal shift of the two sets of green and blue curves. Indeed it is as if the upper plateau of the blue curves at low temperatures was only reached at 730°C for green curves. In the same way the bottom plateau of green curves at high temperatures is only reached by the blue curves at 920°C in this graph window.

The surface morphology of the samples represented in the graph in figure 3.8 is shown in figure 3.9, as imaged by AFM. The z-scale is the same for all images, and these show that atomic step features occur even at low temperatures. Importantly, the GaN surface is similar at 840°C under H_2 to that grown at 1040°C (standard GaN growth temperature), while that grown under N_2 still contains large pits. At 940°C, the layers grown under N_2 have roughly the same morphology as well. This means that as described in the graph, the morphology shows a shift of around 100°C between the two carrier gases. This shows the strong effect which H_2 has on improving the surface morphology at lower temperatures than under N_2. To go further in the thinking on hydrogen and its effects as a kinetic point of view (not

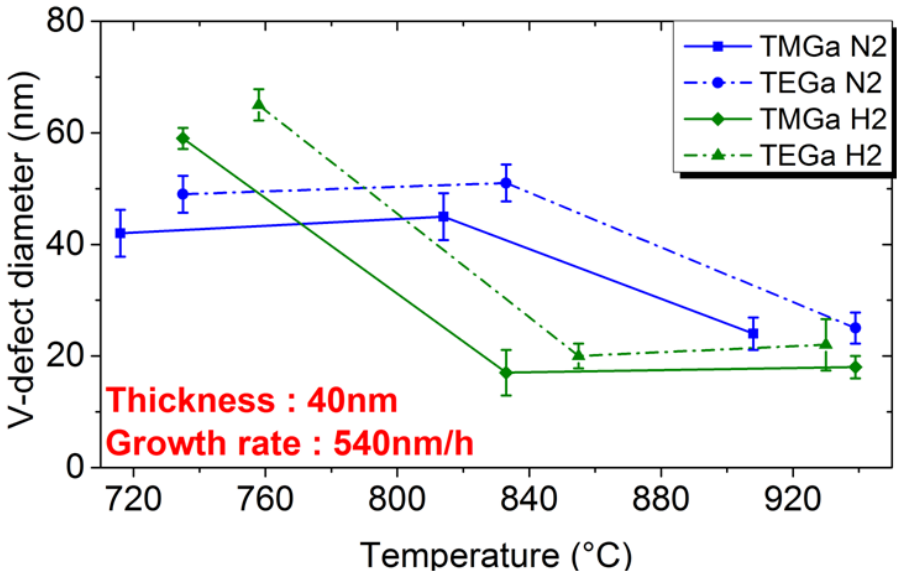

Fig. 3.8 – Average diameter of V-defects in GaN plotted against growth temperature for two MO precursors and two carrier gas. The GaN layers are 40 nm thick with a growth rate of 540 nm/h.

developed here), the reader could have a look at the reference [15].

3.3 | V-defects : a model of formation and evolution

In this section we will build a semi qualitative model that would explain the trends observed while we change the temperature, the thickness, the MO precursors and the carrier gas. We examined an analogy with the surface energy mechanics made by F.C. Frank [11] (cf. figure 3.10), which describes the strain energy density resulting from the strain field around a dislocation, associating an energy with the dislocation (E_D). From this energy of the dislocation, we can imagine that there is an equilibrium corresponding to the energy of the system containing the dislocation and the inclined planes minus the energy of the system without any dislocation, which means only the (0002) plane. We determined the orientation of the inclined planes ; from the profile in figure 3.11 obtained by AFM measurements, we have measured an angle of 63°between two opposite sides of the V-defects, which is the calculated value of two opposite (11-22) planes in wurtzite GaN [16]. This analysis is coherent with the orientation of the GaN layers, as confirmed by XRD (not shown here), so we can assume that the inclined planes in each V-defect are oriented to (11-22). Thus :

$$E_D = A_{(11-22)}.E_{(11-22)} - A_{(0002)}.E_{(0002)} \tag{3.1}$$

where $A_{(11-22)}$ and $A_{(0002)}$ are the surface areas of the six (11-22) planes and the (0002) planes respectively, and $E_{(11-22)}$ and $E_{(0002)}$ are the surface energies of the (11-22) and (0002) planes respectively. Using the lattice parameters a=3.189Å and c=5.185Å of the GaN lattice cell, we can show that :

$$A_{(11-22)} \approx 2.A_{(0002)} \tag{3.2}$$

Therefore :

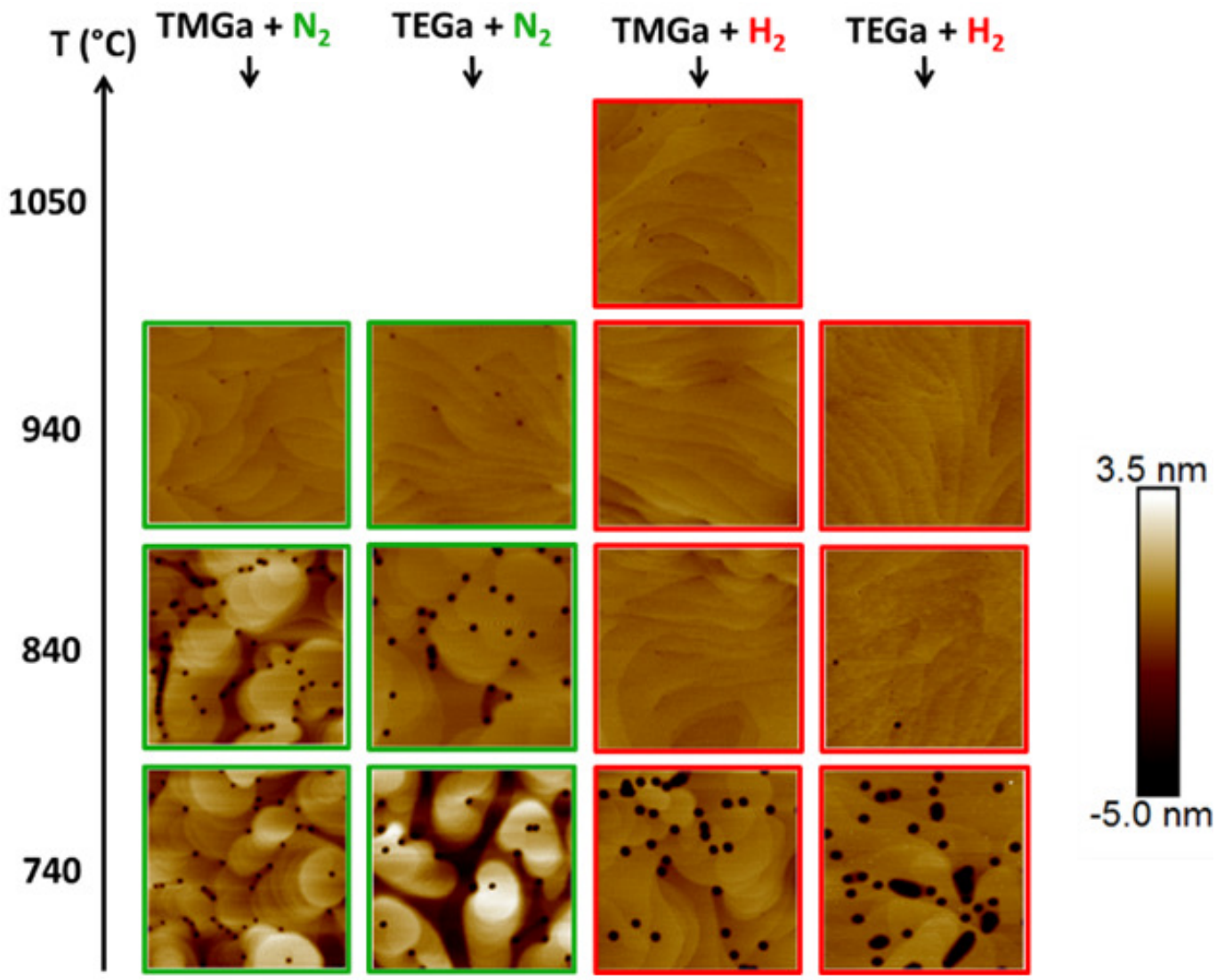

Fig. 3.9 – 1x1 μm^2 AFM images of GaN grown at various temperatures, using H_2 and N_2 as carrier gas and TMGa and TEGa as gallium precursors.

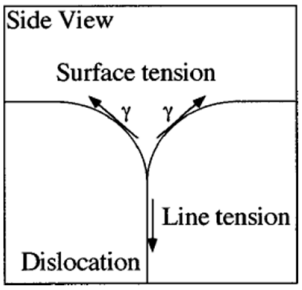

Fig. 3.10 – V-defect model by Franck [12].

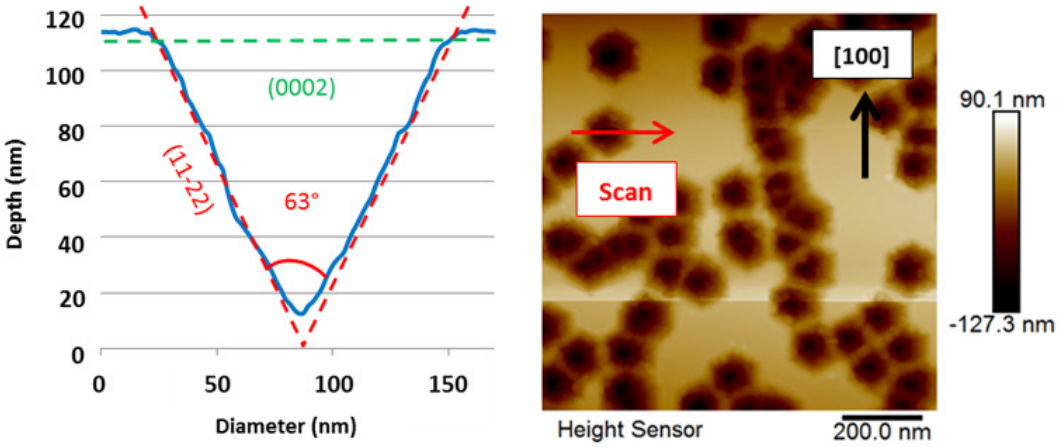

Fig. 3.11 – Left, the V-defect profile obtained by AFM measurements on a low temperature GaN layer. The blue line corresponds to the measured height, and the red and green lines are the expected angles of crystallographic planes. Right, a 1x1 μm^2 AFM image showing V-defects from which the profile on the left was extracted (red line).

$$E_D = A_{(0002)}.(2E_{(11-22)} - E_{(0002)}) \tag{3.3}$$

From this formula we can now describe two growth scenarios according to the relative energies of the two planes :

Case A : $2E_{(11-22)} - E_{(0002)} > 0$: there is a defect size at which the defect is in equilibrium, and the defect will not grow any larger with increasing thickness of the film. Effectively, the V-defect "floats" on the film.

Case B : $2E_{(11-22)} - E_{(0002)} < 0$: the defect will continue to grow larger as the film becomes thicker, without limit, and the bottom of the V-defect stays at the bottom of the layer. As the film becomes thicker, these defects would eventually join together to make the entire film rough.

The value of $2E_{(11-22)} - E_{(0002)}$ may be positive, negative or equal to zero due to elements affecting the surface energy of the planes during the growth. This surface energy comes from the atomic arrangement of the atoms in the plane which is a constant value, but also from the adsorbed species during the growth [14][17]. These adsorbed species clearly depend on the environment (N_2 or H_2 carrier gas for example) and they are also likely to be temperature dependent since they are related to a physical adsorption model.

Case A and B are described in figure 3.12.

Looking back at the experimental data, the graph in figure 3.5 suggests that for growth at 940°C, we are in Case A of our model, with the size of the defects defined by the energies of the planes. For the lower temperatures we are either below the critical thickness for Case A, or we are in Case B of our model. As the angle of the V-defect sides is defined by the plane $(11-22)$, it is logical that we have the same size defects when we are below the critical thickness for Case A. Equally, this explains why the size of the defects increases with the film thickness at 740°C and 840°C, while at 940°C the defect

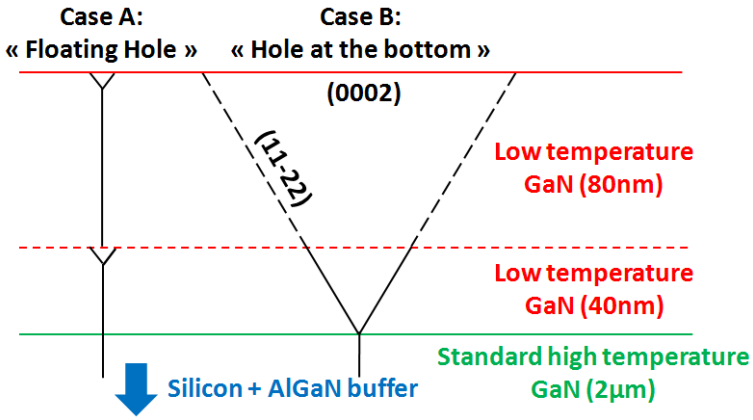

Fig. 3.12 – Schematic of the different growth scenarios, with a "floating" V-defect on the left.

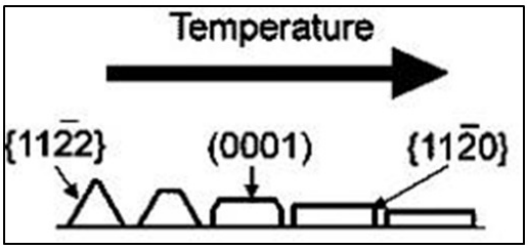

Fig. 3.13 – Epitaxial lateral overgrowth (ELOG) [5] and favored planes versus growth temperature

size is independent of the film thickness.

The experimental data from the study of MO precursors and carrier gas studies can also be interpreting using our model. We see that under H_2 we are already in Case A at 840°C, while under N_2 we may be in Case B. This implies that H_2 increases the relative energy of the planes (11-22) compared to the (0002) and encourages a flatter surface. We can see that changing the energy of the planes should not change the defect size at multiple temperatures, and so this explains our suggestion that the difference between TEGa and TMGa defect size is likely to be due to a difference in film thickness.

Our analysis is reinforced by results in the literature regarding conditions for Epitaxial Lateral Overgrowth (ELOG) of GaN [13]. In that article, increasing the temperature makes the (0002) plane more energetically favourable, while decreasing it favours inclined planes such as (11-22), which is the same conclusion as we have found in this work.

Summary of chapter 3

We explained the challenges of III-nitrides growth at low temperature especially for indium containing alloys, looking in particular at the problem of the presence of V-defects at the surface of such alloys. Thus we tried different growth parameters for the production of GaN layers below usual growth temperature of 1050°C under nitrogen carrier gas and using TMGa precusor which is our standard for indium containing alloys growth. The change of growth temperature ranging from 740°C to 940°C show the effect on the V-defect size which decreases above a certain critical temperature. Also increase the thickness increases the V-defect size but not at the highest temperature which means 940°C. In parallel, wwe saw that the growth rate did not influence the V-defect size or even surface morphology and 540nm/h was kept as reference in this study.
Next, we used hydrogen as the carrier gas and the critical temperature for the reduction in V-defect size was decreased by around 100°C. Effectively, under hydrogen, the V-defects size is similar to those under nitrogen but 100°C hotter. The change of MO precursors from TMGa to TEGa seemed to increase the V-defects diameter of a dozen of nm at lower temperature, we attribute to slight differences in the growth rates.
Next, we developed a model based on that of Frank in the 1950's, and we examined the role played by the surface energy of the inclined planes in the V-defects. We suggest that they are balancing the force resulting of the strain field around the dislocation line opening under the V-defect. Depending on the temperature and the atmosphere during the growth, the surface energy of inclined planes may change, resulting in two cases. Case A where the defect reaches its equilibrium size and "floats" on the surface, and case B where the defect continues to grow indefinitely. This model matches well with our experimental results and implies that hydrogen carrier gas stabilises the (0002) plane, reducing the critical temperature for avoiding large defects. Thus we show the positive impact of using hydrogen as a carrier gas for low temperature GaN layers.

Bibliographie

[1] N. Duxbury, U. Bangert, P. Dawson, E. J. Thrush, W. V. der Stricht, K. Jacobs et I. Moerman, « Indium segregation in ingan quantum-well structures », *Applied Physics Letters*, vol. 76, no. 12, p. 1600–1602, 2000. 86

[2] A. Sánchez, M. Gass, A. Papworth, P. Goodhew, P. Singh, P. Ruterana, H. Cho, R. Choi et H. Lee, « V-defects and dislocations in ingan/gan heterostructures », *Thin Solid Films*, vol. 479, no. 1, p. 316 – 320, 2005. 86, 87

[3] Y. Chen, T. Takeuchi, H. Amano, I. Akasaki, N. Yamada, Y. Kaneko et S. Y. Wang, « Pit formation in gainn quantum wells », *Applied Physics Letters*, vol. 72, no. 6, p. 710–712, 1998. 86

[4] X. H. Wu, C. R. Elsass, A. Abare, M. Mack, S. Keller, P. M. Petroff, S. P. DenBaars, J. S. Speck et S. J. Rosner, « Structural origin of v-defects and correlation with localized excitonic centers in ingan/gan multiple quantum wells », *Applied Physics Letters*, vol. 72, no. 6, p. 692–694, 1998. 86

[5] P. H. Weidlich, M. Schnedler, V. Portz, H. Eisele, R. E. Dunin-Borkowski et P. Ebert, « Meandering of overgrown v-shaped defects in epitaxial gan layers », *Applied Physics Letters*, vol. 105, no. 1, p. 012105, 2014. xiv, 86, 96

[6] H. Liang, Y. Saripalli, P. K. Kandaswamy, E. P. Carlson, P. Favia, O. Richard, H. Bender, M. Zhao, S. B. Thapa et E. Vancoille, « Growth techniques to reduce v-defect density in gan and algan layers grown on 200 mm si (111) substrate », *Physica Status Solidi*, vol. 11, p. 533–536, 2014. 86

[7] N. Sharma, P. Thomas, D. Tricker et C. Humphreys, « Chemical mapping and formation of v-defects in ingan multiple quantum wells », *Applied Physics Letters*, vol. 77, no. 9, p. 1274–1276, 2000. 86, 87

[8] H.-L. Tsai, T.-Y. Wang, J.-R. Yang, C.-C. Chuo, J.-T. Hsu, Z.-C. Feng et M. Shiojiri, « Observation of v defects in multiple ingan/gan quantum well layers », *MATERIALS TRANSACTIONS*, vol. 48, no. 5, p. 894–898, 2007. 86

[9] P. H. Weidlich, M. Schnedler, H. Eisele, U. Strauss, R. E. Dunin-Borkowski et P. Ebert, « Evidence of deep traps in overgrown v-shaped defects in epitaxial gan layers », *Applied Physics Letters*, vol. 103, no. 6, p. 062101, 2013. 86

[10] W. T. C., C. S. J., L. C. T., L. W. C. et S. J. K. *IEEE Trans Electron Devices*, vol. 51, p. 1743, 2004. 86

[11] F. C. Frank, « Capillary equilibria of dislocated crystals », *Acta Crystallographica*, vol. 4, p. 497–501, 1951. 86, 93

[12] B. Heying, E. J. Tarsa, C. R. Elsass, P. Fini, S. P. DenBaars et J. S. Speck, « Dislocation mediated surface morphology of gan », *Journal of Applied Physics*, vol. 85, no. 9, p. 6470–6476, 1999. xiv, 86, 90, 94

[13] B. BEAUMONT, P. VENNÉGUÈS et P. GIBART, « Epitaxial lateral overgrowth of gan », *Physica Status Solidi*, vol. 221, p. 1–43, 2001. 86, 96

[14] K. HIRAMATSU, K. NISHIYAMA, A. MOTOGAITO, H. MIYAKE, Y. IYECHIKA et T. MAEDA, « Recent progress in selective area growth and epitaxial lateral overgrowth of iii-nitrides : Effects of reactor pressure in movpe growth », *Physica Status Solidi*, vol. 176, p. 533–545, 1999. 86, 95

[15] N. A. KAUFMANN, L. LAHOURCADE, B. HOURAHINE, D. MARTIN et N. GRANDJEAN, « Critical impact of ehrlich–schwöbel barrier on gan surface morphology during homoepitaxial growth », *Journal of Crystal Growth*, vol. 433, p. 36 – 42, 2016. 93

[16] M. LEVY et M. REGNIER, « Mesure des energies de surface », *Journal de Physique Colloques*, vol. 31, p. 159–173, 1970. 93

[17] V. BESSOLOV, E. KONENKOVA, S. KUKUSHKIN, A. OSIPOV et S. RODIN, « Semipolar gallium nitride on silicon : Technology and properties », *Rev.Adv. Mater.*, p. 75–93, 2014. 95

4 | InAlN and InGaAlN : a study of indium incorporation and gallium contamination.

Sommaire

4.1 Indium content determination : issues of XPS, WDXRF, and XRD 102

4.2 InGaAlN growth by MOCVD : process conditions, characterizations, and indium incorporation 104

4.2.1 InGaAlN growth under nitrogen carrier gas 105

4.2.2 InGaAlN growth under hydrogen carrier gas 121

4.3 Growth of InAlN layers without gallium pollution 124

Bibliographie 129

Chapter 4 is dedicated to the study of InGaAlN and InAlN layers whose general properties and benefits are detailed in chapter 1. As a replacement for AlGaN barrier layers in high electron mobility transistors (HEMTs), InAlN and InGaAlN layers are gaining interest due to lattice matching on GaN while containing 18% indium [1] and the benefit of a stronger spontaneous polarization [2]. This results in higher sheet carrier density, and therefore lower electrical resistance in the 2-dimensional electron gas (2DEG) [2]. Thus in the fabrication of InAlN ternary and InGaAlN quaternary alloys by metal organic vapor phase epitaxy (MOVPE), the accurate control of the indium content in the material has a strong impact on its physical and electrical properties.

InAlN and especially InGaAlN alloys represent the main bulk of the experiments in this thesis. Thus here we will focus on reviewing the different series of samples we produced changing each time one growth parameter. Then we will have an overall point of view to examine the influence of each of them on topology, alloy stoichiometry, crystal and luminescence properties, amongst other data. We will each time complete our descriptive analysis with physical notions and mechanisms to explain the observed trends. The discussion on certain phenomena like indium rich and poor phases separation, gallium pollution and the summary of electrical results will be treated in next chapter.

4.1 | Indium content determination : issues of XPS, WDXRF, and XRD

The principal chemical characterization of the InGaAlN layers was X-ray Photoelectron Spectroscopy (XPS) which is a direct chemical characterization making it a good technique for measuring InGaAlN layers. This direct characterization simplifies interpretation compared to X-ray diffraction (XRD) or photoluminescence (PL) in which the determination of the composition requires indirect calculations, made complicated by the quaternary alloy formed with the gallium pollution we are suffering as described in next chapter. We have also used Auger spectroscopy (AES) which gives us better spacial resolution, but does not have the capability of giving a depth profile.

XPS characterization is an accurate and relatively fast characterization giving a result in three hours (depending on the quality of your XPS spectrum) but requiring a cleavage of the wafer to get small samples. Along with argon sputtering to get the composition profile, this makes XPS a destructive technique, which is not compatible with on-line testing of wafers for a future device fabrication. So we also tested Wavelength Dispersive X-ray Fluorescence (WDXRF), a technique available in our clean room in order to : have a quick chemical measurement (few minutes) giving us the alloy composition in several points on the wafer, without breaking it. This would allow the wafer to undergo a chain of characterization such as AFM, XRR, XRD and PL essential to its control and study but allowing us to continue the manufacture of devices like diodes, HEMTs, LEDs, LDs, etc. However WDXRF penetrates a long way into the sample, and so because we are growing these layers on top of GaN layers, we cannot measure the gallium content in the InAlGaN layers with this technique. To have an idea of the penetration depth, we measured a sample made of a $1.5\mu m$ thick GaN pseudo-substrate without an InGaAlN layer and we detected the aluminum of the AlGaN layer in the buffer below. We tried also with a GaN layer thickness of $2\mu m$ and in this case, the signal of aluminum was extremely low, only two times the amplitude of the noise measurement. This suggests that we should be able to

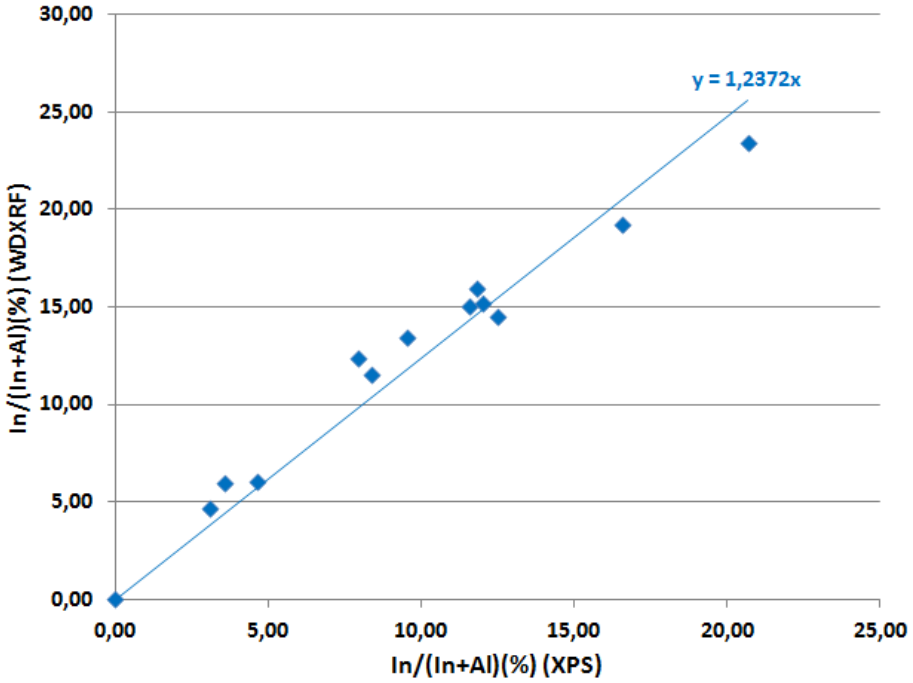

Fig. 4.1 – $In/(In + Al)$ ratio measured by WDXRF versus XPS for thirteen InGaAlN samples.

accurately measure the $In/(In + Al)$ ratio using this technique as long as the GaN layer is over $2\mu m$ thick, as was the case for this study.

We used WDXRF on thirteen InGaAlN samples grown under nitrogen and hydrogen carrier gas. In the first instance, the objective was to correlate the WDXRF results with the XPS, to compare the $In/(In + Al)$ ratio, as we cannot use this to get any information on the gallium content by WDXRF. The correlation graph is shown in figure 4.1.

This graph presents two good points : it is linear and the line passes through zero. The linear dependence with y = 1.23x indicates that WDXRF and XPS methods are compatible, but we require a common calibration to get directly comparable results. The fact that the correlation line passes through zero reassures us that we are not detecting the aluminium in the buffer, and that we don't have any other anomolies.

We can conclude that the use of WDXRF is difficult on GaN pseudosubstrates, unless we are sure that there is no gallium in the layer (or a very low percentage). However, as we will discuss later, this could potentially be combined as an in-line measurement with XRD to give a full characterization of InGaAlN layers.

At the beginning of our work we produced samples with different thickness ranging from 7nm to 200nm. Although 200nm is very thick compared to barrier layers of HEMT devices or LED requirements, we processed these thick layers to look for a signal using XRD $\omega - 2\theta$ measurements (cf. figure 4.2). For characterization of InAlN layers, X-ray diffraction is commonly used to determine their composition [3]. Below 200nm we never had any signal by this characterization, and we can see the problem in the figure 4.2. Growth on silicon requires AlGaN buffer layers which have broad peaks in (0002) XRD profiles.

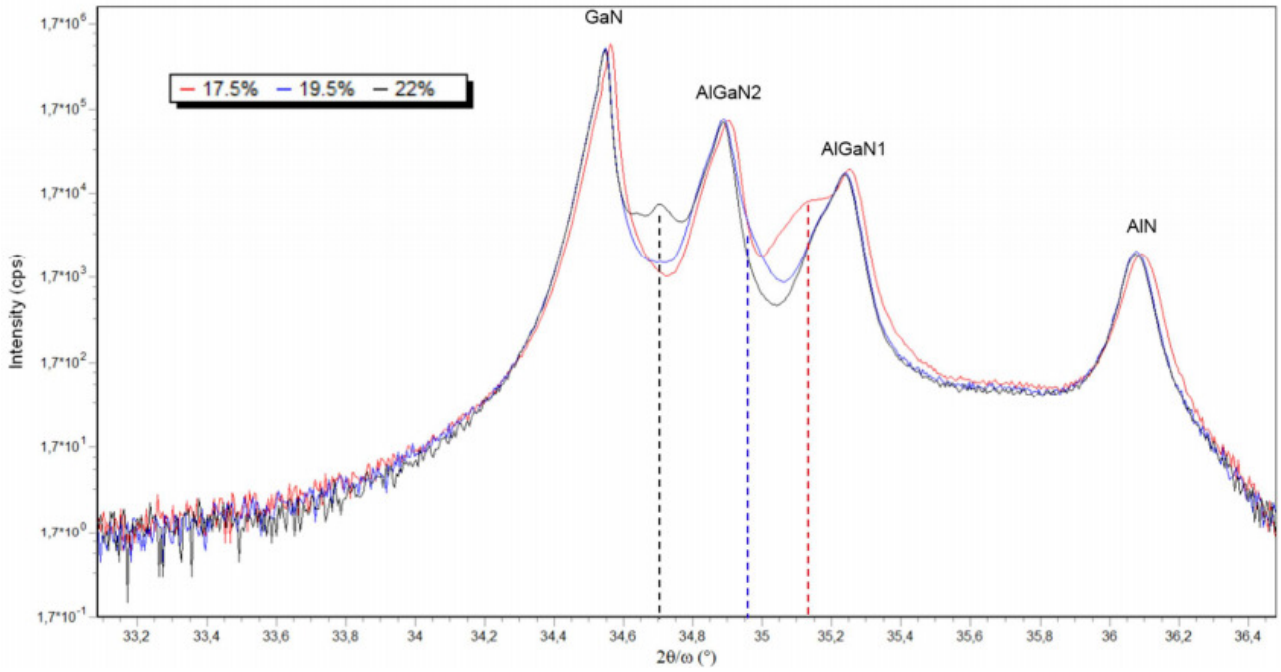

Fig. 4.2 – XRD measurement on 3 different InGaAlN samples 200nm thick. InGaAlN peak positions are given by dotted lines, with indium composition in insert estimated from Bragg's law assuming relaxed layers with no gallium pollution.

These can hide other peaks which have similar peak diffraction angles such as those corresponding to InGaAlN layers, which have a low intensity, especially for layers of only 10s of nm thick. Even for 200nm thick layers, certain composition layers are hidden by these layer peaks. We have kept the first indium content estimation on the $In/(In + Al)$ ratio, because this technique can only find the composition of relaxed InAlN layers, and when we performed these experiments, we were not aware that gallium was incorporated in the layers because of reactor pollution (cf. chapter 5 section 5.2).

As mentioned above, in order to avoid cleaving the wafers, we could combine the results of the reciprocal space map (RSM) measurements with the WDXRF ones to get the composition of our InGaAlN. RSM measurements, as shown in section 4.2.1.2 allow us to find the average in-plane (a) and out-plane (c) lattice parameters of our layer. As WDXRF gives us the In/(In+Al) ratio, we have 3 independent data points for 3 independent unknown elements (x, y and strain for $In_xGa_yAl_{1-x-y}N$ layers), and thus a solvable system. Although this is technically possible, we were not able to find coherent results using this technique, which may be due to the low quality RSM maps which were obtained.
In summary, the physical and chemical characterisation of quaternary nitride layers was extremely difficult, and the only reliable and simple technique available was XPS, which is why this was principally used in the study.

4.2 | InGaAlN growth by MOCVD : process conditions, characterizations, and indium incorporation

The study of InGaAlN alloys will start with the use of nitrogen carrier gas N_2, and then the use of hydrogen H_2. It is important to keep in mind that these layers contain Ga pollution. The gallium

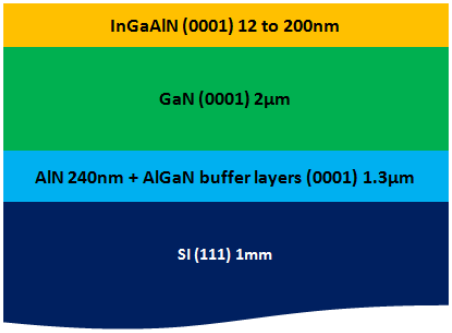

Fig. 4.3 – Structure of the studied stack of layers : orientation and thickness

present in the layers is not wanted but still allowed us to characterize the layers and study the indium integration. In all cases we are particularly interested in the $In/(In + Al)$ ratio in order to have lattice matched layers on GaN. If we want to examine the polarization in the layers or the bandgap for photoluminescence, we will need to take the gallium concentration into account.

Below the InGaAlN or InAlN layer, the nitride structures used for this study have a simple buffer layer using an AlN nucleation layer on nominally on-axis silicon (111) substrates, followed by AlGaN layers to control the strain in the GaN, followed by a 2 μm thick bulk layer of GaN grown at a temperature of 1035°C, and finally the InGaAlN layer (cf. figure 4.3). The precursors were tri-methyl indium (TMI), tri-methyl gallium (TMGa), tri-methyl aluminum (TMAl) and ammonia for indium, gallium, aluminum and nitrogen respectively.

4.2.1 | InGaAlN growth under nitrogen carrier gas

In the study of the growth of InAlN and InGaAlN alloys, the use of N_2 as carrier gas was the first choice, since it inhibits indium desorption from the growing layers. This desorption is a common problem with H_2 growth, as InN is a lot more volatile than GaN or AlN. We grew layers changing the thickness, the growth temperature, the growth rate, the ammonia flow, and the TMIn/TMAl ratio as summarized in table 1. We kept a V/III ratio between 9000 and 18000 depending of the growth rate or TMIn flow, and the pressure was at 100 mbar unless otherwise stated.

4.2.1.1 Effect of layer thickness

In a first study we analyzed the effect of the growth time and thus the thickness of InGaAlN layers on morphology. We start with a layer of 15nm which correspond roughly to the thickness of a barrier layer in a HEMT structure. 30nm is more appropriate to the cumulated topology of several layers measuring few nm in a multi-quantum well structure. Compared to these, 100nm and 200nm thick layers are used in some applications such as back barriers in HEMT devices.

If we examine the surface morphology of the 1x1μm^2 AFM pictures, in figure 4.4 it starts at 15nm with the formation of a step structure surrounding different holes attributed to mixed and edge dislocations (according to our study on low temperature GaN and hole density, cf. chapter 3). It is quite similar to the spiral hillocks that we find usually at the surface of MBE (molecular beam epitaxy) grown layers.

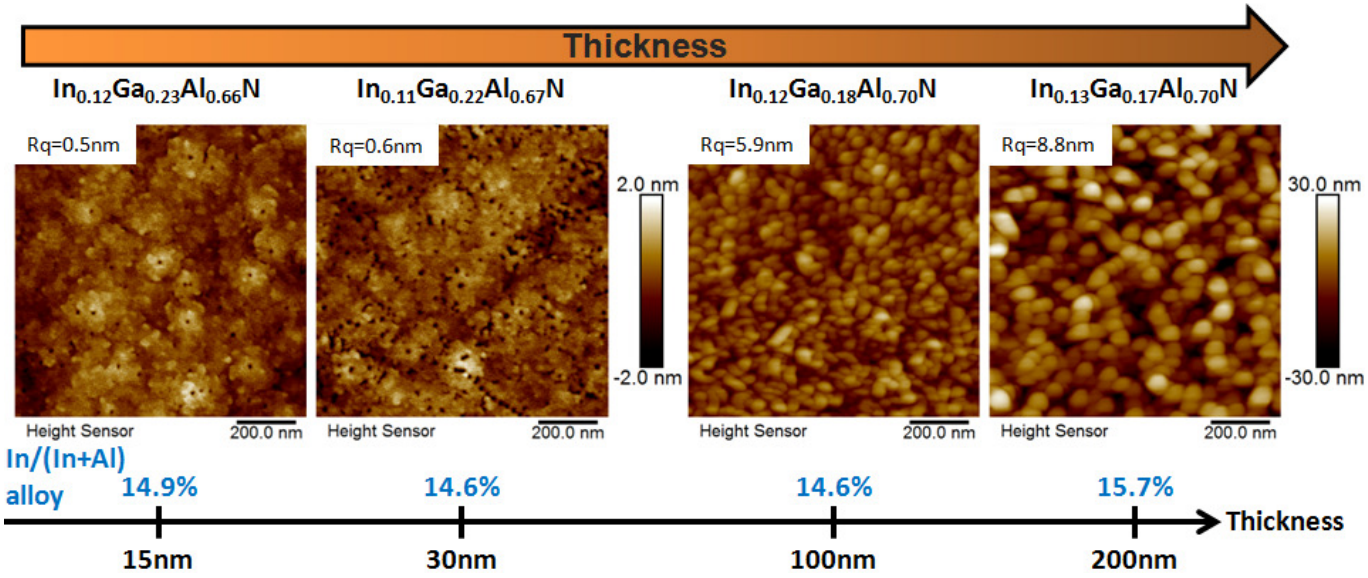

Fig. 4.4 – Effect of thickness on topology on 1x1μm^2 AFM pictures, and alloy composition by XPS. T=730°C, Vg=3nm/min, TMIn/(TMIn + TMAl) : 41% in the gas phase, carrier gas : N_2.

At 30nm the steps spiral diameter is enough large to merge with the closest neighbors. The surface appears more flat and new holes are formed by this merging process. Finally at 100 and 200nm we see a strong roughening of the surface, and we should note that there is a change of z-scale between the left and right hand sides of the figure. A grain structure is visible and these grains get bigger with the increase of the thickness. HRTEM cross-section images on similar layers having this grain structure, for 30nm thickness show that the grain height is less than that of the overall InGaAlN layer, and so the layer is continuous. Although the roughness increases, it does so at the same rate as the thickness, so this is not necessarily very surprising.

Another interesting trend was shown in the photoluminescence measurements we did on these four wafers. For the samples in figure 4.4, two peaks are visible for each measurement. The peak corresponding the GaN luminescence is on the right with a wavelength of 365nm corresponding to the 3.4eV band gap. We note that it is saturated in intensity for the two thinnest layers but not for the thickest. This is coherent since the PL laser is absorbed gradually by the top layers of the material depending on its absorption coefficient at 266nm (4.66eV). Thus the thicker the barrier layer, the less the GaN is excited. The second peaks, to the left in the figures is the luminescence peak attributed to InGaAlN barrier layer. These peaks shows a shift of the maximum intensity towards higher wavelengths as the thickness is increased, from 318nm to 341nm. This is shown schematically in figure 4.5.

The observed shift should not appear in that direction according to the XPS composition. We calculated the theoretical band gap energy of each sample knowing that we used a linear relation between the composition and each binary band gap energy. The reason is that XPS shows very similar compositions, and so we do not expect a wavelength shift. Values of both composition and theoretical band gaps and wavelengths are shown in table 4.1. Here the band gap energy appears higher than the experimental one measured by PL. They are to visible reasons. First our XPS potentially suffer of a little lack of calibration even if the uncertainty is close to 4% as shown in future sections. Secondly a part of

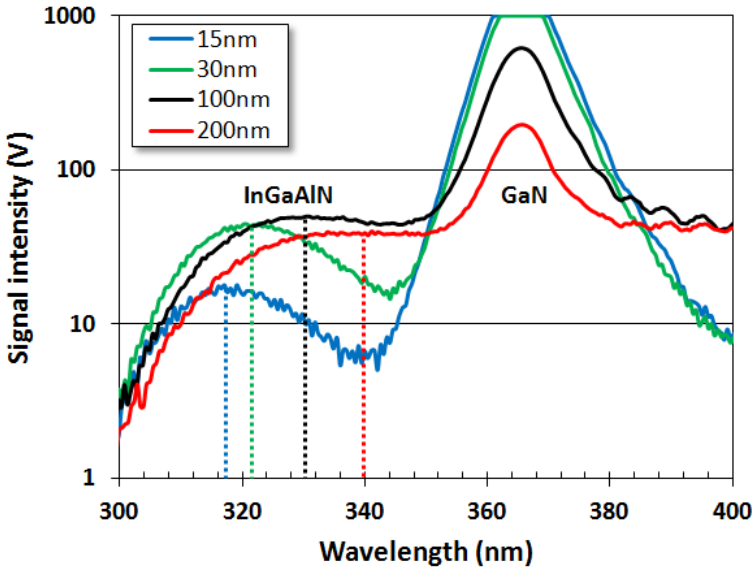

Fig. 4.5 – PL measurements on 15nm, 30nm, 100nm, and 200nm thick InGaAlN samples grown under N_2 and with the same conditions. The dashed lines show the maximum intensity and thus the luminescence wavelength of each sample.

Sample	**Thickness (nm)**	**%In**	**%Ga**	**%Al**	**In/(In+Al) (%)**	**PL**	**Band gap (eV)**	**λ (nm)**
1	15	11.5	23	65.5	14.9	320	4.93	251
2	30	11.4	22	66.6	14.6	322	4.97	250
3	100	12	18	70	14.6	328	5.05	246
4	200	13	17	70	15.7	334	5.02	247

Tab. 4.1 – Summary of XPS compositions, barrier layer PL peak positions and theoretical linear band gaps and wavelenghts of four samples having different thicknesses : 15nm, 30nm, 100nm, and 200nm.

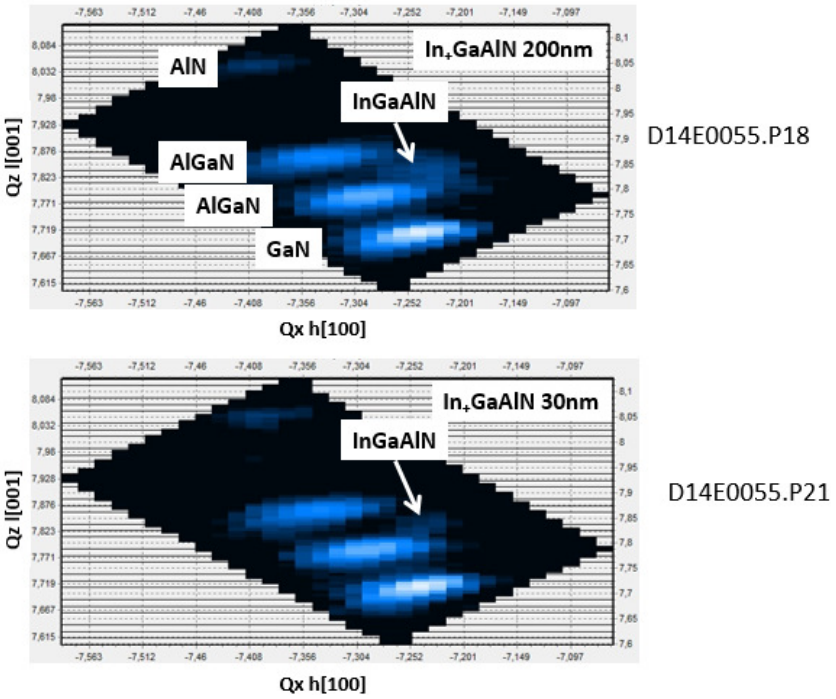

Fig. 4.6 – RSM measurements of 30nm and 200nm thick InGaAlN barrier layers.

this difference is due to irxch and poor indium phases separation we are trying to highlight in this section.

RSM measurements are shown in figure 4.6 on 30nm and 200nm thick samples, which, as for the XPS, suggest that the composition is the same for both samples. The center of the blue spot corresponding to the InGaAlN layer is at the sample position on both RSM pictures, which means that if they are both relaxed, they have the same composition.

We suggest that the reason for this shift in emission wavelength with no change in average composition is likely to be due to phase separation between rich and poor indium phases. We can suggest qualitatively that while the rich indium phases increase in density or size with the growth time [4], they can progressively play the role of quantum wells or simply areas having a lower band gap than the remainder of the InGaAlN layer. Therefore the recombination of electron-hole pairs occurs preferentially in these areas causing a decrease of measured InGaAlN band gap.

We show the relationshiop between the luminescence wavelength and associated band gap energy, versus the thickness of these four samples which is proportional to the growth time (cf. figure 4.7). The trend is linear in this thickness range and the y-intercept of the graph in both wavelength and band gap energy could give us a boundary limit which would correspond to the luminescence of a material without phase separation under these conditions. If we assume that this is a sample without phase separation, this value can be used to have an access to the bowing parameter using the XPS composition unless the stress in the layer is too high.

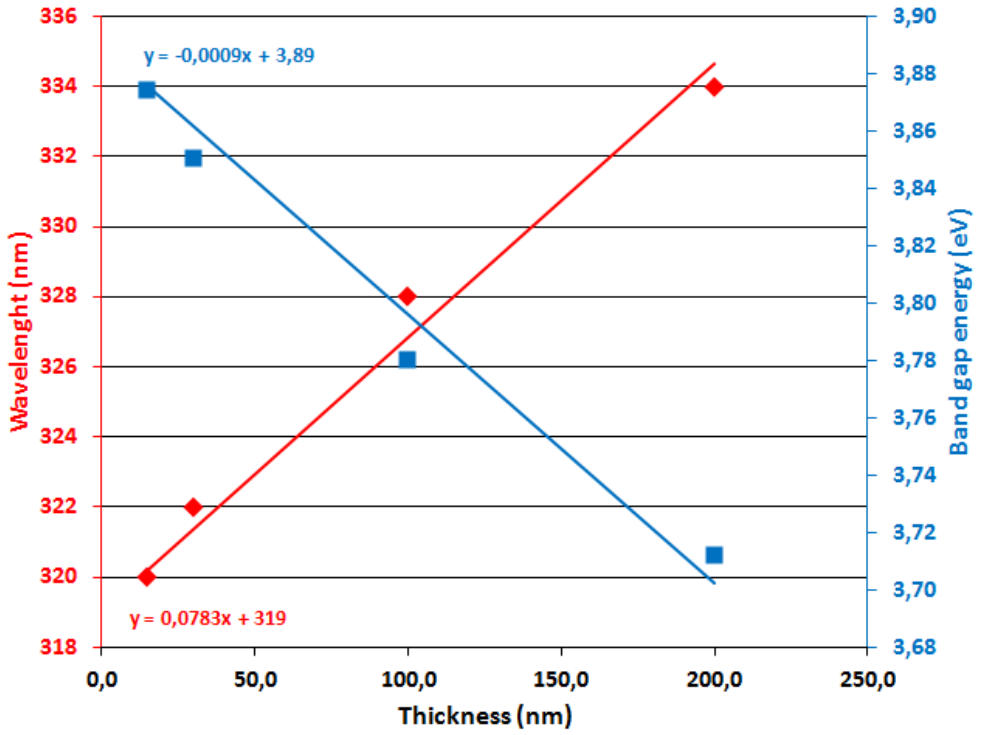

Fig. 4.7 – Luminescence wavelength and band gap energy versus layer thickness of InGaAlN layers grown under same conditions.

4.2.1.2 Effect of TMIn flow and TMIn/TMAl ratio

Next, we examined the effect of changing the TMIn flow and keeping the TMAl flow constant on the morphology and the indium composition in the InGaAlN layers. Figure 4.8 shows the AFM scans with the indium composition in the gas phase and in the alloy shown below.

According to AFM and XPS measurements we see that if we increase the TMIn flow at a constant TMAl flow we increase the indium incorporated in the alloy, as expected, increasing the incorporated indium from 14.5% to 23.4%. There is also a direct effect on the morphology, with increasing indium increasing the diameter of grains in the surface structure. Keeping the phase separation hypothesis of section 4.2.1.1 in mind, we can imagine that the more we try to incorporate indium in the layer, the more it will be segregated, which could then increase the size of indium rich areas which could be those grains.

We measured the PL spectra of these three samples as shown in figure 4.9. While the indium content increases the peak corresponding to InGaAlN is shifted to low energy and it ends up being masked by the peak of GaN. The energy value of the sample having the most In content is roughly evaluated from the beginning of the shoulder on the right of the GaN signal. We have verified these luminescence measurements with cathodoluminescence (CL).

In CL, the electron-hole pair generation is due to an injection of electrons on a small area at the surface of the material, rather than by laser excitation in PL. We used the lowest acceleration voltage (3keV) available to probe the material with a penetration depth of close to 60nm. This means that the GaN signal will not appear on the spectra in the case of InGaAlN samples having more than 60nm of

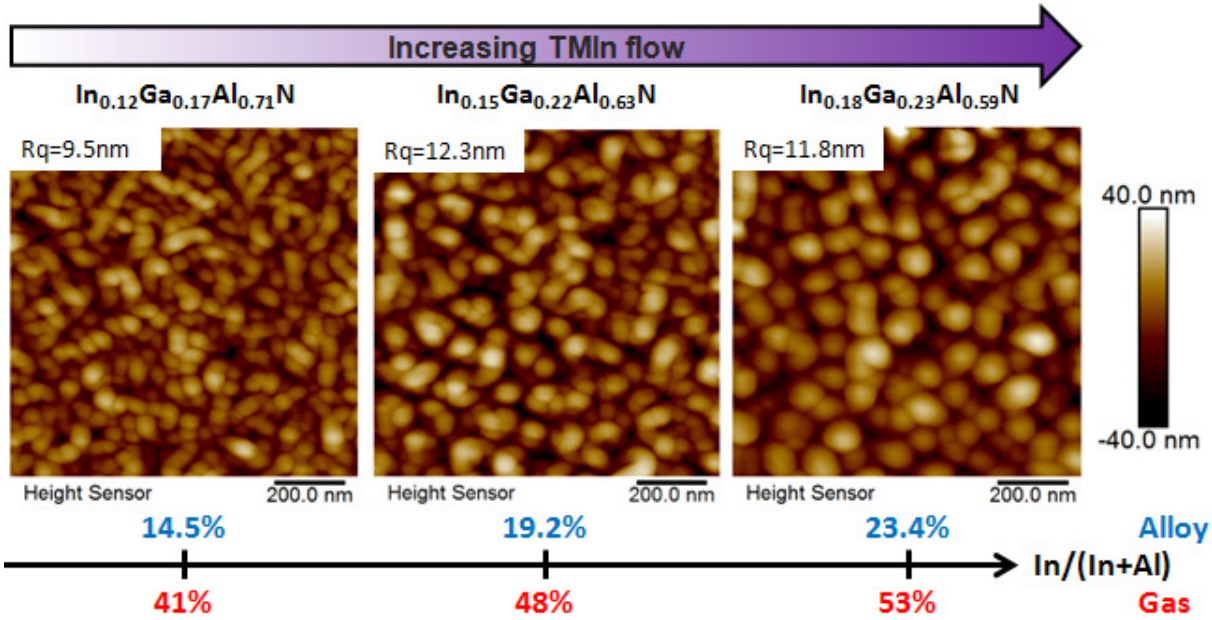

Fig. 4.8 – Effect of TMIn flow at fixed TMAl flow : on topology on 1x1μm^2 AFM pictures, and gas-alloy composition by XPS. Thickness=200nm, T=730°C, Vg=3nm/min, carrier gas : N_2.

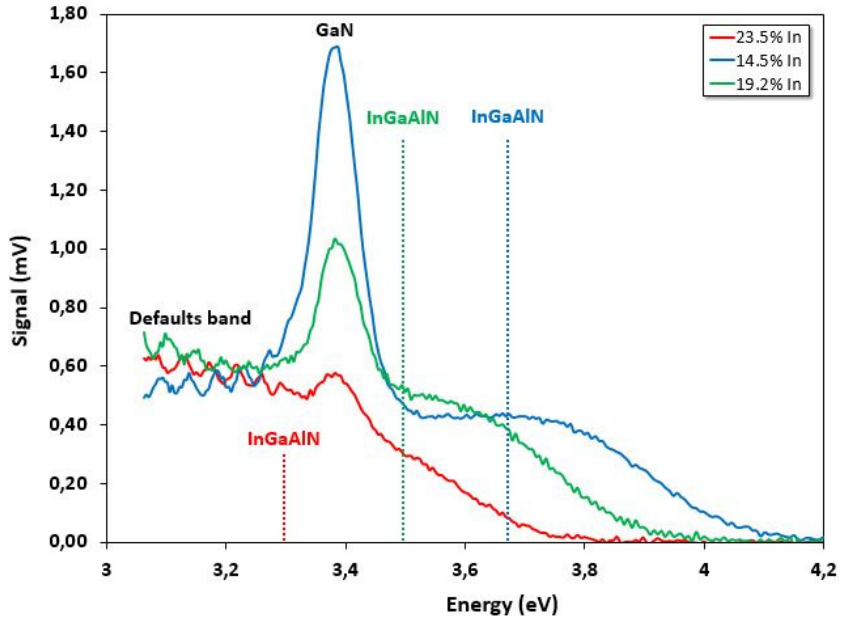

Fig. 4.9 – PL spectra of three 200nm thick samples having a In/(In+Al) ratio of 14.5%, 19.2%, and 23.4%.

Sample	Thickness (nm)	Temperature (°C)	Vg (nm/min)	PL(eV)	CL (eV)	
1	200	733	3.3	3.7	3.6	-
2	200	733	3.3	3.3	3.1	-

Tab. 4.2 – Summary of experiments showing the comparison between different barrier layers peak positions in photo and catodoluminescence spectra. TMIn flow study

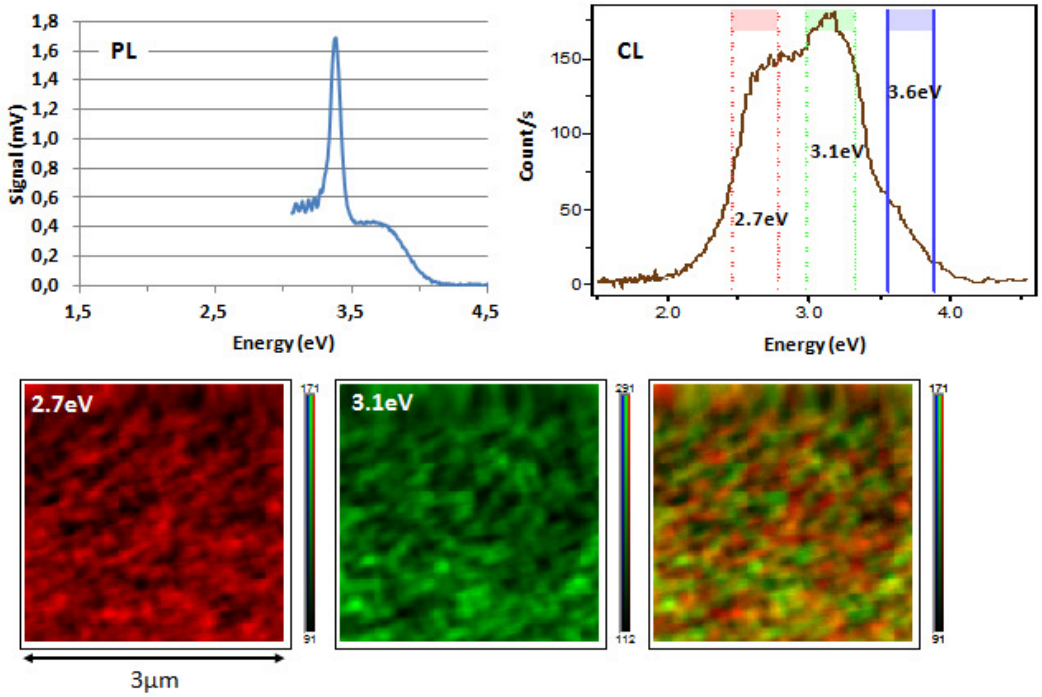

Fig. 4.10 – Spectra of sample 1 : comparison of PL and CL. 3x3μm^2 pictures showing with luminescence at different energy. TMIn flow study

layer, which is the case for the current samples which are 200nm thick. In table 4.2 is a summary of the two samples we measured using CL and the comparison with PL. In sample 1 and 2 (cf. figure 4.10 and 4.11), a slight shoulder is visible on the right of the central peak at respectively at 3.6ev and 3.1eV. They should correspond to InGaAlN layers. Sample 2 containing more indium than sample 1, the results are coherent and pretty close to those got by photoluminescence even if just below in terms of energy measured. Also, we can identify one peak near 3.1eV and 2.7eV which could be that of InGaAlN defects respectively in sample 1 and 2. Indeed, a defects band at lower energy than GaN one, is generally observed when we perform PL or CL measurements on GaN samples. We expect that it could be the same case in other kind of III-N layers like InGaAlN. On its left, a new peak at 2.7eV in sample 1 and 2.3eV in sample 2, is visible and could also correspond to a specific type of defects.

We performed XRD measurements in reciprocal space (RSM) on the three 200nm thick barrier layers mentioned above (cf. figure 4.12). We see that the InAlGaN peak changes position as the indium concentration increases. In the first image, the layer is lattice matched to the GaN pseudosubstrate, as the peak is vertically aligned to the GaN peak, meaning that they have the same a-parameter.

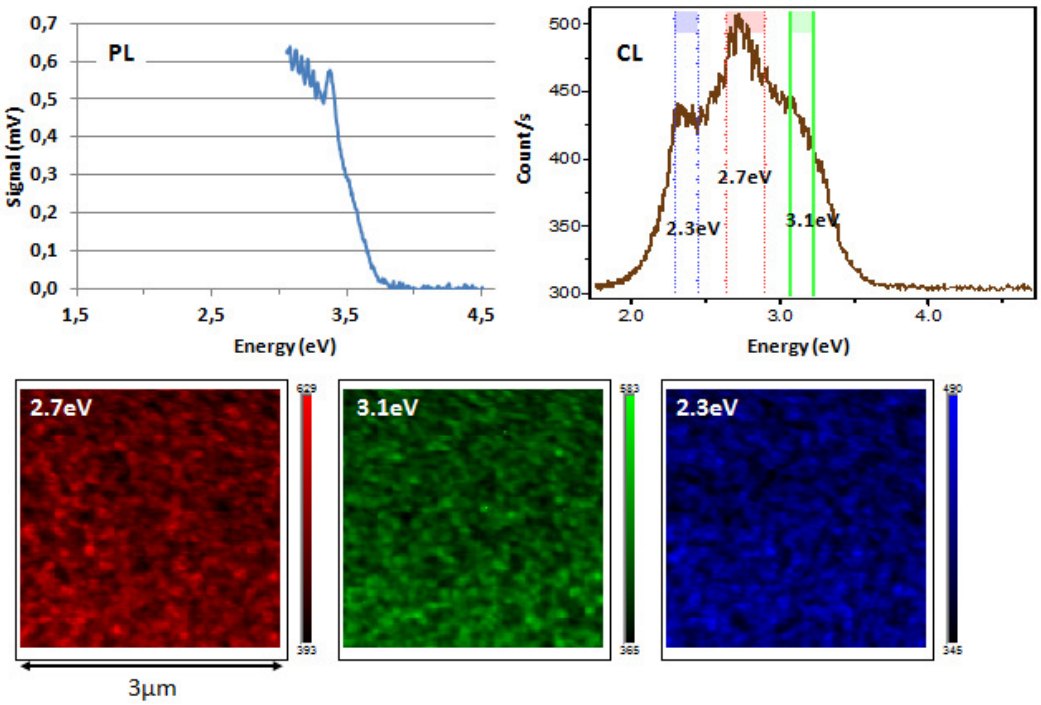

Fig. 4.11 – Spectra of sample 2 : comparison of PL and CL. 3x3μm^2 pictures showing luminescence at different energy. TMIn flow study.

As the indium concentration increases, the peak moves to the bottom right. This is to be expected, because as explained above, this means that the a and c lattice parameters are increasing. The InGaAlN layer which has the same a lattice parameter as GaN should have an In/(In+Al) ratio close to 18%. By XPS evaluation we find a lower value than this : 14.5%. Thus we can expect that we have an uncertainty of $(18 - 14.5)/18 = 19.4\%$ on the In/(In+Al) ratio measured by XPS. We will see further that according to RBS measurements which are very accurate (+/-0.5% on this ratio evaluation) that we are actually very close using XPS measurements. It may be that the layer is strained, or that the two peaks are not exactly aligned, as these RSM measurements do not have very high resolution.

We applied the calculation expressed in chapter 2 to estimate both a and c lattice parameters from each RSM measurements of the InGaAlN layer on thick GaN (cf table 4.3). The lattice parameters are evolving in the expected direction when we increase the indium content for samples shown in figure 4.12. As InN has a larger lattice parameter than AlN or GaN, a and c of our InGaAlN layer are increasing too. This implies a material under a little compression as an average along the barrier layer. These increased lattice parameters are also in good agreement with the XPS measurements as the two last samples show an increased In/(In+Al) ratio in the solid : respectively 19.2% and 23.4%.

4.2.1.3 Effect of growth temperature

In figure 4.13, we can see the effect of the temperature on the In(Ga)AlN layers. Indium is known to be volatile compared to aluminum and gallium and therefore likely to be sensitive to temperature. When we increased the temperature by 80°C we lost nearly half of the initial indium content, dropping from 15% In at 730°C to 6% In at 810°C. Layers are 30nm thick which explains the big difference

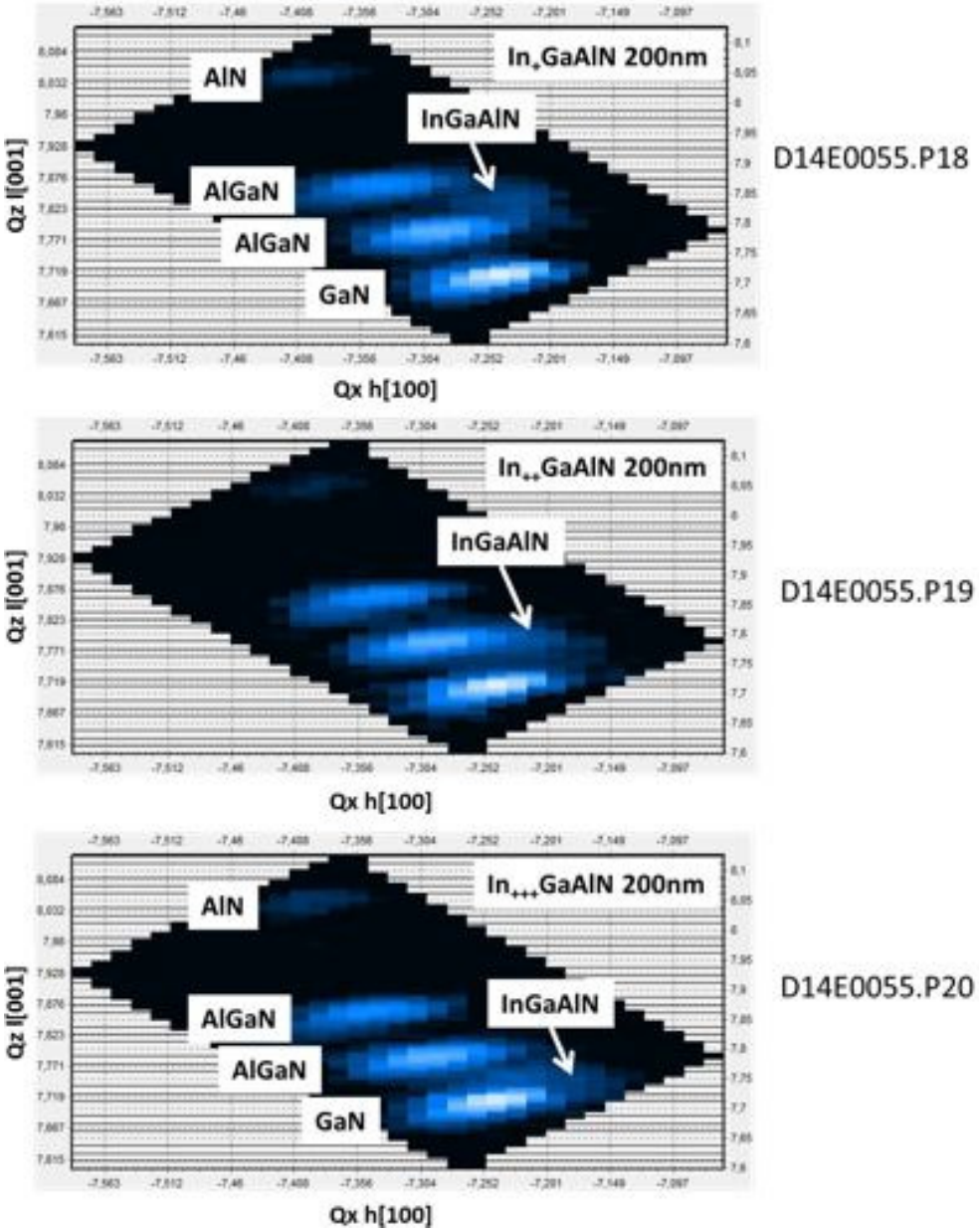

Fig. 4.12 – RSM measurements on InGaAlN barrier layers with increasing indium content from top to bottom.

Sample	**Thikness (nm)**	**a (Å)**	**c (Å)**
$In_{+}GaAlN$	30	3.19	5.10
$In_{+}GaAlN$	200	3.19	5.10
$In_{++}GaAlN$	200	3.20	5.14
$In_{+++}GaAlN$	200	3.21	5.16

Tab. 4.3 – Summary of a and c lattice parameters calculated using RSM measurements, the strain associated with the in-plane lattice parameter a, and the composition calculated from the equation described in the text.

Sample	**Thickness (nm)**	**Temperature (°C)**	**Vg (nm/min)**	**PL(eV)**
1	30	735	3	3.9
2	30	811	3	No signal
3	12	729	6	GaN shoulder

Tab. 4.4 – Summary of experiments showing the comparison between different barrier layers peak positions in photo and catodoluminescence spectra.Temperature study.

in morphology compared to the AFM scans in figure 4.8. Note that for the lowest indium content the lattice mismatch between InGaAlN and GaN is increased and the layer becomes under tension, resulting in the appearance of cracks. We can notice that the more the indium content decreases (according to the XPS measurements), the more the islands formed around the holes at the surface are getting bigger. This is a result which is coherent and that is what we usually see on AlGaN layers as the highest temperature layers begin to resemble AlGaN layers.

These three samples give also interesting results by PL measurements. As shown in figure 4.14, the peak corresponding to the InGaAlN layer is shifting toward high band gap energies and thus low indium content when the temperature is increased which confirm the trend observed by XPS measurements. The peak corresponding to the alloy having the lowest indium content did not appear during the measurement and we suggest that it has an energy that is either out of the detection window at an energy higher than 4,5eV, or has too high a band gap to be excited by the laser.

We also analyzed the behavior of 12nm thick layers, which is our standard for HEMT fabrication, with the temperature below 730°C. We kept all the other growth parameters of samples shown in figure 4.13, and the results are shown in figure 4.15. First, the indium content seems to be constant below a certain temperature below 730°C. We will see that it is not the case under hydrogen carrier gas in

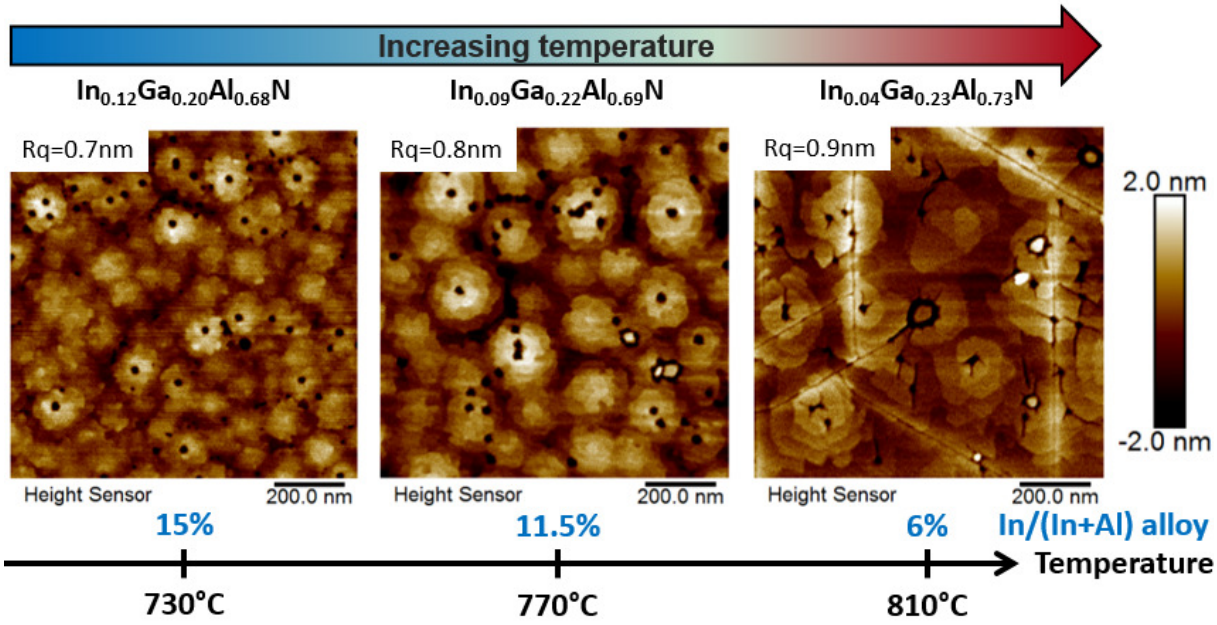

Fig. 4.13 – Effect of growth temperature : 1x1μm^2 AFM images, and alloy composition by XPS. Thickness=30nm, gas mixture : 41% of indium precursors in the gas phase, Vg=3nm/min, carrier gas : N_2.

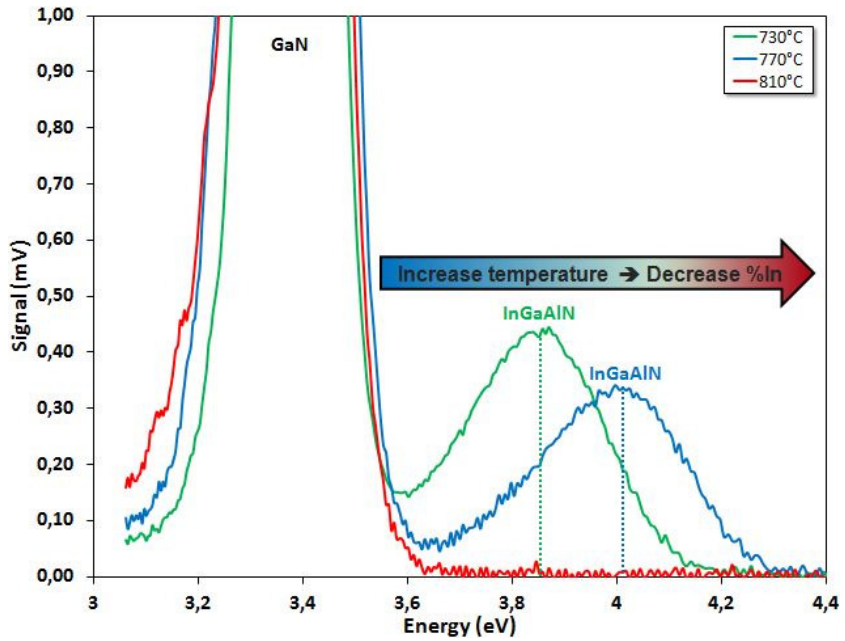

Fig. 4.14 – PL spectra of three 30nm thick samples having a, In/(In+Al) ratio of 6%, 12%, and 15%.

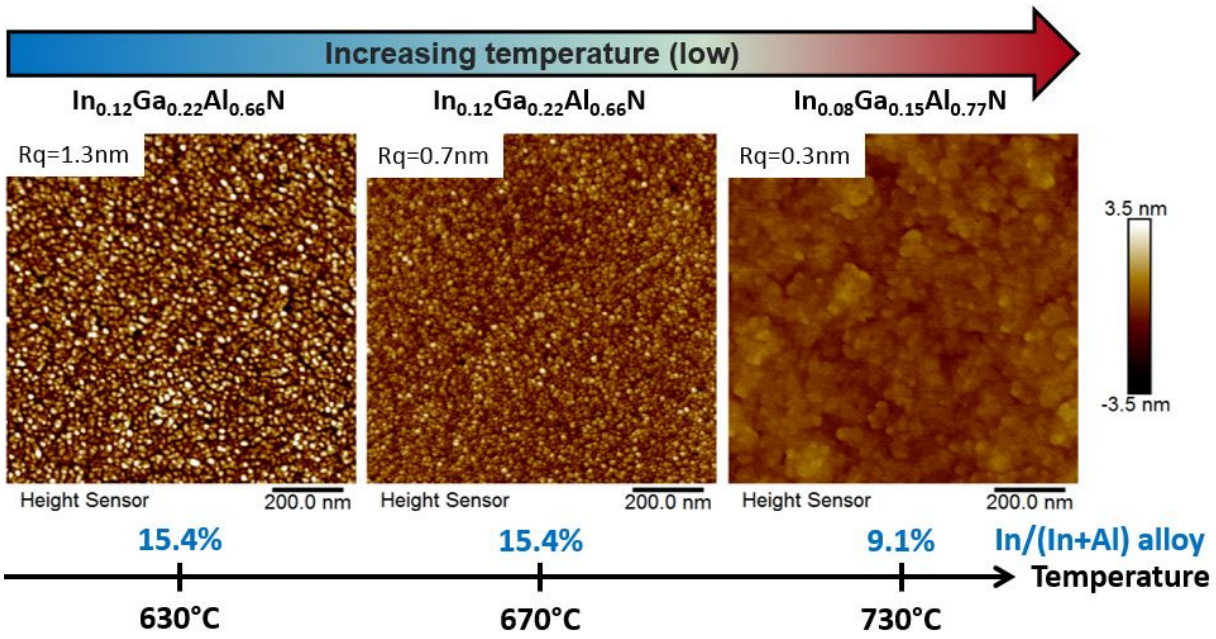

Fig. 4.15 – Effect of growth temperature : 1x1μm^2 AFM images, and alloy composition by XPS. Thickness=12nm, gas mixture : 41% of indium precursors in the gas phase, Vg=3nm/min, carrier gas : N_2.

section 4.2.2. Secondly, the morphology is changing, with the lowest temperature having a surface with a grainy structure. When the temperature increases, the roughness decreases, and the grains become flatter before disappearing. As we found previously in the study of 200nm thick layers, we suggest that this grain morphology is surface roughness above a continuous InGaAlN layer. This is in good agreement with a sectional view by AFM in figure 4.16. In both cases we can see that the peak to valley of each profile represents a maximum of 25% of the total thickness. Essentially, we can differentiate two surface structures : one corresponds to a step structure organized around holes at the surface, and the second is made of grains with different sizes which appear either at low temperature (below 730°C) or when the InGaAlN layer reaches at least 100nm of thickness. The first case is probably related to the difficulty for indium to be correctly incorporated in the crystal lattice according to phase diagram of indium containing III-nitrides. The second emerged from our indium segregation highlighting.

In contrast to the 30nm thick samples, we did not get PL peaks corresponding to the different InGaAlN compositions, even though we would expect to find them according to their XPS values. We suggest that the layers are too thin and thus the majority of electron-hole pairs are lost in the GaN layer which has a lower band gap energy, and so no emission is seen from the InGaAlN layers. However, we performed cathodoluminescence on a sample which has been grown in the same conditions as sample 1 except a growth rate multiplied by 2, and which also does not show any InGaAlN signal by PL. In the CL (cf. figure 4.17), we see a very small peak at 1.7eV (second order of the spectrometer of the GaN luminescence at 3.4 eV) and one at 2.8eV (defects band).

4.2.1.4 Effect of growth rate

We also examined the effect of the growth rate on the InGaAlN layers, with AFM images and indium content shown in figure 4.18. We expected that at higher growth rates we would have more

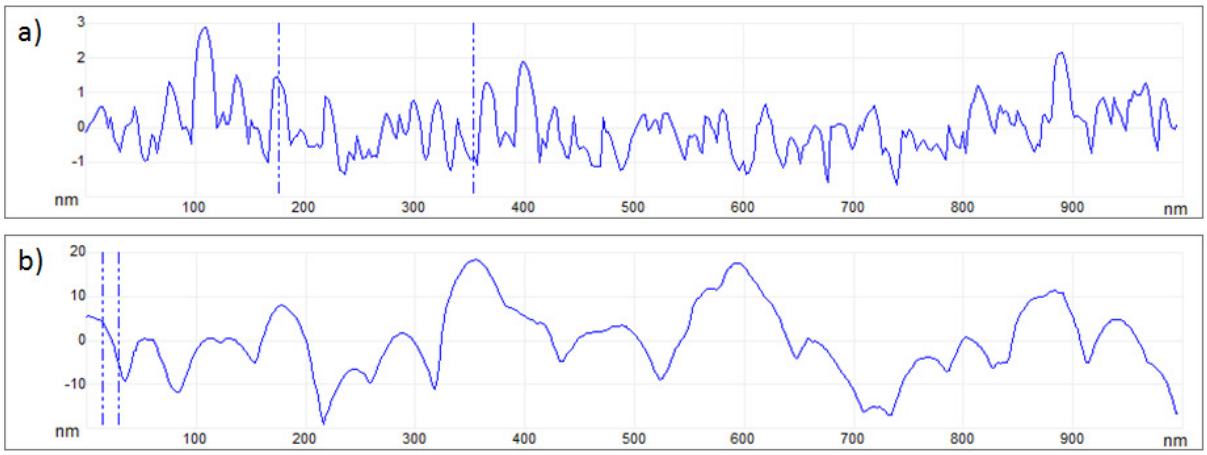

Fig. 4.16 – Cross-sectionnal view from 1x1μm^2 AFM images on a) 12nm, and b) 200nm thick InGaAlN sample showing the grain structure at the surface.

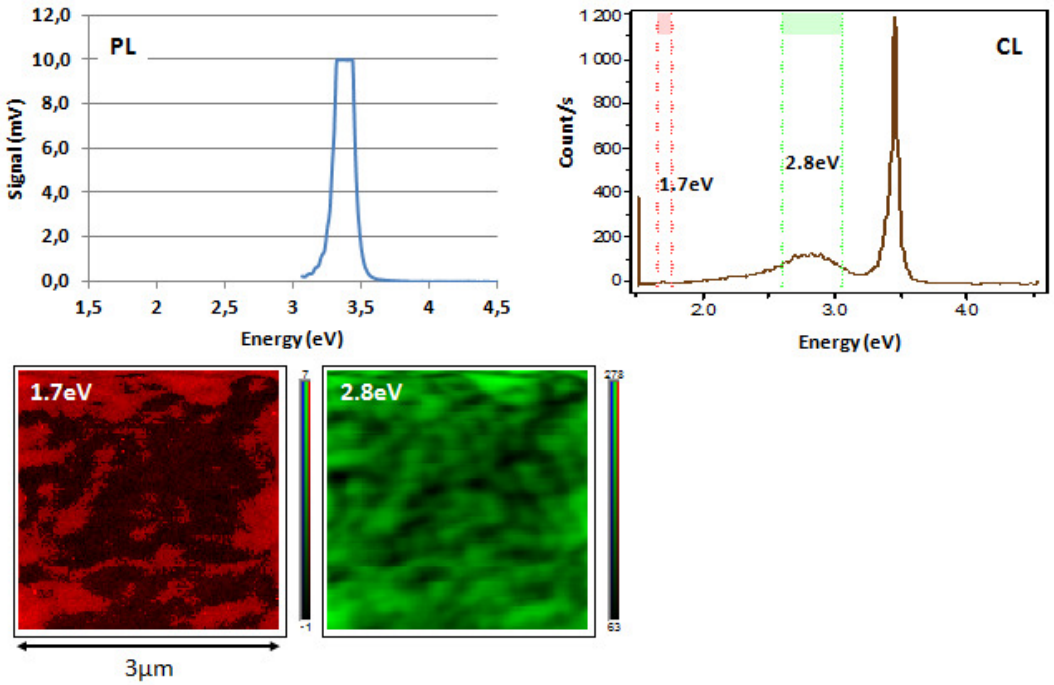

Fig. 4.17 – Spectra of sample 3 : comparison of PL and CL. 3x3μm^2 pictures showing luminescence at different energy. Temperature study.

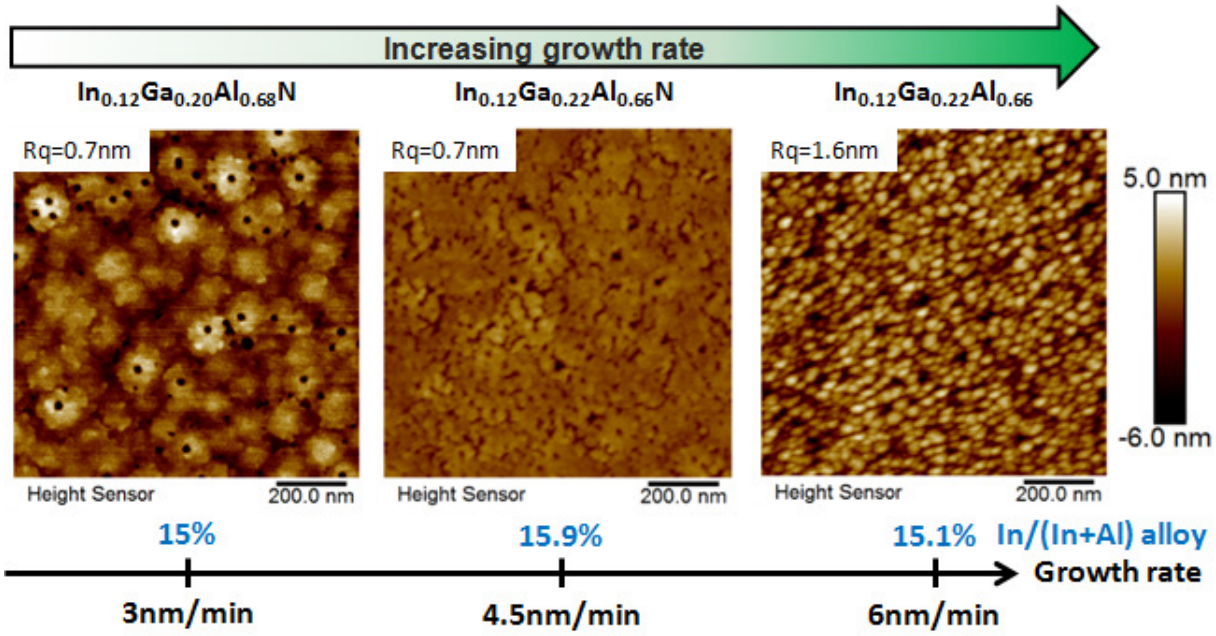

Fig. 4.18 – Effect of growth rate : 1x1μm^2 AFM images, and alloy composition by XPS. Thickness=30nm, gas mixture : 41% of indium precursors in the gas phase, T=730˚C, carrier gas : N_2.

indium in the alloy, as this would reduce the indium desorption during growth. However, figure 4.18 shows that within this growth rate range we don't see significant changes in indium content as measured by XPS. Nevertheless there are strong changes in surface morphology, with in particular a strong degradation of the roughness with the highest growth rate. When we increase the growth rate, the surface morphology is finally varying in the same way as if we were decreasing the temperature. In the previous section, we showed that at low temperatures (equivalent to low surface mobility, as for high growth rate), the surface has a grainy structure (cf. figure 4.15. At higher temperatures (equivalent to high surface mobility, as for low growth rate) the step structure appears progressively and the roughness decreases. The similar effect of both growth parameters on surface structure can be attributed to an effect of surface mobility of ad-atoms which is increasing when the temperature increases and the growth rate decreases.

We expected that the growth rate would have an effect on indium composition which was not the case. However, the photoluminescence spectrum shows a shift of the InGaAlN toward lower energies when the growth rate increases. If phase separation was avoided by increasing the growth rate, we would get a shift on the opposite side toward higher energies since less indium-rich region would appear to be the preferential centers of electrons-holes recombination. This appears not to be the case in these samples. We currently do not have an explanation for this phenomenon, and further work would be need to reproduce these results or to better understand the mechanisms behind this shift in photoluminescence, and the potential effects on phase separation within InGaAlN alloys.

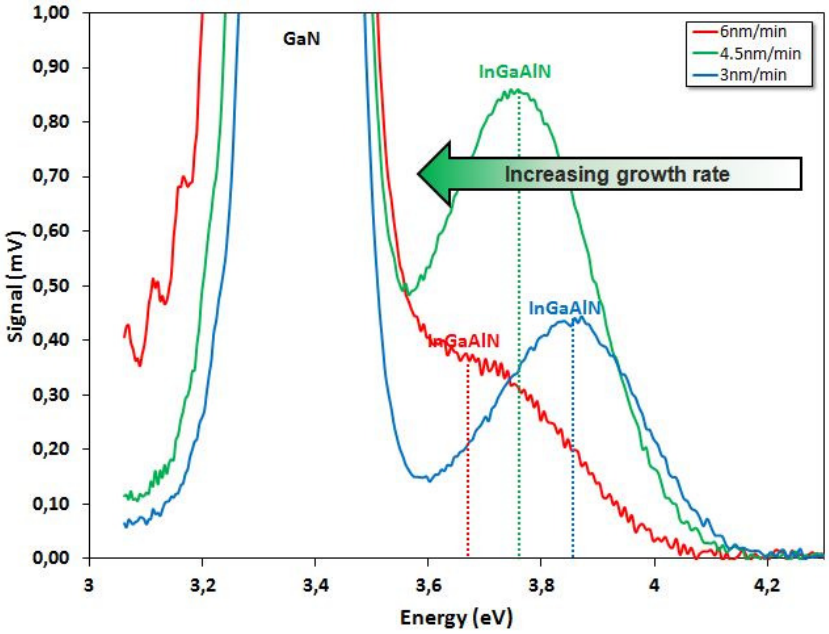

Fig. 4.19 – PL spectra of three 30nm thick samples having a growth rate of 3nm/min, 4.5nm/min, and 6nm/min.

Sample	Thickness (nm)	Temperature (°C)	Vg (nm/min)	PL(eV)	CL (eV)	
1	30	735	3	3.9	3.8	1.7
2	30	736	3	3.9	3.85	-

Tab. 4.5 – Summary of experiments showing the comparison between different barrier layers peak positions in photo and cathodoluminescence spectra. Ammonia flow study.

4.2.1.5 Effect of ammonia flow

Finally, we compared samples with different ammonia flows during growth, again looking at the influence on the topology and indium content. The requirements of III-N materials growth imply a large V/III ratio as explained in chapter 2. Our standard value was 15slm, with growth rates of 3nm/min at 41% Indium in the gas phase. We both reduced and increased the NH_3 flow away from this point, using 10slm and 20slm, with the results shown in figure 4.20. There is no real difference between the three samples, with the indium content staying the same for all three samples, although the RMS measured by AFM decreased slightly as the NH_3 flow was increased.

We measured the samples (referred to as sample 1 and 2) with 15slm and 20slm of ammonia during growth by PL and CL. Photoluminescence is observed at 3.87eV for both samples (cf. figure 4.21 and 4.22). This is coherent with CL measurements where the InGaAlN peak is at 3.8 and 3.85eV respectively for samples 1 and 2. Once again we also see peaks at 2,8eV and 1,7eV, which may be related to phase separation into indium rich regions.

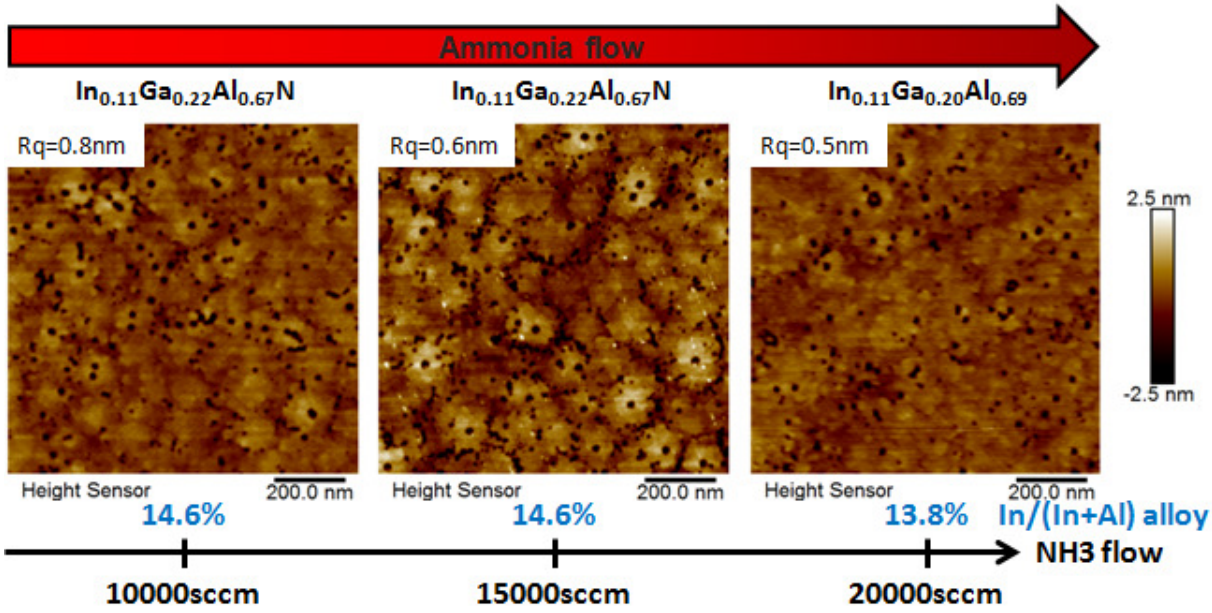

Fig. 4.20 – Effect of ammonia flow : 1x1μm^2 AFM images, and alloy composition by XPS. Thickness=30nm, gas mixture : 41% of indium precursors in the gas phase, T=730°C, Vg=3nm/min, carrier gas : N_2.

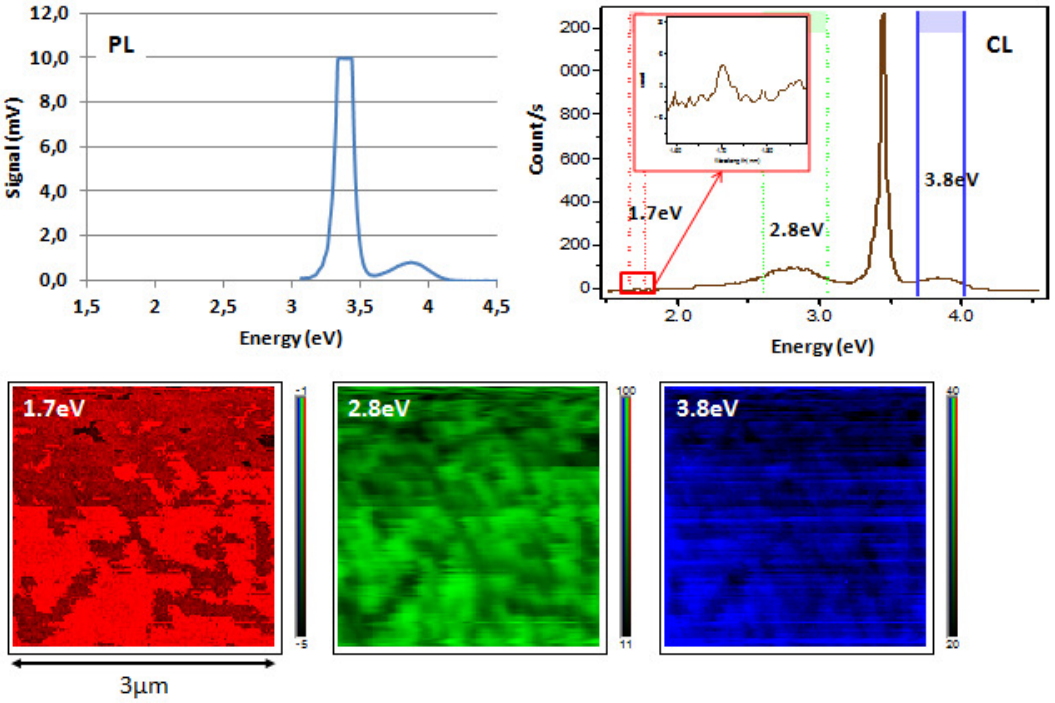

Fig. 4.21 – Spectra of sample 1 : comparison of PL and CL. 3x3μm^2 pictures showing luminescence at different energy.

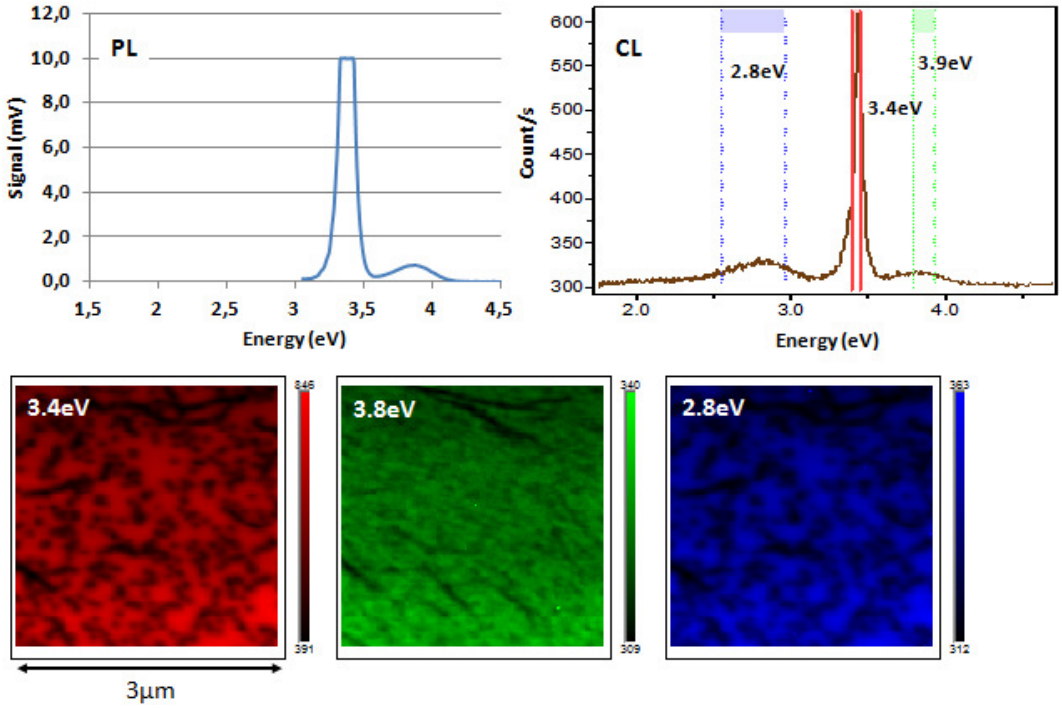

Fig. 4.22 – Spectra of sample 2 : comparison of PL and CL. 3x3μm^2 pictures showing luminescence at different energy.

4.2.2 | InGaAlN growth under hydrogen carrier gas

In chapter 3, we showed the benefits of hydrogen carrier gas compared to nitrogen on the surface morphology of low temperature GaN. At temperatures below 940°C, V-defects appear where edge and mixed dislocation lines meet the surface. We showed that growing under hydrogen allows us to grow layers with the same morphology as layers under nitrogen carrier gas which have a growth temperature 100°C higher. For instance V-defect diameters at 840°C under nitrogen are the same as those at 740°C under hydrogen. Moreover the hydrogen carrier gas also improved the overall topology of the surface. These previous results motivated the comparison of InAlN layers under nitrogen carrier gas and under hydrogen carrier gas, even though hydrogen is known to make it harder to incorporate indium [5].

4.2.2.1 Effect of growth rate and TMIn/TMAl flows

As expected, hydrogen makes it harder to integrate indium into alloy layers. As shown in figures 4.23 and 4.24, for a wide range of growth parameters, no indium was incorporated.

In addition to the difficulty of incorporating indium with hydrogen carrier gas, there is also a thermal effect. Hydrogen has 10 times higher thermal conductivity than nitrogen. As the temperature in the growth chamber is controlled using a thermocouple beneath the susceptor, a higher temperature is found on the wafer surface under hydrogen than under nitrogen for the same set-point. Typically where the temperature was 730°C under nitrogen, we had 750°C under hydrogen. We saw in section 4.2.1.3 that an increase of 40°C between 730°C and 770°C produces a loss of 3.5% on the $In/(In+Al)$ ratio under N_2 carrier gas. So although an increase of 20°C would potentially reduce the indium content,

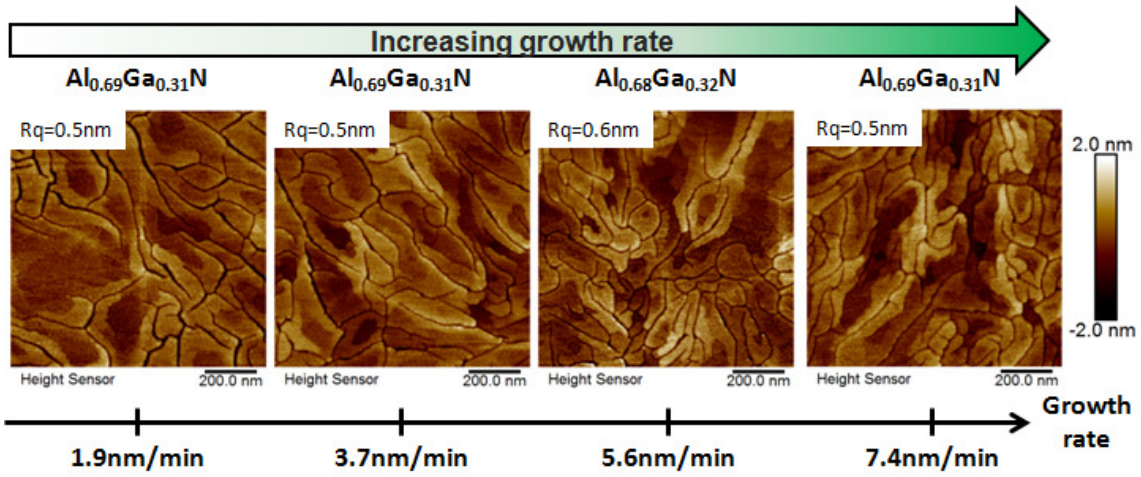

Fig. 4.23 – Effect of TMIn and TMAl flow : 1x1μm^2 AFM images. Gas phase composition specified below AFM pictures. Thickness=13nm, gas mixture : 41% of indium precursors in the gas phase, T=750°C, carrier gas : H_2.

it is not sufficient to induce the loss of all the indium. This effect must therefore be due to the carrier gas.

Figures 4.23 and 4.24 showed the effect of varying the growth rate, increasing the TMIn flow, and finally reducing the TMAl flow in order to give a higher TMIn to TMAl ratio in the gas phase. None of these changes gave any significant indium incorporation, suggesting that we are outside the window where we can grow InGaAlN. The AFM morphology shows highly tensile layers, with cracks across the whole film. As the composition shows that the layers are high aluminum content AlGaN layers grown on GaN, this is not surprising, as the AlN a-lattice parameter is smaller than that of GaN. The four samples of figure 4.23 are 13 nm thick while those of figure 4.24 are 30nm thick which explain the difference of surface morphology. Probably the thinnest shows longer cracks and as the material is growing they are filled and reduce in size, staying only at holes proximity.

Finally we reduced the temperature significantly below 750°C, as shown in the images figure 4.25. Even at 675°C, we were not able to incorporate any indium into the layers, but finally at 610°C we began to see incorporation of indium. At this point, increasing the growth rate by a factor of 2 from 1.3nm/min to 2.6nm/min increased the In/(In+Al) ratio from 4.7% to 6%, meaning that we are approaching a process window where it would be possible to grow InAlN under hydrogen.

These results show that it is possible to incorporate indium into InAlN layer under hydrogen, but that it requires a significant reduction in the growth temperature. However, the final layer is relatively smooth, and therefore this may be a technique which is worth pursuing, especially with higher growth rates, which incorporate more indium, and produce smoother layers. However, we are already over 100°C colder than for the layers grown under nitrogen, which means that according to the work on low temperature GaN, we may be too low to see significant benefits. The idea of the study in chapter 3 was to improve the surface morphology of gallium nitrides and more generally nitrides, since we saw that holes are also there in InGaAlN layers, but without increasing too much the temperature, hence the switch from nitrogen to hydrogen. But with InGaAlN layers, we now need to decrease the temperature

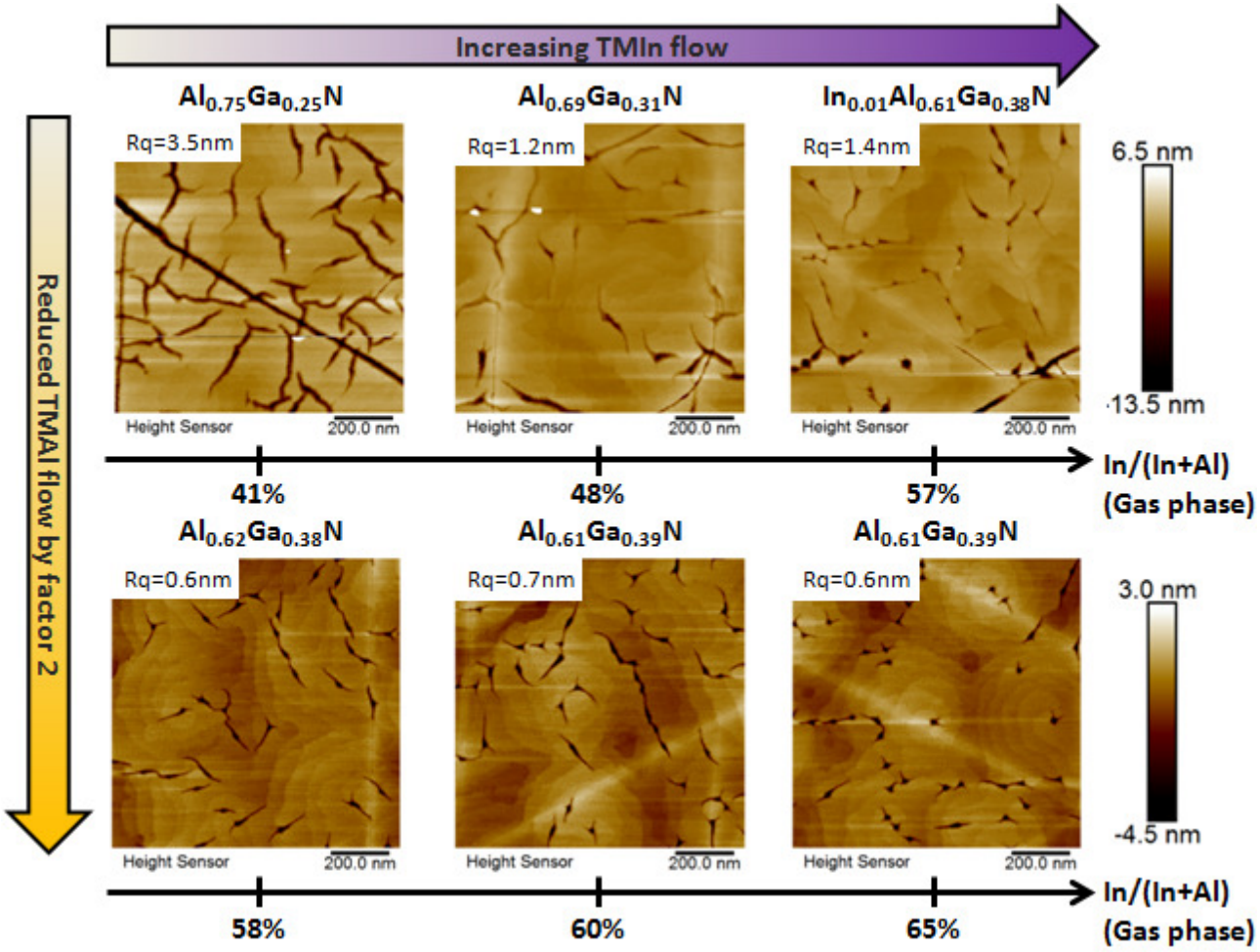

Fig. 4.24 – Effect of TMIn and TMAl flow : 1x1μm^2 AFM images. Gas phase composition specified below AFM pictures. Thickness=30nm, T=750°C, Vg=3nm/min , carrier gas : H_2.

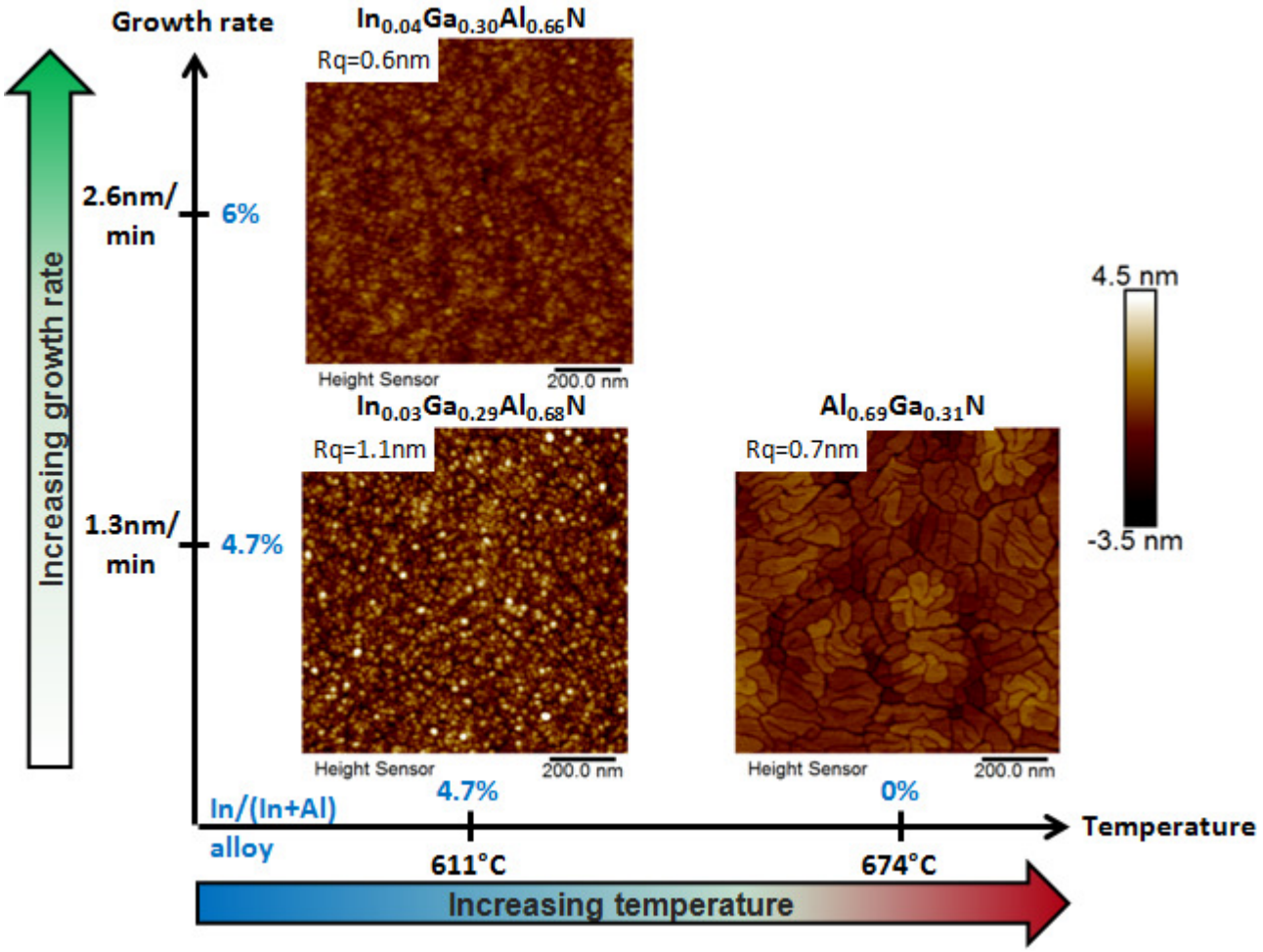

Fig. 4.25 – Effect of T and Vg : 1x1μm^2 AFM pictures. Gas phase composition specified below AFM images. Thickness=13nm, gas mixture : 41% of indium precursors in the gas phase, carrier gas : H_2.

to incorporate the indium into the layers, and we start to lose the benefits. Overall it is not clear that there is a benefit to using hydrogen as a carrier gas for these layers.

4.3 | Growth of InAlN layers without gallium pollution

As we have seen in this chapter, the vast majority of our InGaAlN samples contained gallium pollution : it was not intentionally added into the layers. However, we should note that the very first samples we grew by MOCVD were gallium free. The reason for this is rather obscure even today, but we suggest that it is due to hardware upgrades of our reactor. At the beginning, the graphite shield on the showerhead was spaced 1mm away from the showerhead, while afterwards, it was clamped against the showerhead. This upgrade reduced the temperature of the shield, which reduced pre-reactions in the gas phase, improved uniformity, and improved reproducibility. However, it appears that this also resulted in the gallium pollution which has been seen for standard close-coupled showerhead reactors, which do not have the shield, and so have a lower effective temperature at the showerhead. This explanation suggests that the source of gallium is mainly the showerhead and shield zones.

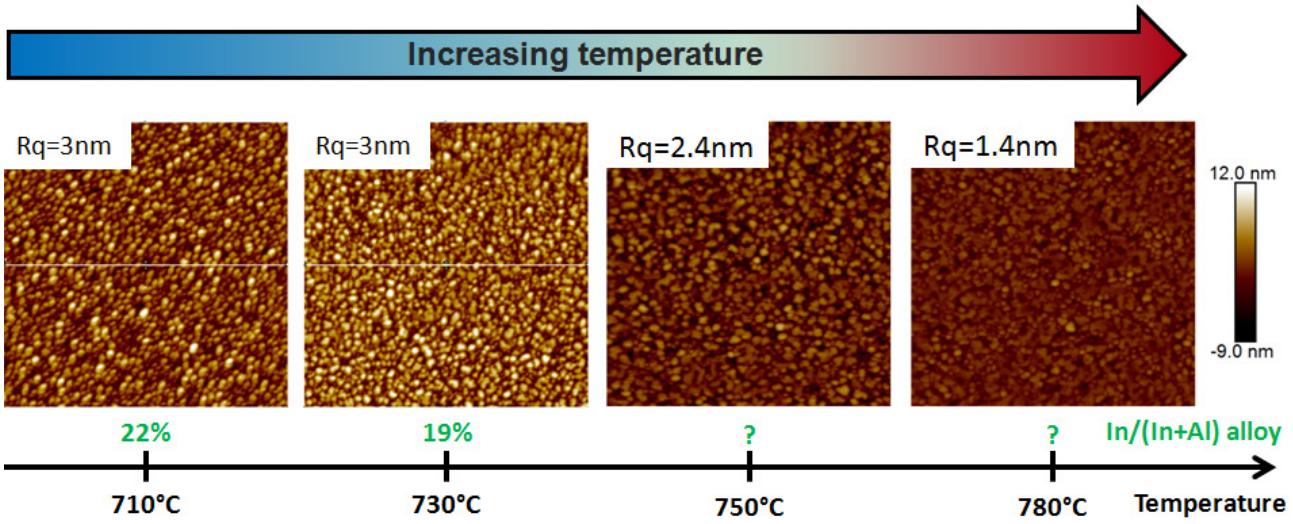

Fig. 4.26 – Effect of growth temperature : on topology on 1x1μm^2 AFM pictures, and alloy composition by XPS. Thickness=30nm, gas mixture : 41% of indium precursors in the gas phase, Vg=3nm/min, carrier gas : N_2.

We have fewer characterization measurements for these InAlN samples than for the InGaAlN previously treated but it is nevertheless interesting to compare the trends to the studies of InGaAlN layers.

Figure 4.26 shows the evolution of 30nm thick InAlN versus temperature. The two XPS measurements are sufficient to show the decrease of In content with the temperature, as for InGaAlN. In terms of surface morphology, the grain structure is present from 30nm on InAlN surface while it requires a thickness of nearly 100nm on InGaAlN layers (cf. figure 4.4), and generally the layers without gallium tend to have a more grainy structure than those with gallium. Also while the temperature is increasing these grains appear to be flattened and seem disappear gradually. We can suppose that these grains are a consequence of the presence of indium and potentially of its segregation, and that gallium may have a beneficial effect on the surface morphology.

In order to know if the InAlN layers were continuous below the grain structure, we analyzed it by TEM observation. AFM gives us a first answer to that in figure 5.6 of chapter 5 but TEM cross-section is more accurate (cf. figure 4.28). First we can see a continuous InAlN layer below the rough surface corresponding to the grain structure. At the top of the InAlN layer the contrast in dark field seems to match with the thickness exposed to a maximum of oxygen content and thus being oxidized. It is worth noticing that the thickness of oxidation is less than the value we can measure on the TEM picture. Indeed it is a cross-sectional view of the material with a thickness higher than 0nm obviously. Therefore, in the rough area, we have the view of a superposition of few grains. And if one grain is oxidized on a thickness of 2-3nm, its projection in the observation direction of the cross-section gives us the illusion of a 10nm thick oxide.

Even if we only have a few chemical characterizations, we learned interesting facts from these pure InAlN samples, and further comparisons will be made in the next chapter, where we found another way to avoid gallium contamination.

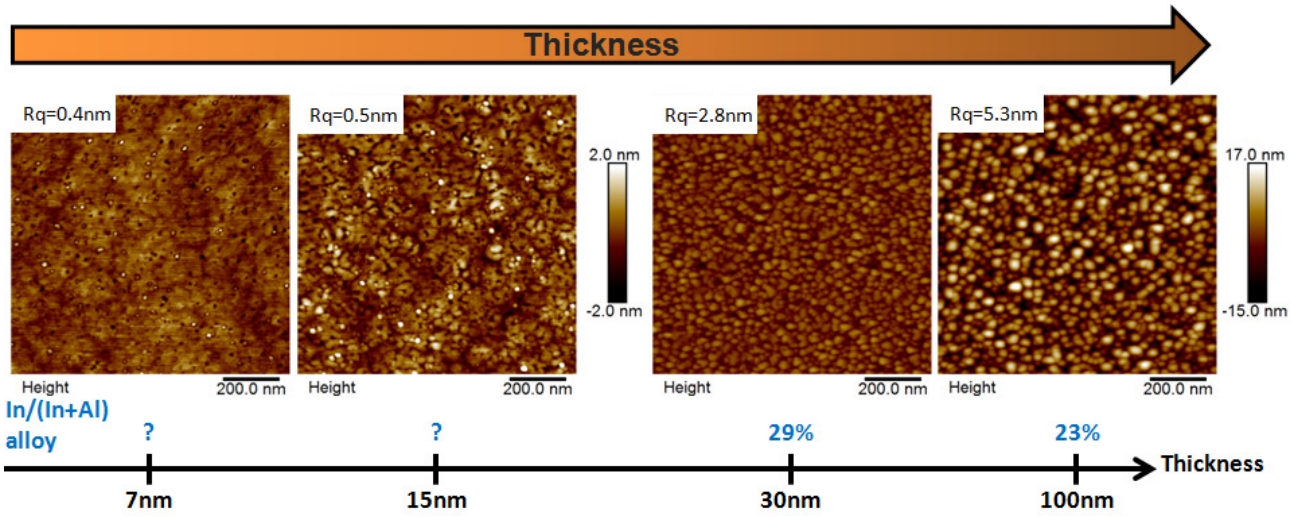

Fig. 4.27 – Effect of thickness : on topology on 1x1μm^2 AFM pictures, and alloy composition by XPS. T=730°C, Vg=3nm/min, gas mixture : 41% of indium precursors in the gas phase, carrier gas : N_2.

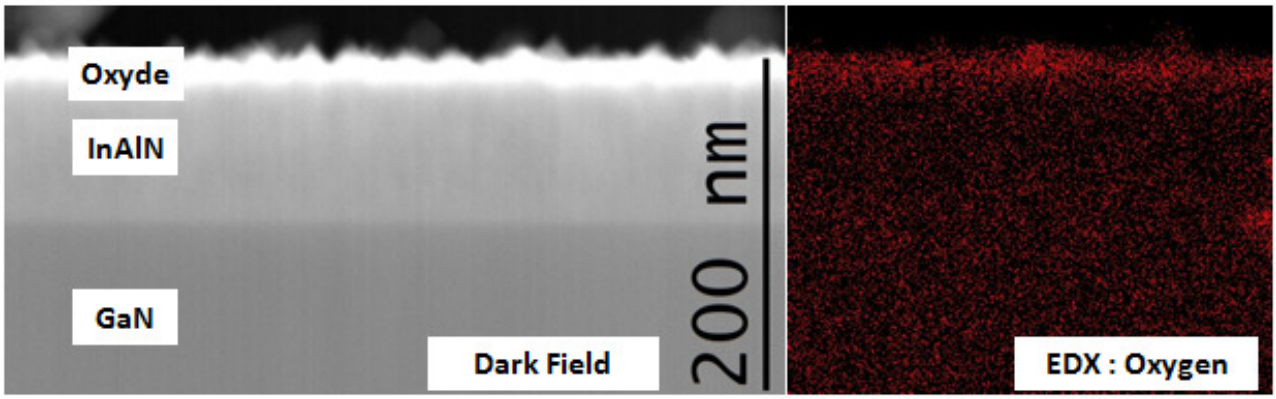

Fig. 4.28 – TEM cross section of 100nm thick InAlN with EDX analysis on oxygen.

Summary of chapter 4

Before any discussion concerning our alloys composition, we fixed the idea about how we proceeded to determine their stoichiometry. As XRD is usually used but suffering from our complex structure with a multiple buffer layers, we decided to use systematically XPS measurements with 5% uncertainty, and for a set of sample, WDXRF technique which is non destructive (several spot on wafer possible) and faster. The correlation between both techniques was linear and interesting.

Then we investigated InGaAlN under two carrier gas which are nitrogen and hydrogen. Under nitrogen, known to stabilize indium incorporation, we analyzed the effects of growth time, temperature, TMIn/TMAl flows ratio, and growth rate and finally ammonia flow on surface morphology, alloys composition, luminescence and electrical performances. The growth time study revealed a lot about roughness versus growth thickness and first highlighted the separation phase phenomenon in indium containing III-N materials through photoluminescence measurements. However, an increase in growth rate showed a reduction in PL peak emission band gap, despite a constant composition. This may be an effect linked to phase separation, but this has not been understood. To increase the incorporation of indium incorporation, temperature decrease to at least 670°C and TMIn flow increase seems to favor it.

Under hydrogen carrier gas, indium integration in the same process windows as under nitrogen is impossible even if we increase strongly the TMIn flow and/or reduce the TMAl. The key is in the temperature decrease between 611°C and 674°C to start the indium incorporation in InGaAlN layers. There, the growth rate has a stronger influence and while doubled, increased the indium content significantly.

Finally, while the majority of InGaAlN layers had gallium pollution from reactor, the very first samples were pure InAlN and thus gallium free. So some trends especially on roughness behavior and indium content were extracted from series of temperature and thickness changes.

A final positive result is that we have succeeded in producing layers with large band gaps >4eV, which is not easy due to separation phase in these types of quaternary layers.

Bibliographie

[1] R. Butté, J.-F. Carlin, E. Feltin, M. Gonschorek, S. Nicolay, G. Christmann, D. Simeonov, A. Castiglia, J. Dorsaz, H. J. Buehlmann, S. Christopoulos, G. B. H. von Högersthal, A. J. D. Grundy, M. Mosca, C. Pinquier, M. A. Py, F. Demangeot, J. Frandon, P. G. Lagoudakis, J. J. Baumberg et N. Grandjean, « Current status of alinn layers lattice-matched to gan for photonics and electronics », *Journal of Physics D : Applied Physics*, vol. 40, no. 20, p. 6328, 2007. 102

[2] L. Semra, A. Telia, M. Kaddeche et A. Soltani, « Effects of spontaneous and piezoelectric polarization on alinn/gan heterostructure », *in 2012 International Conference on Engineering and Technology (ICET)*, p. 1–4, Oct 2012. 102

[3] P. Gamarra, C. Lacam, M. Magis, M. Tordjman et M.-A. di Forte Poisson, « The effect of ammonia flow in the aln spacer on the electrical properties of inaln/aln/gan hemt structures », *Physica Status Solidi*, vol. 209, p. 21–24, 2012. 103

[4] D. Doppalapudi, S. N. Basu, K. F. L. Jr. et T. D. Moustakas, « Phase separation and ordering in ingan alloys grown by molecular beam epitaxy », *Journal of Applied Physics*, vol. 84, no. 3, p. 1389–1395, 1998. 108

[5] T. C. Sadler, M. J. Kappers et R. A. Oliver, « The impact of hydrogen on indium incorporation and surface accumulation in inaln epitaxy », *Journal of Crystal Growth*, vol. 331, no. 1, p. 4 – 7, 2011. 121

5 | InGaAlN alloys : phase separation, gallium pollution of MOCVD reactors, and electrical properties.

Sommaire

5.1 A study of phase separation in InGaAlN alloys 132
5.1.1 Correlation between band gap energy and lattice parameter 132
5.1.2 PL non emission by InGaAlN samples 133
5.1.3 Quantification of indium segregation using AES measurements 136
5.2 Gallium pollution in MOCVD reactors growing Ga containing alloys 141
5.2.1 Calculation of a virtual TMGa flow from pollution sources in the reactor 142
5.2.2 Cleaning test with Cl_2 : growth of pure InAlN 143
5.3 Surface diagram of InGaAlN layers 144
5.4 Electrical characterization : Rsheet measurements 148
Bibliographie 153

The production and study of InGaAlN layers on GaN pseudosubstrates is a large part of this thesis. As we decided to concentrate the experimental results and trends that we extracted from the characterizations with the intentions to give a physical sense in chapter 4, this chapter will focus more on a summary of our characterizations to discuss more deeply of phase separation, gallium pollution and electrical properties.

5.1 | A study of phase separation in InGaAlN alloys

Indium segregation and phase separation is a well-known phenomenon in III-N materials containing indium [1][2][3][4][5][6]. Our samples also seem to have this problem according to different characterization results. The phase separation was first highlighted by optical measurements such as photoluminescence and cathodoluminescence, but also by AES measurements whose goal was to detect chemical composition fluctuation in small area at the surface of various samples. The strongest evidence of phase separation was the change in photoluminescence peak position with increasing sample thickness, despite having the same bulk composition as measured by XPS.

5.1.1 | Correlation between band gap energy and lattice parameter

We constructed a graph linking the band gap energy and the lattice parameter of samples from which we got a photoluminescence signal. The goal of such a correlation is to check the validity of our XPS and PL analysis since our experimental points should be in the triangle formed by AlN, GaN and InN points. In our graph, we connected the three binary points using the formula of lattice parameter versus the ternary alloy composition (Vegard's law), and the band gap energy versus the composition using the linear relation plus the quadratic term containing the bowing parameter. For the AlGaN alloy, we plotted lines which used the most extreme bowing parameters found farthest in the literature : $b_1 = 0.62eV(+/-0.45eV)$ and $b_2 = 1.3eV$ [7]. For the other alloys, InGaN and InAlN, we used mean values of bowing parameters to draw the boundaries.

The results presented in figure 5.1 show that the experimental points are inside the curved triangle formed by the three binary points corresponding to AlN, GaN and InN. Note that some of these points could be outside the triangle in the case of the lowest bowing parameter we used for theoretical AlGaN alloys (gray dashed line). We have not been able to include all of our samples in the graph for two reasons. Firstly, there is a detection window ranging from 3.07eV to 4.5eV during the PL measurement. So depending on the InGaAlN composition the PL peak may be outside these limits of detection. Secondly, the GaN peak is quite large and very intense, so again, depending on a certain composition range, the InGaAlN peak may be hidden by the GaN peak. Very often we can observe shoulder on the right of the GaN peak. This is typically insufficient to determine the energy at the maximum intensity of the peak.

Something which we may find strange about this graph is that although we are adding indium to the layers, all the points appear to be very close to the AlN-GaN boundary. As we have up to 20% indium in the layers, this unexpected. We could explain this as errors of measurement, but we can also explain it in terms of phase separation, which causes the points to move down. As mentioned

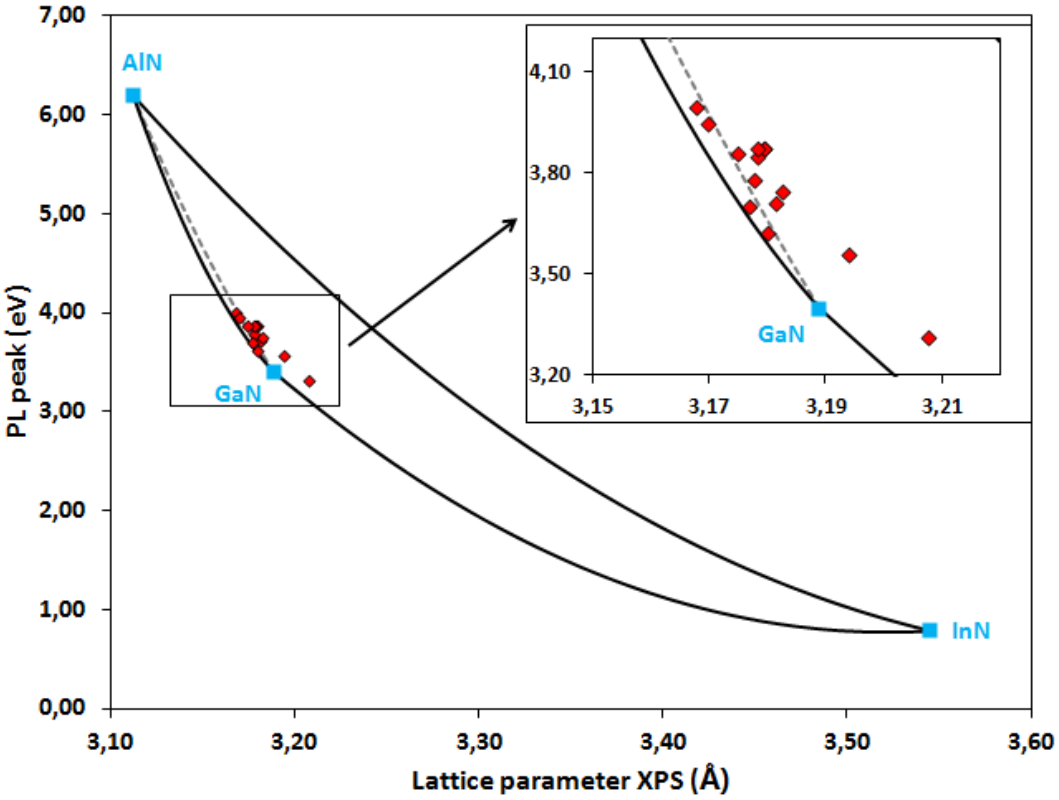

Fig. 5.1 – Band gap energy measured by PL versus lattice parameter extracted using XPS measurements.

previously in this chapter, separation of indium rich and poor phases would generate lower band gap energy areas in which recombination take place. In that case, the theoretical band gap energy directly linked to the composition would be higher. Thus we can imagine an upward shift of all the experimental points if there was no segregation, and this shift would depend on the amount of segregation. If we were able to measure the composition of the different phases, we could calculate the different lattice parameters and thus get different points on the graph. If we imagine two points (one for rich indium and one for poor indium phases), the one corresponding to rich indium phases would be associated to the luminescence measured by PL, but this point would be shifted to the right because of a higher calculated lattice parameter (more indium). The other point would be shifted up and to the left and get a higher luminescence energy. Obviously this analysis is complicated since we aren't able to get a separated luminescence peak from low and rich indium phases in the alloy. And also, it is difficult to characterise the composition in two different areas of the sample.

5.1.2 | PL non emission by InGaAlN samples

We tried in this section to understand why half of our samples are not emitting a PL peak. There could be several explanations :

— Some points can be outside of the detection window. This mainly concerns the samples having very low indium content and thus a band gap energy higher than 4.5eV.

— Samples whose PL peak corresponds to InGaAlN or InAlN are hidden by the GaN peak.

— Thin InGaAlN layer of nearly 12nm could be subjected to recombination only in GaN pseudo-

substrate due to an electron transfer in the lower band gap material which is the GaN, and so the luminescence peak is too low to be measured.

The first data treatment we did was to make the correlation between the band gap measured by PL and the linear theoretical band gap calculated from the XPS compositions, shown in figure 5.2. There appears to be a roughly linear trend for the points with PL emission, which given the variety of samples contained on this graph is a positive result. We also plotted the points without signal, or seen as a shoulder on the GaN along the x-axis. We can see that the samples which are not emitting in photoluminescence are not supposed to be out of the detection window going from 3ev to 4.5eV, thus disproving the first hypothesis, as we expect only one point (the furthest to the right) to be really out of detection. This was one of the samples included into a temperature study discussed in the previous chapter where the other samples at lower temperature had more indium and they show clear photoluminescence signal.

Then there are three points (round orange markers) for which we saw a little shoulder against the GaN peak on the higher energy side of the photoluminescence analysis. It is difficult to estimate where would be the maximum intensity of the peaks since the shoulders are slight. On the other hand the bottom leftmost point of the graph, corresponding to one 200nm thick sample, showed the beginning of a peak from which we were able to estimate the maximum intensity position in energy. However, as if the shoulders are a little above the GaN peak energy, (3.5—3.6eV), they would not be a long way from the linear trend, and so this hypothesis of peaks being hidden by the GaN peak could also be valid for the blue triangles close to the orange dots.

The purple points are layers with a thickness of only 12nm, and so clearly it is possible to have emission from such thin layers. Therefore this last hypothesis is cannot account for the lack of emission wavelength.

In summary, using the three hypotheses above, we are not able to fully explain the blue triangle markers which correspond to samples which did not exhibit a PL response for the barrier layer. We suspect that some of the points are due to a peak which is hidden by the GaN one. However, we should keep in mind that a correlation between a linear theoretical band gap and a PL peak subjected to segregation phenomena cannot be consider as a definitive rule. It gives a rough trend but it would be surprising if the segregation was so linear. If we have different amounts of segregation, different samples with different compositions may still result in peaks hidden by the GaN. We can look at the new PL versus lattice parameter figure we got by adding the new points which did not emit in PL measurements. In figure 5.3, we can first see that half the theoretical points we have added in purple are outside the InN-GaN-AlN triangle while the other half is inside. This is probably due to our correlation between PL peak positions and theoretical linear band gaps which was rough as explained previously. From our point of view and as a conclusion, such a figure makes us believe that we do not control the influence of some growth parameters on the segregation, and thus on the wavelength of PL emitted by all the barrier layers.

Finally, there may be other effects such as crystal defects and non-intentional intrinsic doping which may reduce photoluminescence intensity, and so stop the PL emission from being measurable.

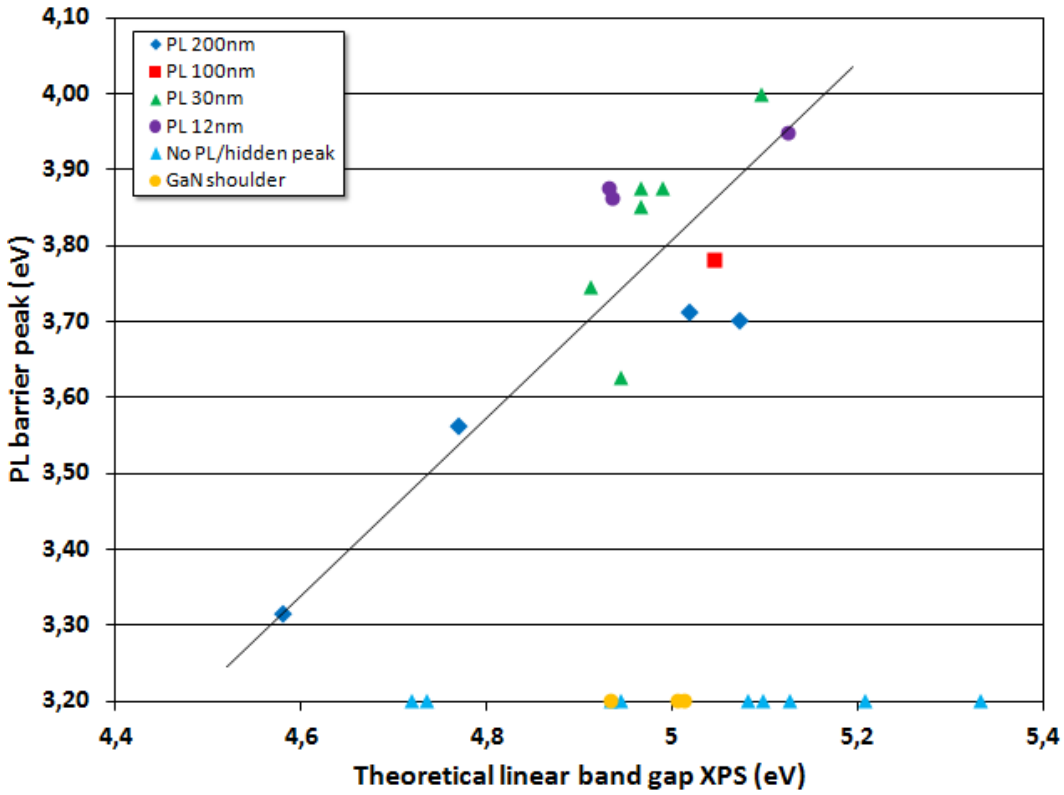

Fig. 5.2 – Correlation between PL peaks and theoretical band gap energy using XPS measurements. Samples without PL emission are plotted on the x-axis.

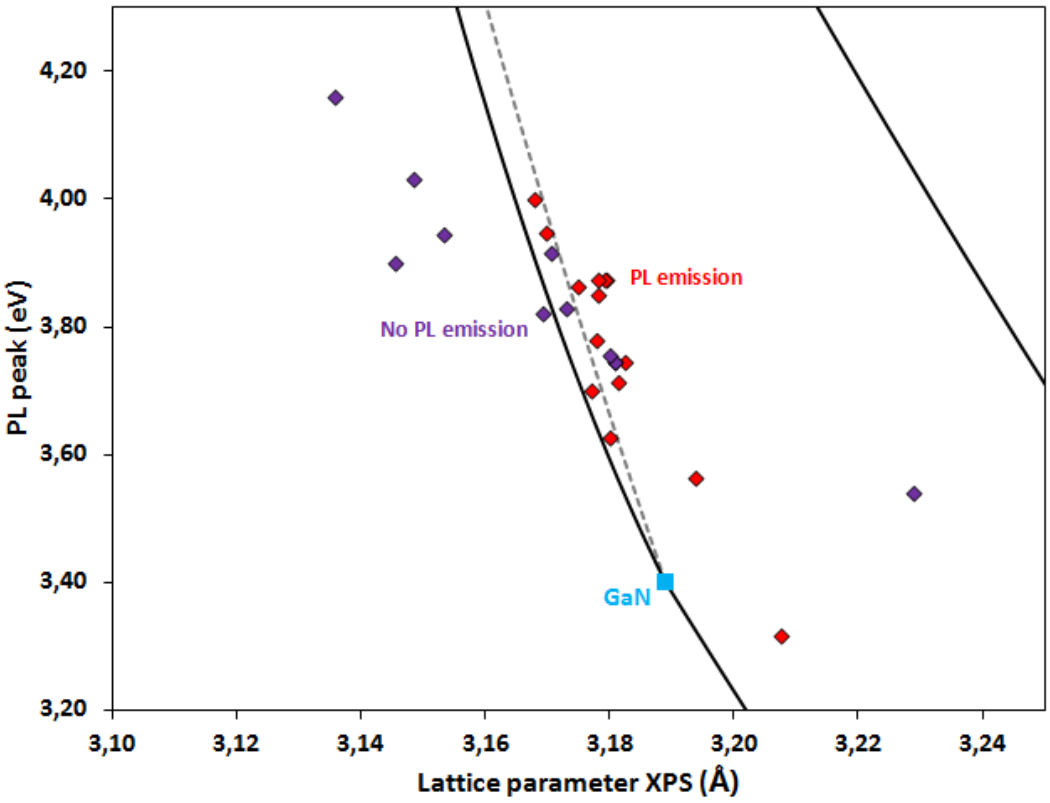

Fig. 5.3 – Band gap energy measured by PL versus lattice parameter extracted using XPS measurements. Points with theoretical PL peak for barrier layer have been added.

5.1.3 | Quantification of indium segregation using AES measurements

We used AES measurements in order to try to quantify the segregation of indium in our InGaAlN alloys. As mentioned in chapter 2, the benefit of AES compared to XPS is the lateral resolution of the measurement. In a window of 1x1μm^2, we analysed thick samples showing a rough surface as shown in section 5.1.1. We used the SEM integrated into the AES tool to zoom on the sample and we did measurements at different points, corresponding to a dark and a light area at the edge and centre of a grain. Each point of measurement has a diameter of 10nm. If the measured composition is changing between these different points, it implies that we are highlighting the pahse separation between indium rich and poor phases at this scale, and that we can estimate it even roughly and at the surface only (3-4 first nm).

Before analyzing the results get by AES, it is worth noticing that AES as for XPS methods are semiquantitative and thus contain an uncertainty when we look at the composition of one of our alloy. However the measure is very accurate in relative terms. This means that if a difference in composition is detected in two separate points at the surface of one sample or even between two samples, there is really a difference. Also we would add that it is difficult to have an idea of the size of the different phases composing our alloy. This makes our measurements limited, but it is a good starting point for understanding indium segregation in our layers.

5.1.3.1 InAlN free of gallium

The measurements were performed on three samples : one 100nm thick and two 200nm thick. The first we examined is a sample which does not contain gallium ($In_{0.23}Al_{0.77}N$) and was grown at the beginning of the thesis (cf. annex). We can see in figures 5.4 and 5.5 two separate areas of a few microns in which we did two AES measurements. If we choose two areas too far from each other, the compositions may be different from each other but this could be attributed to small variations due to process inhomogeneity.

Note that the observed morphology is close to that measured by AFM in figure 5.6. For both SEM and AFM, we can distinguish the grain structure with nearly the same grain size. The SEM image may appear fuzzier since we are close to the limit of the SEM capacity and we are exposed to a lot of vibrations mainly due to turbo pumps attached to the tool.

Table 5.1 shows a summary of the AES results on sample 1 for the four points indicated on SEM pictures in figure 5.4 and 5.5. While the composition of our alloy is not changing between the two measurements points in the first zone, we saw a 3% absolute difference of indium content in zone number 2. Based on these four measurements on sample 1, 3% is the maximum value we got as an alloy composition difference in two close areas on the sample (centre). These are also the maximum and minimum of all 4 measurement points. This seems to be a small value, but it represents just under half of the initial 7% value measured in sample 1 zone 2, and thus corresponds to a relative difference of nearly 50%.

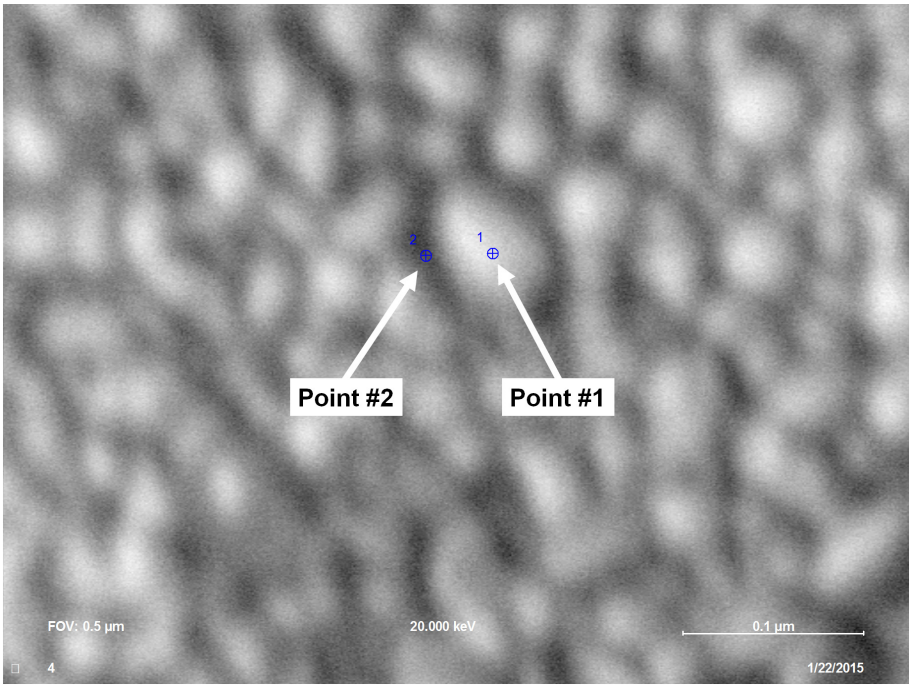

Fig. 5.4 – SEM picture (zone1) of 100nm thick InAlN surface (sample 1) and two points of measurements for indium segregation study.

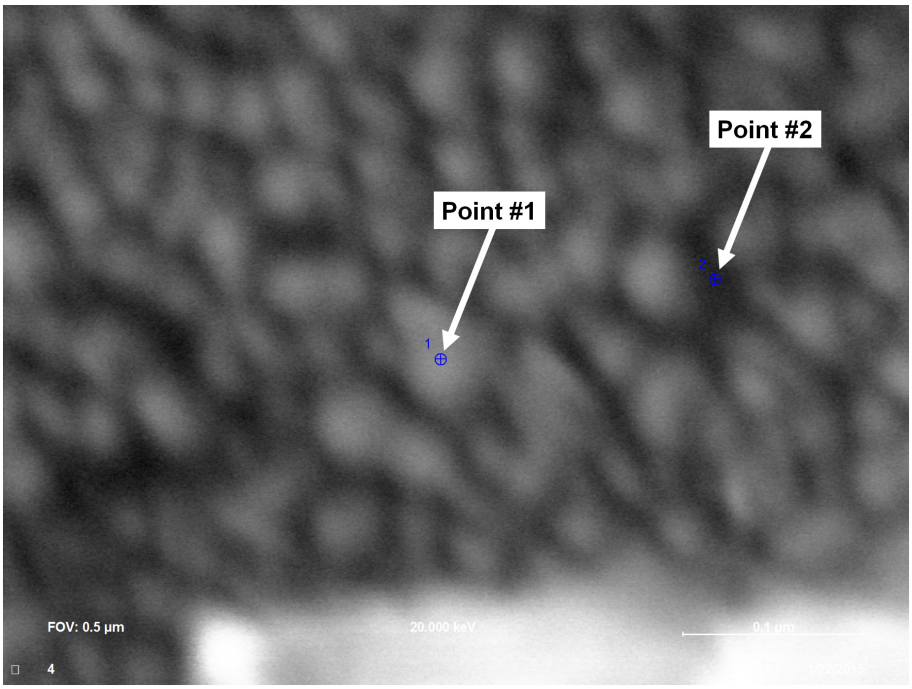

Fig. 5.5 – Second SEM picture (zone2) of 100nm thick InAlN surface (sample1) and two points of measurements for indium segregation study.

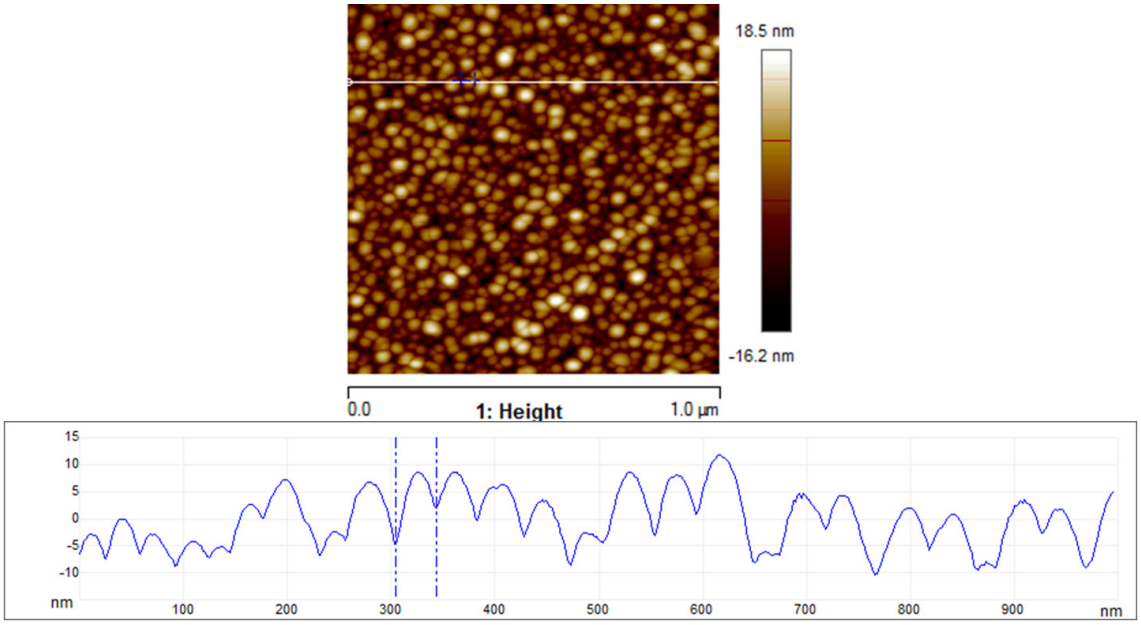

Fig. 5.6 – 1x1μm^2 AFM picture showing the surface morphology of a 100nm thick InAlN sample (sample1). Below, a section showing the profile of the topology.

Sample	**Thickness (nm)**	**Zone**	**Point**	**AES composition**			
				%In	**%Ga**	**%Al**	**In/(In+Al)**
1	100	1	#1	8	0	92	0.080
			#2	8	0	92	0.080
		2	#1	10	0	90	0.100
			#2	7	0	93	0.070
2	200	1	#1	7	10	83	0.078
			#2	8	11	81	0.090
3	200	1	#1	13	12	75	0.148
			#2	13	13	74	0.149

Tab. 5.1 – Summary of samples used for In segregation study by Auger electron spectroscopy.

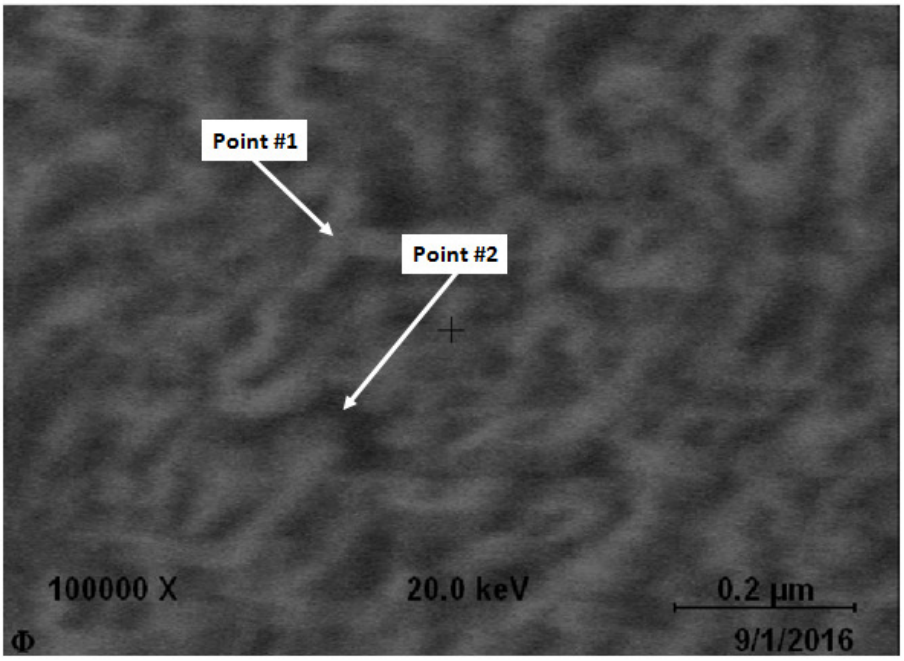

Fig. 5.7 – SEM picture of 200nm thick InGaAlN surface (sample 3) and two points of measurements for indium segregation study. Sample 2 is similar.

5.1.3.2 InAlN containing gallium

The other two samples are identical to one another except for the $In/(In + Al)$ precursors ratio. The SEM image of sample 3 is shown in figure 5.7 and both samples showed the same morphology. For sample 2 had a lower indium content in the gas phase, and this is shown in the solid composition of $In_{0.12}Ga_{0.17}Al_{0.71}N$ versus $In_{0.18}Ga_{0.23}Al_{0.59}N$ for sample 3. There is a slight difference between the two measurement points for sample 2, but no difference for sample 3, so we have not clearly demonstrated segregation in these thick layers, despite indium content up to 13%.

5.1.3.3 Indium segregation analysis

As discussed above, sample 1 shows an indium content variation of 42% when going from 7 to 10%, and sample 2 a variation of 14%.These values are therefore the minimum indium content variation for these two samples. We consider the indium variation detected by AES as a minimum, as shown in the following analysis. Imagine four cases showed in figure 5.8, where the red squares represent the measurement spot, and the light and dark blue areas represent low and high indium content areas respectively.

1. The spot size is less than the size of indium rich areas and the two successive measurements are performed entirely on an indium-rich phase and on an indium-poor phase (a). In this case, the indium variation measured is correct.
2. If the two successive measurements, or one of them, straddle indium-rich and -poor phases (b), the evaluated variation is less than the reality due to averaging over the measurement spot.
3. If both areas are on indium-rich or -poor phases (c), there is no or very low variation, so we underestimate the variation.

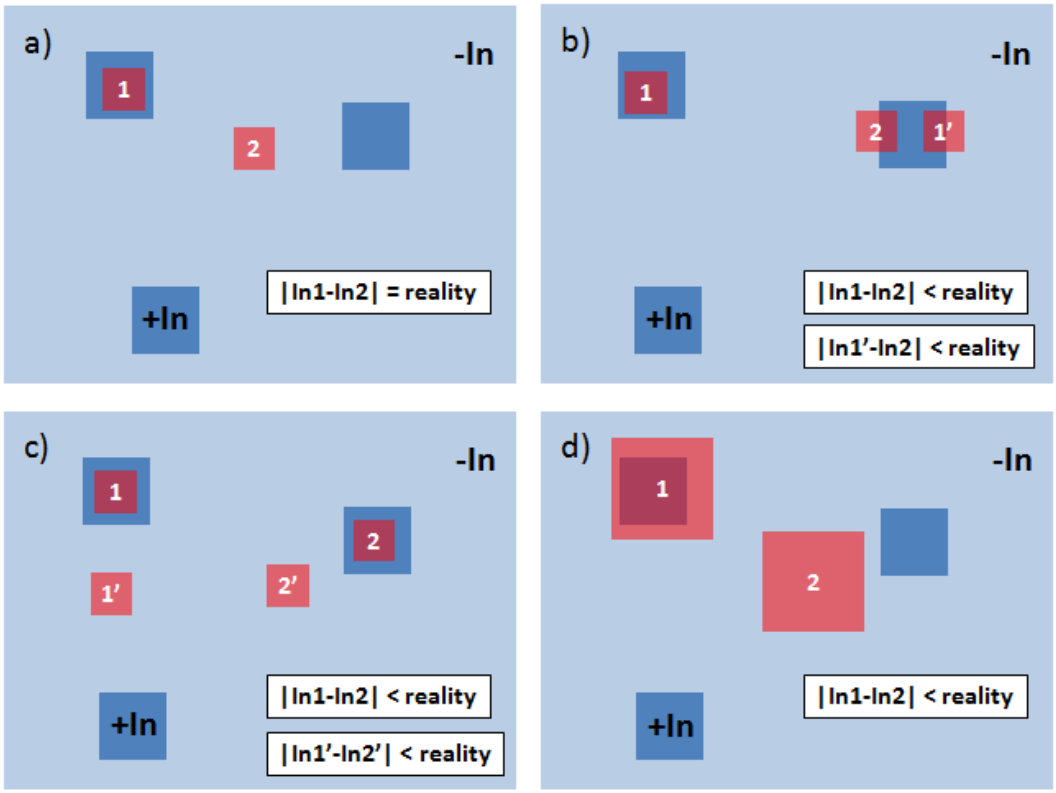

Fig. 5.8 – Different cases of indium variation detection by AES as a function of spot size, indium-rich phases size and spot position. The red squares represent the measurement spot, and the light and dark blue areas represent low and high indium content areas respectively

4. If the spot size is too big (d) we always measure the two phases, and so the measured indium variation will be underestimated

So for all these cases, the indium variation measured will be either correct or less than the reality.

We quantified the observed indium variations for each sample from one AES measurement point to another, and calculated different horizontal shifts on the graph 5.9 for all the other points. We chose 42%, as this was the minimum value measured by AES, and 100%, as another example which kept all the points within the curve. In our analysis we can alter only the lattice parameter which depends on the indium, gallium and aluminum content, to match the measured PL signal. As discussed earlier, we suppose, as already detailed, that the PL signal we got for each sample is at a wavelength corresponding to indium-rich areas in a segregated material.

Thus we formulated some hypothesis and interesting points to improve. First, if we would continue further AES measurements, it would be good to try a more complete mapping of each area, with a lot more points to increase the statistics. Secondly, AES measurements may not have a good enough spatial resolution (10nm diameter) or even depth resolution since the incident electron diffusion volume is probing 3 to 4nm in the material. Thirdly, we do not have any characterisation in the bulk of the material also subjected to indium segregation.

To further advance this study, it would be interesting to use atom probe tomography (even if sample

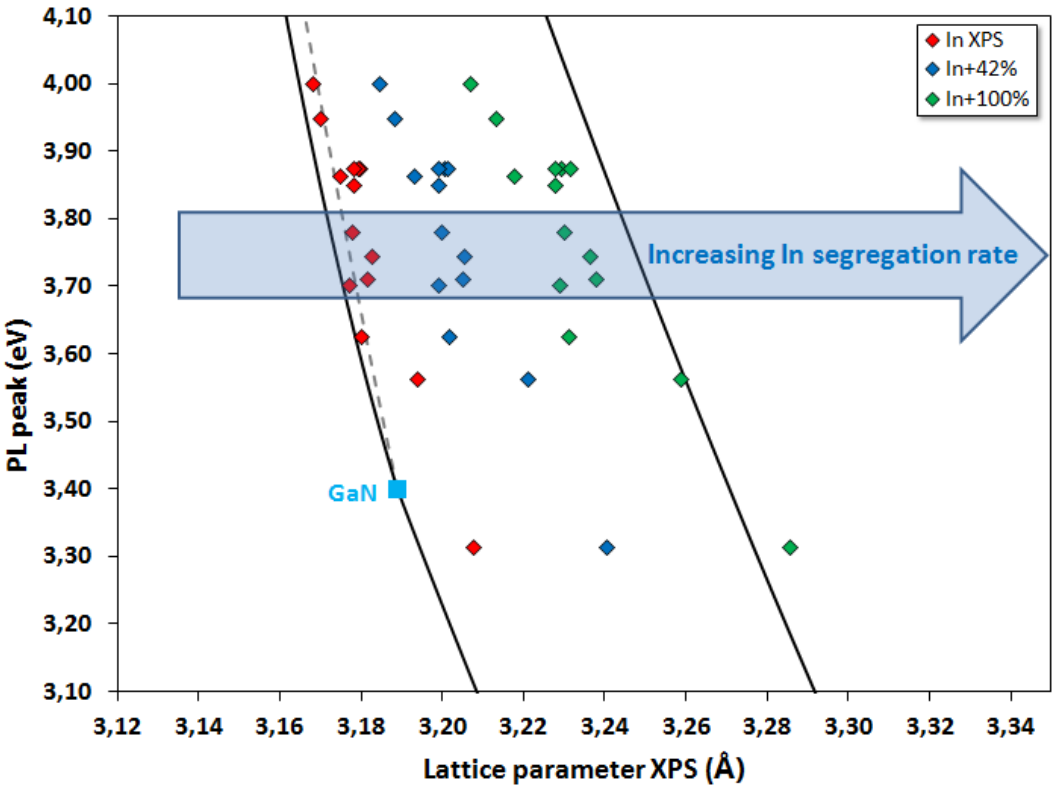

Fig. 5.9 – Theoretical influence of indium segregation rate on a lattice parameter. Correlation with PL peak position.

preparation of III-N materials can be subject to difficulties like gallium implantation [8][9]) since it allows the detection of composition variations over areas with a diameter of 20nm [10]. This is the next step for an optimal measure of the indium segregation and its quantification. It would strongly enhance the photoluminescence results analysis. Also, previously, we did some TEM measurements on sample 1. The EDX analyses on the InAlN layer of sample 1 (cf. figure 5.10) do not appear to demonstrate any segregation of indium. This could be for a variety of reasons. Perhaps this sample had less segregation, perhaps the measurement lacks sensitivity due to the effects of projection on the segregation or that the contrast of the blue color is not large enough to perceive this segregation. Finally, perhaps further work with XRD RSM, using longer more detailed scans would enable the measurement of two different peaks, to clearly identify the different phases in the layers.

5.2 | Gallium pollution in MOCVD reactors growing Ga containing alloys

In almost all of the InGaAlN layers we investigated previously, the XPS measurements showed gallium incorporated in various quantities. We decided to understand how the gallium content evolved with growth parameter and to see if this was linked with the TMIn flow. Finally we found a technical solution to grow pure InAlN samples.

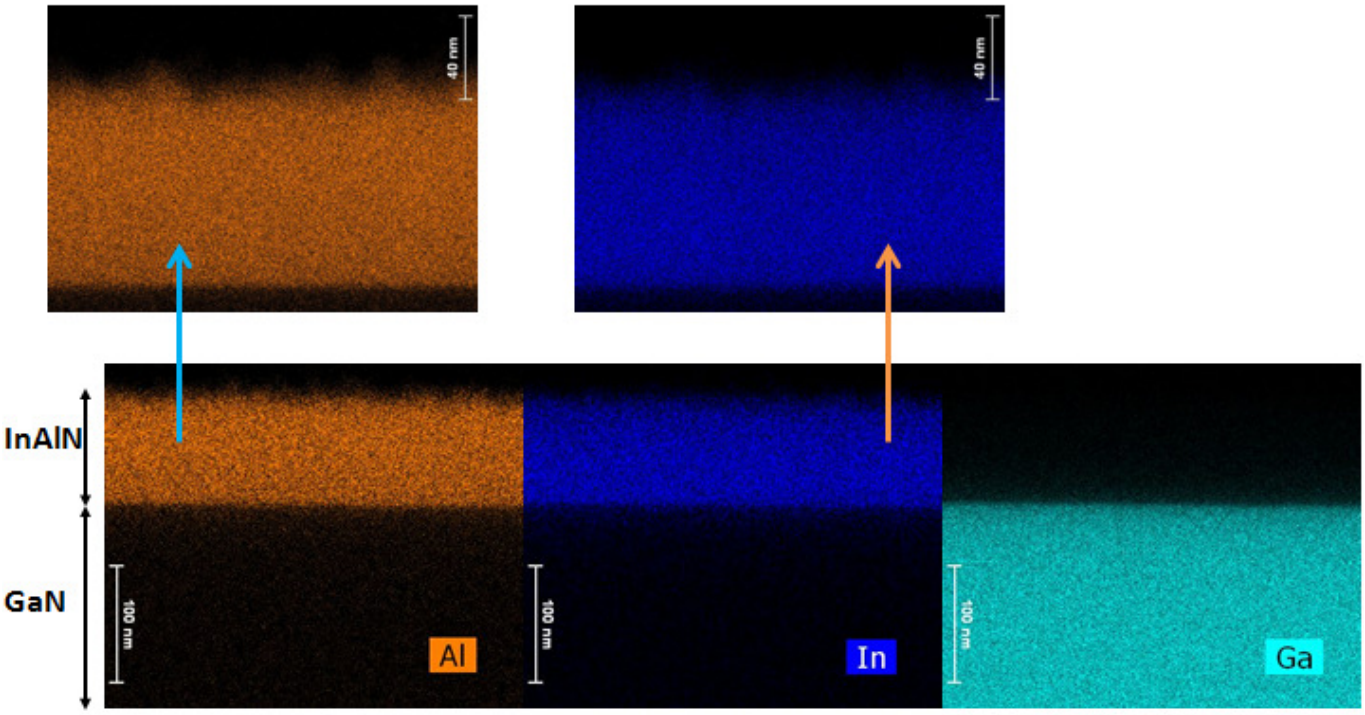

Fig. 5.10 – EDX analysis of TEM pictures of InAlN/GaN (sample 1)

5.2.1 | Calculation of a virtual TMGa flow from pollution sources in the reactor

To understand how growth parameters have an impact on gallium incorporation, we calculated an effective TMGa flow coming from the pollution sources as if there were a real TMGa flow. The calculation was performed as follows. First we divide the total InGaAlN quaternary layer with a thickness $t_{InGaAln}$ into three InN, GaN, AlN binary layers with respective thicknesses : $t_{InN} = \%In \times t_{InGaAlN}$, $t_{GaN} = \%Ga \times t_{InGaAlN}$, and $t_{AlN} = \%Al \times t_{InGaAlN}$. In the same way we can define the growth rate of each binary by : $Vg_{InN} = \%In \times Vg_{InGaAlN}$, $Vg_{GaN} = \%Ga \times Vg_{InGaAlN}$, and $Vg_{AlN} = \%Al \times Vg_{InGaAlN}$.

Now, we assume that our effective TMGa flow is normalized compared to TMAl flow. It is simpler to normalize the layers relative to the TMAl, because indium is volatile and this can complicate the calculations. For this normalization, the ratio of TMGa to TMAl in the gas phase is considered to be the same as the ratio of Ga content to Al content in the solid phase. This gives the equation :

$$\frac{TMGa_{Effectiveflow}}{TMAl_{Realflow}} = \frac{Vg_{GaN}}{Vg_{AlN}} \tag{5.1}$$

If we apply equation 5.1 to our experimental points we can produce the graph shown in figure 5.11. This is a plot of many different samples grown at various temperatures, growth rates and indium flows. Despite this wide variety of parameters, the graph shows a linear evolution of TMGa effective flow coming from the pollution versus real TMIn flow ; with only the carrier gas and the chamber pressure significantly changing the behavior. We verified that there was no external source of gallium reaching the reactor, and so we have to assume that the gallium is desorbing from the GaN deposition on the walls which occurred during the growth of our buffer layers.

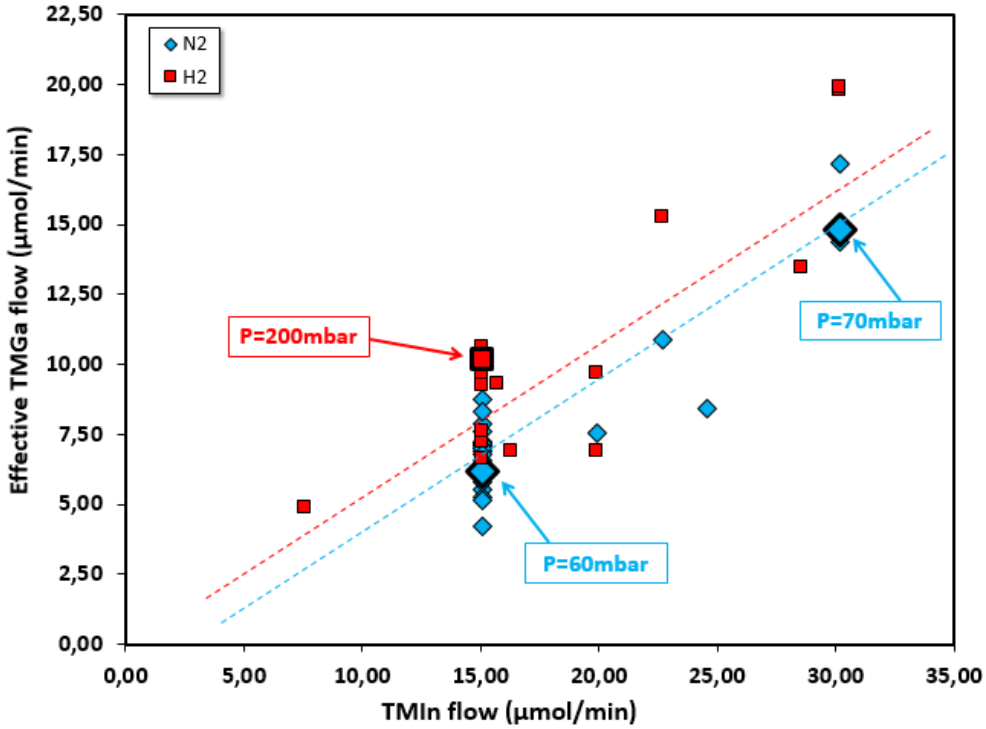

Fig. 5.11 – Effective TMGa flow coming from the pollution versus real TMIn flow. Except for two points indicated by arrows, all the other samples were grown at 100mbar.

Figure 5.11 implies that increasing the TMIn flow will always increase the pollution by gallium, and therefore suggests that the TMIn is somehow catalyzing the desorption of gallium from the chamber. The only parameter which seem to affect the gallium desorption are the carrier gas and the pressure. The use of hydrogen as a carrier gas increases the pollution, but this change may be more related to a decrease of the indium content therefore promoting an increase of the gallium content. In any case, as we have shown in the previous chapter, this is a difficult condition for InAlN growth. The reduction of chamber pressure appears to cause a slight improvement in gallium pollution, but the effect is very limited.

We did not see a clear effect of temperature on this relationship, which means that potentially a reduction in TMIn flow accompanied by a reduction in temperature (which has been previously seen to increase indium incorporation) could be a way to keep the indium constant in the layers while reducing the gallium pollution. However, this would only give a slight decrease, so a more radical solution is required.

5.2.2 | Cleaning test with Cl_2 : growth of pure InAlN

As the gallium appears to be coming from the wall and showerhead deposition during the GaN layer growth preceding the InGaAlN layers, we performed a test using the Cl_2 cleaning of the chamber to avoid this effect (cf. figure 5.12). After the GaN layer was grown, the sample was removed from the chamber and stored in a load-lock under low pressure N2 atmosphere. The chamber was cleaned, before reintroducing the wafer to the chamber and performing growth of the InAlN.

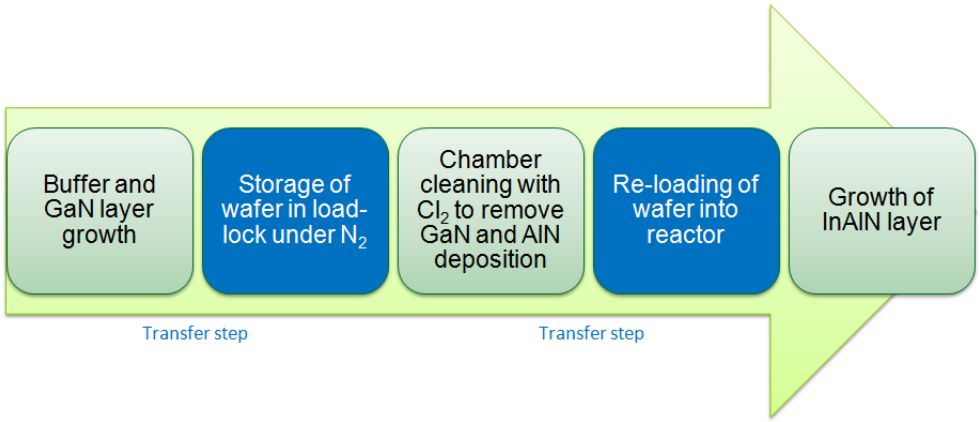

Fig. 5.12 – Cleaning process between GaN and InAlN layers.

The resulting InAlN layers are totally free of gallium, when using either carrier gas, confirming the hypothesis of the source of the gallium as the wall or the showerhead in the growth chamber. And even more interestingly, this significantly increased the indium content in the layers. Under nitrogen we got 18% indium and 11% under hydrogen, where without the cleaning, using the same conditions, we had previously incorporated only 7.5% and 4% respectively. This may suggest that indium was in competition with gallium for its incorporation into the layer, or that the interaction between TMIn and the chamber, which resulted in the gallium pollution, was also consuming some of the indium.

The surface morphology of these four samples, with and without clean, and under the two carrier gases, are shown in figure 5.13. There is not a huge difference with and without cleaning, but globally we see a smoother surface morphology after cleaning, even though we have a higher indium content. This is again a positive result, showing the potential of using the cleaning between wafers to get high quality layers without gallium incorporation.

Finally, the sheet resistance of the layer with 18% indium was measured, resulting in a value of 250 Ohm/sq, showing that the GaN channel layer was not strongly impacted by its removal from the chamber during the cleaning. 250 Ohm/sq was also the sheet resistance value measured on the wafer grown without a cleaning process. That suggests that such a low 2DEG resistivity is more related to the presence of an AlN spacer [11][12][13][14] we placed on both samples (before and after cleaning, under nitrogen). A similar layer with 7.5% indium, the wafer without a cleaning process between the GaN and the InGaAlN layers, showed us a sheet resistivity above 350 Ohm/sq.

5.3 | Surface diagram of InGaAlN layers

In the previous chapter, we have measured a wide variety of surface morphologies of our InGaAlN samples across several growth parameters. We can assemble these images to look for trends, allowing us to classify and group morphologies according to different growth conditions.

Figure 5.14 shows how the topology of InGaAlN is changing when we vary the growth temperature and indium content. First of all, a very fine grain structure seems to appear at low temperatures

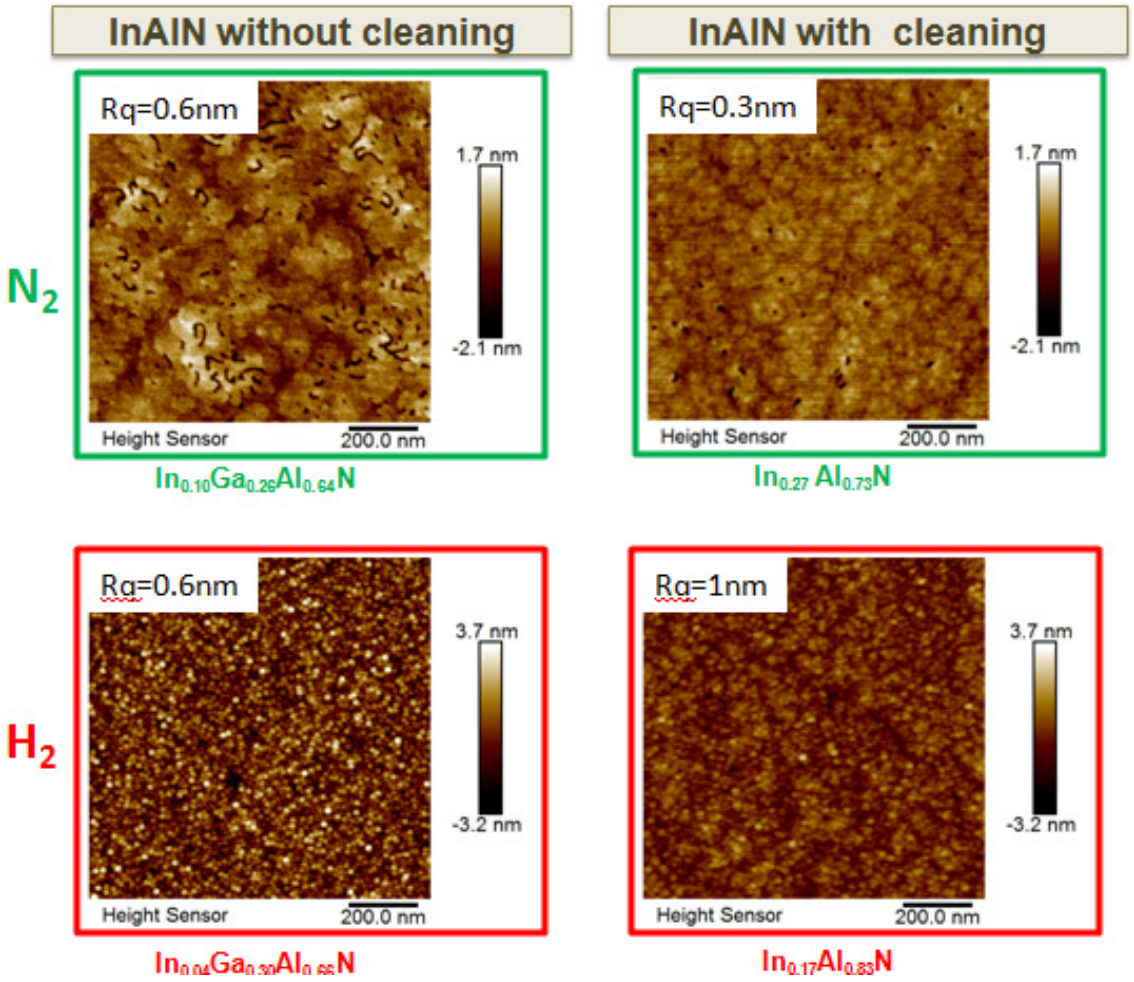

Fig. 5.13 – Comparison between topologies (1x1μm^2 AFM pictures) and compositions (XPS), of InGaAlN samples with and without Cl_2 cleaning after the GaN buffer layers.

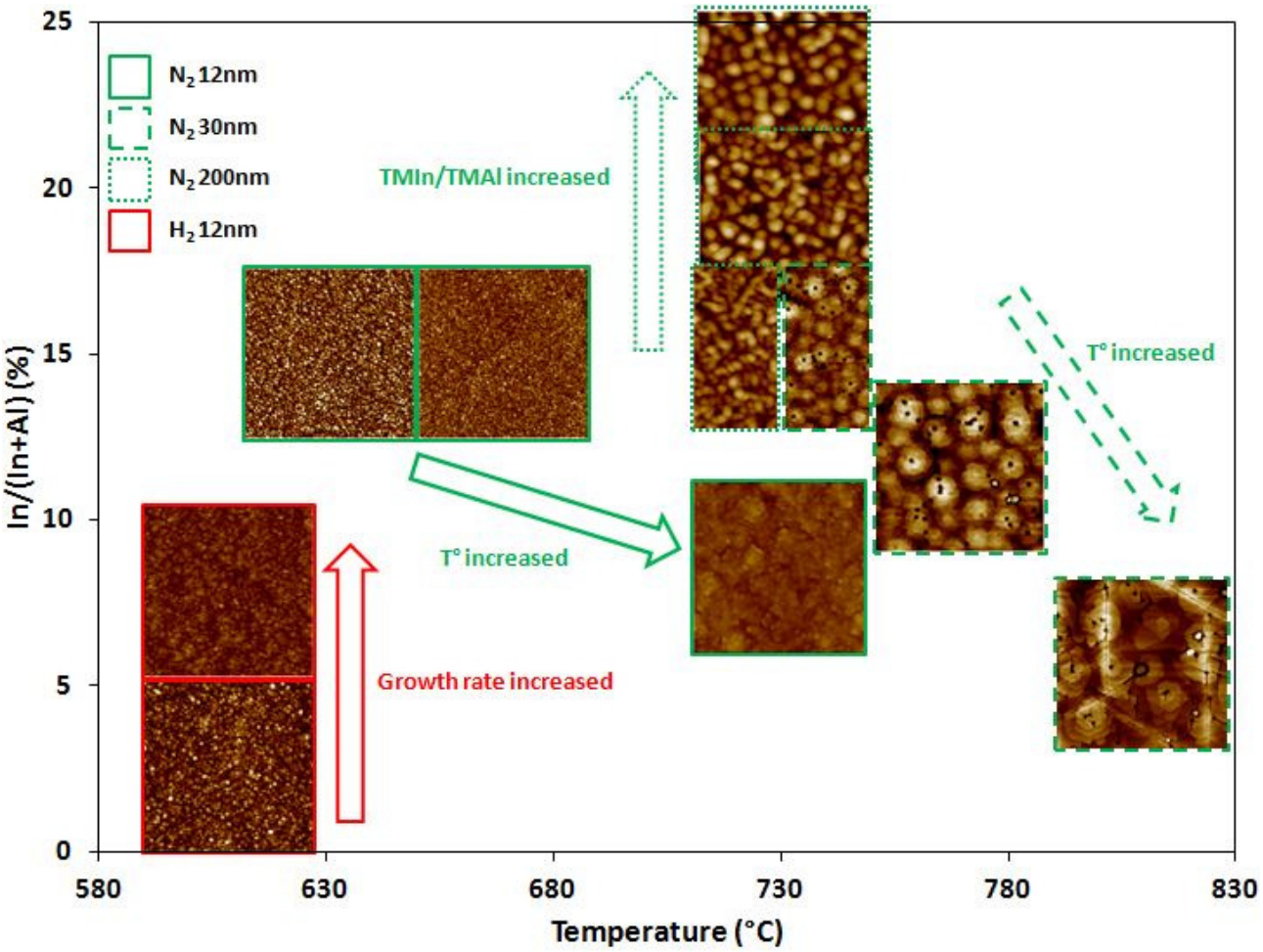

Fig. 5.14 – Surface diagram of InGaAlN samples using 1x1μm^2 AFM pictures. Correlation of morphology, indium content and temperature.

below a certain threshold between 670˚C and 730˚C for 12nm thick samples. Typically, at 730˚C the step structure is favored for these thinner structures less than 30nm. At this temperature we also see two other cases. For 30nm layers, we see that round steps are appearing that reminds us the morphology we see usually during the growth of III-N using MBE technique and we call spiral hillocks [15]. These round structures become flatter and larger as the indium content is decreased and as the gallium is increased. This starts to resemble the growth of AlGaN layers. Finally as the thickness is increased further, a larger grain structure is appearing. As these layers being thicker, the atoms are exposed to longer growth time, and has more time to move in the crystal lattice to regroup and form islands.

In figure 5.15, we reproduce the same graph as figure 5.14 except that we have superposed the series of samples with a change in the growth rate at constant temperature. The changes in the morphology correlate well with the similar trend occurring with an increase in temperature. Increasing growth rate reduces effective adatom mobility by giving the atoms less time to move at the surface ; this is also an effect of decreasing the temperature of the growth, as this reduces directly the surface mobility. The fact that the temperature and growth rate have the same effect on surface morphology suggests that the morphology is primarily governed by the surface mobility of adatoms.

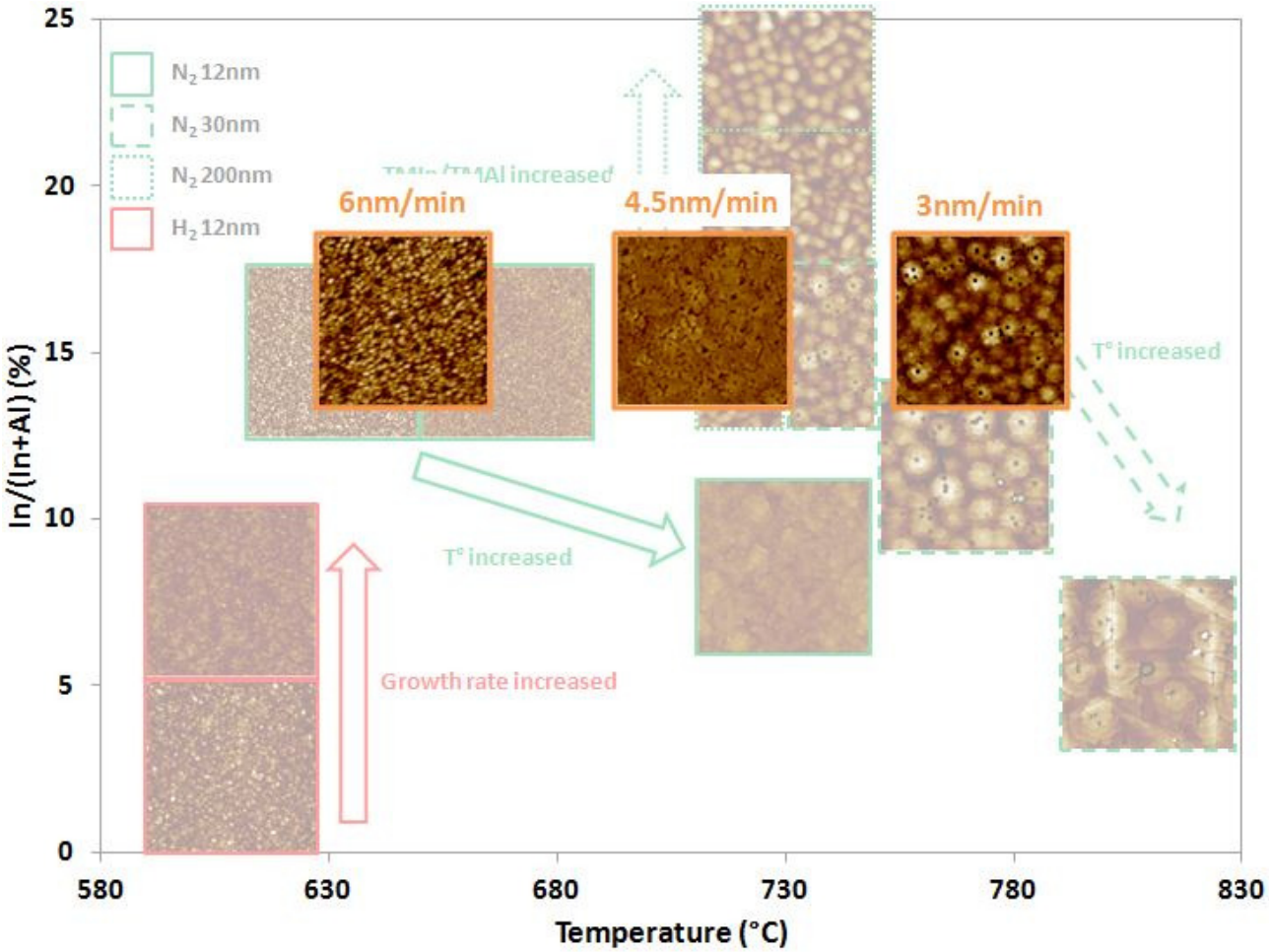

Fig. 5.15 – Surface diagram of InGaAlN samples using 1x1μm^2 AFM pictures. Correlation of morphology, indium content and temperature, with samples showing differences in growth rates superposed at 730°C.

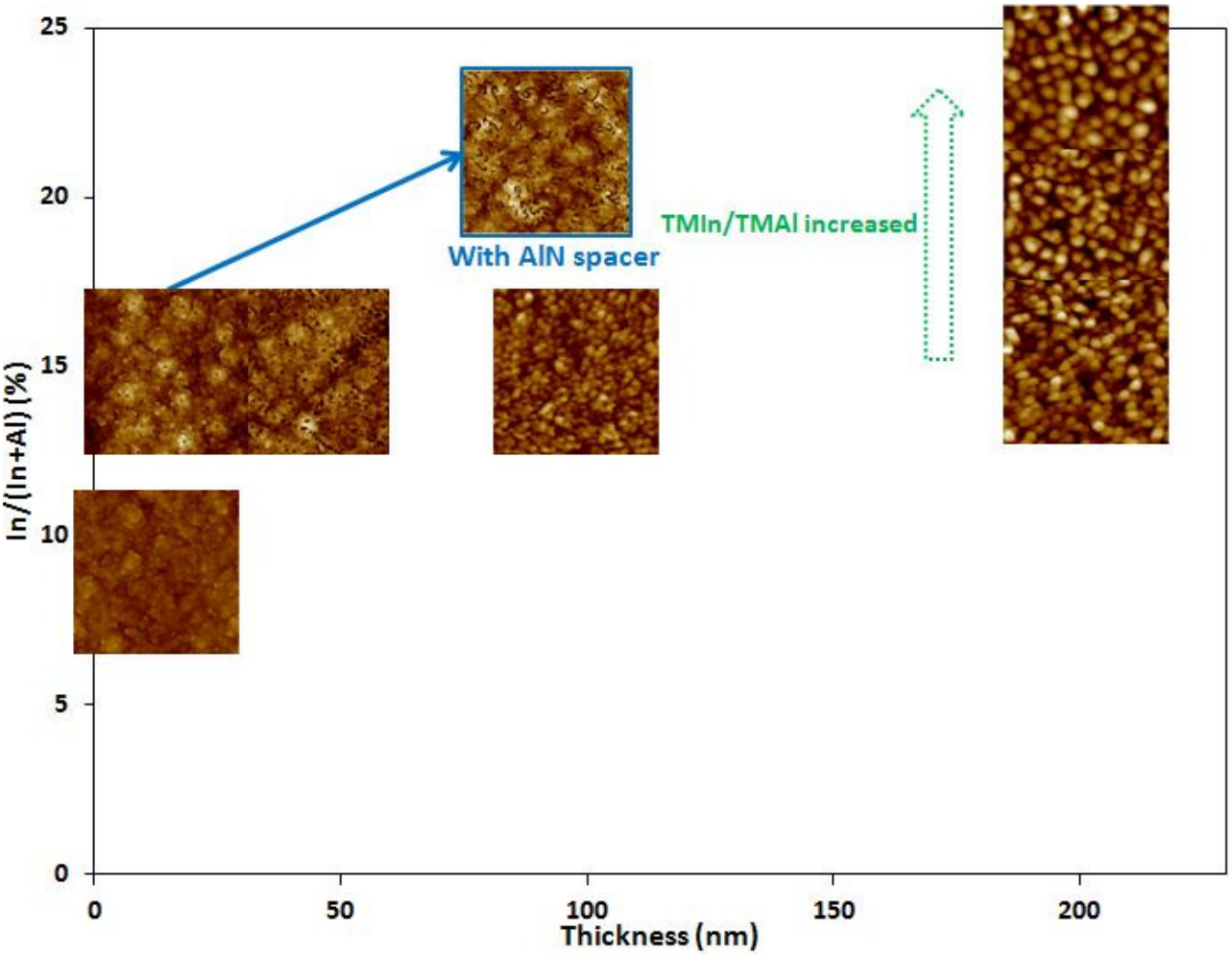

Fig. 5.16 – Surface diagram of InGaAlN samples using 1x1μm^2 AFM pictures. Correlation of morphology, indium content and thickness at 730°C.

To finish, figure 5.16 shows the correlation between the topology, the thickness and the indium content. This mostly gives us the transition between 12nm and 200nm thicknesses. The grains at the surface are at least formed at 100nm and increase in size then. We also see how the surface is roughening between 12nm and 30nm with the formation of holes outside dislocation centers we usually see in the middle of round step structures. We also added the surface morphology of a 12nm thick InGaAlN with an AlN spacer to compare at least at 12nm thickness the topology, and we show in figure 5.19, that there is not a significant difference with the addition of the AlN spacer. Some little curved defaults are visible probably induced by the slight stress induced by the spacer on the InGaAlN spacer.

5.4 | Electrical characterization : Rsheet measurements

As described in chapter 2, a 4-points Rsheet tool has been developed at LETI to measure HEMT structures. This technique uses high voltage to cause electrical breakdown across the barrier layer. This works very well for typical AlGaN layers, but we were not always able to measure our InGaAlN layers. When we were able to breakdown the barrier layer by applying this high voltage, we measured the sheet resistivity of the 2DEG. We think that the problems of electrical breakdown in the barrier were linked to two factors. Firstly, the thicker the barrier layer, the more the applied voltage has to be high.

That is the reason why thick barrier layers of even 30nm and higher did not automatically allow us to get a 2DEG resistivity measurement. Secondly, the barrier composition, if too rich in aluminum, seems to push the minimum threshold voltage too high, as we are limited to 200V on our measurement tools.

If we first look at figure 5.17 we can see all the samples for which we were able to measure the value of sheet resistivity, which we have plotted against the total polarization in the barrier layers. In blue, we can see all the samples made of just an InGaAlN barrier layer on GaN pseudosubstrate. Two thicknesses are shown : 12nm and 30nm represented by square and diamond markers respectively. There is a trend that indicates that the more the polarization of the barrier layer is high the more the 2DEG resistivity is low. This is usually what we observe in the case of AlGaN layers usually grown. Indeed, normally we consider that higher polarisation gives more Ns, so that would be coherent with our graph. This may also change the mobility, but this is probably less critical. Nevertheless three points are out of these trend at nearly 730 Ohm/sq, 1900 Ohm/sq and 1630 Ohm/sq. Interestingly, if we use the Rsheet values measured at the edge of the three wafers rather than at the center, we get the results shown in figure 5.18. In this case we can see that new Rsheet values are more coherent. In the case of 30nm thick InGaAlN layers, we now have a trend decreasing the Rsheet from 1000 Ohm/sq to just over 400 Ohm/sq, while the trend for the 12nm layers is similar, but shifted to lower polarizations. The difference between the two thicknesses is normal since the more you increase it the more the charge carrier density is high in the 2DEG, up to a critical thickness. [16]

We currently do not have a clear explanation for the high values of Rsheet in the centre for some wafers, and this would need to be further studied to better understand the differences. As well as differences in the layers, there may also be factors influencing the quality of the Rsheet measurements, which are difficult to perform on these layers.

Figure 5.17 also shows a variety of points using an AlN spacer of 1nm between the thick GaN and the barrier layer (green points). It has already been observed that the AlN spacer has a significant effect on the 2DEG resistivity with its high band gap energy of 6.2eV, giving an increased Ns injection and better confinement of 2DEG electrons in the GaN layer which improves the mobility. The effect of AlN has been reported in a lot of studies [11][12][13][14]. For our data, there is now no real effect of barrier polarization on Rsheet value. All of the values were below 400 Ohm/sq, showing the very strong effect of the AlN spacer. We succeeded in making two samples with excellent Rsheet values of 240 Ohm/sq and 230 Ohm/sq. The first is a 12nm thick $In_{0.10}Ga_{0.26}Al_{0.64}N$ barrier layer grown at 730°C with a growth rate of 3nm/min. The second is a pure $In_{0.27}Al_{0.73}N$ grown in the same conditions. Such values of resistivity show the interest of InAlN or even InGaAlN compared to AlGaN barrier layers. However, we have to keep in mind that the very low Rsheet values occur only with the spacer layer.

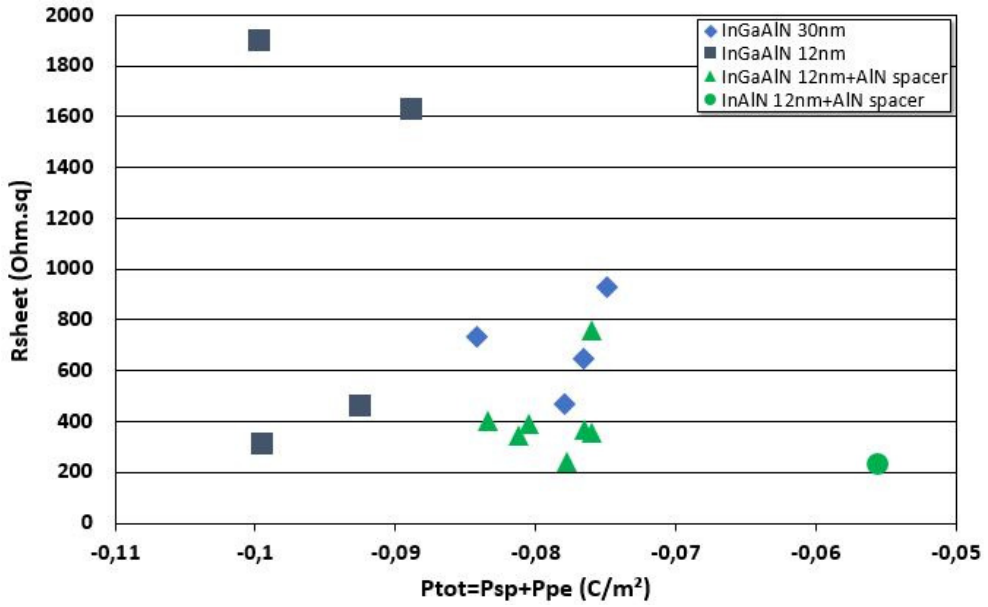

Fig. 5.17 – Rsheet values of InGaAlN and InAlN samples with or without AlN spacer, versus total polarization of the barrier layer. Measurements at the centre of the wafer.

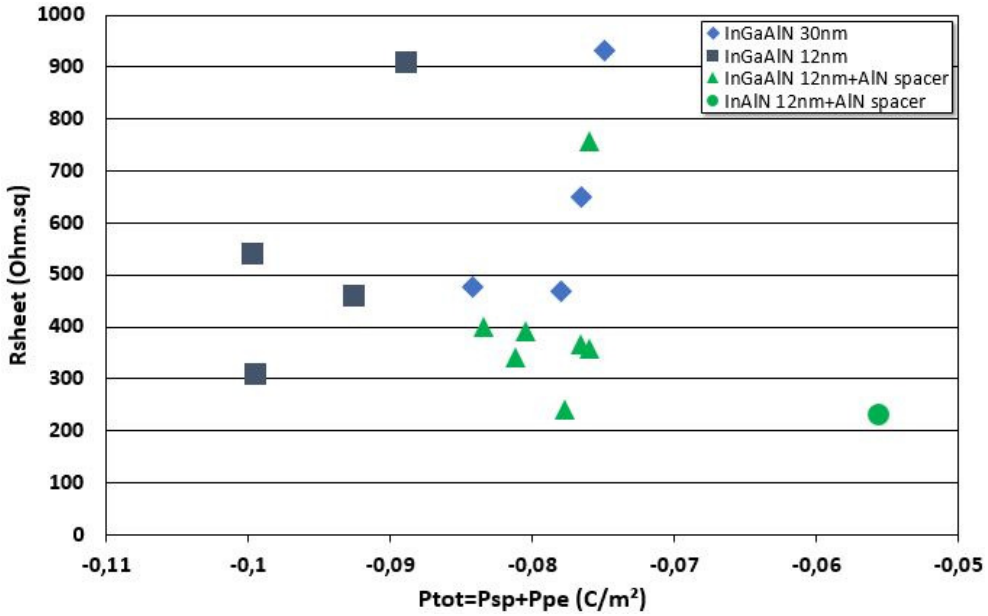

Fig. 5.18 – Rsheet values of InGaAlN and InAlN samples with or without AlN spacer, versustotal polarization of the barrier layer. Measurements at the edge of the wafer.

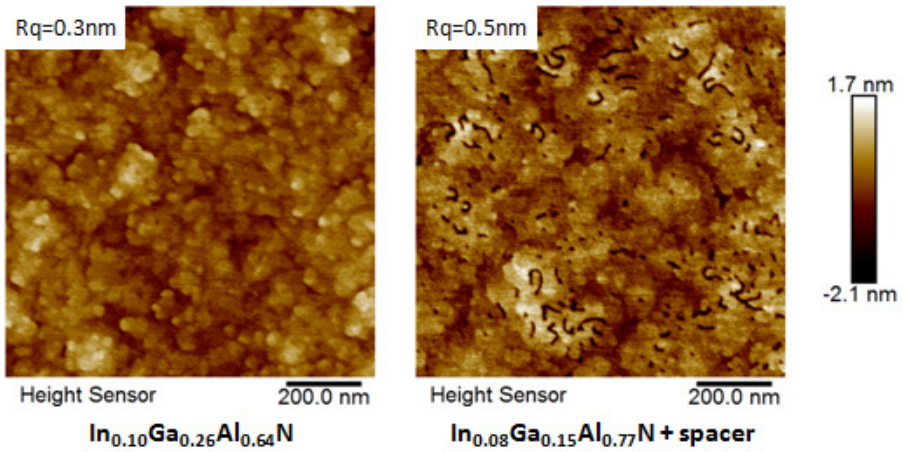

Fig. 5.19 – Comparison of 1x1μm^2 AFM pictures of two 12nm thick InGaAlN samples grown under N_2 with and without an AlN spacer

Summary of chapter 5

We drew the correlation between band gap energy and lattice parameter of many samples. The values of band gap energies are potentially distorted because samples are subjected to phase separation between indium rich and poor phases phenomenon. Therefore the recombination of electron-hole pairs occurs in indium-rich area since the band gap energy is lower compared to the rest of the material. We find that many of our sample points are close to the boundaries formed by the curved lines joining the GaN and AlN binaries, despite the relatively high proportion of indium measured by XPS in the layers.

We tried to measure the indium segregation rate by employing AES measurements, with success only on one sample. This case showed indium composition fluctuations at the surface but we require more measurements than those we have done to really start to understand and quantify the indium segregation phenomenon. Also AES is a surface characterization but phase separation also occurs inside the material. Atom probe tomography would be an interesting technique to further advance this work. The reader could refer to reference [17] to get some interesting points on indium segregation not from a point of view of thermal equilibrium but from that of kinetics.

Then we examined with gallium pollution in our MOCVD reactor. We found an empirical model which predicts the gallium incorporation in samples from gallium pollution sources versus the TMIn flow. The two are strongly correlated, which can make indium integration complex especially under hydrogen carrier gas. In parallel we developed a process to avoid this pollution by clearing the rector between the GaN substrate and the In(Ga)AlN layer.
Next, we summarised the surface morphologies measured by AFM depending on different growth conditions and we built a kind of surface phase diagram which classify the surface morphology looks like, with reference to grains, step structure, cracks, and so on. This allowed us to see a clear correlation between the effect of an increase in temperature and an decrease in growth rate, which implies that the surface morphology is driven by surface mobility.
To finish we measured the sheet resistivity of many of our samples and correlated this vale to the band gap. In the case of an InGaAlN layer on GaN substrate without AlN spacer, the increase the band gap energy decreases the sheet resistivity. On the other hand if we place an AlN spacer known to confine better the 2DEG in the GaN substrate at the interface, the sheet resistivity does not significantly change with the changing band gap energy.

Bibliographie

[1] J. Jinschek, R. Erni, N. Gardner, A. Kim et C. Kisielowski, « Local indium segregation and bang gap variations in high efficiency green light emitting ingan/gan diodes », *Solid State Communications*, vol. 137, no. 4, p. 230 – 234, 2006. 132

[2] B. P. Burton, A. van de Walle et U. Kattner, « First principles phase diagram calculations for the wurtzite-structure systems aln-gan, gan-inn, and aln-inn », *Journal of Applied Physics*, vol. 100, no. 11, p. 113528, 2006. 132

[3] Z. Deng, Y. Jiang, W. Wang, L. Cheng, W. Li, W. Lu, H. Jia, W. Liu, J. Zhou et H. Chen, « Indium segregation measured in ingan quantum well layer », *Scientific Reports*, vol. 4, 2014. 132

[4] D. Doppalapudi, S. N. Basu, K. F. L. Jr. et T. D. Moustakas, « Phase separation and ordering in ingan alloys grown by molecular beam epitaxy », *Journal of Applied Physics*, vol. 84, no. 3, p. 1389–1395, 1998. 132

[5] N. Duxbury, U. Bangert, P. Dawson, E. J. Thrush, W. V. der Stricht, K. Jacobs et I. Moerman, « Indium segregation in ingan quantum-well structures », *Applied Physics Letters*, vol. 76, no. 12, p. 1600–1602, 2000. 132

[6] T. Matsuoka, « Phase separation in wurtzite in1-x-ygaxalyn », *MRS Internet Journal of Nitride Semiconductor Research*, vol. 3, 1998. 132

[7] S. R. Lee, A. F. Wright, M. H. Crawford, G. A. Petersen, J. Han et R. M. Biefeld, « The band-gap bowing of alxga1-xn alloys », *Applied Physics Letters*, vol. 74, no. 22, p. 3344–3346, 1999. 132

[8] F. Tang, M. P. Moody, T. L. Martin, P. A. Bagot, M. J. Kappers et R. A. Oliver, « Practical issues for atom probe tomography analysis of iii-nitride semiconductor materials », *Microscopy and Microanalysis*, vol. 21, no. 3, p. 544–556, 2015. 141

[9] M. K. Miller, K. F. Russell, K. Thompson, R. Alvis et D. J. Larson, « Review of atom probe fib-based specimen preparation methods », *Microscopy and Microanalysis*, vol. 13, no. 6, p. 428–436, 2007. 141

[10] E. C. Kyle, S. W. Kaun, F. Wu, B. Bonef et J. S. Speck, « High indium content homogenous inaln layers grown by plasma-assisted molecular beam epitaxy », *Journal of Crystal Growth*, vol. 454, p. 164 – 172, 2016. 141

[11] S. Elhamri, W. C. Mitchel, W. D. Mitchell, G. R. Landis, R. Berney et A. Saxler, « Study of the effects of an aln interlayer on the transport properties of algan/aln/gan heterostructures grown on sic », *Applied Physics Letters*, vol. 90, no. 4, p. 042112, 2007. 144, 149

[12] J. Xue, J. Zhang, W. Zhang, L. Li, F. Meng, M. Lu, J. Ning et Y. Hao, « Effects of aln interlayer on the transport properties of nearly lattice-matched inaln/gan heterostructures grown on sapphire by pulsed metal organic chemical vapor deposition », *Journal of Crystal Growth*, vol. 343, no. 1, p. 110 – 114, 2012. 144, 149

[13] J. XIE, X. NI, M. WU, J. H. LEACH, Ümit ÖZGÜR et H. MORKOÇ, « High electron mobility in nearly lattice-matched alinn/aln/gan heterostructure field effect transistors », *Applied Physics Letters*, vol. 91, no. 13, p. 132116, 2007. 144, 149

[14] M. GONSCHOREK, J.-F. CARLIN, E. FELTIN, M. A. PY et N. GRANDJEAN, « High electron mobility lattice-matched alinn/gan field-effect transistor heterostructures », *Applied Physics Letters*, vol. 89, no. 6, p. 062106, 2006. 144, 149

[15] B. HEYING, E. J. TARSA, C. R. ELSASS, P. FINI, S. P. DENBAARS et J. S. SPECK, « Dislocation mediated surface morphology of gan », *Journal of Applied Physics*, vol. 85, no. 9, p. 6470–6476, 1999. 146

[16] O. AMBACHER, J. SMART, J. R. SHEALY, N. G. WEIMANN, K. CHU, M. MURPHY, W. J. SCHAFF, L. F. EASTMAN, R. DIMITROV, L. WITTMER, M. STUTZMANN, W. RIEGER et J. HILSENBECK, « Two-dimensional electron gases induced by spontaneous and piezoelectric polarization charges in n- and ga-face algan/gan heterostructures », *Journal of Applied Physics*, vol. 85, no. 6, p. 3222–3233, 1999. 149

[17] G. PERILLAT-MERCEROZ, G. COSENDEY, J.-F. CARLIN, R. BUTTÉ et N. GRANDJEAN, « Intrinsic degradation mechanism of nearly lattice-matched inaln layers grown on gan substrates », *Applied Physics Letters*, 2013. 152

6 | InGaAlN capping by SiN and GaN

Sommaire

6.1 SiN capping of InGaAlN layers 156
6.1.1 SiN deposition under nitrogen 156
6.1.2 SiN deposition under hydrogen 161
6.2 GaN capping of InGaAlN and InAlN layers 164
6.2.1 Thickness GaN cap optimization 166
6.2.2 Cap temperature variations 167
6.2.3 GaN cap on InAlN barrier layer 169
Bibliographie 175

In order to produce devices requiring different process steps, we would like to protect our barrier layer by capping it with a thin layer of a stable material like SiN, AlN or GaN. The heterostructure can be subjected to thermal budgets which could make indium desorb from the layer, and changing the surface state can also change the electrical properties of the 2DEG. Secondly, a surface oxidation after the epitaxy process is detrimental for further devices operation since it also degrades the 2DEG[1][2][3]. Finally roughness, surface defects and dislocations [4] at the interface between the different metal levels of the devices and the InGaAlN barrier layer can produce electron traps and scattering effect still decreasing the resistivity of the 2DEG [5][6][7]. An in-situ deposition of SiN, or epitaxial growth of GaN can smooth the surface, allowing us to avoid indium desorption problems, and also stabilize the surface states [3]. We tried to implement these two materials on our barrier layers with the aim of having a layer thick enough to cover the roughness of the layer below, and that shows a good morphology and surface structure.

6.1 | SiN capping of InGaAlN layers

We started our experiments with the study of SiN passivation. These in-situ layers have been studied a lot for standard AlGaN [4][8][9][10][11][12] layers but are less common for InAlN layers [13][14][15] and quasi inexistent for InGaAlN layers[16][17]. The characterization of these layers can be difficult if they are very thin, but we have several reference points from the work on SiN passivation on AlGaN. For thicker layers greater than a few nanometers, we can measure their thickness by XRR. For very thin layers, too thin for XRR, we can detect the presence of silicon on the top of the barrier layer by XPS measurements, although it is not possible to specify if it is a strong doping or a real SiN layer, as both hypotheses involve Si-N bonds. As indirect measurements, we can look at the morphology of the surface. If we look at an AlGaN barrier layer with and without a 10nm thick SiN cap, we can clearly see the topology changes, as shown in figure 6.1. The roughness decreases with SiN caps compared to AlGaN without cap layers and the morphology is improved. While the AlGaN surface shows a rather chaotic structure, even if we can make out the atomic steps, the surface is much smoother with an SiN layer, whether it has a thickness of 1nm, 2nm, or 10nm. Thus we could expect a similar morphology improvement, even with thin SiN layers on InGaAlN. Also the Rsheet measurements by four points probe performed at LETI on AlGaN/GaN heterostructures including an SiN cap have shown that when we deposit an SiN cap on an AlGaN layer, the measurement noise decreases with increasing SiN layer thickness until a thickness of 2nm, after which the noise doesn't change, as shown in figure 6.2. This can also be used as indirect evidence of an SiN layer.

6.1.1 | SiN deposition under nitrogen

As the use of hydrogen carrier gas tends to give more indium desorption in our InGaAlN or InAlN layers, we performed the first SiN growths under nitrogen. The other growth parameters are identical to those for InGaAlN which means a temperature close to 730°C and pressure of 100 mbar. Even at higher temperatures of around 1000°C typically used for the capping of AlGaN layers, we are still in the kinetic regime of deposition. This means that the growth rate will depend on the temperature, and being nearly 300°C colder, we can expect much slower growth rates.

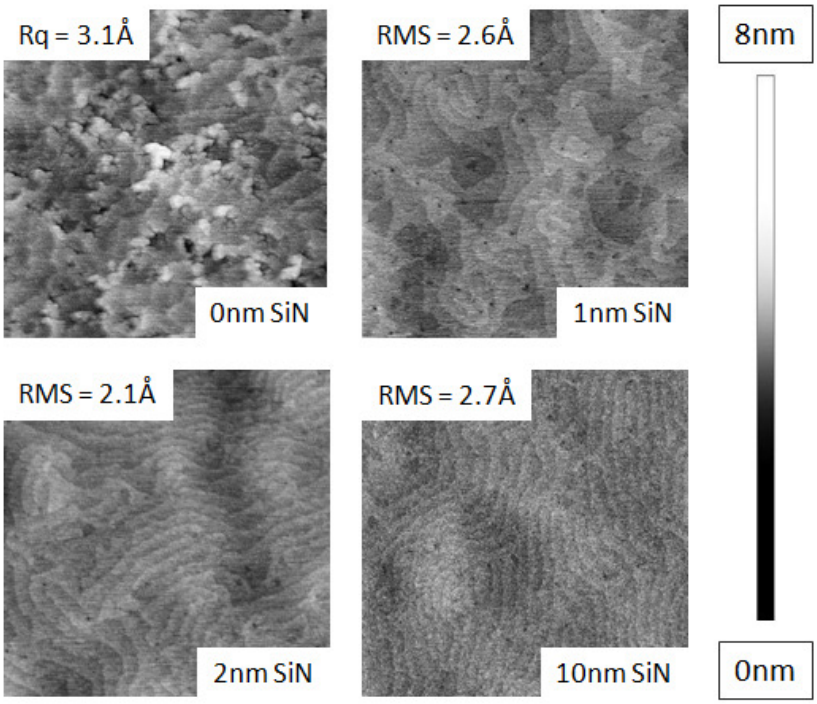

Fig. 6.1 – 1x1μm AFM pictures of 25nm thick $Al_{0.25}Ga_{0.75}N$ layers having different SiN cap thicknesses.

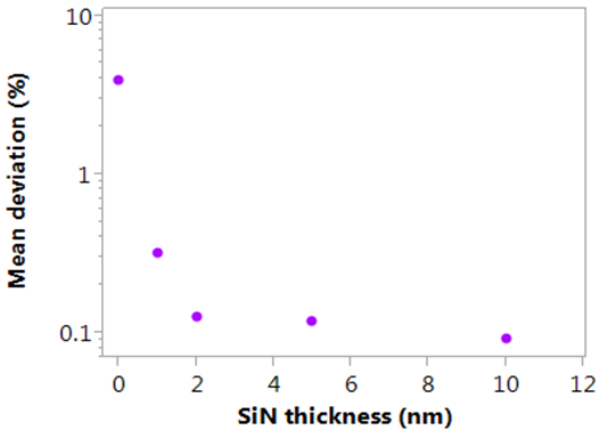

Fig. 6.2 – Comparison of noise in Rsheet measurements on AlGaN barrier layers different thicknesses of SiN cap.

Sample	**SiH4 flow (sccm)**	**Temp (°C)**	**Time (s)**	**Theoretical thickness (nm)**	**Carrier gas : barrier/cap**
1	1000	725	80	0.3	N_2/N_2
2	1000	725	160	0.7	
3	1000	725	320	1.3	
4	1000	825	320	2.8	
5	1000	845	320	3.2	N_2/H_2
6	1000	845	320	3.2	
7	1000	845	960	9.7	
8	1000	750	320	1.6	H_2/H_2

Tab. 6.1 – Summary of SiN cap experiments performed on InGaAlN barriers grown under nitrogen and hydrogen. Theoretical deposition rate and thus thicknesses of SiN are calculated using the Arrhenius law that we can be drawn in kinetic regime (cf. figure 6.3) using experimental data of SiN cap on AlGaN layers deposited under hydrogen. Therefore values for SiN cap under nitrogen are not exactly the real theoretical ones but nevertheless close to reality.

Our MOCVD tool is equipped with one diluted silane inlet, with the input gas of 200ppm silane in N_2. This gas is typically used to dope the GaN and so we are able to deliver only low molar flows of silane. Even with the maximum gas flow of 1000sccm, this is equivalent to 0.2sccm of pure silane, which leads to growth rates of around 100nm/hr at 1000°C. We used this maximum value in all our growth tests to increase our chances of growing an SiN layer. Under nitrogen carrier gas, at 730°C and 830°C, these corresponds respectively to growth rates of 15nm/h and 30nm/h. Under hydrogen carrier gas, at 750°C and 850°C, this corresponds respectively to growth rates of 17nm/h and 35nm/h.

For the first tests, we grew InGaAlN layers under nitrogen and continued the growth of SiN with the same carrier gas. All of our InGaAlN layers were 12nm thick and had the same growth parameter with an $In/(In + Al)$ ratio of 41%, and a growth rate of 3nm/min. In table 6.1 we show a summary of the different SiN conditions tested. The three first caps have a temperature which is the same as that of InGaAlN to avoid desorbing any indium during a temperature ramp. For these samples, we changed the growth time to vary the cap thickness. These wafers were followed by a test at a higher temperature of 825°C to try to increase the growth rate as were in the kinetic regime.

AFM images are shown in figure 6.4 for the three samples grown at 725°C, along with a reference sample without capping. The surface morphology appears nearly identical between the different cap thickness and the sample having no SiN cap. This suggests that there is no SiN cap present. We don't see any improvement in morphology as was seen for SiN grown on AlGaN, shown in figure 6.1.

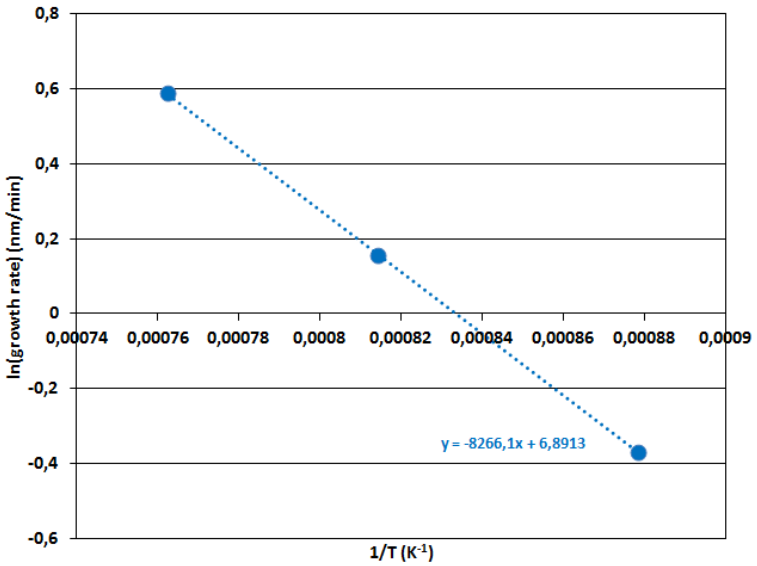

Fig. 6.3 – Natural logarithm of SiN deposition rate versus inverse of deposition temperature. The linear behavior indicates that the growth rate follows the Arrhenius law in kinetic regime.

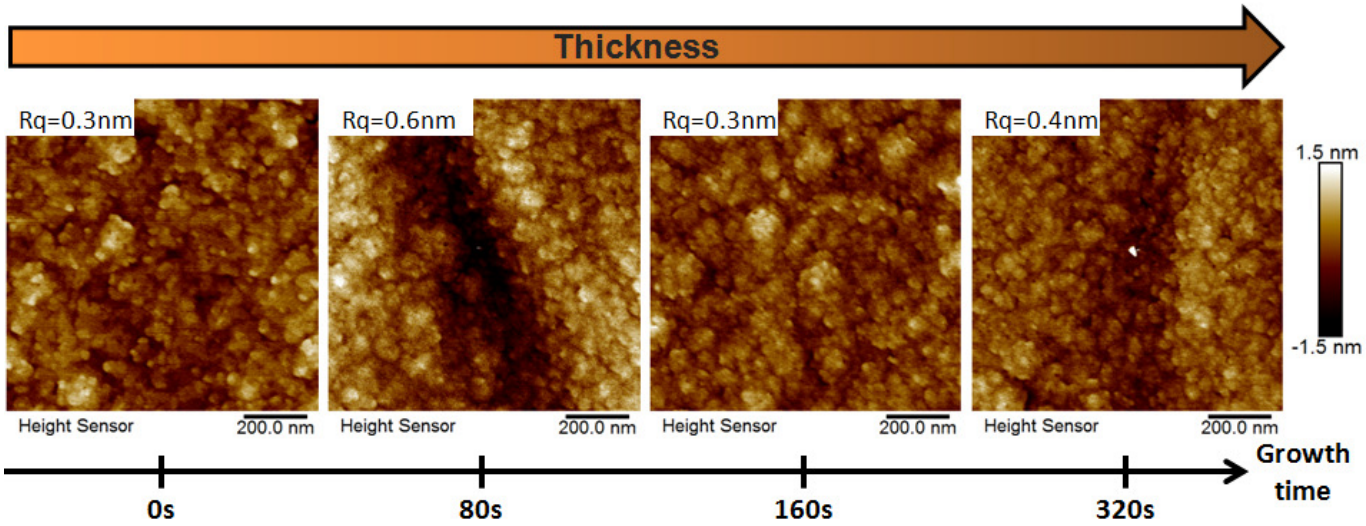

Fig. 6.4 – 1x1μm^2 AFM images of 12nm thick InGaAlN layers having different SiN deposition time grown under nitrogen at 725°C.

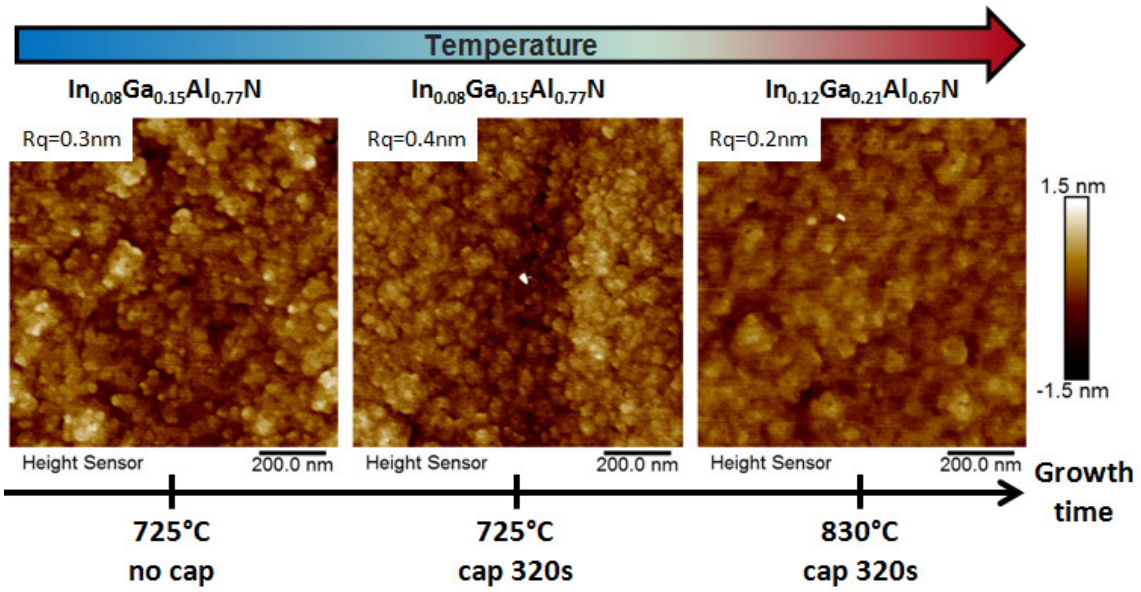

Fig. 6.5 – 1x1μm^2 AFM pictures of 12nm thick $In_{0.08}Ga_{0.21}Al_{0.71}N$ layers having SiN caps grown at different temperatures under nitrogen at 725˚C.

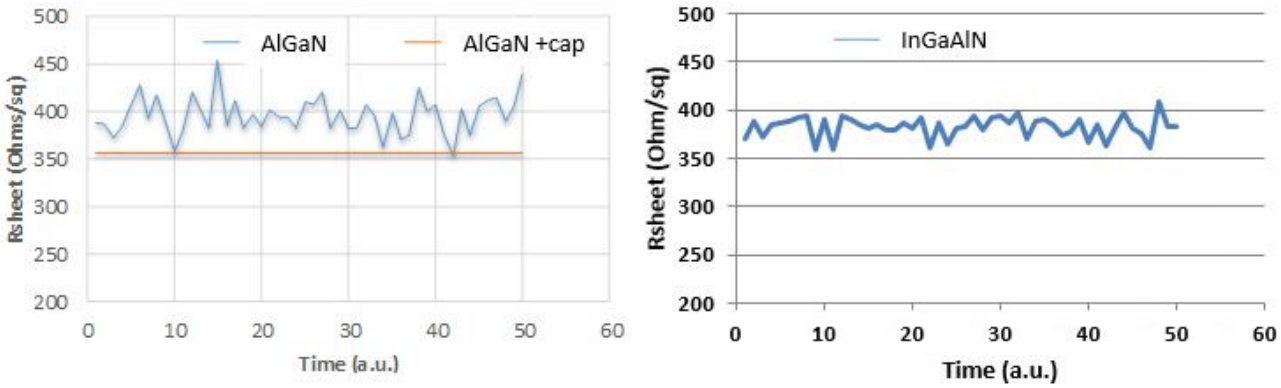

Fig. 6.6 – Comparison between Rsheet measurements on AlGaN barrier layers with and without an SiN cap, and on an InGaAlN barrier with a SiN cap grown at 830˚C during 320s.

The AFM image of the SiN cap layer grown at 830˚C is shown in figure 6.5, along with a reference without cap, and with an SiN at 725˚C. The roughness is lowest with the high temperature cap than the InGaAlN barrier without a cap or with growth at 725˚C, although the morphology is very similar, so it is hard to be sure that there is a difference. There may also be an effect of annealing the InGaAlN layer during the SiN growth. Once again, there is no conclusive evidence that we have grown an SiN layer.

The left hand side of figure 6.6 shows the effect of the SiN cap on Rsheet measurements for AlGaN, where the sheet resistance is measured many times in quick succession. We see that the measurement is constant with an SiN cap, but noisy without the cap, as described in figure 6.2. Returning to the right hand side of figure 6.6, we can see the Rsheet measurement on our sample supposed to have an SiN cap grown at 830˚C. The noise is unchanged compared to other typical uncapped layers, which seems to confirm the fact that no significant SiN layer is deposited. The conclusion was the same for the growth of SiN caps at 725˚C.

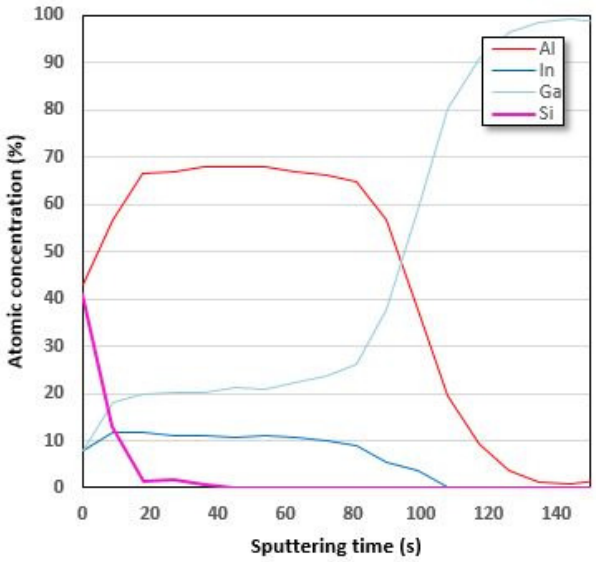

Fig. 6.7 – In, Ga, Al and O concentration profiles by XPS measurement along a SiN cap and InGaAlN barrier layer, both grown under nitrogen.

We also did an XPS measurement on the sample where we attempted to grow an SiN cap at 830˚C under nitrogen (cf. 6.7). Silicon is detected at the surface of this sample, and its profile decreases from the surface, which would imply that we have either a silicon doping or a very thin SiN deposition on the surface of our InGaAlN layer. Note that for all other InAlN or InGaAlN samples grown under nitrogen or hydrogen carrier gas on which we did not try to deposit an SiN layer, we didn't find any silicon incorporated in the layer.

6.1.2 | SiN deposition under hydrogen

After these SiN tests under nitrogen, we switched the carrier gas to hydrogen, which is the typical gas for growing SiN caps on AlGaN barriers. Hydrogen is normally used when we deposit SiN caps on AlGaN, but we were aware that a hydrogen carrier gas was likely to desorb indium from the InGaAlN barrier layer. The switch from nitrogen to hydrogen was performed in a few seconds, and the growth of the SiN layer started immediately for the growth at 750˚C, while for the higher temperature growths, the gas was switched before ramping to higher temperature (due to limitations in the geometry of the growth chamber, which cannot switch nitrogen to hydrogen at higher temperatures). The final experiment was to grow SiN on an InGaAlN barrier which had already been grown under hydrogen. As shown in chapter 4, these conditions were likely to give very little indium incorporation during the InGaAlN growth, and so this is the equivalent of growth of SiN on low temperature AlGaN layers.

As described in table 6.1, we grew the SiN layer for 320s for two samples (750˚C and 850˚C) and 960s for the third one sample (850˚C). Their AFM images are shown in figure 6.8. Here the morphology is very different from the previous samples in figure 6.5, and appear to be strongly affected by the change of growth atmosphere to hydrogen after the InGaAlN barrier. The roughness increased a little and several areas appear separated from each other, with the final sample in particular appearing to have cracks across the whole surface, which we might expect to be due to indium desorption.

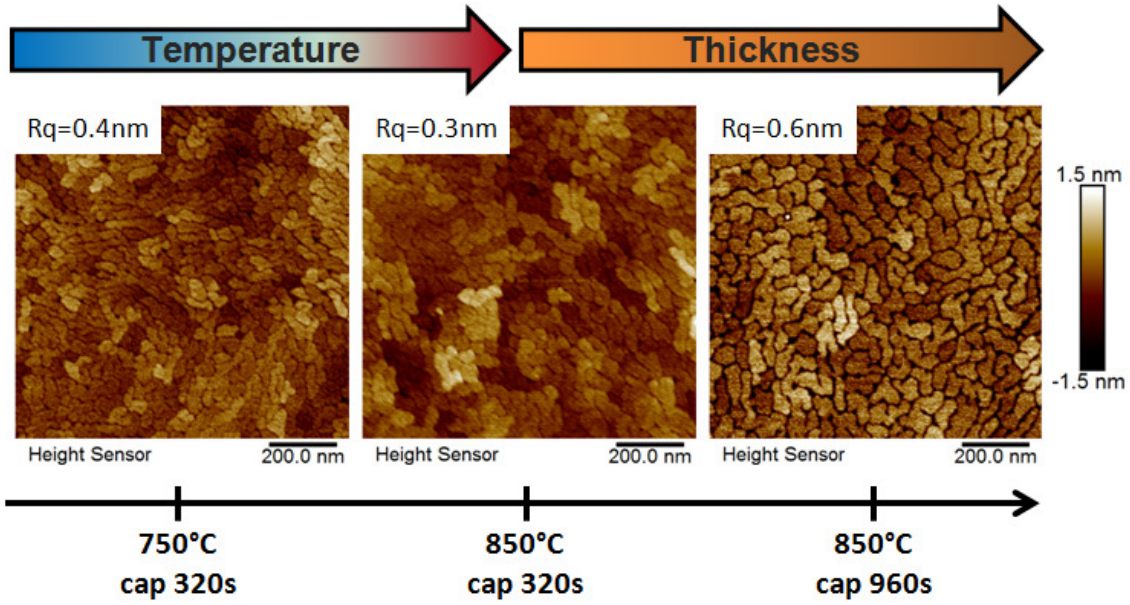

Fig. 6.8 – 1x1μm^2 AFM pictures of 12nm thick $In_{0.10}Ga_{0.19}Al_{0.71}N$ layers having different SiN cap SiN growth temperature grown under hydrogen.

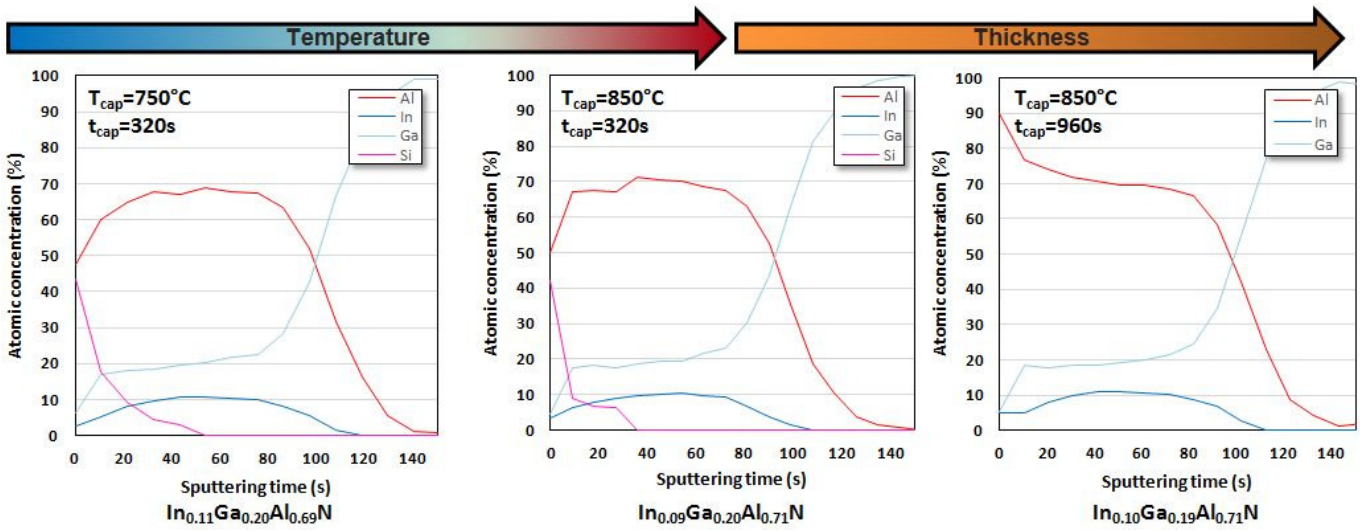

Fig. 6.9 – In, Ga, Al and O concentration profiles by XPS measurement along a supposed SiN cap and an InGaAlN barrier layers, under different cap process conditions. Si element shown only in the first second samples but present in each one.

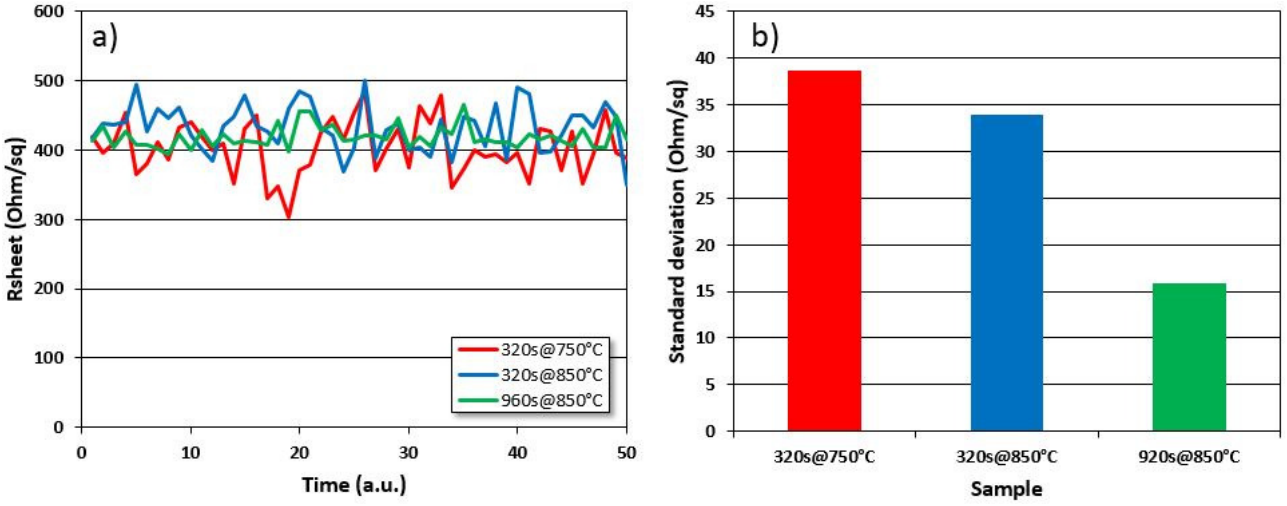

Fig. 6.10 – Rsheet measurements on InGaAlN barrier layers under nitrogen carrier gas with different growth conditions of an SiN cap under hydrogen carrier gas (left). The standard deviation of Rsheet measurements on the same three same samples.(right)

Figure 6.9 shows the XPS measurements of the three samples with an SiN cap grown under hydrogen. Although the AFM images could suggest that there is indium desorption, with the formation of cracks in the layers, the XPS shows no evidence for this. The alloy composition is very similar for the all two samples, and it is noticeable that there is no major loss of indium, even for the third sample, which had 960s at 850°C under hydrogen. If we compare these compositions with the composition of the InGaAlN layer without any cap growth ($In_{0.08}Ga_{0.15}Al_{0.77}N$) we can see that we have kept a similar indium content, and so there is no evidence of losing indium. We think that the surface cracks could be either related to a desorption of indium only in certain parts of the sample. Also silane is known to open some surface defects at III-nitrides surface. [18]

An examination of the XPS profile of silicon for the sample with caps grown at T_{cap}=750°C and at T_{cap}=850°C and a t_{cap}=320s, once again it decreases from the surface and we cannot determine whether this is a doping or thin SiN layer. Silicon concentration was not measured for the sample having undergone an SiN growth during 960s. But we suggest that the Si profile would have the same shape as for the two others.

To examine the formation of an SiN cap layer we looked at electrical characterizations to see if there is a change in the mean deviation as previously observed in SiN on AlGaN layers. Electrical results are shown on the left of figure 6.10, and as we can see, there is still a large mean deviation (noise measurement) of the Rsheet value along the time axis, although for the final sample of 960s at 850°C the noise appears to be reduced. This would be coherent with deposition of an SiN layer (cf. experimental graph 6.2 on SiN deposited on AlGaN barrier layers). It is also coherent between the two SiN caps deposited during 320s at 750°C and 850°C. As shown on the right of the figure, the measurement noise appears less important than for the first, and actually the theoretical SiN growth rate is higher at 850°C than at 750°C since we are in the kinetic regime, therefore the SiN layer would be likely to be thicker at 850°C. We should note that there is no change in the average resistivity, while if doping were occurring, we would expect to have a lower resistivity after a longer deposition time.

The final InGaAlN layer with an SiN cap had both barrier and cap grown under hydrogen, with AFM image and XPS data shown in figure 6.11. The AFM morphology of this sample is that of an AlGaN with a strained (tension) layer undergoing cracks, as may be expected from the results in chapter 4, due to the hydrogen reducing indium incorporation. Once again, the AFM images do not show any evidence of an SiN layer. As previously for these barriers grown under hydrogen, Rsheet measurements were not possible, making the mean deviation analysis impossible. This is likely due to the fact that the barrier layer thickness is close to 30nm compared to all the other samples of this chapter having a barrier layer thickness of 12nm, making it harder to perform the breakdown required for the formation of an ohmic contact. In addition, the aluminum content of the AlGaN barrier layer is high, which also makes the breakdown harder. However, XPS profile once again seems to confirm the presence of some silicon in the surface of the barrier layer as for the samples above. This attempt to grow SiN on what is essentially an AlGaN layer is interesting, because it implies that the problem of growing these layers is due to the temperature, and not only due to the change of material from AlGaN (our standard barrier layer) to InGaAlN.

We should note that XRR measurements were performed for all of these samples, but we were not able to find any evidence of a SiN layer using this technique. However, it is difficult for us to measure layers less than 2nm with this technique on our samples, and so we cannot exclude the possibility of having grown very thin SiN layers.

We have not been able to prove the presence of an SiN capping of our InGaAlN layers even if we change the temperature from 725°C to 850°C, the growth time and the carrier gas. There is silicon present on the surface, but it is unclear if this is a very thin layer of SiN, or doping in the surface layers. One important parameter was not changed since we reached the maximum value : the silane flow. It may be that this flow is too low to allow us to nucleate an SiN cap on our InGaAlN, and a recent publication has shown that higher silane flows to allow the growth of SiN layers on InGaAlN barriers at low temperature [17].

For four samples, we had a look at their sheet resistivity and it was compared to those from InGaAlN samples measurements described in chapter 5. Results are shown in figure 6.12. We can see that effectively the trends of cap samples without AlN spacer follows the trend of uncapped barrier layers with an AlN spacer. In that case we could say that the sheet resistivity is lower than for samples without a spacer but we cannot rule on the presence or absence of a doping.

6.2 | GaN capping of InGaAlN and InAlN layers

Having difficulty characterizing SiN cap layers on InGaAlN barriers, we then focused on the epitaxy of a thin GaN cap. Indeed in chapter 3 we developed a study whose goal is to allow us to grow low temperature GaN with a good morphology and we will now apply it to the InGaAlN barrier layer capping. The main advantage is that we will make the surface smoother and protect it with a layer which can be grown in the same temperature range as that of InGaAlN, therefore not degrading it. The caps grown in this section are all in nitrogen atmosphere.

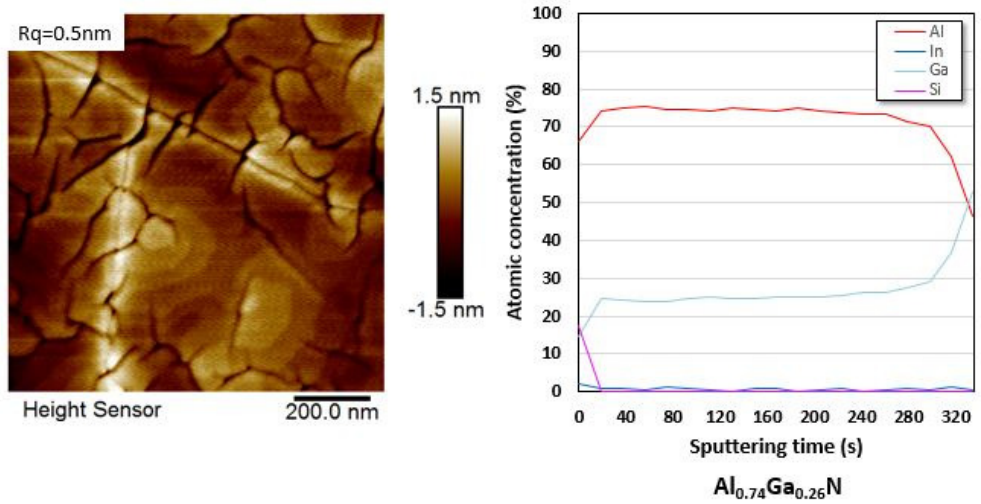

Fig. 6.11 – 1x1μm^2 AFM picture, and concentration profile by XPS along an SiN cap and an InGaAlN barrier layer, both under hydrogen carrier gas at 750°C during 320s.

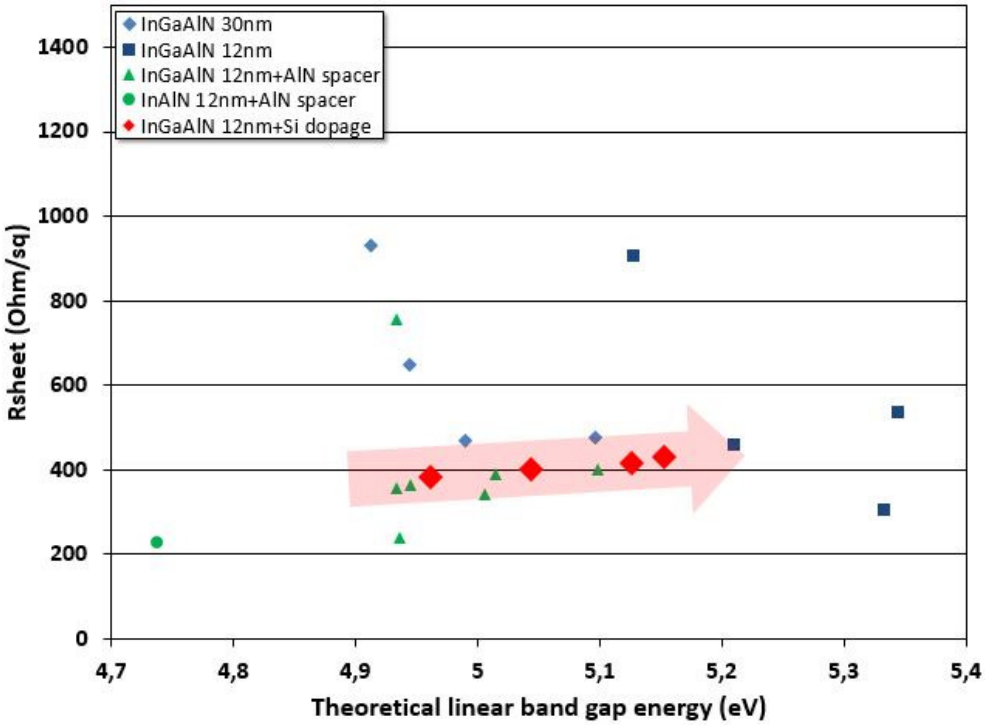

Fig. 6.12 – Rsheet measurements of InGaAlN barrier layers covered or not by an SiN cap versus the barrier band gap energy.

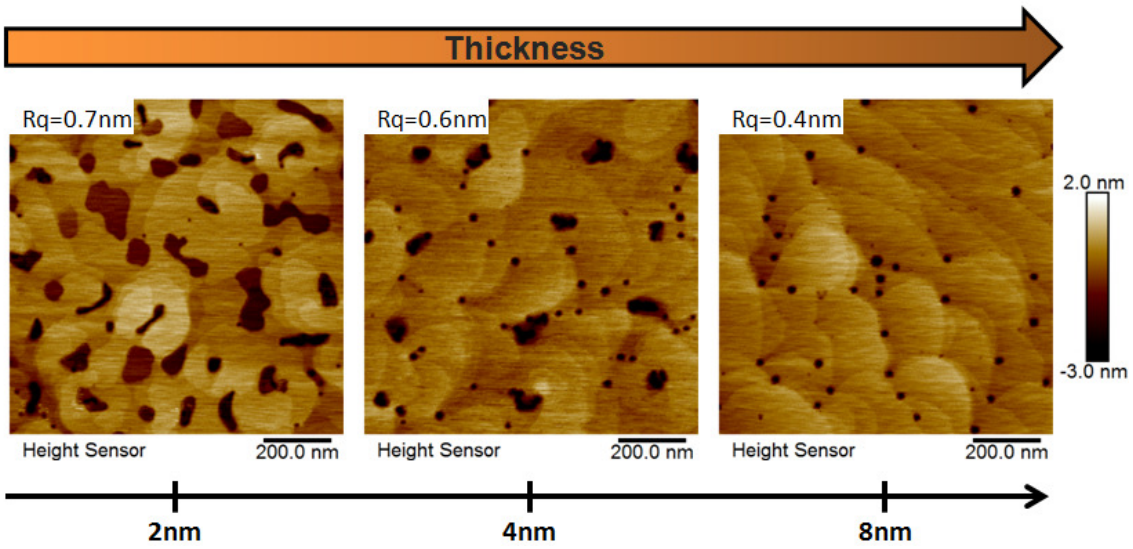

Fig. 6.13 – 1x1μm^2 AFM pictures of three different thicknesses of GaN caps on12nm thick InGaAlN barrier layer. T_{cap}=730°C.

6.2.1 | Thickness GaN cap optimization

For the first three samples, we studied the thickness of GaN caps and its effect on surface morphology. Thus we can estimate the thickness which is required to entirely smooth over the barrier layer. The samples were grown at 730°C at 20nm/min. We focused on three thicknesses : 2nm, 4nm, and 8nm, with their surface morphology shown in figure 6.13. The first thing we notice is that the InGaAlN barrier layer is totally covered in the image on the far right where we grew an 8nm thick GaN cap. In the two other cases to the left, we see a transition where we progressively cover the entire surface. Once again, we find the low temperature GaN surface morphology with its V-defects as in chapter 3. We are in the case of low temperature GaN growth at 730°C where the V-defect is starting from the interface and increases in size (diameter and depth) when we increase the cap layer thickness. Here the V-defects are smaller than in chapter 3 at 730°C under nitrogen carrier gas since we have grown only a few nanometers compared to 40nm and 120nm in chapter 3 figure **??**

We examined the cross section extracted from AFM measurements to visualize how the cap is covering the barrier layer surface. The results are shown in figure 6.14 where we see the flat areas at a certain thickness (2nm for sample 1 and 4nm for sample 2) where no cap is covering the barrier layer. We also see the inverted peaks in the first and third sample which correspond to the V-defects. These defects cross the entire cap layer, as we expect from our analysis in chapter 3, and are even continuing in the InGaAlN barrier layer also grown at low temperatures, as suggested by certain growth conditions shown in chapter 4. Moreover the fact that some areas are not covered by a GaN cap is not normal since the gas flow bringing the precursors at the sample surface is homogenous on the entire substrate. InGaAlN layers are quite rough compared to AlGaN layers for which SiN or GaN cap are easily deposited. Such a roughness or the chemical behaviour of the surface could make it difficult to wet the film with the growing GaN, leaving some bare areas. If the growth rate is too low, adatoms have too much time to move at the surface and to gather at certain areas before being covered by an overlying atomic layer. We were not able to perform subsequent experiments to test this hypothesis.

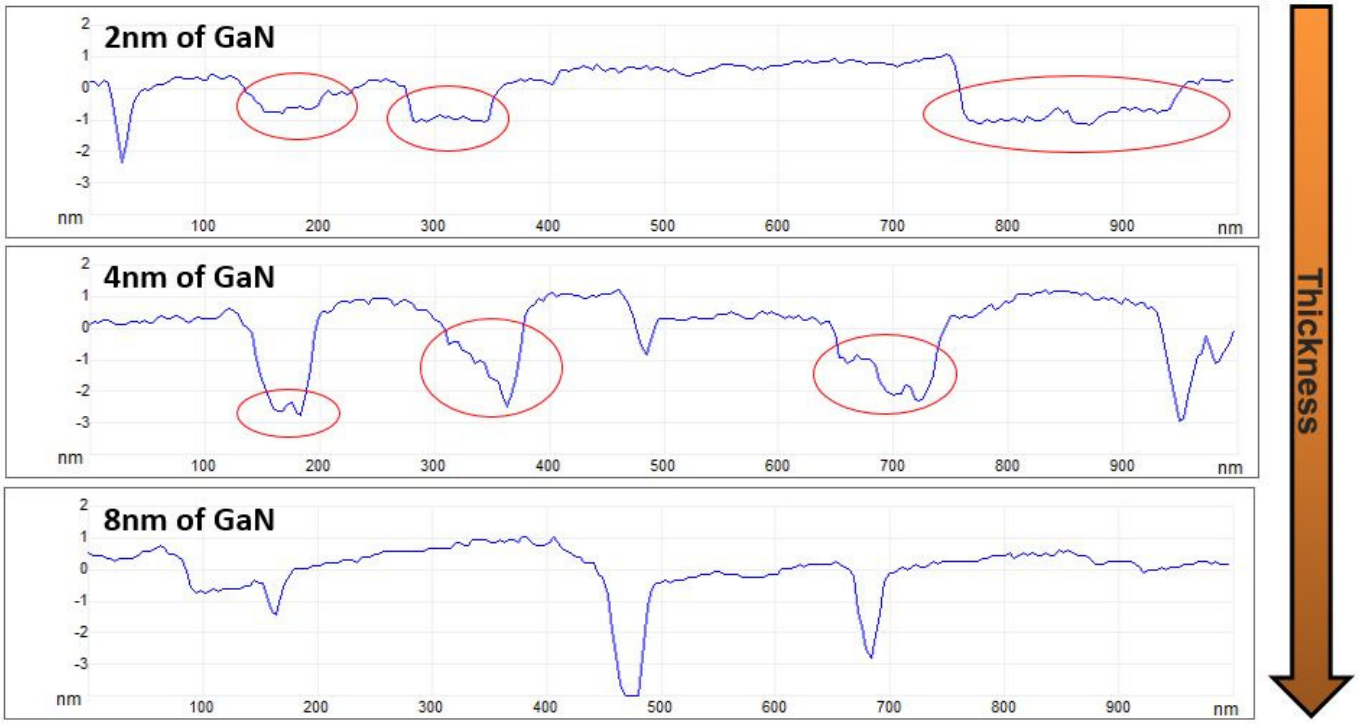

Fig. 6.14 – Cross sections from 1x1μm^2 AFM pictures of three different thicknesses of GaN caps on 12nm thick InGaAlN barrier layer. T_{cap}=730°C. In red ovals, non covered InGaAlN areas.

We also measured the 2DEG resistivity by Rsheet measurements on these three samples. When a GaN cap is grown on a barrier layer, this is not supposed to reduce the mean deviation of the resistivity as for SiN. However we see that when we increase the thickness, the Rsheet value starts to increase, as shown in figure 6.15. For a cap of 2 or 4 nm, we find Rsheet values in the same range than for a bare InGaAlN barrier layer, with only a small increase, while for 8 nm, we have a much stronger increase. This effect is known in AlGaN barriers with GaN caps, where the effect of epitaxial growth of GaN changes the band structure and reduces the density of carriers in the channel. Note that for these samples we don't have an AlN spacer. Therefore the Rsheet values are similar to those in chapter 5, when we treated Rsheet measurements on InGaAlN layers without AlN spacer. The optimal cap we have grown is therefore slightly above the 4nm thickness we have tried. Indeed in that case, the barrier layer was nearly entirely covered and the resistivity was not too much changed.

6.2.2 | Cap temperature variations

In this section we focused on a GaN cap thickness of 4nm that we estimated as the minimum required to cover the InGaAlN barrier layer, and we changed only the temperature. The goal is to see if we can slightly improve the roughness and reduce the V-defect size without too much damage the InGaAlN layer. We grew layers at two temperatures : 660°C and 730°C. The surface morphology is shown in figure 6.16 and we should mention that the InGaAlN barrier layer composition is not identical in the two samples. At the lowest temperature we have a morphology which shows the grain structure of low temperature (below 680°C) InGaAlN layers grown under nitrogen we studied in chapter 4. The GaN cap is well grown according to our in situ reflectometer. The InGaAlN surface may be too rough

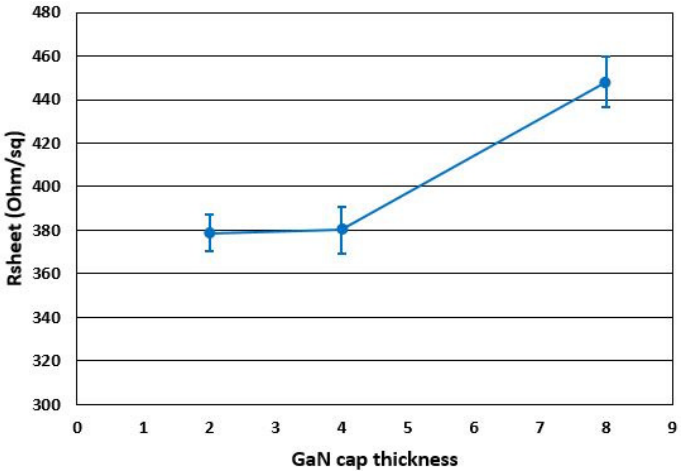

Fig. 6.15 – Rsheet versus GaN cap thickness : 2nm, 4nm, 8nm. No AlN spacer between GaN pseudosubstrate and InGaAlN barrier layer.

Sample structure	**Rsheet (Ohm/sq)**
12nm InGaAlN @660°C	358
12nm InGaAlN + 4nm GaN cap @660°C	366
12nm InGaAlN @730°C	370
12nm InGaAlN + 4nm GaN cap @730°C	379
AlN spacer + 12nm InGaAlN @730°C	241
AlN spacer + 12nm InGaAlN + 4nm GaN cap @730°C	270
AlN spacer + 12nm InAlN @730°C	230
AlN spacer + 12nm InAlN + 4nm GaN cap @730°C	409

Tab. 6.2 – Summary of Rsheet values depending on the heterostructure in the GaN cap study.

and the GaN cap too thin to smooth it. On the other sample we can see the step structure of GaN and some V-defects are present as seen for the previous layers.

Once again, the benefit of AlN interlayer between the GaN pseudosubstrate and the InGaAlN layer is important. We did some Rsheet measurements at the center of these wafers shown in table 6.2. On the sample (barrier layer + cap) grown at 660°C and on the one grown at 730°C, they demonstrate an Rsheet value of respectively 366 Ohm/sq and 270 Ohm/sq (379 Ohm/sq without spacer). As a reminder the same sample grown at 730°C without the GaN cap, but having the spacer, showed an Rsheet value of 241 Ohm/sq. So except a nice Rsheet value for these InGaAlN samples, the trends are coherent. The sheet resistivity strongly drops down with the presence of the AlN spacer, and the GaN cap increases slightly the Rsheet value.

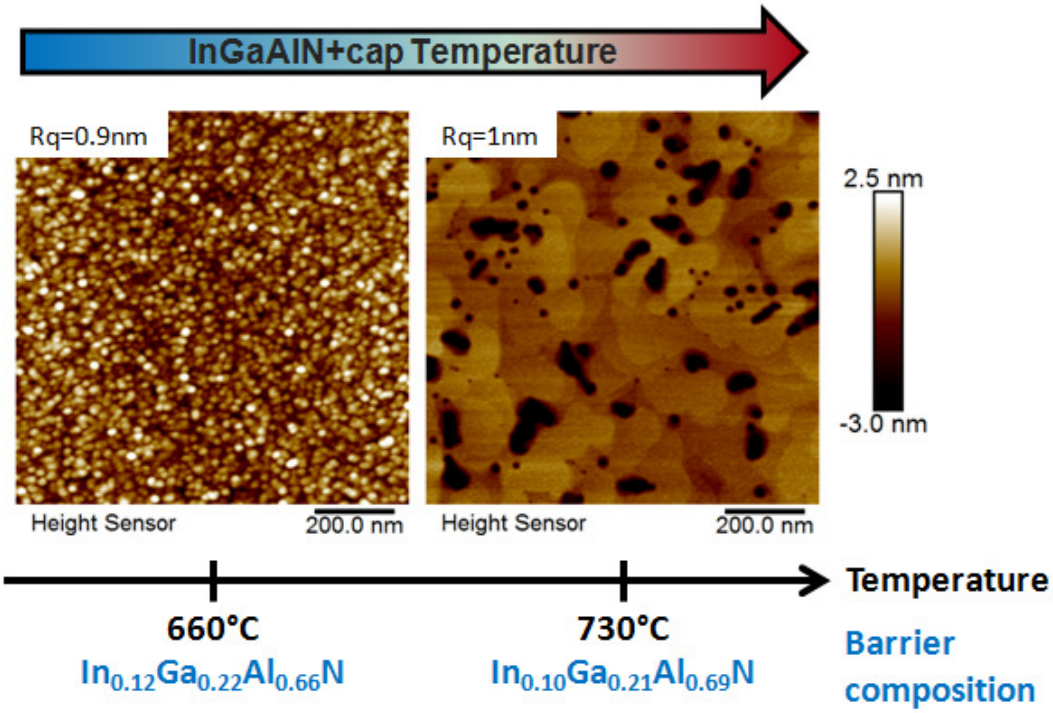

Fig. 6.16 – 1x1μm^2 AFM pictures of GaN cap 4nm thick grown on 12nm thick InGaAlN layer at 660°C, 730°C. Carrier gas for barrier and cap : N_2. InGaAlN composition shown below each picture.

6.2.3 | GaN cap on InAlN barrier layer

As we succeeded in fabricating pure InAlN layers in chapter 5, we decided to grow an optimized heterostructure containing the AlN spacer, the InAlN barrier layer and a good quality GaN cap. The surface morphology is shown in figure 6.17. We can see that the InAlN layer is nicely covered by the GaN cap. Results of this capping are similar to those on InGaAlN layers.

However while the Rsheet measurement on the InAlN barrier layer showed a value of 230 Ohm/sq, the presence of GaN cap seems to degrade it since it reaches 409 Ohm/sq on in the middle of the wafer and 395 Ohm/sq as a mean on the edges. This 2DEG resistivity value is a big increase, which we are currently not able to explain. It would be useful to redo this experiment to confirm the results.

We did a TEM analysis on this InAlN layer covered by a GaN cap and an equivalent without cap. In figure 6.18 we aligned the two samples with the same scale. That allows us to estimate the GaN thickness which is nearly 3-4nm and the InAlN which is 10-11nm. Note that without the GaN cap the InAlN layer thickness is closer to 7-8nm. This is surprising since we have the same growth recipe for the two barrier layers. We suggest that this is due to a desorption of atoms from the material during the cooling down after InAlN growth. As seen previously in AFM images, we see that the InAlN layer roughness is strongly improved when a cap is grown above, which confirms the interest of the GaN capping layer on the InAlN. This InAlN barrier layer thickness variation may participate in the reduction of sheet resistivity on the sample having a GaN cap but the influence of this cap is probably too strong.

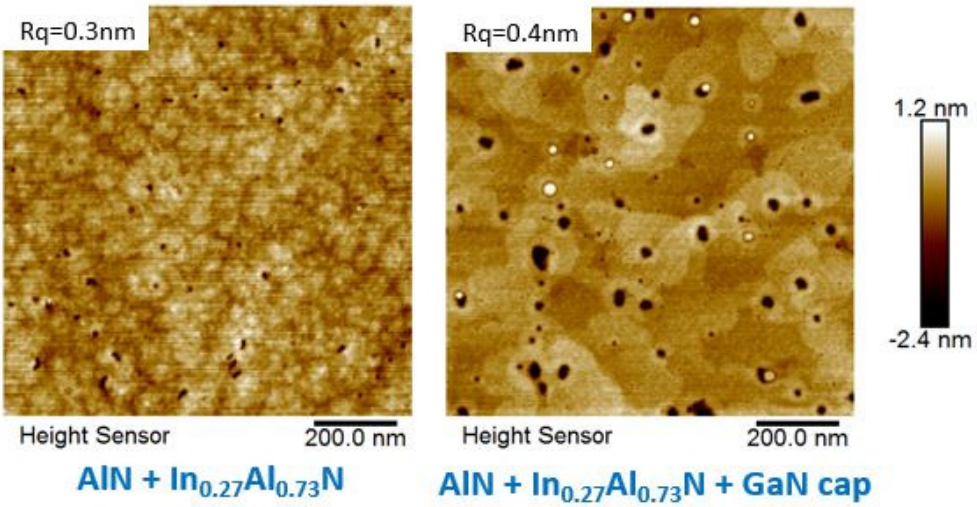

Fig. 6.17 – 1x1μm^2 AFM pictures of a 12nm thick $In_{0.27}Al_{0.73}N$ barrier layer, and of a 5nm thick GaN cap grown on 12nm thick $In_{0.27}Al_{0.73}N$ layer.

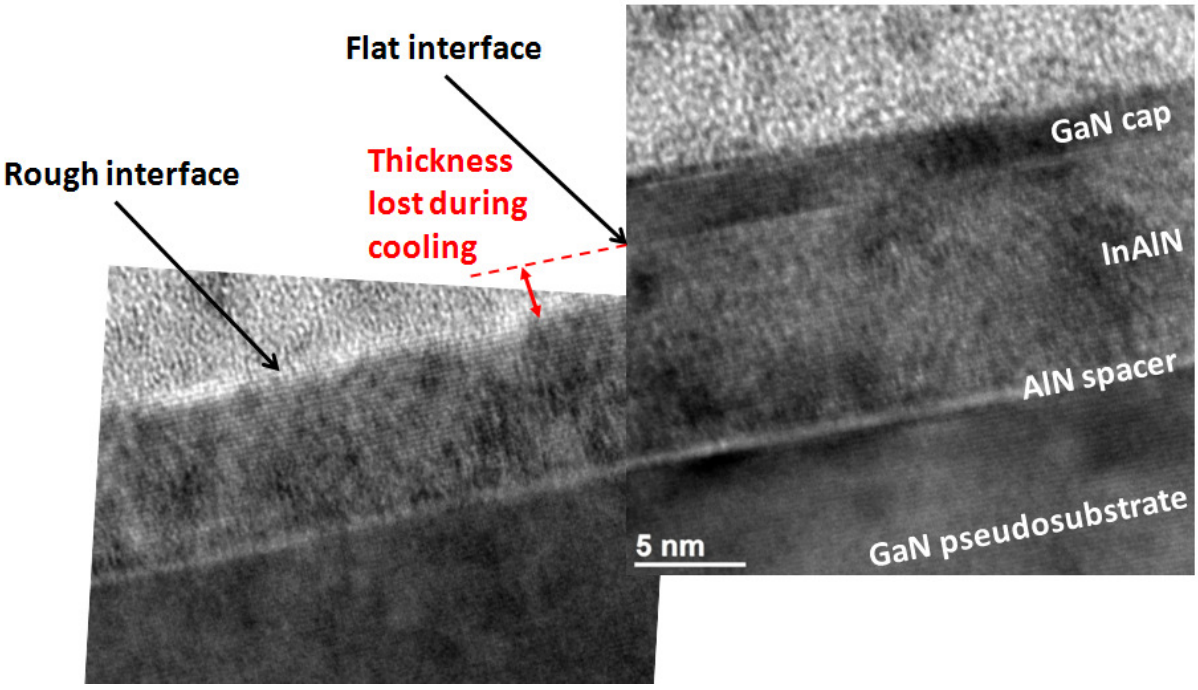

Fig. 6.18 – Two TEM pictures placed side by side of GaN pseudo-substrate, AlN spacer and InAlN layer. Left picture : 7-8nm thick InAlN layer. Right picture 3-4nm thick GaN cap on 10-11nm thick InAlN.

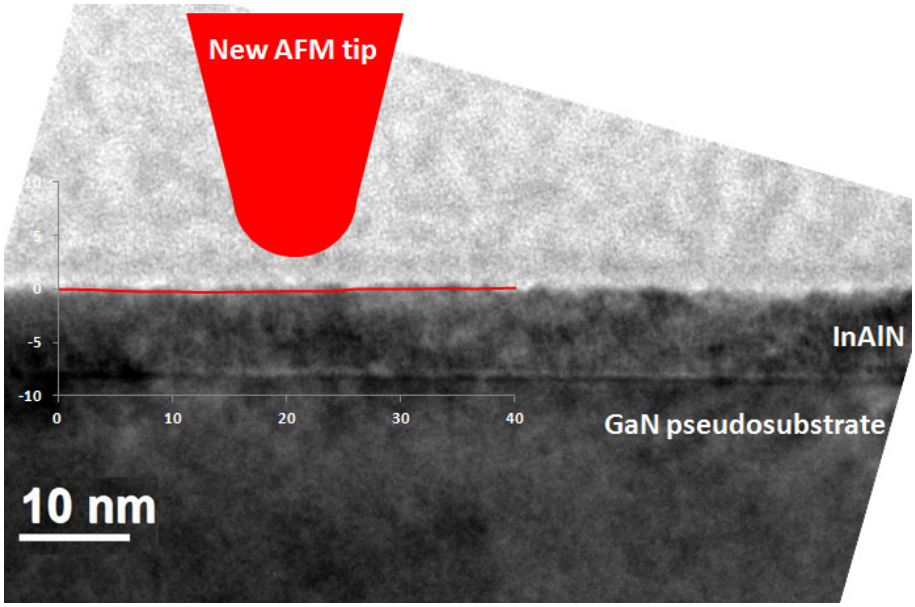

Fig. 6.19 – Comparison of AFM tip size versus InAlN layer roughness on TEM picture. Red curve : roughness profile from an AFM picture on the same sample.

We also compared the roughness from the TEM image with a roughness profile that we measured during a 1x1μm^2 AFM scan, as shown in figure 6.19 to confirm that our measurements are coherent. The roughness profile from the AFM image is shown as a red line superimposed with the TEM picture at the InAlN surface. While the roughness profile appears more flat than the real topology, the difference can be explained by the size of the AFM tip compared to the details of the surface morphology we are looking for. Indeed, when the tip is new we can expect a tip radius of 5nm but which could reach 12nm according to the supplier. This confirms the measurements, and shows the interest of including higher resolution characterizations like TEM in addition to AFM imaging.

We also compared the XRR profiles for InAlN without and with a GaN cap 6.20. We were not able to see the convolution of the two layers on the blue profile, but we can see the reduction of arches thickness compared to the red profile. This indicates that as expected, the pair of the InAlN layer and GaN is thicker than the structure without GaN cap. Also it seems that the red profile decreases in intensity more quickly after the critical angle which seems to confirm a rougher surface of only InAlN layer compared to the surface of the InAlN barrier layer with the GaN cap.

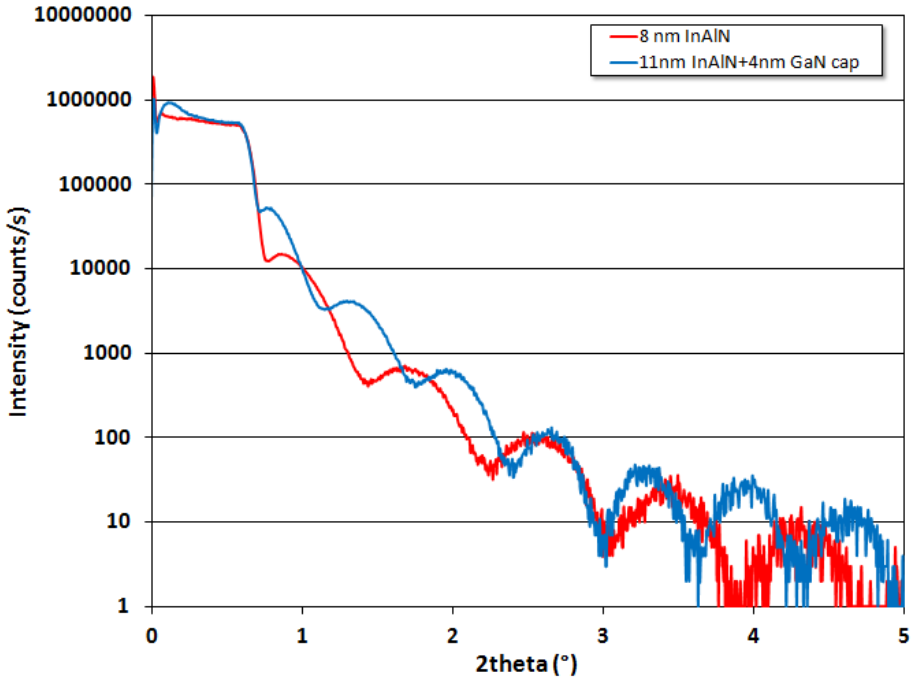

Fig. 6.20 – XRR profiles of 8nm thick InAlN barrier layer and an 11nm thick InAlN barrier layer with a 4nm thick GaN cap.

Summary of chapter 6

Experiments of InGaAlN barrier layers capping by SiN caps started with the use of nitrogen carrier gas in order to not desorb indium from the surface. A similar surface morphology between samples with and without a theoretical cap makes us think that the SiN was either not deposited or very thin. Even a temperature increase from 730˚C to 830˚C to promote the kinetics did not change it. In parallel Rsheet measurements showed a noisy Rsheet value versus the time, which is not correlated with usual response from SiN caps on AlGaN barrier layers. XPS measurements allow us to clearly identify the presence of silicon in (dopage) or on (SiN cap) the InGaAlN layer.
Switching the carrier gas to hydrogen, to examine the SiN deposition compared to that under nitrogen. The results were identical except for a long deposition time of 960s at 850˚C which should correspond to an SiN cap of 9.7nm. There, the sample surface presented cracks which could be attributed either to very surface indium desorption or to the effect of silane on surface defaults. This long SiN time deposition also gives a sample having a lower Rsheet measurement noise compared to the two ones whose cap where at 750˚C and 850˚C but during 320s which may be due to very thin SiN caps. In any case, under nitrogen or hydrogen, the Rsheet measurements showed values close to uncapped InGaAlN samples having an AlN spacer, which were not inserted in the SiN capping study. This argument may suggest some Si doping, but ultimately it is hard to be sure.
Finally we capped our InGaAlN samples with GaN layers. Three thicknesses of 2nm, 4nm, and 8nm where first grown and there was uncapped areas until 4nm GaN cap thicknesses. Also, above this thickness, we showed that the 2DEG resistivity was increased. The change of growth temperature, for the barrier layer and the 4nm thick GaN cap at the same time, demonstrates that the rough grain structure of the barrier layer at low temperature is not flattened by the GaN cap. On the other hand we successfully capped an InAlN layer with 5nm thick GaN cap and we clearly saw its benefits on the roughness according to TEM measurements even if the Rsheet increased from 230 Ohm/sq to 409 Ohm/sq.

Bibliographie

[1] T. Onuma, S. F. Chichibu, A. Uedono, T. Sota, P. Cantu, T. M. Katona, J. F. Keading, S. Keller, U. K. Mishra, S. Nakamura et S. P. DenBaars, « Radiative and nonradiative processes in strain-free alxga1-xn films studied by time-resolved photoluminescence and positron annihilation techniques », *Journal of Applied Physics*, vol. 95, no. 5, p. 2495–2504, 2004. 156

[2] K. Ooyama, K. Sugawara, S. Okuzaki, H. Taketomi, H. Miyake, K. Hiramatsu et T. Hashizume, « Deep electronic levels of alxga1-xn with a wide range of al composition grown by metal-organic vapor phase epitaxy », *Japanese Journal of Applied Physics*, vol. 49, no. 10R, p. 101001, 2010. 156

[3] A. Uedono, S. Ishibashi, S. Keller, C. Moe, P. Cantu, T. M. Katona, D. S. Kamber, Y. Wu, E. Letts, S. A. Newman, S. Nakamura, J. S. Speck, U. K. Mishra, S. P. DenBaars, T. Onuma et S. F. Chichibu, « Vacancy-oxygen complexes and their optical properties in aln epitaxial films studied by positron annihilation », *Journal of Applied Physics*, vol. 105, no. 5, p. 054501, 2009. 156

[4] W. Lu, V. Kumar, R. Schwindt, E. Piner et I. Adesida, « A comparative study of surface passivation on algan/gan hemts », *Solid-State Electronics*, vol. 46, no. 9, p. 1441 – 1444, 2002. 156

[5] R. Vetury, N. Q. Zhang, S. Keller et U. K. Mishra, « The impact of surface states on the dc and rf characteristics of algan/gan hfets », *IEEE Transactions on Electron Devices*, vol. 48, p. 560–566, Mar 2001. 156

[6] B. M. Green, K. K. Chu, E. M. Chumbes, J. A. Smart, J. R. Shealy et L. F. Eastman, « The effect of surface passivation on the microwave characteristics of undoped algan/gan hemts », *IEEE Electron Device Letters*, vol. 21, p. 268–270, June 2000. 156

[7] S. Trassaert, B. Boudart, C. Gaquiere, D. Theron, Y. Crosnier, F. Huet et M. A. Poisson, « Trap effects studies in gan mesfets by pulsed measurements », *Electronics Letters*, vol. 35, p. 1386–1388, Aug 1999. 156

[8] S. Arulkumaran, T. Egawa, H. Ishikawa, T. Jimbo et Y. Sano, « Surface passivation effects on algan/gan high-electron-mobility transistors with sio2, si3n4, and silicon oxynitride », *Applied Physics Letters*, vol. 84, no. 4, p. 613–615, 2004. 156

[9] H.-C. Chiu, C.-H. Chen, C.-W. Yang, H.-L. Kao, F.-H. Huang, S.-W. Peng et H.-K. Lin, « Highly thermally stable in situ sinx passivation algan/gan enhancement-mode high electron mobility transistors using tiw refractory gate structure », *Journal of Vacuum Science & Technology B, Nanotechnology and Microelectronics : Materials, Processing, Measurement, and Phenomena*, vol. 31, no. 5, p. 051212, 2013. 156

[10] W. S. Tan, P. A. Houston, P. J. Parbrook, G. Hill et R. J. Airey, « Comparison of different surface passivation dielectrics in algan/gan heterostructure field-effect transistors », *Journal of Physics D : Applied Physics*, vol. 35, no. 7, p. 595, 2002. 156

[11] J. SHEALY, T. PRUNTY, E. CHUMBES et B. RIDLEY, « Growth and passivation of algan/gan heterostructures », *Journal of Crystal Growth*, vol. 250, no. 1, p. 7 – 13, 2003. Proceedings of the Fourteenth American Conference on Crystal Grow th and Epitaxy. 156

[12] J. BERNAT, P. JAVORKA, A. FOX, M. MARSO, H. LÜTH et P. KORDOS, « Effect of surface passivation on performance of algan/gan/si hemts », *Solid-State Electronics*, vol. 47, no. 11, p. 2097 – 2103, 2003. 156

[13] K. CHABAK, D. W. JR., M. TREJO, A. CRESPO, M. KOSSLER, J. GILLESPIE, R. GILBERT, B. POLING, S. TETLAK, R. FITCH et G. VIA, « Performance of strained alinn/aln/gan hemts with si3n4 and ultra-thin al2o3 passivation », *in CS MANTECH Conference, Palm Springs, California, USA*, May 16th-19th 2011. 156

[14] H. BEHMENBURG, L. R. KHOSHROO, C. MAUDER, N. KETTENISS, K. H. LEE, M. EICKELKAMP, M. BRAST, D. FAHLE, J. F. WOITOK, A. VESCAN, H. KALISCH, M. HEUKEN et R. H. JANSEN, « In situ sin passivation of alinn/gan heterostructures by movpe », *Physica Status Solidi*, vol. 7, p. 2104–2106, 2010. 156

[15] L. LUGANI, J.-F. CARLIN, M. A. PY et N. GRANDJEAN, « Thermal stability and in situ sin passivation of inaln/gan high electron mobility heterostructures », *Applied Physics Letters*, vol. 105, no. 11, p. 112101, 2014. 156

[16] M. RZIN, J. M. ROUTOURE, B. GUILLET, L. MÉCHIN, M. MORALES, C. LACAM, P. GAMARRA, P. RUTERANA et F. MEDJDOUB, « Impact of gate-drain spacing on low-frequency noise performance of in situ sin passivated inalgan/gan mis-hemts », *IEEE Transactions on Electron Devices*, vol. PP, no. 99, p. 1–6, 2017. 156

[17] P. GAMARRA, C. LACAM, M. TORDJMAN, F. MEDJDOUB et M.-A. di FORTE-POISSON, « In-situ passivation of quaternary barrier inalgan/gan hemts », *Journal of Crystal Growth*, vol. 464, p. 143 – 147, 2017. Proceedings of the 18th International Conference on Metal Organic Vapor Phase Epitaxy. 156, 164

[18] R. OLIVER, M. J. KAPPERS, J. SUMNER et R. DATTA, « Sih4 exposure of gan surfaces : A useful tool for highlighting dislocations », *in MRS Proceedings*, no. 892, 2011. 163

General conclusion

This three-year work allowed us to take up several challenges in the manufacture of III-Ns grown on 200mm large silicon substrates. Although the core of this work has been centered around growth of indium containing III-N materials from the beginning, the necessity of a GaN growth in the same temperature ranges for optical prospects, and a cap deposition, to protect our layers and allow a backup of layers quality during steps of the manufacturing process of electronic devices, quickly and progressively appeared as the studies progressed.

A first study, whose goal was to improve the surface structure of GaN layers grown at low temperatures, less than 1050°C, started our experimental results description. The work was in the context of indium containing III-N alloys capping and the manufacture of multi quantum-well including the entanglement of InGaAlN and GaN layers, and also a way to better understand the low temperature growth of III-N materials. It was an opening of the development of InAlN and InGaAlN alloys to optical applications and it was easy to implement during a sample growth. There, we decided to improve the surface quality of GaN layers and thus MQWs ones by reducing the V-defects size at their surface. An increase of the temperature from 730°C to 930°C shows us a transition point at which the V-defects were becoming small (a dozen of nanometers large), rather than increasing with the thickness of the film. But it implies high temperatures for InAlN and InGaAlN alloys which could be present in a potential MQWs. Thus a switch from nitrogen to hydrogen carrier gas solved a part of the problem since it first allows to us to gain at least 100°C reduction on the transition temperature and moreover decreases global the surface roughness. All of these trends where explained by analytical model we built based on strain from the dislocation line in the material which is in competition with surface energy of inclined planes forming the V-defects. This showed that there are two modes ; one where the V-pits are limited in size, regardless of the film thickness ; and another where the V-pits continue to grow as the film increases thickness, without limit.

In the field of indium containing III-N alloys growth like InAlN and InGaAlN, we examined how the indium is integrated depending on growth condition. In particular we confronted the dependence of growth parameters versus the use of two carrier gases : nitrogen and hydrogen. Under nitrogen, the temperature had a strong effect on indium incorporation, measured by XPS, due to the high vapor pressure of InN compared to GaN and AlN binaries, where a reduction down to 670°C still allowed us a increase of the indium content. The TMIn/TMAl ratio was the second varied parameter that influenced a lot the indium content in the alloys, as would be expected, while the growth rate did not strongly influence the indium incorporation. Other growth parameters like growth time, or ammonia flow did not impact the indium content.

Under hydrogen, which does not thermodynamically favor indium integration, we had to decrease the temperature to 611°C to have some indium in the layers. At this temperature, an increased growth rate strongly increased the indium content in the alloys, and we successfully managed to integrate 6% indium into the alloy. Although this was a good result, the films do not necessarily have improved surface morphology versus those under nitrogen due to the greatly reduced growth temperature. There was also a slight increase in gallium pollution from the chamber.

We had the first indications of phase separation phenomenon in indium containing III-Ns since the photoluminescence peak and thus the measured band gap energy was changed with changing thickness, while the indium content was the same in all the layers. In addition, we saw that changing the growth rate also changed the photoluminescence peak, while the overall composition stayed the same. To try to understand these results we used other techniques to measure the composition, such as XRD, and Auger electron spectrometry characterization to start a quantification and a comprehension of the indium segregation in InGaAlN and InAlN. First results with Auger were encouraging but further work using new characterizations like atom probe tomography are needed to better understand these phenomenon.

While investigating the integration of indium we highlighted the problem of gallium pollution in showerhead MOCVD reactors. We successfully isolated growth parameters which are influencing the gallium content increase during the growth of theoretical InAlN layers, with principally the TMIn flow needing to be reduced to reduce the gallium content. This suggests that the TMIn is somehow interacting with a GaN coating in the reactor to bring gallium into the layer. This is difficult to deal with because the TMIn flow also directly controls the indium content in the material, for specific process conditions. To overpass this problem, we successfully developed a procedure with a chamber cleaning process after the GaN substrate growth and before the InAlN layer growth to successfully grow a pure InAlN sample. From this improvement of our process, we have been able to get more than 18% in the In/(In+Al) ratio under nitrogen carrier gas, and 17% under hydrogen carrier gas.

We were also successful in creating a “phase diagram” of surface morphology for different growth conditions, with a transition from very finely grained structures to large island growth. Comparison of growth temperature and growth rate evolution suggested a strong influence of the surface mobility on morphology generated at the surface.

Our work was directed toward a material study but the final objective of InAlN and InGaAlN layers was still the production of HEMTs. It was difficult to measure the sheet resistivity of the 2DEG when the barrier layers made of the ternary of quaternary alloy was thicker than 30nm. But when we successfully measured the sheet resistivity, we saw that the decrease of indium content, and thus the increase of the piezoelectric effect due to the increase of strain in the material which is not matched on GaN substrate below 18% In/(In+Al), implies a decrease of the resistivity down to around 300 Ohm/sq. Moreover, for a given composition, thicker barrier layers imply lower resistivity. To get lower resistivity than 300 Ohm/sq we inserted an AlN spacer between the GaN substrate and InAlN or InGaAlN barrier layer. This allowed us to reach 240 Ohm/sq and 230 Ohm/sq for our best samples with InGaAlN and InAlN.

This validates the new approach of cleaning the reactor between growth of the GaN and growth of the barrier layer for future HEMT fabrication.

To finish, the capping of our barrier layers we encountered difficulties to deposit SiN layer on InGaAlN ones during the growth process. The different characterizations realized on them, whether it is AFM, XPS or XRR techniques did not allowed us to decide between a very thin SiN layer and a silicon doping of the barrier layer. Electrical results could possibly lean in favour of doping, but this is still uncertain. It appears that a higher silane flow is necessary for growth of these films at such low temperatures. On the other hand, we produced good surfaces using GaN capping layers. We calibrated the right thickness of nearly 4-5nm that combined a good surface coverage of InGaAlN and InAlN barrier layers and a sheet resistivity not too much increased which reached 270 Ohm/sq for an InGaAlN barrier layer with an AlN spacer, and 390 Ohm/sq for an InAlN barrier layer still with an AlN spacer. There, we were able to produce high performance HEMT heterostructures with InGaAlN and InAlN barrier layers with a high quality capping.

Our study could be completed and we would guide future work on these areas. First, in the field of GaN grown at low temperature, we would suggest experimental data that could underline the transition temperature from which V-defects are decreasing in diameter at fixed other growth conditions. In the same way our model could be improved. Then, about the phase separation study, we would suggest an increase of statistics by Auger spectroscopy measurements at different scales on several samples, and eventually a try of atom probe tomography. Also, we produced few InAlN samples after our process improvements, and a deep investigation of this ternary alloys would require more data. Then a comparison with InGaAlN quaternay alloys should be interesting in term of their performance in HEMT heterostructures. To finish, SiN cap layers could be grown with increased silane flows and that could be an interesting way of improvement, but requiring hardware changes which is not easy. On the other side, growth parameters of GaN caps could be adjust to entirely cover the barrier layer surface for low thicknesses since in our case, holes emerged on the surface of the barrier layer below a cap thickness of 4-5nm.

Appendix : Composition and strain calculation in InGaAlN and InAlN layers using RSM and WDXRF measurements

We propose here a series of equations that can allows us to estimate the InGaAlN (or even InAlN) alloy composition and the biaxial strain in the material using XRD-RSM and WDXRF characterisations. The first gives us a and c lattice parameters and the second the In/(In+Al) ratio. This procedure follows the calculation of the lattice parameters shown in chapter 2 by means of the RSM measurement. Thus we can express a system of six equations and six variables.

The two first equations are linking a and c lattice parameters of InGaAlN (from XRD RSM) with the atomic fraction of each binary in equations 6.1 and 6.2, according to Vegard's law.

$$a_{InGaAlN} = x_{In}a_{InN} + x_{Ga}a_{GaN} + x_{Al}a_{AlN} \tag{6.1}$$

$$c_{InGaAlN} = x_{In}c_{InN} + x_{Ga}c_{GaN} + x_{Al}c_{AlN} \tag{6.2}$$

But here $a_{InGaAlN}$ and $c_{InGaAlN}$ are values when the material is relaxed since the lattice parameters of each binary in the literature are given without any stress. We know that :

$$\epsilon_x = \frac{a_{RSM} - a_{InGaAlN}}{a_{InGaAlN}} \tag{6.3}$$

Also using the deformation matrix and its symmetry for III-N hexagonal structure, we have

$$\epsilon_z = -2\frac{C13_{InGaAlN}}{C33_{InGaAlN}}\epsilon_x = \frac{c_{RSM} - c_{InGaAlN}}{c_{InGaAlN}} \tag{6.4}$$

Note that ϵ_x and ϵ_z are respectively the in-plane and out-plane biaxial strain, a_{RSM} and c_{RSM} are respectively the a and c lattice parameters of InGaAlN extracted from RSM measurements, and $C13_{InGaAlN}$ and $C13_{InGaAlN}$ are two elastic coefficients of deformation matrix of our alloy. Therefore equations 6.1 and 6.2 become :

$$a_{RSM} = (x_{In}a_{InN} + x_{Ga}a_{GaN} + x_{Al}a_{AlN}).(1 + \epsilon_x) \tag{6.5}$$

$$c_{RSM} = (x_{In}c_{InN} + x_{Ga}c_{GaN} + x_{Al}c_{AlN}).(1 - 2\frac{C13_{InGaAlN}}{C33_{InGaAlN}}\epsilon_x) \tag{6.6}$$

Then we can express $C13_{InGaAlN}$ and $C13_{InGaAlN}$ assuming linearity as a function of C13 and C33 of

each binary. So we get :

$$C13_{InGaAlN} = x_{In}C13_{InN} + x_{Ga}C13_{GaN} + x_{Al}C13_{AlN} \tag{6.7}$$

$$C33_{InGaAlN} = x_{In}C33_{InN} + x_{Ga}C33_{GaN} + x_{Al}C33_{AlN} \tag{6.8}$$

The two last equations are simply :

$$x_{In} + x_{Ga} + x_{Al} = 1 \tag{6.9}$$

$$r_{WDXRF} = \frac{x_{In}}{x_{In} + x_{Al}} \tag{6.10}$$

Communications and publications

Communications

1. Poster at the European Workshop of MOVPE : Improvements in the surface morphology of low temperature GaN grown by MOVPE.
2. Oral at the International conference of MOCVD : Growth by MOCVD of In(Ga)AlN alloys, and a study of gallium contamination in these layers under nitrogen and hydrogen carrier gas.

Publications

1. R. Bouveyron, M.B. Charles, Growth by MOCVD of In(Ga)AlN alloys, and a study of gallium contamination in these layers under nitrogen and hydrogen carrier gas, Journal of Crystal Growth, vol. 464, p. 105-111, 2016.
2. R. Bouveyron, M.B. Charles, Improvements in the surface morphology of low temperature GaN grown by MOVPE. To be submitted in Surface Science in 2018
3. M. Charles, Y. Baines, A. Bavard, R. Bouveyron, High growth rate GaN on 200mm silicon by Metal-Organic Vapor Phase Epitaxy for High Electron Mobility Transistors, Journal of Crystal Growth, vol. 483, p. 89-93, 2018.
4. Y. Mazel, E. Nolot, J.-P. Barnes, M. Charles, R. Bouveyron, M. Mrad, Multitechnique elemental depth profiling of InAlGaN and InAlN films. Submitted in Journal of Vacuum Science and Technology B in 2017.

Résumé

Cette thèse est principalement axée sur le développement des matériaux III-N pour les transistors de puissance HEMTs, ainsi que les multipuits quantiques et les applications optroniques qui en découlent dans une moindre mesure. Suite à un rappel des propriétés des nitrures, des différentes applications possibles, du principe de la MOCVD et des différentes caractérisations retenues pour ce travail, nous avons traité dans un premier temps la croissance de GaN à basse température, c'est-à-dire en dessous de 1050°C. La fabrication de multipuits impliquant l'alternance des couches de GaN et d'InAlN ou InGaAlN nous contraint de travailler à ces températures ce qui génère l'apparition d'un défaut en surface du GaN que l'on nomme V-defect. Une étude expérimentale poussée nous a permis de comprendre comment apparaissent et évoluent ces défauts selon les paramètres de croissance. Un modèle basé sur les énergies de surface à pu être élaboré et explique l'évolution de ces défauts. Ensuite nous avons défini l'influence de nombreux paramètre de croissance par MOCVD et tiré, des multiples tendances mises en relief, des modèles et explications justifiant telle ou telle propriété physique et chimique du matériau. En aval, ce sont des caractérisations électriques et principalement des mesures de résistivités qui ont été traitées afin de comparer la performance de nos échantillons à base d'indium à ceux de type AlGaN/GaN. Le problème de la pollution au gallium dans les réacteurs MOCVD verticaux a été mis en évidence et nous avons proposé différentes solutions pour la limiter, voire l'annihiler. Pour terminer ce sont des couches de protection à base de SiN et GaN que nous avons tenté de développer afin de protéger nos alliages à base d'indium pour la suite des étapes technologiques nécessaires à la fabrication d'un composant par exemple.

Abstract

This thesis is mainly focused on the development of III-N materials for HEMTs power transistors, as well as quantum wells and optronics applications that result to a lesser extent. Following a reminder of the properties of nitrides, the different possible applications, the principle of the MOCVD and the different characterizations used for this work, we first treated the growth of GaN at low temperature, that is to say below 1050°C. The manufacture of multiple quantum wells involving the alternation of GaN and InAlN or InGaAlN layers forces us to work at these temperatures, which generates the appearance of a defect in surface of the GaN which is called V-defect. An advanced experimental study allowed us to understand how these defects appear and evolve according to the growth parameters. A model based on surface energies could be developed and explains the evolution of these defects. Then we defined the influence of many MOCVD growth parameters by MOCVD and derived, from the multiple trends highlighted, the models and explanations justifying this or that physical and chemical property of the material. Downstream, these are electrical characterizations and mainly resistivity measurements that have been processed to compare the performance of our indium-based samples to those of AlGaN/GaN type. The problem of gallium pollution in vertical MOCVD reactors has been highlighted and we have proposed different solutions to limit or even annihilate it. Finally, we have tried to develop protective layers based on SiN and GaN in order to protect our indium-based alloys for the next technological steps required to manufacture a component, for example.